

# Synthesis of Materials for Energy Applications Focusing on MAX Phases

---

*Submitted for the fulfilment of the requirement for the Degree of Doctor of  
Philosophy (Mechanical Engineering)*

*at the*

*University of Newcastle, Australia*

Dylan Thomas Cuskelly B.Eng (Mechanical) (Hons)



**Submission date:** January 2016

*Principal supervisor: Professor Erich Kisi*

*Co-supervisor: Doctor Heber Sugo*



## **Statement of Originality**

The thesis contains no material which has been accepted for the award of any other degree or diploma in any university or other tertiary institution and, to the best of my knowledge and belief, contains no material previously published or written by another person, except where due reference has been made in the text. I give consent to the final version of my thesis being made available worldwide when deposited in the University's Digital Repository\*\*, subject to the provisions of the Copyright Act 1968. \*\*Unless an Embargo has been approved for a determined period.

I hereby certify that the work embodied in this thesis has been done in collaboration with other researchers, or carried out in other institutions I have included as part of the thesis a statement clearly outlining the extent of collaboration, with whom and under what auspices.

I hereby certify that the work embodied in this thesis contains a published paper/s/scholarly work of which I am a joint author. I have included as part of the thesis a written statement, endorsed by my supervisor, attesting to my contribution to the joint publication/s/scholarly work.



## **Acknowledgments**

This thesis would have not been possible without the help of a great many people. First and foremost to Erich Kisi for your teaching and support but most of all for your encouragement. At every occasion you helped to push me forward, not ever holding me back, regardless of how many half-baked ideas I had. The work environment you created ensured that my time never really felt like work and I always felt valued. I hope I have gone some way to fulfilling the faith you have shown in me.

To Heber Sugo, for your guidance, advice, help and patience. Your willingness to share your knowledge, expertise and time no matter how many other things you had going on is so greatly appreciated. Each time you were involved in an idea or project it was always improved.

I could not ask for better supervisors.

To Jenny Zobec and Dave Phelan, for your time, guidance and friendship. You helped to make the long days spent doing data analysis an enjoyable experience, which is not a thing most people get to say about their work. I always looked forward to going to XRD.

To all the guys in the Mech Eng workshop, and especially Dean, Mitch and Ian. I asked for more help than almost anyone, and you guys never turned me away. I appreciate all of it, there is no way I could have achieved half of the work I did without you guys

around to make me a custom part, fix one of my poor designs or teach me how to do a job right.

Last but by no means least, The Condors. Otterking Rawtones, Daniel bad knees, Sam Swan, The Post Box, Jossby and Erin Richards. You're all great! I'm proud to call you both great colleagues but better great friends. Monday morning scotch and creative Fridays as well as afternoon cricket are all memories I'll carry even after I've forgotten everything else in this thesis. A special thank you to Erin, you contributed more to what's actually in my thesis than anyone else.

I am a thankful recipient of both an Australian postgraduate award and an ARENA scholarship top-up. I am also very thankful to Glen and Ken Moss for the scholarship which helped me to secure my initial funding. Without your support this project would never have even been started, thank you.

## Table of contents

|        |  |     |
|--------|--|-----|
| 1.     | Introduction.....  | 13  |
| 1.1.   | Thesis synopsis.....   | 13  |
| 1.2.   | General context.....   | 14  |
| 1.3.   | MAX phases .....   | 20  |
| 1.3.1. | Synthesis .....  | 26  |
| 1.3.2. | Thermodynamic stability .....  | 28  |
| 1.3.3. | Kinetic accessibility .....  | 33  |
| 1.3.4. | Reactants and reaction mechanisms.....   | 38  |
| 1.4.   | Thermal energy storage introduction.....   | 40  |
| 1.5.   | Thermionic energy conversion.....  | 45  |
| 2.     | Scope statement .....  | 53  |
| 3.     | Publications.....  | 55  |
| 3.1.   | Statements of contribution.....  | 58  |
| 4.     | Methodology.....   | 66  |
| 4.1.   | Sample preparation.....  | 66  |
| 4.2.   | X-ray diffraction analysis.....  | 72  |
| 4.3.   | Scanning electron microscope (SEM) analysis .....  | 81  |
| 4.4.   | Additional Experimental Methods .....  | 85  |
| 4.4.1. | Schottky chamber.....  | 85  |
| 4.4.2. | Thermal testing.....   | 89  |
| 5.     | Publication 1: MAX phase - alumina composites <i>via</i> exchange reaction in the $M_{n+1}AlC_n$ systems ( $M= Ti, V, Cr, Nb, or Ta$ ) .....                 | 92  |
| 6.     | Publication 2: MAX phase – alumina composites via elemental and exchange reactions in the $Ti_{n+1}AC_n$ systems ( $A = Al, Si, Ga, Ge, In$ and $Sn$ ). .... | 117 |
| 7.     | Publications 3: Single step carbothermal synthesis of high purity MAX phase powders .....  | 144 |
| 8.     | Publication 4: $Ti_3GaC_2$ and $Ti_3InC_2$ : first bulk synthesis, DFT stability calculations and structural systematics .....                               | 156 |
| 9.     | Publication 5: Miscibility gap alloys with inverse microstructures and high thermal conductivity for high energy density thermal storage applications .....  | 183 |
| 10.    | Publication 6: High conductivity phase change materials for thermal energy storage – miscibility gap alloys .....  | 204 |
| 11.    | Publication 7: Development of a thermionic converter for CSP application....   | 220 |
| 12.    | Publication 8: Low temperature synthesis of low thermionic work function ( $La_xBa_{1-x}B_6$ ). ....   | 238 |

|       |   |     |
|-------|---|-----|
| 13.   | Additional results .....  | 258 |
| 13.1. | Separation of $Ti_3SiC_2 - Al_2O_3$ composites .....                                  | 258 |
| 13.2. | <i>In situ</i> neutron diffraction of $Ti_3SiC_2 - Al_2O_3$ composite formation ..... | 262 |
| 13.3. | Alternative reducing agents (Mg and B) .....  | 266 |
| 13.4. | MGA synthesis .....   | 268 |
| 14.   | General discussion and future work .....  | 271 |
| 14.1. | Optimisation and expansion of aluminothermic MAX phase synthesis....                  | 271 |
| 14.2. | Expansion of the carbothermal reaction mechanism .....                                | 275 |
| 14.3. | Other reducing agents .....   | 278 |
| 14.4. | MAX phase - $Al_2O_3$ composite.....  | 278 |
| 14.5. | Miscibility Gap Alloys .....  | 280 |
| 14.6. | Thermionic emission .....   | 282 |
| 15.   | Conclusions .....   | 285 |

## List of figures

|  |     |
|--|-----|
| Figure 1 A typical power cycle similar to that used in the conversion of thermal energy to electricity. An electrical generator is normally attached to the turbine <sup>[2]</sup> .....   | 15  |
| Figure 2 Concentrated solar power plant showing mirros on left focusing solar raditation onto the collector tower on the right. <sup>[5]</sup> .....   | 18  |
| Figure 3 Solar radiation and power consumption on a typical day in Newcastle, NSW, Australia. Note the intermittency of solar radiation and the offset between peak solar insolation (~12:00) and peak power consumption (~17:00).....   | 18  |
| Figure 4 Elements known to make up the MAX phases. Red denotes M-elements, blue A-elements and grey X-elements. ....   | 21  |
| Figure 5 $M_3AX_2$ crystal structure. Green octahedra represent MX bonding, white layers are the A-element <sup>[13]</sup> .....   | 22  |
| Figure 6 Crystal structures of the MAX phases; (a) 211 or n = 1 and (b) 312 or n=3 type. Purple indicates M-elements, blue A-elements and black X-elements <sup>[15]</sup> .....   | 23  |
| Figure 7 Ternary phase diagram in the Ti-Si-C system at 1200°C with the MAX phase composition highlighted. The many competing phases can also be seen <sup>[24]</sup> .....  | 28  |
| Figure 8 Ellingham diagram showing common oxides. Lines representing more stable metal oxides can be seen at the bottom of the chart whereas more easily reduced oxides appear higher up. $CO_2$ and CO are the dashed lines with zero and negative gradient respectively. <sup>[25]</sup> ..... | 31  |
| Figure 9 Molten salt tanks and infrastructure for thermal storage in a trough collector solar field <sup>[14]</sup> .....  | 42  |
| Figure 10 Simplified thermionic converter showing the basic configuration of key components. ....  | 46  |
| Figure 11 Common metallic crystal lattices. ....   | 74  |
| Figure 12 Principles of X-ray diffraction .....  | 75  |
| Figure 13 Typical XRD pattern from the program Highscore for a $Ti_3SiC_2$ sample. Blue lines represent $Ti_3SiC_2$ and green lines represent TiC. ....  | 77  |
| Figure 14 Refined XRD pattern from the program Rietica. Black markers are data, red line is the calculated pattern. The green line is a difference plot between calculated and data. Blue markers are expected peak positions for the phases. ....   | 78  |
| Figure 15 Electron interactions used for imaging which occur in an SEM .....   | 82  |
| Figure 16 Backscattered electron SEM image of the microstructure of a $Ti_3SiC_2 + Al_2O_3$ composite made via an exchange reaction. The MAX phase is the lighter phase and $Al_2O_3$ the darker. ....   | 83  |
| Figure 17 EDS maps of the elements in Figure 16. Individual maps are created for each element and a composite map also created. ....   | 84  |
| Figure 18. (a)Schottky curves and (b) Richardson plot for $GdB_6$ alloy. ....  | 86  |
| Figure 19 Schottky chamber with outer casing and radiation shielding removed. The sample sits inside the innermost alumina crucible. ....  | 87  |
| Figure 20 Configuration for measuring thermal conductivity .....   | 90  |
| Figure 21 Typical DTA data for an Mg – Fe MGA .....  | 91  |
| Figure 22 XRD data of $Ti_3SiC_2 - Al_2O_3$ mixtures before (top) and after separation (bottom). Markers represent $Ti_3SiC_2$ (upper) and $Al_2O_3$ (lower). ....   | 260 |
| Figure 23 Relative fraction of $Ti_3SiC_2$ in the sample after separation. ....  | 261 |
| Figure 24 Neutron diffraction data of a $Ti_3SiC_2 + Al_2O_3$ sample forming. ....   | 264 |
| Figure 25 Expanded view of the SHS reaction with intermediate TiC peaks highlighted. ....  | 265 |
| Figure 26 Refined XRD data of a sample made according to Eq. 13. Markers top to bottom represent $Ti_2AlC$ , $Ti_3AlC_2$ , TiC and $MgAl_2O_4$ . ....  | 267 |
| Figure 27 Al - C MGA microstructure under SEM analysis. The lighter Al particles can be seen as encapsulated by the darker graphite. ....  | 269 |
| Figure 28 $\varepsilon$ -brass MGA in graphite matrix. ....  | 270 |
| Figure 29 Cu Zn phase diagram. ....  | 288 |



## List of tables

|   |    |
|---|----|
| Table 1– Systematics of MAX phase formation. The Table shows known carbide MAX phases arranged by M and A-element. Combinations where the higher order phases i.e. 312 and 413 phases occur are shown in darker grey and can be seen to exclusively occupy the Al column and the Ti row <sup>[22]</sup> ..... | 25 |
| Table 2 The table shows the known nitride MAX phases and is organised in a similar way to Table 1. This table is sparsely populated, with considerably fewer nitride MAX phases having been discovered.....   | 26 |
| <i>Table 3 Some common MAX phase synthesis methods</i> .....  | 36 |
| Table 4. Commonly used XRD parameters for refinement.....   | 79 |



## Abstract

This thesis is primarily concerned with a series of experimental investigations into the synthesis of materials for energy conversion and related applications in hostile environments. The  $M_{n+1}AX_n$  (MAX) phases contain an early transition metal ( $M$ -element) a group 3 or 4 element ( $A$ -element) and either C or N ( $X$ -element) and are a group of ceramics with interesting properties that make them perfectly suited to many difficult and demanding applications. The high potential of the MAX phases has been largely frustrated by difficulties in large scale, economic synthesis. The formation of  $M_{n+1}AX_n$  phases was extensively studied throughout this thesis. Use of  $M$ -element oxides as reactants has been intensively investigated with great success. The processing involved in obtaining the metallic form of the  $M$ -elements contribute considerably to the high cost of the MAX phases, along with complex and small scale synthesis methodologies currently used. Methods have been developed throughout this work as a means of reducing the  $M$ -element oxides, considerably cheaper starting materials, and producing MAX phases via a single step pressureless reactive sintering process. Aluminium has been extensively explored as a reducing agent and aluminothermic reduction was proven capable of forming the majority of tested systems. Separation of the MAX phase alumina composite formed by the exchange reaction has been demonstrated in simple sedimentation experiments, allowing for purification of the MAX phase product. Alternatively carbothermal reduction has been shown in selected systems to produce self-separating products. This process has been shown to produce pure MAX phase products in a single step reaction, a highly desirable trait, and the first time a pure MAX phase has been produced by carbothermal reduction. Additionally investigations into the synthesis

and stability of MAX phases in general lead to the discovery of two new compounds belonging to this family,  $Ti_3GaC_2$  and  $Ti_3InC_2$ .

Issues of energy conversion have been addressed in two ways, through the creation of a novel thermal energy storage material using immiscible materials known as Miscibility Gap Alloys and through the development of a thermionic converter for conversion of heat directly into electricity. Thermal energy storage is critical as it allows for the intermittency of a concentrator solar power plant to be overcome. Misibility Gap Alloys provide high energy density, constant temperature storage in a highly thermally conductive material. A thermionic converter, although in its most preliminary stages with very low power output and efficiency, was designed for high temperature energy conversion. This device can be used as a test bed for the design of a system which could be used as a topping cycle on a concentrated solar thermal power plant. To enhance the power output of the thermionic device, low work function hexaboride materials were investigated and synthesised at considerably lower temperatures than conventionally used.

Overall several contributions have been made in novel and potentially economic methods for the production of MAX phases. The development of these synthesis methodologies may allow for these materials to fulfil their long desired place in demanding environments such as efficient energy conversion. A new class of thermal storage materials was developed which can be used for overcoming the intermittency of concentrated solar thermal power production, which could be coupled with low work function materials in a thermionic energy conversion device in order to improve the efficiency of electricity generation.

## 1. Introduction

### 1.1. Thesis synopsis

This thesis is by publication and as such has a slightly different layout to what is common. The work primarily concerned with the development of synthesis methods of novel materials considering applications for energy conversion and more specifically electricity production. Throughout the work four published papers are presented concerning the synthesis of a group of materials referred to as  $M_{n+1}AX_n$  (MAX) phases and this makes up the main body of the thesis. These are accompanied by two publications on the development of a new class of metal alloys intended for thermal energy storage and two publications on high temperature thermionic electricity production. A brief explanation of the background and importance of the work along with a potential application is given in the following introduction. The running examples of materials for energy conversion is just one application, the work itself is considered to be relevant to a wide number of fields. The papers have been reformatted wherever possible for consistency throughout and are each contained within their own chapter. Each paper contains its own figure and table numbers as they appear in print and references are included at the end of each chapter. A brief overview of the most commonly used experimental and analytical methods used throughout this work is given after the introduction. This is followed by a summary of each publications and then the declarations for contributions of the candidate to these publications. All articles are accepted for publication at time of submission of this thesis. Although the majority of the work is contained within the supplied publications, the brief nature of these limits the ability for supplementary investigations and wider discussion. As a result two more chapters appear after the publications with supplementary results followed by general discussion and future work.

## 1.2. General context

Conventional engineering solutions have always been built around the materials available at the time, so much so that entire periods of time became known by the most important material being made use of; the Bronze Age, Iron Age and the Silicon Age we now live in. Today, as much as ever, we look towards material science to help us to overcome the challenges we face as a society. The drive to a sustainable future relies on the more efficient use of our remaining fossil fuels, and the development of alternative means of large scale electricity production.

Currently most of the energy humanity uses comes from the combustion of fossil fuels (~82%)<sup>[1]</sup>. This is used mainly for electricity generation or transport in internal combustion engines or jet turbines. For electricity production the energy released from combustion is used to heat steam in a power cycle (Figure 1)<sup>[2]</sup>, which expands through a turbine connected to a generator to produce electricity. Alternative methods of electricity production are numerous. Nuclear and concentrated solar power production, for example, use a similar power cycle however the heat source is different. Solar panels and wind turbines operate on different principles entirely, more directly converting energy into electricity. Each method comes with its own limitations such as intermittency or waste production. The steam based power cycle is already established on the scale required to replace fossil fuels and so there is a considerable world wide effort to find an effective way of transforming a renewable source of energy into the heat required for the power cycle.

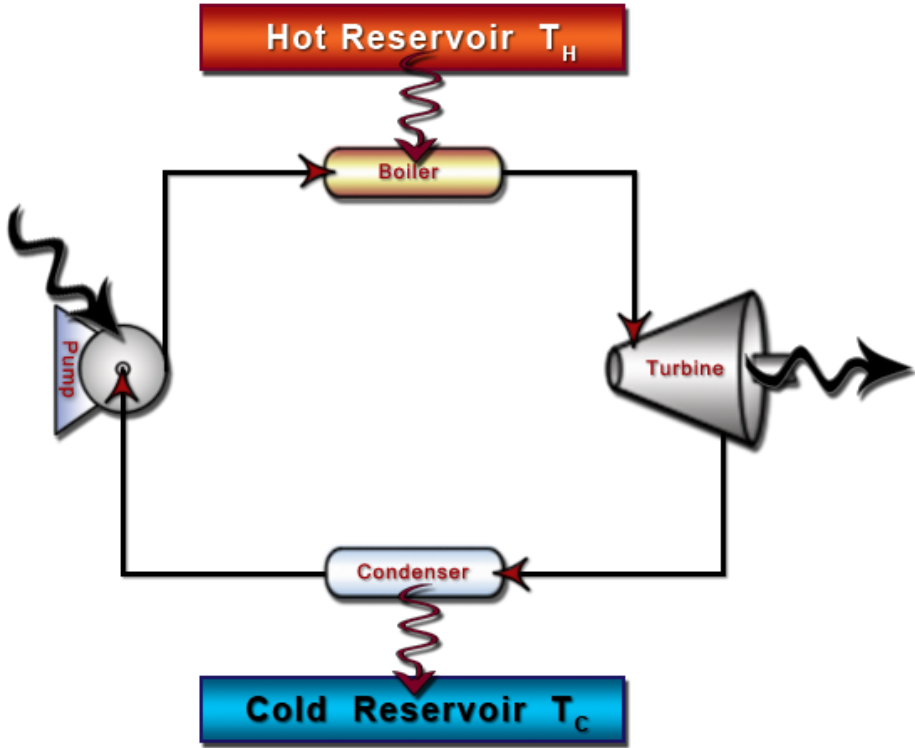


*Figure 1 A typical power cycle similar to that used in the conversion of thermal energy to electricity. An electrical generator is normally attached to the turbine<sup>[2]</sup>.*

The maximum efficiency of any power cycle is fundamentally governed by thermodynamics, the Carnot efficiency ( $\eta$ ) being the upper limit

$$\eta = 1 - \frac{T_c}{T_h} \quad \text{Eq. 1}$$

It can be seen that increasing the temperature difference between the hot ( $T_h$ ) and cold ( $T_c$ ) reservoirs increases the efficiency of the system. It is practically difficult to decrease  $T_c$  below that of the ambient environment, however increasing  $T_h$  is possible with not only current fossil fuel combustion but also with concentrated solar power or nuclear power. Unfortunately current power stations are forced to operate well below the maximum temperature that the power source can provide due to limitations in the maximum operating temperature of the materials used in key components such as turbine blades and steam piping.

## Introduction

One of the main issues faced by engineers is that different material properties are generally related. A material which is highly stiff for example is also normally brittle, low melting temperature materials are normally soft and so on. Material properties and indeed the relationships between properties is often determined by the bonding between atoms at the smallest scale in the material. It is from this bonding that we begin to classify materials into different groups. Metals and alloys are dominated by free electron sharing. These free electrons grant the high macroscopic electrical and thermal conductivity as well as the characteristic shiny lustre of metals. The lattice of atoms generally allows for the motion of dislocations required for plastic deformation granting high damage tolerance and ductility. Ceramics rely on a network of covalent or ionic bonds which create a highly rigid structure that is very elastically stiff, even at high temperatures, as well as resistant to chemical attack and oxidation. Unfortunately the rigid bonds make ceramics highly susceptible to fracture and catastrophic failure. Turbine blades (both steam and jet) are currently made from metals and operate at their limit of oxidation resistance and creep rupture temperature. Ceramic blades could offer higher temperature operation and superior stiffness but their lower tensile strength and fracture toughness make them unsuitable. The current state of the art of both metals and technical ceramics is both advanced and diverse, and by no means limited to or as simplistic as what has been stated here. However this is a good example of the difficulties that can arise from related material properties. The MAX phases, which comprise the lion's share of this thesis, are interesting engineering materials. MAX phases such as  $Ti_3SiC_2$  are materials that exhibit some properties of ceramics such as high stiffness, high temperature stability, oxidation resistance coupled with properties normally associated with metals such as electrical conductivity, thermal shock resistance and the ability to be machined<sup>[3]</sup>. The

unique property set of the MAX phases makes them applicable for use in hostile situations like turbine blades, and can lead to greatly improved efficiencies thus generating more power from our finite fossil fuels<sup>[4]</sup>. In the application of renewable energy Stirling engines, for example, would benefit greatly in efficiency from pistons and cylinders made of MAX phase due to the very low friction, oxidation resistant, machineable nature of the material.

Additional advances can be envisioned if the heat source in a power cycle could be replaced with concentrated solar radiation where mirrors focus sunlight to heat a receiver (Figure 2)<sup>[5]</sup> making the process of energy input independent of fossil fuels. However solar power, like wind power suffers from one main issue, intermittency. Solar power is inconsistent, varying most obviously through the day/ night cycle, but also on shorter time scales due to cloud motion and longer time scales due to seasonal affects. The variations in solar flux prevent solar power production from taking over from base load electricity supply (Figure 3) and thus can only be used to supplement power generation. It can quickly be seen that increasing supply of solar based power such as PV (photo voltaic) panels does little to compensate for the need to produce power at peak household power consumption (16:00-22:00) where solar flux is at or approaching its minimum. The ability to store the energy available at periods of high flux is essential to compensate for the lack of power throughout the majority of the cycle. It has now been recognised that it is the requirement for energy storage that is holding back large scale renewable power production more than the ability to generate power.

## Introduction



Figure 2 Concentrated solar power plant showing mirrors on left focusing solar radiation onto the collector tower on the right. [5]

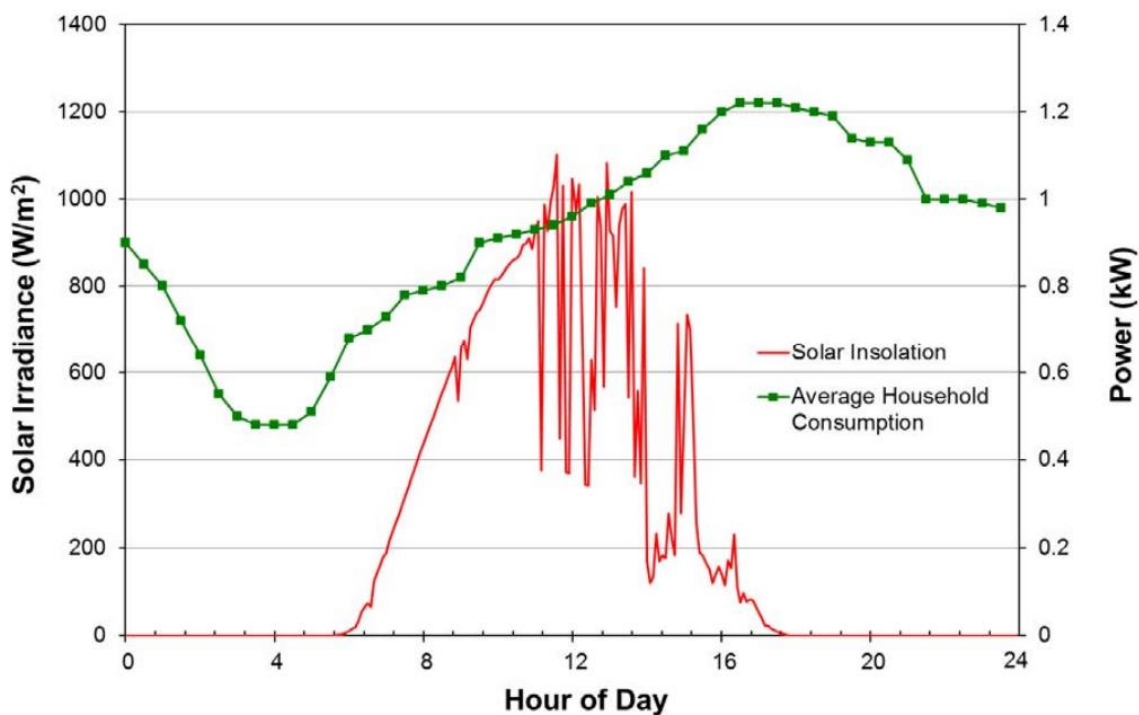


Figure 3 Solar radiation and power consumption on a typical day in Newcastle, NSW, Australia. Note the intermittency of solar radiation and the offset between peak solar insolation (~12:00) and peak power consumption (~17:00)

The excellent potential of solar thermal power stations to produce electrical power on a *large* scale, drove the development of the thermal storage medium in this thesis. Also the ability for concentrated solar radiation to reach very high operating temperatures led to the concept of using a thermionic generator as a means of electrical power production. Another application of the high temperatures available from concentrated solar thermal power is through the use of a supercritical CO<sub>2</sub> Brayton cycle. Although higher efficiencies may become available over a conventional Rankine cycle, the demand on materials becomes a limiting factor.<sup>[6]</sup>

Energy conversion as discussed above is the envisioned application of much of the work presented here. However the work itself has mainly been on the synthesis of materials, not on their properties or their use. It is expected that most of this work (particularly the work on MAX phases) may find other more diverse applications or be valued more as an academic pursuit than an engineering application.

As the majority of the work presented in the following publications is on MAX phases, a more comprehensive introduction to those materials will be provided in the next section, in order to give the reader a better understanding of the history and state of the art. Basics of material synthesis are also included with respect to MAX phase formation. The following two sections in this chapter are shorter review sections, provided for the topics of energy storage and thermionic conversion to contextualise the respective papers. The majority of the specific technical literature review is contained within the introductions of the publications presented in Chapters 5-12.

### 1.3. MAX phases

The  $M_{n+1}AX_n$  (MAX) phases are a group of ternary carbides and nitrides first discovered in 1963 by Nowotny et. al. and identified as  $H$ -phases<sup>[7]</sup>. Some 30 phases were discovered, all of the composition  $H_2AC$ . The phases were identified and the structure crystal determined however, bulk phase - pure samples were never successfully produced, therefore material property testing was not undertaken. Later it was discovered that  $Ti_3SiC_2$ <sup>[8]</sup> and then  $Ti_4AlN_3$ <sup>[9]</sup> also belonged to the group and the realisation was made that this was a much larger field of phases than first realised. MAX phase research gained significant momentum in the 1990's primarily thanks to the implementation of the reactive hot pressing technique by Barsoum et. al. which allowed for the synthesis of phase – pure, highly dense, bulk samples<sup>[3, 10, 11]</sup>. Samples which could be used for accurate, comprehensive physical property testing. It was through this method that many of the MAX phases have been synthesised and many of their interesting material properties were discovered<sup>[12]</sup>.

The MAX phases have now been shown to include over 90 different compounds. In all cases they are comprised of an early transition metal  $M$ -element, a group  $A$ -element and C or N as the  $X$  element (Figure 4). The integer  $n$  takes the values 1, 2 or 3. Taking for example,  $M = Ti$ ,  $A = Si$ ,  $X = C$  and  $n = 2$  yields  $Ti_3SiC_2$  the most commonly studied of the MAX phases.

|    |    |    |    |    |    |    |    |    |    |    |    |    |    |    |    |    |    |  |  |    |
|----|----|----|----|----|----|----|----|----|----|----|----|----|----|----|----|----|----|--|--|----|
| H  |    |    |    |    |    |    |    |    |    |    |    |    |    |    |    |    |    |  |  | He |
| Li | Be |    |    |    |    |    |    |    |    |    |    |    |    |    |    |    |    |  |  |    |
| Na | Mg |    |    |    |    |    |    |    |    |    |    |    |    |    |    |    |    |  |  |    |
| K  | Ca | Sc | Ti | V  | Cr | Mn | Fe | Co | Ni | Cu | Zn | Ga | Ge | As | Se | Br | Kr |  |  |    |
| Rb | Sr | Y  | Zr | Nb | Mo | Tc | Ru | Rh | Pd | Ag | Cd | In | Sn | Sb | Te | I  | Xe |  |  |    |
| Cs | Ba | Lu | Hf | Ta | W  | Re | Os | Ir | Pt | Au | Hg | Tl | Pb | Bi | Po | At | Rn |  |  |    |
| Fr | Ra | Lr | Rf | Db | Sg | Bh | Hs | Mt | Ds | Rg |    |    |    |    |    |    |    |  |  |    |

Figure 4 Elements known to make up the MAX phases. Red denotes M-elements, blue A-elements and grey X-elements.

The hexagonal MAX phase crystal structure in space group  $P6_3/mmc$  is arranged in a layered form, with rigid  $MX$  octahedra separated by pure  $A$ -element layers as seen in Figure 5<sup>[13]</sup>. In the illustration the  $M$  atoms can be seen to sit at the edges of the green octahedra, with  $X$  atoms shown in black, in the centre. All of the  $M$ -elements that form MAX phases also form a  $M-X$  binary compound, a more ‘standard’ ceramic. For example the  $M-X$  compound of Ti and C, TiC, is a hard, brittle, thermally stable material used in high speed cutting tools. The coordination and position of the atoms in the  $MX$  octahedra of the MAX phase is very similar to that in the corresponding binary compound, providing a highly rigid structure. It is from here that many of the ceramic-like properties of the MAX phase originate. The  $A$ -element atoms (white atoms in Figure 5) form layers that separate the octahedra, these atoms share free electrons<sup>[10]</sup>. The number of  $MX$  octahedra separated by each  $A$  layer gives rise to the integer  $n = 1, 2$  or  $3$  or  $M_2AX$ ,  $M_3AX_2$  or  $M_4AX_3$  compositions, commonly referred to as 211, 312 or 413 phases respectively<sup>[14]</sup>. The 211 and 312 structures are illustrated in Figure 6. The  $M$  atoms occupy two sites in the 312 (and the not shown 413) structure, one bounded by  $X$  atoms on both sides, the other bounded by  $X$  and  $A$  atoms. It can be seen in Figure 6 that the 211 structure does not have

## Introduction

an  $M$  atom bounded by 2  $X$  atoms, i.e. there is only one  $M$ -element coordination in the 211 phases.

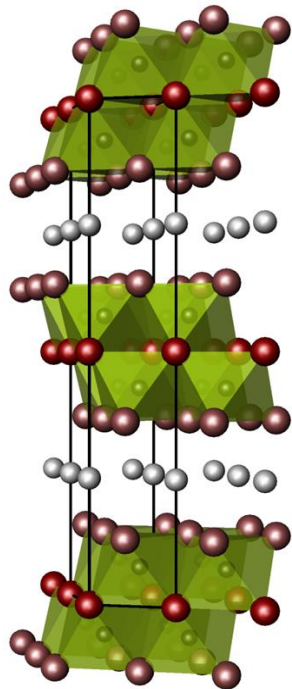
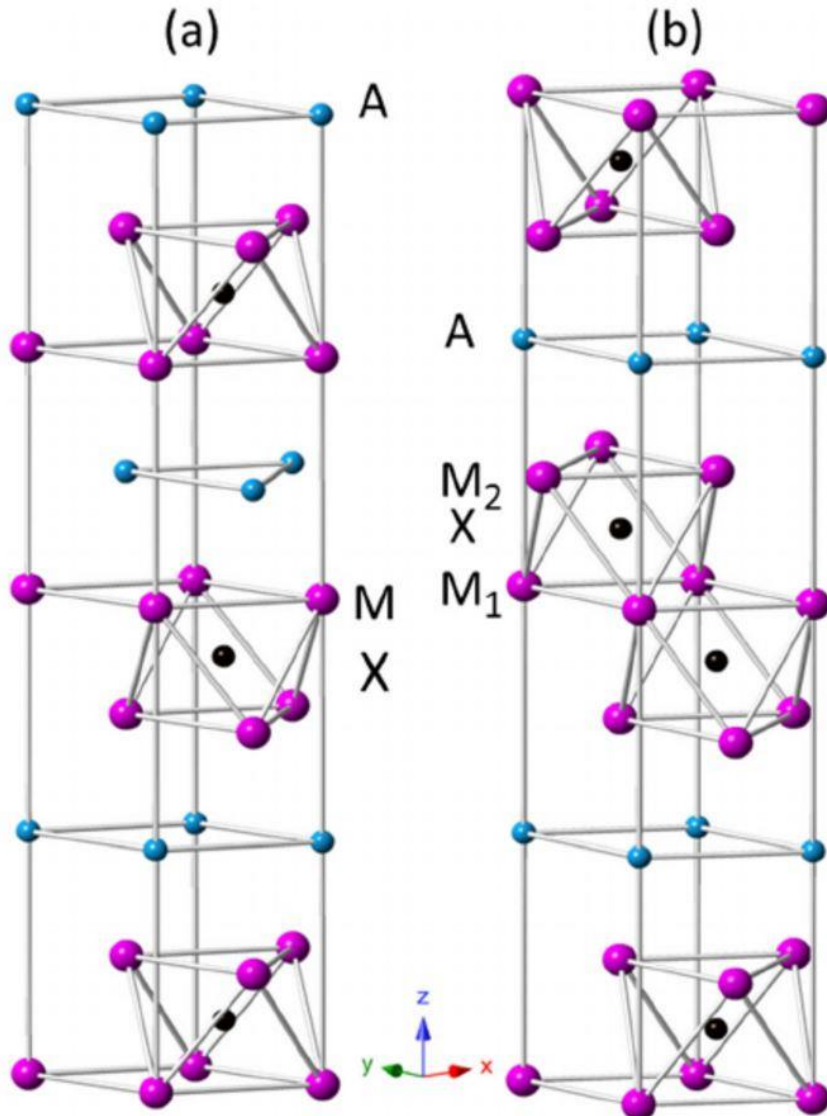


Figure 5  $M_3AX_2$  crystal structure. Green octahedra represent MX bonding, white layers are the A-element<sup>[13]</sup>.



*Figure 6 Crystal structures of the MAX phases; (a) 211 or  $n = 1$  and (b) 312 or  $n=3$  type. Purple indicates M-elements, blue A-elements and black X-elements<sup>[15]</sup>.*

Recently other compositions of MAX phases have been discovered. Both 523 and 725 compositions have been found<sup>[16-18]</sup>. These are not new values of  $n$  nor changed crystal structures. They are intergrown layers of the 211 and 312 or 312 and 413 MAX phases. This stacking effectively creates a double unit cell with, for example, a 211 phase sitting atop a 312. Through the method of ordered stacking of layers it may be possible to create a large number of different polytypes. It is also possible to substitute certain elements, provided the correct system is chosen<sup>[19]</sup>. For example,  $Ti_3Al_ySi_{1-y}C_2$  can exist through

## Introduction

the entire range of  $0 < y < 1$ . Other systems show similar solubility on the  $A$  or  $M$  site although not always through the full range, additionally many can be ordered. Although both of these methods can produce chemistries that may not immediately look like they are of the form  $M_{n+1}AX_n$  they are essentially ordered stacking of the MAX phases.

The mixed bonding within, and layered nature of the unit cell is what gives MAX phases their unique combination of properties. The combination of metallic and covalent bonding gives rise to properties, which are normally considered to be mutually exclusive of metals and ceramics, in the same material. The layered structure also gives rise to anisotropic properties. Crystals tend to grow faster in the  $a-b$  plane than along the  $c$  axis, thus producing flat tabular shapes. The direction of the  $c$ -axis during synthesis and crystal growth can be influenced, most easily by the addition of axial pressure during sintering<sup>[20]</sup>. The axial pressure results in the slow growing  $c$ -axis aligning with the pressing direction and monolithic bulk samples can be created with very high texture. Highly oriented samples then display the anisotropic properties of the unit cell on macroscopic scales, scales that allow for conventional property testing. This has been important since growing large single crystals of MAX phases is not yet achievable making single crystal property measurements practically difficult<sup>[21]</sup>.

Based on Figure 4 there are 9  $M$ -elements, 12  $A$ -elements and 2  $X$ -elements, as well as 3 values of  $n$ . Mathematically this gives over 200 different element systems ( $M-A-X$ ) and over 600 possible MAX phases. However to date only about 90 MAX phases have been discovered in approximately 50 discrete element systems. The known carbide MAX phases are summarised in Table 1 and nitrides in Table 2<sup>[22]</sup>. From investigation of the tables the following observations can be made

- i) Most of the potential combinations of elements have not been found to form a MAX phase
- ii) The carbides are more numerous than the nitrides
- iii) The  $211$  ( $n=1$ ) MAX phases are far more common than  $312$  or  $413$  phases
- iv) The  $M$  and  $A$ -elements that form the most phases are Ti and Al respectively.
- v) All higher order MAX phase ( $312$  or  $413$  phases) contain either Ti as the  $M$ -element or Al as the  $A$ -element and have a corresponding  $211$ , with the notable exception of  $Ti_3SiC_2$ .

*Table 1– Systematics of MAX phase formation. The Table shows known carbide MAX phases arranged by M and A-element. Combinations where the higher order phases i.e.  $312$  and  $413$  phases occur are shown in darker grey and can be seen to exclusively occupy the Al column and the Ti row<sup>[22]</sup>.*

| M<br>VS<br>A | Al                | Si         | P   | S   | Ga                | Ge                | As  | Cd  | In         | Sn         | Tl  | Pb  |
|--------------|-------------------|------------|-----|-----|-------------------|-------------------|-----|-----|------------|------------|-----|-----|
| Sc           |                   |            |     |     |                   |                   |     |     | 211        |            |     |     |
| Ti           | 211<br>312        | 312<br>413 |     | 211 | 211<br>312<br>413 | 211<br>312<br>413 |     | 211 | 211<br>312 | 211<br>312 | 211 | 211 |
| V            | 211<br>312<br>413 |            | 211 |     | 211               | 211               | 211 |     |            |            |     |     |
| Cr           | 211               |            |     |     | 211               | 211               |     |     |            |            |     |     |
| Zr           |                   |            |     | 211 |                   |                   |     |     | 211        | 211        | 211 | 211 |
| Nb           | 211<br>413        |            | 211 | 211 | 211               |                   | 211 |     | 211        | 211        |     |     |
| Mo           |                   |            |     |     | 211               |                   |     |     |            |            |     |     |
| Hf           |                   |            |     | 211 |                   |                   |     |     |            | 211        |     | 211 |
| Ta           | 211<br>312<br>413 |            |     |     | 211               |                   |     |     | 211        |            | 211 |     |

*Table 2 The table shows the known nitride MAX phases and is organised in a similar way to Table 1. This table is sparsely populated, with considerably fewer nitride MAX phases having been discovered.*

| M<br>VS<br>A | Al         | Si | P | S | Ga  | Ge | As | Cd | In  | Sn  | Tl  | Pb |
|--------------|------------|----|---|---|-----|----|----|----|-----|-----|-----|----|
| <b>Sc</b>    |            |    |   |   |     |    |    |    |     |     |     |    |
| <b>Ti</b>    | 211<br>413 |    |   |   | 211 |    |    |    | 211 |     |     |    |
| <b>V</b>     |            |    |   |   | 211 |    |    |    |     |     |     |    |
| <b>Cr</b>    |            |    |   |   | 211 |    |    |    |     |     |     |    |
| <b>Zr</b>    |            |    |   |   |     |    |    |    | 211 |     | 211 |    |
| <b>Nb</b>    |            |    |   |   |     |    |    |    |     |     |     |    |
| <b>Mo</b>    |            |    |   |   |     |    |    |    |     |     |     |    |
| <b>Hf</b>    |            |    |   |   |     |    |    |    |     | 211 |     |    |
| <b>Ta</b>    |            |    |   |   |     |    |    |    |     |     |     |    |

### 1.3.1. Synthesis

Before discussing the MAX phases specifically it is important to note that, in general, ceramic synthesis involves producing large quantities of a phase-pure powdered ceramic material. The product of the synthesis needs to be suitable for downstream processing into components by various shaping processes (uniaxial pressing, cold isostatic pressing, extrusion etc.). Shaping is then followed by sintering to produce dense, strong

components. The shaping and sintering processes are well established and outside the scope of this thesis; the following will focus on the synthesis of the MAX phases themselves. The analysis is broken into two parts, thermodynamic stability and kinetic accessibility.

Manufacturing difficulties have plagued the formation of the MAX phases throughout their short history. The ternary systems involved typically contain many local free energy minima surrounding the MAX phase composition. Taking the Ti-Si-C system as an example in Figure 7, MAX phase formation is competing with the formation of the binary carbides, TiC as well as SiC, multiple Ti-Si intermetallic compounds and sometimes other ternary phases<sup>[23]</sup>. In many *M-A-X* systems there is a set of competing phases which are more stable than the potential MAX phase and the MAX phase cannot form. In other cases the problem is that a practical synthesis route has not be found to form the desired compounds. It is predominantly for the first reason that the vast majority of potential *M-A-X* combinations discussed with reference to Table 1 and Table 2, do not form the potential MAX phase, i.e. the MAX phase is not the most thermodynamically stable state. It is the second reason that explains why the synthesis of known MAX phases is still such an intensely studied subject.

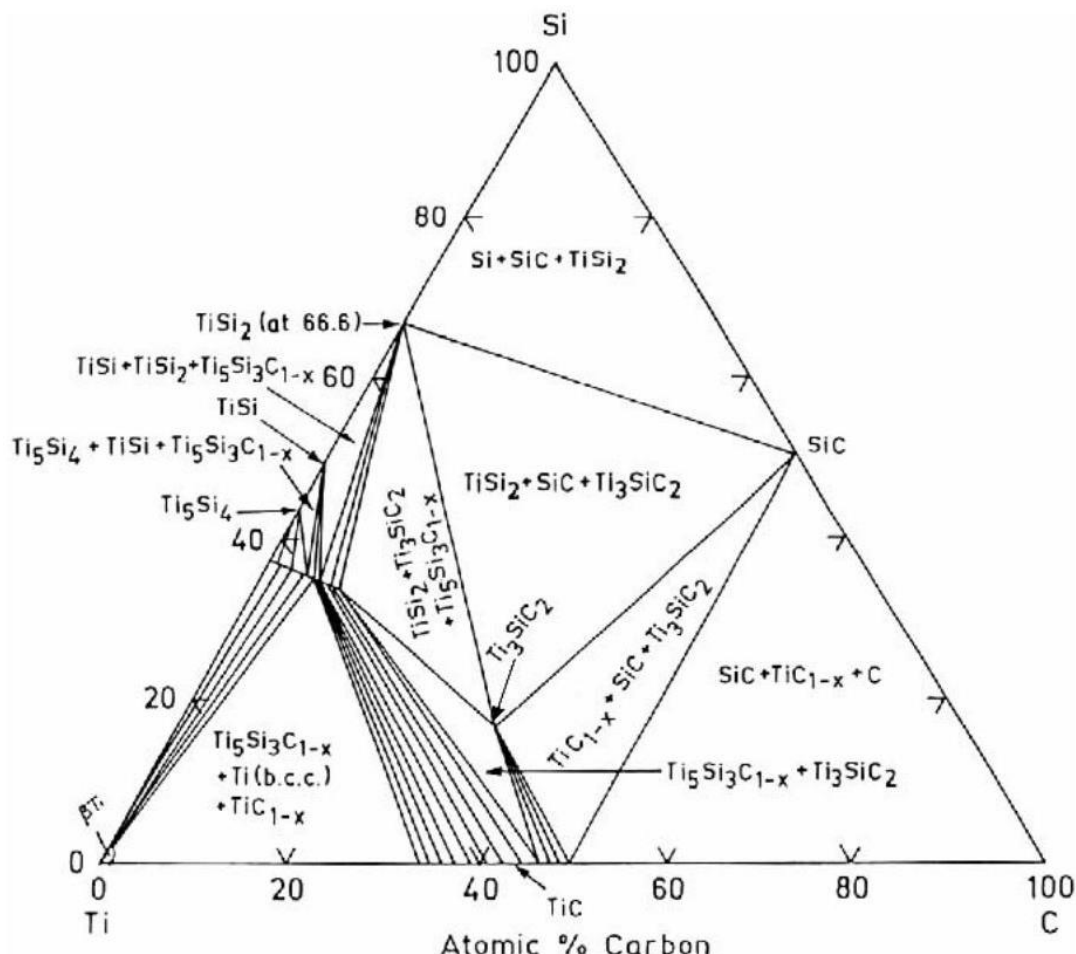


Figure 7 Ternary phase diagram in the Ti-Si-C system at 1200°C with the MAX phase composition highlighted. The many competing phases can also be seen<sup>[24]</sup>.

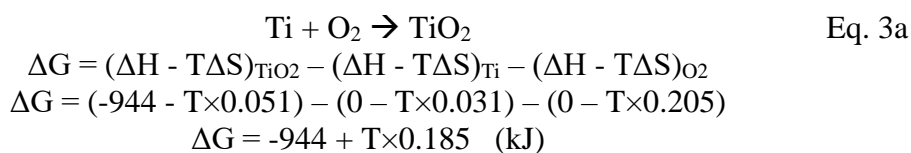
### 1.3.2. Thermodynamic stability

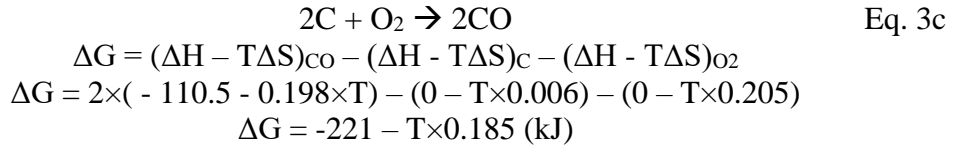
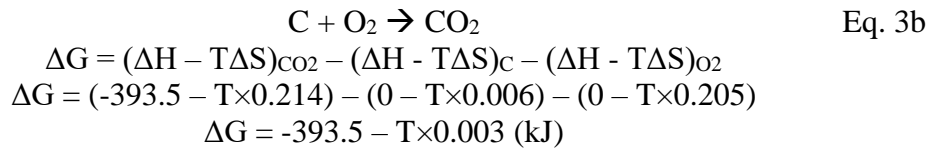
Phase stability as mentioned directly above is determined by Gibbs free energy, a measure of the work that can be done in the system. In the case of compounds forming, the work available is the energy difference between the components existing in their natural state as elements and the energy in the combined compound state. As the energy is normally referenced to a change from one state to another, it is generally preceded by a delta, thus Gibbs free energy change is denoted as  $\Delta G$ .  $\Delta G$  is comprised of two parts, the enthalpy

of formation  $\Delta H$  (which is normally negative), and a change in entropy at a temperature  $T\Delta S$  can be seen in Eq. 2a. Any combination of elements, will be driven towards the lowest  $G$  or greatest negative  $\Delta G$ , and this will determine the ‘stable’ products when more than one set of products are available. When multiple reactants and products are possible the free energy of formation is used ( $\Delta G^\circ_f$ ) which, for each substance in the reaction, is the difference between the free energy of that substance and the free energy of its elements, illustrated in Eq. 2b. The superscript  $^\circ$  represents standard state conditions (pressure = 1 atmosphere and temperature assumed to be 25°C) at which the entropy and enthalpy terms are generally well known. Classically  $\Delta H$  is the larger term in solid – solid and solid – liquid reaction and thus the governing factor. The  $T\Delta S$  term commonly becomes more significant when a gas is being produced or consumed, as the gaseous state has very high entropy and solids have a low entropy leading to a large  $\Delta S$ . Eq. 3a, 3b and 3c demonstrate the difference in the entropy and enthalpy terms for selected oxidation reactions. This contribution is also strongly temperature dependant and thus the decomposition of oxides to produce products with more moles of gas can be possible at high temperatures. This is most apparent with the example of the stability of the carbon oxides. Below about 700°C  $\text{CO}_2$  is the stable oxide due to the larger entropy of formation ( $\Delta H$ ), however at higher temperatures, the larger molar entropy ( $S$ ) of  $\text{CO}$  makes it the stable phase according to Eq. 3 with twice the number of moles of gas.

$$\Delta G = \Delta H - T\Delta S \quad \text{Eq. 2a}$$

$$\Delta G = \sum \Delta G^\circ_f(\text{Products}) - \sum \Delta G^\circ_f(\text{Reactants}) \quad \text{Eq. 2b}$$





It should be noted that the number of starting moles of  $\text{O}_2$  is kept constant, which implicitly assumes that the system is free to undergo complete reaction. Eq. 3c can be forced to occur below 700°C by oxidising C in low  $\text{O}_2$  conditions. Ellingham diagrams<sup>[25]</sup> plot the  $\Delta G^\circ$  of reactions against temperature to allow for easy comparison across many different compounds. A metal oxide Ellingham diagram is shown in Figure 8. The y intercept (0 K) is the  $\Delta H^\circ$ , and the gradient of the line is controlled by  $\Delta S$ . Relevant areas of interest are

- i) Materials with lower  $\Delta G^\circ$  will form preferentially from materials with higher  $\Delta G^\circ$ . The lower down the more stable.
- ii) Most of the oxides have a similar positive gradient meaning  $\Delta S$  is similar and the oxides get less stable at higher temperatures, eventually decomposing.
- iii)  $\text{CO}_2$  has a zero gradient and  $\text{CO}$  has a negative gradient (dashed lines) as the oxides of C have equal or more moles of gas than the reactants respectively.
- iv)  $\text{CO}$ , at high enough temperatures, becomes more stable than all metal oxides, thus C is a universal reducing agent, but this is highly temperature dependant.

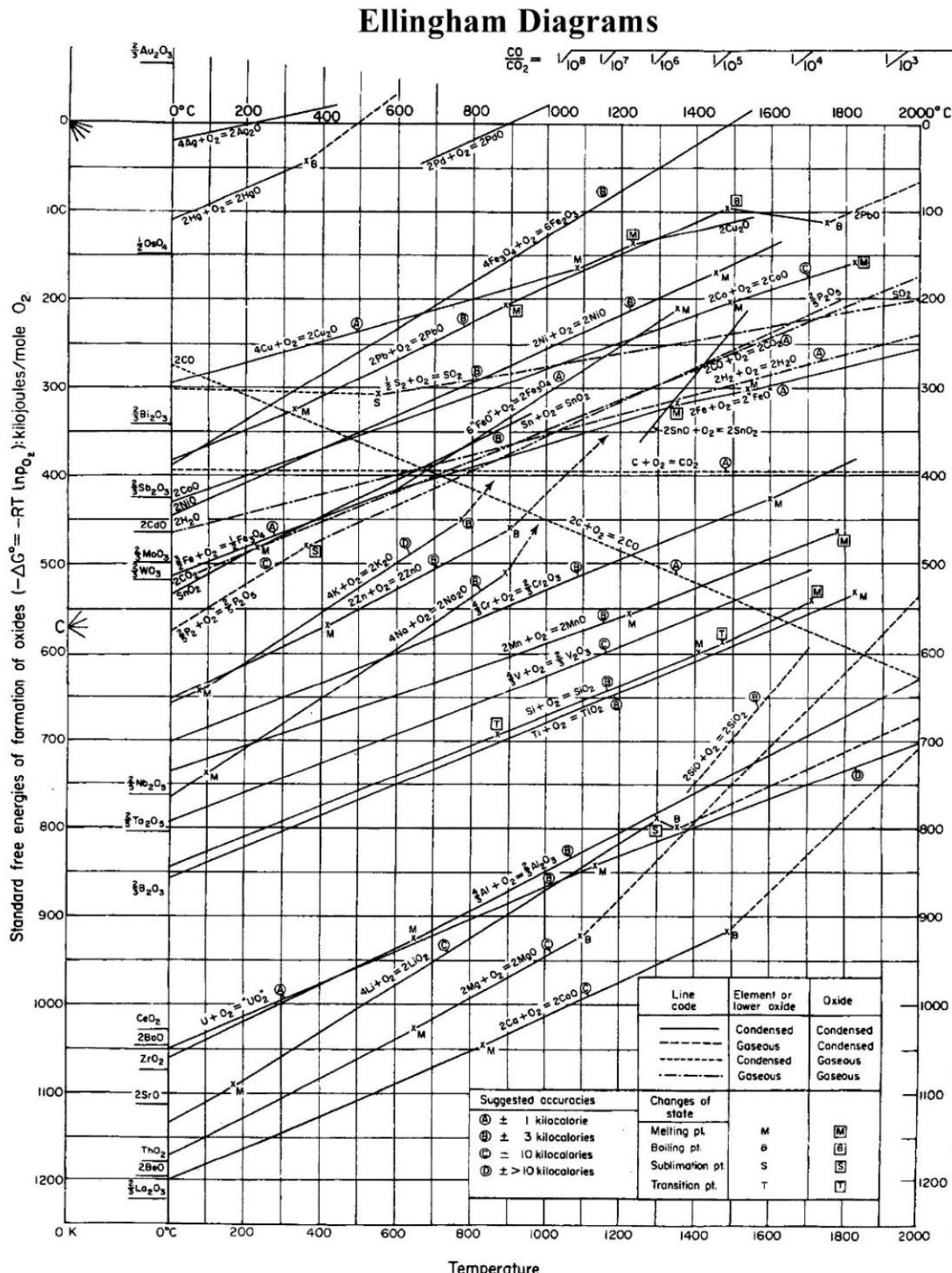


Figure 8 Ellingham diagram showing common oxides. Lines representing more stable metal oxides can be seen at the bottom of the chart whereas more easily reduced oxides appear higher up.  $CO_2$  and  $CO$  are the dashed lines with zero and negative gradient respectively.<sup>[25]</sup>

## Introduction

The metal oxides have been used as an example here (and will become relevant in later publications) but the concepts of  $\Delta G$  controlling the stable state of reactants can be applied to MAX phase formation, along with almost any other branch of science. The combination of any set of *M-A-X* elements will be driven to form the set of phases on the ternary phase diagram with the lowest total Gibbs free energy. In some cases it will be the MAX phases but in many others it will not.

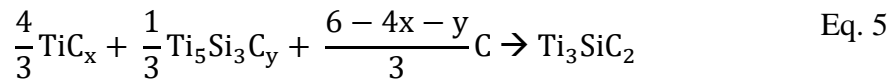
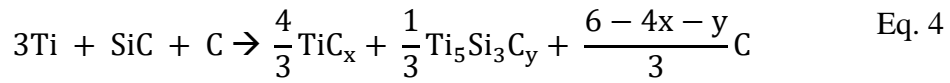
Thermodynamic analysis of MAX phase systems can be difficult as the  $\Delta H$  and  $S$  is generally unknown, and for potential new phases that are yet to be synthesised, certainly unknown. However through modelling the electronic structure of a crystal computationally, the enthalpy of formation for a phase can be approximated. The process of computationally modelling crystals using a physical approach is known as *ab initio* calculation. The most widespread method of *ab initio* calculation relies upon the density functional theory (DFT). DFT *ab initio* calculation relies upon a plane-wave approximation to solve the equations governing the electron density of a multi-atom system in a periodic potential (i.e. a crystal). It is an incredibly powerful tool in the analysis of crystal structures and a rapidly expanding field with the development of increased computing power. However the process is limited to the electronic ground state (i.e. 0 K) where the entropy contribution to  $\Delta G$  is zero. Methods for handling temperature effects ( $S$ ) such as combined DFT and Molecular Dynamics ((MD) simulation have been developed but are prohibitively computational-intensive for complex systems. The method does allow the enthalpy of a phase to be compared with the enthalpy of all competing phases in the system, in order to determine which products are most stable. A full description of the process will not be given here, but a selected application of DFT to MAX phases is highlighted<sup>[26]</sup>. DFT was used to examine a selection of the currently

known MAX phases to see whether the predictions of stability align with the experimentally formed MAX phases. It was found that in all systems where the MAX phase was the lowest energy state, a MAX phase has been found experimentally and in all systems where a MAX phase has not been found experimentally a set of competing phases were found that formed the lowest energy state. Overall it was shown that DFT can be used to gain a good initial understanding of the system and that in many cases the  $\Delta H$  is the main driving force in formation. Unfortunately the stability of some MAX phases are known to be affected by temperature. Some 312 MAX phases for example, decompose into the 211 and MX binary phases at high temperatures. Despite these limitations DFT is still an excellent starting point when investigating the formation of novel materials as the synthesis will always be fundamentally governed by Gibbs free energy and this should always be the first consideration.

### 1.3.3. Kinetic accessibility

Despite many MAX phases being thermodynamically stable their synthesis is still complex. This is because kinetics play an important role. As the starting elements cannot be intimately mixed on an atomic scale before reaction, MAX phase synthesis is not a single step process. Intermediate phases precede the MAX phase and complete conversion is often difficult. The intermediate phases are generally very stable, reducing the thermodynamic drive for complete reaction. Diffusion rates can be very slow and so high reaction temperatures (in the order of  $1400^{\circ}\text{C} \pm 200^{\circ}\text{C}$ ) are normally required to facilitate reaction. An example of the reaction mechanism in the formation of  $\text{Ti}_3\text{SiC}_2$  is presented in Eqs. 4 and 5<sup>[27]</sup>.

## Introduction



The high reaction temperatures can result in irregular losses of elements, most commonly of the A-element, which along with any inhomogeneous mixing then move the system away from the required stoichiometry. Although this may be compensated for in some respect by the addition of excess material, local variations still play an important role and saturating the systems can drive the reactants to form other products. The problem of vapour phase transport of the reactants is exacerbated by the requirement of a protected atmosphere during synthesis, normally achieved by flowing Ar or vacuum. A protected atmosphere prevents oxidation however it also prevents the reactants forming a stable partial pressure, greatly increasing losses even at temperatures well below boiling.

The MAX phases also have a maximum temperature above which they decompose. This temperature varies by hundreds of degrees across the MAX phase systems and even varies based on the value of  $n$ , in general 211 phases are stable to higher temperatures<sup>[28]</sup>. So a successful synthesis must take place below the decomposition temperature, yet at a high enough temperature to allow complete reaction of the stable intermediate phases, without suffering excessive vaporisation losses. That is to say, even if a phase is thermodynamically favourable it still needs to be kinetically accessible.

Although the problem as stated here may appear simple, it is this aspect, practical synthesis techniques, that a majority of research into MAX phases is focused. High levels

of conversion are important as small amounts of secondary phases in the bulk of a sample can severely compromise the desired properties. Taking the Ti-Si-C system as an example, it is normally the binary carbide TiC that is problematic in the products. Two common causes for the retention of TiC are depletion of Si generally through vaporization loss, or the formation of TiC as an intermediate phase which does not fully react (with its fellow Ti-Si intermediates) and is therefore retained. In this field TiC should more correctly be written  $\text{TiC}_x$  as the compound has a wide stability range ( $~0.5 < x < 1$ ). The value of x in the  $\text{TiC}_x$  may play an important role with stoichiometric TiC ( $x=1$ ) resisting further reaction while sub stoichiometric  $\text{TiC}_{0.67}$  ( $\text{Ti}_3\text{C}_2$ ) is perfectly placed to form into a  $\text{Ti}_3\text{AC}_2$  phase. Often a combination of factors play a role with required temperatures for complete reaction of the intermediates phases causing vaporisation losses of reactants in the protected atmosphere required to prevent oxidation. Desirable properties such as machinability of  $\text{Ti}_3\text{SiC}_2$  are heavily compromised by only a few percent of TiC which is the bane of Ti-based MAX phase synthesis. Many synthesis techniques have been applied with varying levels of success, but a method that produces high quality products that can be used in economically large batch sizes has remained elusive. A brief summary of different techniques has been presented in Table 3.

*Table 3 Some common MAX phase synthesis methods*

| <b>SYNTHESIS METHOD</b>  | <b>POSITIVES</b>   | <b>NEGATIVES</b>   | <b>USES</b>   | <b>GENERAL PHASE PURITY</b>    |
|--|--|--|---|--------------------------------|
| <b>REACTIVE HOT PRESSING (RHP)<sup>[4, 8, 14, 29-31]</sup></b>                 | Produces highest quality samples<br>Most established method<br>High density products     | Inherently small batch sizes<br>Equipment costs are high   | High quality samples for subsequent property testing<br>Single step synthesis of pieces for machining into small components (< 100mm) | >99%                           |
| <b>PRESSURELESS REACTIVE SYNTHESIS<sup>[13, 22]</sup></b>                      | Simplest setup<br>Can produce high purity samples<br>Easily scalable                     | Higher reactant losses<br>Generally lower conversion than RHP samples<br>Low density products (~70%) | Synthesis investigations<br>Produce MAX phases suitable for grinding to powder  | Up to 99% generally much lower |
| <b>CHEMICAL VAPOUR DEPOSITION<sup>[32-36]</sup></b>                            | High purity thick films<br>Efficient use of reactants<br>Only way to produce some phases | Cannot produce bulk samples<br>Equipment costs are high  | Coating on objects such as turbine blades<br>Synthesis investigations   | >99%                           |
| <b>SELF-PROPAGATING HIGH TEMPERATURE SYNTHESIS (SHS)<sup>[23, 37-43]</sup></b> | Significantly decreased energy input and reaction times<br>Potentially scalable          | Lack of control over reaction<br>Lower conversion than other methods<br>Low density products (<50%)  | Rapid energy efficient method of producing material suitable for grinding into power.   | ~90%                           |
| <b>MECHANICALLY ACTIVATED SHS<sup>[39]</sup></b>                               | Very low reaction temperatures reduce losses<br>Materials contained in milling vial      | Lack of control over reaction<br>Intensive energy input<br>Equipment costs are high<br>Not scalable  | Investigations into low temperature synthesis   | ~75%                           |

|   |  |   |                                     |      |
|---|--|---|-------------------------------------|------|
| <b>PULSE<br/>DISCHARGE<br/>SINTERING<sup>[20, 44,<br/>45]</sup></b> | High density products<br>Short reaction time<br>Slightly lower reaction temperatures | Inherently small batch sizes<br>Equipment costs are high<br>Lower conversion than RHP | Similar to RHP<br>More novel method | 90%+ |
|---|--|---|-------------------------------------|------|

### 1.3.4. Reactants and reaction mechanisms

Although conceptually it may seem simplest to start with elemental *M-A-X* reactants, this is not always the case. The intermediate phases formed and the losses that occur when using elemental reactants can limit the conversion of products. One method for overcoming some of these issues has been the use of non-elemental reactants. Binary compounds of *M-X*, *A-X* and *M-A* reactants have all been used to either change the reaction mechanism or effectively start the reaction with the compounds normally formed as intermediate phases, which can then be prepared in a desirable way<sup>[46, 47]</sup>. Methods using *AX* compounds have been shown to control the release of the *A*-element, resulting in less loss and higher conversion<sup>[41, 42]</sup>. Using TiC<sub>0.67</sub> (Ti<sub>3</sub>C<sub>2</sub>) and pure *A*-element has been shown to significantly reduce reaction temperatures<sup>[48]</sup>.

The work presented in this thesis will focus heavily on the use of *M*-element oxides as reactants. The reaction will then produce a composite of the desired MAX phase as well as an oxide. It is important that the element to form the oxide is chosen so that the desired products have the lowest possible Gibbs free energy in the system. The Ellingham diagram in Figure 8 shows 5 oxides more stable than TiO<sub>2</sub> (Ca, Mg, Li, U, and Al), and thus the addition of any of these elements will be able to reduce the TiO<sub>2</sub> releasing the Ti, which can subsequently undergo recombination into a MAX phase. Al is the most abundant of these, easiest to work with and has been shown to successfully partake in exchange reaction in other systems such as the reduction of iron oxide in the application of railway track welding, or the formation of MAX phases via SHS reactions<sup>[49]</sup>. As a result the main reducing agent used in this work is Al.

As stated this introduction by no means covers the entirety of MAX phase research. It has been provided to outline the background to what is generally assumed in the introductions of the following publications and to help give context to why this work was undertaken and the overall goals. The introductions of the papers themselves contain the specific knowledge relevant to each work.

#### **1.4. Thermal energy storage introduction**

In section 1.1 the growing need for energy storage was highlighted to convert renewable energy technologies to supply base load power<sup>[50]</sup>. Methods of producing renewable energy are varied and so are the methods of storage. Direct electricity generation techniques such as solar photovoltaic panels (solar panels) or wind turbines lend themselves to electrochemical (battery) storage, as the energy is already in the desired form. Other methods such as concentrated solar power plants produce heat, which must then be converted to electricity and the energy can be stored either thermally before, or electrically after, conversion. Consideration must be given when comparing energy storage media due to the low conversion of most forms of energy to electricity. Conventional coal fired power stations operate between 35-40% efficiency<sup>[51]</sup>, wind turbines when in optimal wind conditions achieve a similar range<sup>[52]</sup> and solar panels practically work at 10-15% efficiency<sup>[53]</sup>. As a result storing the energy before conversion to electricity requires increased energy storage capacity. Storing energy thermally for use in a steam based power cycle requires almost 3 times as much capacity as storing electrically to provide the same amount of electricity to the consumer. Steam is also required at ~600°C for the turbine to operate at maximum efficiency. Lower storage temperature means lower conversion efficiency and hence larger required storage capacity. Despite the increased capacity required, thermal storage is still generally the most cost effective option when scaled to larger sizes for concentrated solar thermal power stations. Costing comparisons are complicated by the difficulties in comparing systems which operate through different mechanisms (PV panels and batteries vs steam power cycles and thermal energy storage). It is important to include operating efficiencies of the plant as well as the storage medium and capital cost of infrastructure required for the system to operate effectively.

Currently large scale thermal storage uses two methods of operation; sensible and latent heat storage<sup>[54]</sup>. Sensible heat storage involves the input of thermal energy to cause a change in temperature of the storage medium. Energy stored sensibly is dependent on the temperature change and specific heat capacity of the material. In this case the storage medium is normally as cheap as possible and materials such as concrete and nitrate salts are used<sup>[55, 56]</sup>. The amount of energy stored is generally limited by the maximum temperature of the medium or the medium's housing. Figure 9<sup>[57]</sup> shows the magnitude of the storage tanks as well as that of the heat exchangers and surrounding infrastructure required. The salt is pumped from the cold tank to the hot tank and heated by thermal oil from the solar field on charging. On discharging hot salt is pumped to the cold tank and heat is extracted through the heat exchanger. It becomes obvious here that the infrastructure surrounding the storage device (tanks, pipework and 3 heat exchange systems) contribute significantly to the cost of the thermal storage system, and simply looking at the raw cost of the storage medium is not enough. It has been estimated that the cost of infrastructure makes up approximately half the cost of the system.

## Introduction

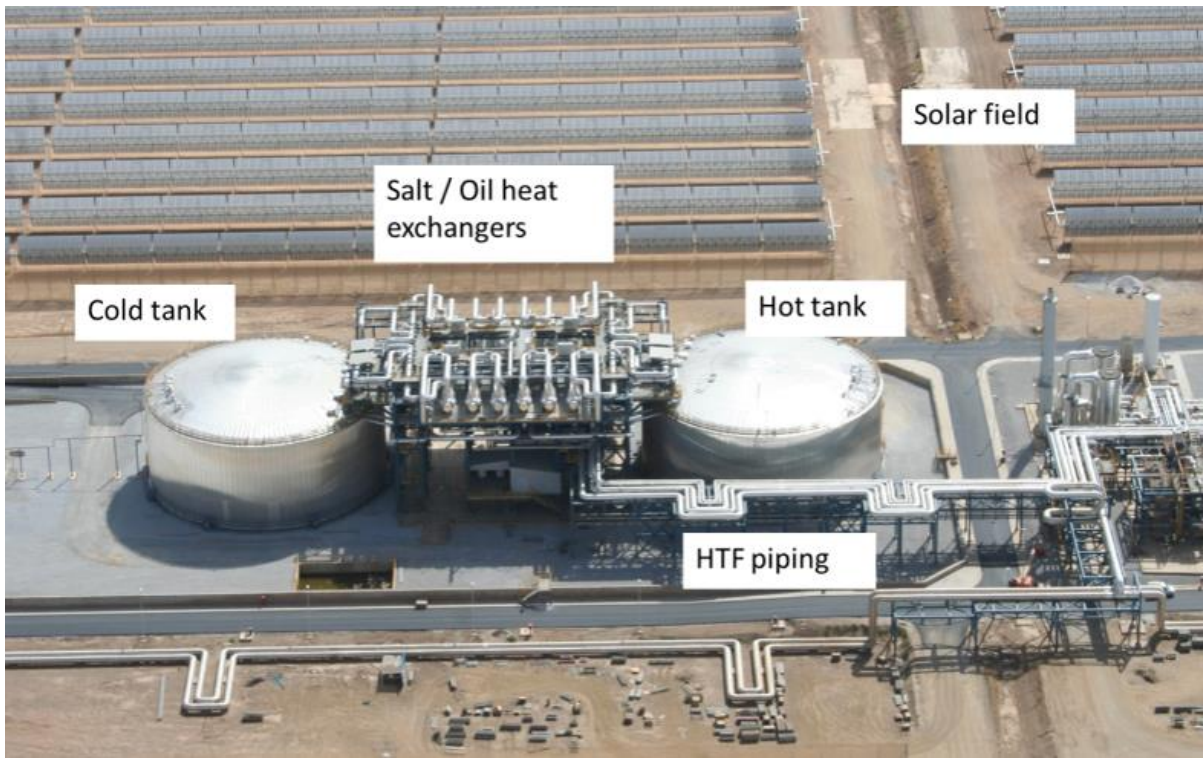


Figure 9 Molten salt tanks and infrastructure for thermal storage in a trough collector solar field<sup>[57]</sup>

Alternatively phase change materials (PCM) can be used to store energy. In these materials the energy is stored in the latent heat of a phase change, commonly solid to liquid but sometimes liquid to gas. PCM's by definition absorb and deliver energy at a constant temperature, a highly desirable attribute for downstream utilisation especially by steam turbines. Currently used PCM's are mainly eutectic salts, waxes, ice and now metals<sup>[58]</sup>. It should be noted that a working fluid can be heated to a constant temperature with a two tank molten salt system, however this adds complexities due to having to pump the salt between tanks. Molten salt can freeze in the pipe work or cold tank on complete discharge, causing large problems. A phase change material however can be configured so that it remains stationary and energy is deposited and extracted far more simply through conduction alone, due to the intrinsic constant operating temperature of a PCM energy storage system.

In the production of electricity from concentrated solar thermal energy, steam is required in the 500-600°C temperature range for efficient operation of the steam powered turbine. Current thermal storage materials fall well short of this operating temperature (molten salt sensible heat storage generally operates between 200°C and 400°C) and thus the ability to transform the energy stored into electricity through a power cycle is greatly reduced according to the Carnot efficiency (Eq. 1). A second issue is that many current storage media have very low thermal conductivity, which invariably requires the use of large and expensive heat exchange systems for the charge / discharge cycle as illustrated in Figure 9. Despite these issues large scale concentrated solar power plants with molten salt thermal storage have been built and are becoming increasingly more economically viable. The state of the art is well advanced and has by no means been covered in its entirety. However salts and other current thermal storage media are limited in both operating temperature and thermal conductivity thus development of salt based systems and alternative storage methods are still being investigated. The publication in this thesis (Chapters 10 and 11) on thermal energy storage investigates a novel method of storing energy through the phase change of a metal imbedded within a matrix of a second metal. The metals offer thermal conductivity greater than 100 times that of the salts (thus requiring significantly smaller heat exchangers), discrete constant temperature phase changes at high temperatures (up to 1085°C) and considerably higher energy densities.

The publications in this thesis were the first on the novel Miscibility Gap Alloys (MGAs) and so are in themselves introductory. Therefore this section will be kept short and a more lengthy discussion will be presented later.

## Introduction

It should be noted here that concentrated solar power plants are the example application discussed here however thermal energy storage also finds applications in the recovery of waste heat, space heating and overload protection for electronics.

### 1.5. Thermionic energy conversion.

This section will address the conversion process of the solar radiation to electricity. Currently concentrated solar radiation drives the power cycles of steam turbines connected to electrical generators. This method of electricity conversion is well established and highly efficient compared with most other methods. However concentrated solar radiation is capable of easily reaching temperatures well in excess of those which can be directly used for steam generation and may be applicable to another type of energy conversion, thermionic conversion.

Thermionic energy conversion is not widely used however it is not completely novel either. It was intensely studied and developed during the “space race” era as a means of powering craft in space. Ultimately photovoltaic (PV) solar cells panels, which were originally developed for the same purpose, won out but some thermionic power converters were produced and utilised, for example in the Russian made TOPAZ nuclear reactors.

Like PV solar panels the technologies originally used to power space craft where fossil fuels were not applicable are now being investigated to power our cities where fossil fuels are becoming increasing less applicable. Solar panels work most efficiently when in direct sunlight and when kept as cold as possible. This makes them perfectly suited for space based applications, but less so on earth, where intense direct sunlight causes the surrounding environment and the solar panels themselves to heat up, reducing their efficiency. An increase in air temperature from 25°C (the temperature at which solar panel efficiencies are quoted) to 45°C can cause an increase in solar panel temperature to up to 75°C (in QLD, Australia) and this results in an ~20% drop in efficiency<sup>[59]</sup>. Alternatively

## Introduction

thermionic converters require a very high heat input ( $>1000^{\circ}\text{C}$ ) not provided by direct solar radiation. This heat can be supplied on earth by concentrated solar radiation or by a nuclear process as it was in the TOPAZ reactors.

In its simplest form, thermionic emission works by imparting thermal energy into a material. The thermal energy is stored in lattice vibrations as phonons and in the kinetic energy of the electrons. If the electrons gain enough kinetic energy to break away from the surface of the material (emitter) they can be considered to be emitted. Alternatively stated, the work function is the latent heat of evaporation required by an electron to permit its escape<sup>[60]</sup>. The emitted electrons can then move through space until they collide with another material (collector). If the collector is then electrically connected to the emitter the electrons can flow around the circuit, through a load, as useable electrical power. A simple schematic is presented in Figure 10.

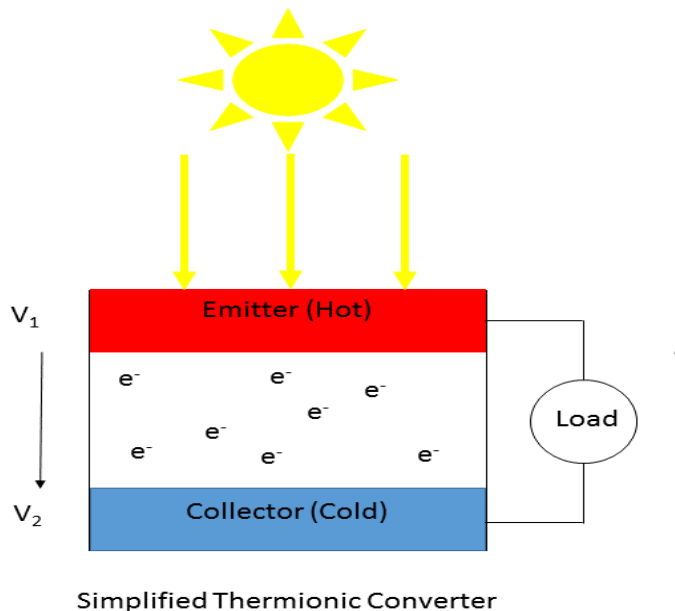


Figure 10 Simplified thermionic converter showing the basic configuration of key components.

A key variable in this process is the work function ( $w$ ), the energy required for an electron to be emitted. Normally if an electron was to escape the surface the resulting net positive charge of the remaining material would attract the electron back. This attraction is the basis of the work function. An electron must then possess more energy than the work function to successfully escape the surface. Additional energy above the work function determines the kinetic energy of the electron. Conceptually this is similar to an escape velocity of an object attempting to leave a planet's gravitation field. The object must possess more energy than the integrated gravitational force to escape.

The Richardson equation governs the maximum current density ( $\text{A}/\text{cm}^3$ ) emitted according to:

$$J = A T^2 e^{-\frac{w}{kT}} \quad \text{Eq. 6}$$

Where  $J$  = current density emitted,  $T$  = temperature,  $w$  = work function,  $k$  = Boltzmann's constant and  $A$  = the emission constant (a second material property). The values in the exponent, temperature and work function most strongly affect the emission current. Work functions of the elements range from ~2-6 eV. Naturally it seems logical to pick the element with the lowest work function and operate at the highest temperature. This is where the first major difficulty of thermionics is encountered. Elements with low work functions such as caesium (2.1 eV) also have low operating temperatures (melting point 28°C), whereas elements with high operating temperatures such as tungsten have high work functions (4.5 eV). Creating low work function high temperature materials, which are electrically conductive and stable under high vacuum is a difficult task and still an area of intense research. This was the focus of the publication in Chapter 13. Considerably more comprehensive explanations of the thermionic process can be found elsewhere<sup>[60, 61]</sup>.

## Introduction

From an engineering point of view there are numerous other difficulties in the thermionic process. Perhaps the most pressing is the space charge. As electrons are emitted into the gap between the emitter and collector (Figure 10) they accumulate as a cloud of negative charge which offers a retarding voltage to all others electrons attempting to cross the gap. This retarding voltage is known as the space charge and can significantly reduce the current of a device. The space charge can be dealt with in two ways. One way is to fill the gap with a positively charged plasma, for example caesium vapour was used in the TOPAZ reactors. This method is incredibly successful, however it is rather hazardous. Although applicable for spaceflight it is often deemed unsafe for terrestrial applications. Alternatively the width of the gap can be shortened, reducing the volume the space charge has to build up in and thus significantly reducing its effects. The smaller the gap the better and gaps in the order of 10-100  $\mu\text{m}$  are often used. This can present the significant engineering difficulty of keeping the emitter and collector uniformly separated, parallel, electrically and thermally isolated at temperatures up to 1500°C. The high temperature, high vacuum environment can also put strain on many other components in a device. As part of this work contribution was made to the design, construction and commissioning of a thermionic emission device was created to directly convert thermal energy into electrical energy, and became the conference proceeding in Chapter 12.

Thermionic emission is currently used in devices such as electron microscopes and the now largely obsolete vacuum tube valves. In these devices, and almost all other applications, a bias voltage is placed on the emitter while it is heated, encouraging the emission of electrons and removing the space charge. This process is known as field assisted emission. Through this method significantly more current can be generated.

Unfortunately power cannot be extracted using a bias voltage in this way. However by measuring the current through a range of bias voltages at a range of temperatures, the work function of an emitter material can be determined. Although not specifically discussed in any of the publications a contribution was made to the design and construction of a Schottky chamber was for the testing of emitter materials. The process is further described in the experimental methods section 4.

Of the areas studied in this work thermionic emission is perhaps both the oldest and least developed. While the MAX phases have been studied in depth and the MGAs developed almost to the point of commercial application, the use of thermionic emission to produce electrical power in terrestrial applications is still very much in its infancy. The development in this field was in proof of concept and problem identification and is by no means at the stage of commercial application.

## References

1. *Key World Energy Statistics* 2014, International Energy agency.
2. Ganguly, A., M.W. Barsoum, and J. Schuster, *The 1300°C Isothermal Section in the Ti–In–C Ternary Phase Diagram*. Journal American Ceramic Society, 2005. **88**: p. 1290-1296.
3. Barsoum, M.W., *The  $M_{n+1}AX_n$  Phases and their Properties*, in *Ceramics Science and Technology: Materials and Properties*, R. Riedel and I.-W. Chen, Editors. 2010, John Wiley and Sons. p. 299-347.
4. Barsoum, M.W., *The  $M_{n+1}AX_n$  Phases: A New Class of Solids; Thermodynamically Stable Nanolaminates*. Solid State Chemistry, 2000. **28**: p. 201-281.
5. McKissick, K. *Power Tower*. 2015 [cited 2016 14/01/16].
6. Moran, M. and H. Shapiro, *Fundamentals of engineering thermodynamics*. 1993, USA: Wiley and Sons.
7. Jeitschko, W., H. Nowotny, and F. Benesovsky, *Die H-Phasen  $Ti_2InC$ ,  $Zr_2InC$ ,  $Hf_2InC$  und  $Ti_2GeC$* . Monatshefte für Chemie und verwandte Teile anderer Wissenschaften 1963. **94**(6): p. 1201-1205.
8. Barsoum, M.W. and T. El-Raghy, *Synthesis and Characterisation of a Remarkable Ceramic:  $Ti_3SiC_2$* . Journal American Ceramic Society, 1996. **79**: p. 1953-1956.
9. W., B.M., *High-Resolution Transmission Electron Microscopy of  $Ti_4AlN_3$ , or  $Ti_3Al_2N_2$  Revisited*. J. Am. Ceram. Soc., 1999. **82**(9): p. 2545 - 2547.
10. Barsoum, M.W., *MAX Phases: Properties of Machineable Ternary Carbides and Nitrides*. 2013: Wiley.
11. Barsoum, M.W. and M. Radovic, *Elastic and Mechanical Properties of the MAX Phases*. Annual Review of Materials Research, 2011. **41**: p. 195-227.
12. Low, I.M., *Advances in science and Technology of the  $M_{n+1}AX_n$  Phases*. 2012: Woodhead publishing.
13. Cuskelly, D.T., E.H. Kisi, and H. Sugo, *MAX phase - alumina composites via exchange reaction in the  $M_{n+1}AlC_n$  systems (M= Ti, V, Cr, Nb, or Ta)*. Journal of Solid State Chemistry, 2015. **223**: p. 150-157.
14. Barsoum M. W. and E.-R. T., *The MAX Phases: Unique New Carbide and Nitride Materials*. American scientist, 2001. **89**(4).
15. Wang, L., P. Rulis, and W. Ching, *Calculation of core-level excitation in some MAX-phase compounds*. J. Appl. Phys, 2013. **114**(2).
16. X. Wang, e.a.,  *$Ti_5Al_2C_3$ : A New Ternary Carbide Belonging to MAX Phases in the Ti–Al–C System*. J. Am. Ceram. Soc., 2012. **95**(5): p. 1508 - 1510.
17. Hu C., Z.H., Li F. Huang Q., Bao Y., *New phases' discovery in MAX family*. International Journal of Refractory metals and hard Materials, 2012. **36**: p. 300 - 312.
18. Lane, N., et al., *Comment on "A new ternary carbide belonging to the MAX phases in the Ti-Al-C system"*. J. Am. Ceram. Soc., 2013. **95**(10): p. 3325-3354.
19. Ganguly, A., *Synthesis and Characterization of Solid Solutions of  $M_{(N+1)}AX_N$  Phases*. 2006, Drexel University.
20. Gao N., Z.D., Miyamoto y., *Rapid synthesis of dense  $Ti_3SiC_2$  by spark plasma sintering*. j. Euro. Cerm. Soc., 2002. **22**(13): p. 2365 - 2370.
21. Zhang J., K.H., Kirstein O., *Quantitative neutron diffraction texture measurement applied to  $\alpha$ -phase alumina and  $Ti_3AlC_2$* . J. Appl. Crystallogr. **2011**(44): p. 1062- 1070.
22. Cuskelly, D.T., et al.,  *$Ti_3GaC_2$  and  $Ti_3InC_2$ : First bulk synthesis, DFT stability calculations and structural systematics*. Journal of Solid State Chemistry, 2015. **230**: p. 418-425.
23. Hendaoui, A., et al., *Synthesis of high-purity polycrystalline MAX phases in Ti–Al–C system through Mechanically Activated Self-propagating High-temperature Synthesis*. Journal of the European Ceramic Society, 2009. **30**(4): p. 1049-1057.
24. Bandyopadhyay, D., *The Ti-Si-C (Titanium - Silicon - Carbon) system*. J. Phase Equilib. Diff., 2004. **25**(5).

25. Salama, I., T. El-Raghy, and M.W. Barsoum, *Synthesis and mechanical properties of Nb<sub>2</sub>AlC and (Ti,Nb)<sub>2</sub>AlC*. Journal of Alloys and Compounds, 2002. **347**(1-2): p. 271-278.
26. Keast, V.J., S. Harris, and D.K. Smith, *Prediction of the stability of the M<sub>n+1</sub>AX<sub>n</sub> phases from first principles*. Physical Reviews B 2009. **80**: p. 214113.
27. Cordoba J., S.M., Alcala M., Gotor F., *Synthesis of Ti<sub>3</sub>SiC<sub>2</sub> Powders: Reaction Mechanism*. J. Am. Ceram. Soc., 2007. **90**(3): p. 825 - 830.
28. Pang, W.K., et al., *Comparison of thermal stability in MAX 211 and 312 phases*. Journal of Physics, 2010. **251**(1): p. 012025.
29. El Saeed, M.A., *Optimization of the Ti<sub>3</sub>SiC<sub>2</sub> MAX phase synthesis*. Refractory Metals and Hard Materials, 2012. **35**: p. 127-131.
30. Li, J.-F., F. Sato, and R. Watanabe, *Synthesis of Ti<sub>3</sub>SiC<sub>2</sub> polycrystals by hot-isostatic pressing of the elemental powders*. Journal of Materials Science Letters, 1999. **18**: p. 1595-1597.
31. Zhang, W., et al., *Reactive Hot Pressing and Properties of Nb<sub>2</sub>AlC*. Journal of the American Ceramic Society, 2009. **92**(10): p. 2396-2399.
32. Eklund, P., et al., *The M<sub>n+1</sub>AX<sub>n</sub> phases: Materials science and thin-film processing*. Thin Film Solids, 2010. **518**(8): p. 1851-1878.
33. Eklund, P., et al., *Discovery of the ternary nanolaminated compound Nb<sub>2</sub>GeC by a systematic theoretical-experimental approach*. Physical Review Letters, 2012. **109**(3): p. 035502.
34. Hfgberga, H., et al., *Growth and characterization of MAX-phase thin films*. Surface & Coatings Technology, 2005. **193**: p. 6-10.
35. Lin, T.-C. and M.-H. Hon, *Synthesis and microstructure of the Ti<sub>3</sub>SiC<sub>2</sub> in SiC matrix grown by chemical vapor deposition*. Ceramics International, 2008. **34**(3): p. 631-638.
36. Palmquist, J.-P., et al., *M<sub>n+1</sub>AC<sub>n</sub> phases in the Ti-Si-C system studied by thin film synthesis and ab initio calculations*. Physical Reviews B 2004. **70**: p. 165401.
37. Chen, J., J. Li, and Y. Zhou, *In-situ Synthesis of Ti<sub>3</sub>AlC<sub>2</sub>/TiC-Al<sub>2</sub>O<sub>3</sub> Composite from TiO<sub>2</sub>-Al-C System*. Journal of Materials Science and Technology, 2005. **22**(4): p. 455-458.
38. Hendaoui, A., et al., *A novel method for synthesis of low-cost Ti-Al-C-based cermets*. International Journal of Self-Propagating High-Temperature Synthesis, 2010. **18**(4): p. 267-272.
39. Riley, D.P., E.H. Kisi, and D. Phelan, *SHS of Ti<sub>2</sub>SiC<sub>2</sub>: Ignition temperature depression by mechanical activation*. Journal European Ceramic Society, 2004. **26**(6): p. 1051-1058.
40. Riley, D.P. and E.K. Kisi, *Self-Propagating High-Tempertue Synthesis of Ti<sub>3</sub>SiC<sub>2</sub>: 1, Ultra High-Speed Neutron Diffraction Study of the Reaction Mechinism*. Journal American Ceramic Society, 2002. **85**(10): p. 2417-2424.
41. Wu, E. and E.H. Kisi, *Synthesis of Ti<sub>3</sub>AlC<sub>2</sub> from Ti/Al<sub>4</sub>C<sub>3</sub>/C Studied by In Situ Neutron Diffraction*. Journal of the American Ceramic Society, 2005. **89**(2): p. 710-713.
42. Wu, E., E.H. Kisi, and D.P. Riley, *Intermediate Phases in Ti<sub>3</sub>SiC<sub>2</sub> Synthesis from Ti/SiC/C Mixtures Studied by Time-Resolved Neutron Diffraction*. J. Am. Ceram. Soc., 2002. **85**(12): p. 3084-3086.
43. Yeh, C.L., R.F. Li, and Y.G. Shen, *Formation of Ti<sub>3</sub>SiC<sub>2</sub>-Al<sub>2</sub>O<sub>3</sub> in situ composites by SHS involving thermite reactions*. Journal of Alloys and Compounds, 2009. **478**(1-2): p. 699-704.
44. Zang, Z.F., et al., *Application of pulse discharge sintering (PDS) technique to rapid synthesis of Ti<sub>3</sub>SiC<sub>2</sub>from Ti/Si/C powders*. Journal of the European Ceramic Society, 2002. **22**(16): p. 2957-2961.
45. Zhang, J., et al., *Rapid fabrication of Ti<sub>3</sub>SiC<sub>2</sub>-SiC nanocomposite using the spark plasma sintering-reactive synthesis (SPS-RS) method*. Scripta Materialia, 2007. **56**(3): p. 241-244.
46. Singh A., B.S., Virzi D., Keshri A., Agarwal A., Harimkar S., *In-situ synthesis of TiC/SiC/Ti<sub>3</sub>SiC<sub>2</sub> composite coatings by spark plasma sintering*. Surface and Coatings Technology, 2011. **205**(13): p. 3840 - 3846.

## Introduction

47. Yang S., M.S.Z., Hashimoto, *Reaction in  $Ti_3SiC_2$  powder synthesis from a Ti–Si–TiC powder mixture*. Journal of Alloys and Compounds, 2004. **368**(1): p. 312 - 317.
48. Kisi, E.H., et al., *Inter-Conversion of  $M_{n+1}AX_n$  Phases in the Ti-Al-C system*. Journal American Ceramic Society, 2007. **90**(6): p. 1912-1916.
49. C., L., *THERMITE RAIL WELDING: HISTORY, PROCESS DEVELOPMENTS,CURRENT PRACTICES AND OUTLOOK FOR THE 21st CENTURY* Conrail Technical Services Laboratory.
50. S., S., et al., *Solar intermittency: Australias clean energy challange - Characterising the effect of high penetration solar intermittency on Australian electricity networks*. 2012, CSIRO.
51. Steam Turbine Efficiency. 2016 [cited 2016 14/01/06]; Available from: <http://www.turbinesinfo.com/steam-turbine-efficiency/>.
52. D., W., *Small wind turbines, analysis design and application*. 2011: Springer.
53. Solar Panel Efficiency. 2014 [cited 2016; Available from: <http://pureenergies.com/us/how-solar-works/solar-panel-efficiency/>.
54. K., L., et al., *Reaslising the potential of concentrating solar power in Australia* 2012, ASI.
55. D., L., et al., *High-Temperature Solid-Media Thermal Energy Storage for Solar Thermal Power Plants*, in *IEEE*. 2012. p. 516-524.
56. M., M., et al., *State of the art on high temperature thermal storage for power production. Part 2 Case studies*. Renewable ans sustaninable energy reviews, 2010. **14**: p. 56-72.
57. Solar, B.D. *CONCENTRATING SOLAR*. 2016; Available from: <http://bigdishsolar.com/the-csp-context/>.
58. A., S., et al., *Review on thermal energy storage with phase change materials and applications*. Renewable ans sustaninable energy reviews, 2009. **13**: p. 318-345.
59. C., C. *Solar Panels And Temperature*. 2012; Available from: <http://gold-coast-solar-power-solutions.com.au/posts/solar-panels-and-temperature/>.
60. S., A., *Direct energy conversion, 4th edition*. 1982, Boston: Allyn and Bacon.
61. G, H., *Therminoic energy conversion*. 1973, Cambridge: MIT press.

## 2. Scope statement

The major focus of this thesis is in the investigation of the synthesis of MAX phases. MAX phases have the potential to be applied in a large number of roles where classical materials are inadequate. They are attractive mainly due to the unique combination of metal – like and ceramic – like properties, which arise from the complex crystal structure and bonding. As yet practical applications have been limited mainly due to difficulties in the synthesis of industrial quantities of pure products and the cost of reactants, which make these phases prohibitively expensive for most applications.

The synthesis of MAX phases with respect to their engineering outcomes was studied extensively. Primarily this involves an in-depth knowledge of the reaction mechanism. The reaction techniques used were limited to pressureless reactive synthesis and self-propagating high temperature synthesis so that the method could be more readily scaled to industrial batch sizes. To minimise cost of reactants, great emphasis was placed on the use of *M*-element oxides as reactants. Metallic *M*-elements normally used as reactants are expensive and this significantly contributes to the cost of the MAX phase.

The conditions stated here shift the goals away from what is normally considered the Holy Grail in MAX phase synthesis, phase pure products. Instead the work focuses on applicability of novel and readily scalable synthesis methods to MAX phases in general.

It was hoped that the MAX phases may find applications in the hazardous conditions of renewable energy production, specifically using concentrated solar radiation. Although the MAX phases themselves have yet to be incorporated, extensive progress has been

## Scope statement

made in the fields of both overcoming the issues of intermittency of solar power through thermal energy storage and in alternative energy conversion methods through thermionic conversion.

The work into thermal storage focused on developing a storage medium which overcame the low thermal conductively issue of current storage media. Specifically the production of steam for a power cycle was a key application.

Thermionic emission was investigated as a proof of concept investigation to see if it was possible to create a working device which would convert the heat which can be generated by concentrated solar power plants into electricity. As a first stage investigation test bed equipment was required for key variables to be identified.

### 3. Publications

A major investigation reported within this thesis was the synthesis of MAX phases via a novel synthesis route, an exchange reaction. Briefly, MAX phase synthesis requires an early transition metal as the *M*-element. These metals are notoriously difficult to refine and often prohibitively expensive in all but the most specific of applications. It has been shown that the *M*-elements can be reduced from their oxides (which are considerably easier to obtain) by relatively inexpensive metals such as Al. The use of *M*-oxides as starting materials thus has the potential of significantly reducing the cost of the MAX phase thus opening up potential use in larger scale applications. The first two papers *MAX phase - alumina composites via exchange reaction in the  $M_{n+1}AlC_n$  systems ( $M = Ti, V, Cr, Nb, or Ta$ )* and *MAX phase – alumina composites via elemental and exchange reactions in the  $Ti_{n+1}AC_n$  systems ( $A = Al, Si, Ga, Ge, In$  and  $Sn$ )* in Chapters 5 and 6 respectively investigate the production of MAX phases via aluminothermic reduction reactions. This expanded the field from the isolated phases previously studied. Within these two papers it is proven that a single step exchange reactions is a general and viable synthesis methodology for almost all MAX phases. In addition the papers present an investigation into the formation of 312 MAX phases from *MX* and 211 MAX phase reactants.

The exchange reaction methodology, by definition, must produce a composite of the desired MAX phase and an oxide product. In the case of aluminothermic reduction a MAX phase – alumina composite is formed. This can be problematic as in most cases a pure MAX phase is desired. The use of carbon as a reducing agent produces a composite where the oxide is a gas and so self-separating, producing a pure product. The fourth

## Publications

publication (Chapter 7), *Single step carbothermal MAX phase synthesis*, investigates carbothermal reduction as a reaction mechanism and provides the world's first pure MAX phase synthesis by this method.

Investigations into the synthesis of MAX phases during this work led to the observation of trends in the stability of MAX phases and from here investigations into the formation of new MAX phases. Two new phases were produced in this work and their synthesis, characterisation and stability, as well as observed trends in MAX phase structures are presented in the Chapter 8, *Ti<sub>3</sub>GaC<sub>2</sub> and Ti<sub>3</sub>InC<sub>2</sub>: First bulk synthesis, DFT stability calculations and structural systematics*.

The first 4 publications complete the aspect of this thesis related to MAX phases. The candidate was the initiator and primary investigator in all of the work on MAX phases and consequently lead author on all work. The remaining work, more closely related to the application of materials to solar thermal power production, was performed as part of a team in a large project.

As mentioned in §1.1 the intermittency of solar power is a great hindrance to its large scale application and a method of energy storage is required to compensate. Novel metal alloys were designed for the application of storing thermal energy from excess solar radiation. The fifth and sixth publications *Miscibility gap alloys with inverse microstructures and high thermal conductivity for high energy density thermal storage applications* and *High conductivity phase change materials for thermal energy storage – miscibility gap alloys* (Chapters 9 and 10) are the first reports of miscibility gap alloys, novel materials designed for thermal energy storage.

The use of thermionic electricity generation was investigated as a potential application for concentrated solar power plants. It was hoped that the high temperatures reachable by concentrated solar power could translate into increased plant efficiencies via thermionic energy conversion, and that MAX phases could play a role in overcoming some of the harsh environments critical components are exposed to. A thermionic emission device was built and tested along with the synthesis of materials for thermionic emitters and collectors. Chapters 11 and 12 *Development of a thermionic converter for CSP applications* and *Low temperature synthesis of low thermionic work function ( $La_xBa_{x-1}B_6$ )* contain the papers related to thermionic emission.

Appendix 1 contains an additional paper which was published during the candidature however not on a topic which is inside the original scope. The paper is concerned with the optical properties of the Cu – Zn brasses originally manufactured for inclusion in MGA thermal storage alloys.

### 3.1. Statements of contribution

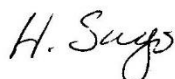
Below are the contributions the candidate made to each paper that is presented in this thesis signed by all co-authors.

By signing below I confirm that Dylan Cuskelly contributed ~80% to the paper *MAX phase - alumina composites via exchange reaction in the  $M_{n+1}AlC_n$  systems ( $M= Ti, V, Cr, Nb, or Ta$ )* as first author by initiating the research, conducting experimentation, performing sample characterisation, data analysis and the drafting and writing of the paper.

Co-author **Erich Kisi**

Signed  Date 27/11/2016

Co-author: **Heber Sugo**

Signed  Date 27/11/2016

Faculty Assistant Dean Research and Training: **Michael Stockenhuber**

Signed  Date 29.1.2016

By signing below I confirm that Dylan Cuskelly contributed ~75% to the paper *MAX phase – alumina composites via elemental and exchange reactions in the  $Ti_{n+1}AC_n$  systems ( $A = Al, Si, Ga, Ge, In$  and  $Sn$ )* as first author by initiating the research, conducting experimentation, performing sample characterisation, data analysis and the drafting and writing of the paper.

Co-author **Erin Richards**

Signed *E. Richards*

Date 25 - 1 - 2016

Co-author **Erich Kisi**

Signed *E. Kisi*

Date 27/1/2016

Faculty Assistant Dean Research and Training: **Michael Stockenhuber**

Signed *M. Stockenhuber*

Date 29.1.2016

## Publications

By signing below I confirm that Dylan Cuskelly contributed ~90% to the paper *Single step carbothermal MAX phase synthesis* as first author by initiating the research, conducting preliminary experimentation, performing sample characterisation, data analysis and the drafting and writing of the paper.

Co-author **Erich Kisi**

Signed  Date 27/1/2016

Faculty Assistant Dean Research and Training: **Michael Stockenhuber**

Signed  Date 29.1.2016

By signing below I confirm that Dylan Cuskelly contributed ~75% to the paper *Ti<sub>3</sub>GaC<sub>2</sub> and Ti<sub>3</sub>InC<sub>2</sub>: First bulk synthesis, DFT stability calculations and structural systematics* as first author by initiating the research, conducting experimentation, performing sample characterisation, data analysis and the drafting and writing of the paper.

Co-author **Erin Richards**

Signed *E. Richards* Date 25-1-2016

Co-author **Erich Kisi**

Signed *E. Kisi* Date 27/1/2016

Co-author **Vicki Keast**

Signed *V. Keast* Date 28/1/2016

Faculty Assistant Dean Research and Training: **Michael Stockenhuber**

Signed *D. S.* Date 29/1/2016

## Publications

By signing below I confirm that Dylan Cuskelly contributed ~30% to the paper *Miscibility gap alloys with inverse microstructures and high thermal conductivity for high energy density thermal storage applications* as third author by, conducting experimentation, performing data analysis and the drafting of the paper.

First-author **Heber Sugo**

Signed *H. Sugo* Date *27/1/2016*

Co-author: **Erich Kisi**

Signed *E. Kisi* Date *27/1/2016*

Faculty Assistant Dean Research and Training: **Michael Stockenhuber**

Signed *D. Suga* Date *29.1.2016*

By signing below I confirm that Dylan Cuskelly contributed ~40% to the paper *High conductivity phase change materials for thermal energy storage – miscibility gap alloys* as second author by conducting experimentation, performing sample characterisation and data analysis, the drafting of the paper and the oral presentation at the solar 14 conference in Melbourne.

First author: **Heber Sugo**

Signed *H. Sugo* Date 27/1/2016

Co-author **Anthony Rawson**

Signed *A. Rawson* Date 27/1/2016

Co-author: **Erich Kisi**

Signed *E. Kisi* Date 27/1/2016

Faculty Assistant Dean Research and Training: **Michael Stockenhuber**

Signed *M. Stockenhuber* Date 29.1.2016

## Publications

By signing below I confirm that Dylan Cuskelly contributed ~35% to the paper *Development of a thermionic converter for CSP applications* as second author by conducting experimentation, performing sample characterisation and data analysis, the drafting of the paper and the oral presentation at the solar 14 conference in Melbourne.

First author: **Heber Sugo**

Signed *H. Sugo* Date 25/1/2016

Co-author **Muhammad Hasan**

Signed *M. Hasan* Date 25.01.2016

Co-author: **Erich Kisi**

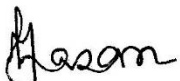
Signed *E. Kisi* Date 27/1/2016

Faculty Assistant Dean Research and Training: **Michael Stockenhuber**

Signed *D. S.* Date 29.1.2016

By signing below I confirm that Dylan Cuskelly contributed ~20% to the paper *Low temperature synthesis of low thermionic work function (La<sub>x</sub>Ba<sub>1-x</sub>)B<sub>6</sub>* as second author by conducting experimentation, performing sample characterisation and data analysis and the drafting of the paper.

First author: **Muhammad Hasan**

Signed  Date 25.01.2016

Co-author **Heber Sugo**

Signed  Date 27/1/2016

Co-author: **Erich Kisi**

Signed  Date 27/1/2016

Faculty Assistant Dean Research and Training: **Michael Stockenhuber**

Signed  Date 29.1.2016

## 4. Methodology

Throughout the thesis many different experimental methods and analysis techniques were utilised. As the nature of publications keeps experimental methods very brief the most commonly used methods will be expanded upon here to give the reader a better understanding of the process involved. It is intended that this section might be useful to an engineering student of PhD level just entering the field.

As a means of explanation the entire process for the synthesis and analysis of a  $Ti_3SiC_2$  sample via an exchange reaction will be followed from start to finish, showing typical results and the most commonly used analysis techniques. Auxiliary methods only used on selected samples are provided in a separate section at the end.

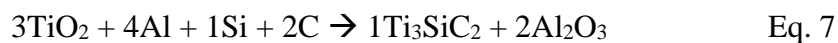
### 4.1. Sample preparation

The first step in the process of producing a new sample was always determining exactly what the goal product is (e.g. proof of concept for a novel phase or, optimisation of a known system etc.). This then determines what reactants will be used. Reactants can vary in both purity and form considerably. For example commercial grade materials are of the order 99% pure whereas laboratory materials are generally closer to 99.99% and some even higher. The products of a reaction cannot be expected to be more pure than the reactants used, however using reactants of higher purity will not necessarily produce better products and increase expense dramatically. Reactants can also vary in physical form, some being solutions, suspensions, gasses and liquids. Of those which are solid,

they may vary in size from solid ingot through granules to powders. Metal powders can then vary from macroscopic (~1 mm) to the nanoscale. Smaller particle size generally means a more homogeneous mix of reactants and shortened diffusion distances, thus more complete reaction. However similar to reactant purity, decreasing particle size will not always give better products, only when the problem is diffusion based. Issues can arise with the use of fine metal powders. As the surface area of these materials become progressively larger, surface affects which are normally ignored can become significant. The most important of these is oxidation. While any metal surface exposed to the atmosphere will begin to oxidise, at room temperature in dry air the process is normally so slow it is not noticeable. However fine metal powders of materials normally considered inert can become highly flammable and spontaneously combust when exposed to air (e.g. <45 micron Ti powder). Even if complete combustion does not occur the surface oxidation can affect purity. Throughout this work, powders of greater than 99% purity at particle sizes which can be handled in air without risk of combustion were used almost exclusively as reactants.

In the cases where fine metal powders were required they were dealt with in a glove box. The glovebox contains an inert Ar atmosphere which allows materials with risk of oxidation to be safely dealt with.

Preparation of samples involves firstly determining the masses of reactants required. This is performed through balanced chemical reaction equations



and then converting the reactant molar ratios into equivalent mass ratios. The appropriate masses of reactants can then be weighed out. The accuracy of the weighing procedure is

## Methodology

important as electronic balances can vary significantly. Increasing the total weight of a sample decreases the relative error caused by the accuracy of the scales. Standard samples were of 10 g total mass and weighing was performed on scales of 0.01 g accuracy.

Correctly weighed reactants need to be mixed thoroughly to ensure a homogeneous composition. This can be done by simply stirring or shaking the reactants, although long mixing times are often required and this become impractical. Differences in densities can lead to separation regardless of mixing time. High energy ball milling is a process in which the reactants are placed in a vial with a number of milling balls. The milling vial is then placed into a milling machine (SPEX 800 high energy ball mill) which oscillates the milling vial around multiple axes and keeps the reactant powders and milling balls in constant motion. High energy ball milling is aggressive enough to make the milling balls (and reactants) bounce around inside the mill causing collisions and crushing. This is opposed to low energy ball milling where the balls roll around in the milling chamber with a grinding action. The milling process not only causes mixing of reactants on a fine scale but also changes the microstructure. Brittle reactants are crushed into smaller particles whereas malleable materials are deformed and often fuse together. A mixture of malleable metals and brittle ceramic powders produces a microstructure where the ceramic particles become embedded into a matrix of the softer metal. The microstructure becomes analogous to sand particles kneaded into dough. This is important as without milling reactant powders normally have only very small point contacts which limit the diffusional cross-section hence slowing the reaction. The new microstructure caused by milling can greatly increase the contact area, improve reaction rates and decrease self-propagating synthesis ignition temperatures. Extending the process to longer milling times will eventually cause the materials to react at the ambient temperature inside of the

mill. The process is known as mechanically activated self-propagating high temperature synthesis (MASHS) and has been used to successfully produce MAX phases previously, and once unintentionally in this thesis. Milling was generally used only to the extent of ensuring uniformly mixed materials.

The milling process relies on two main variables, the milling time and the charge ratio. The charge ratio is the ratio of the mass of the milling balls to the mass of the reactants. In this work a charge ratio of 7:1 and 15 min of milling was generally used to prepare samples for sintering. All milling was performed in hardened steel milling vials using steel milling balls. Should it be desired to mix powders with no change in microstructure, plastic (PMMA) milling balls can be used. The lighter soft balls do not deform the reactants.

A safety consideration arises after reactants have been balled milled. The decreased particle size and large clean surface area can produce materials which will spontaneously combust when exposed to the atmosphere. Materials with a known risk of combustions were handled inside of an Ar filled glove box.

After milling the reactant powder mixture was pressed into a pellet. The pressing process predominantly densifies the reactants, increasing the surface contact thereby assisting in complete reaction. Green pellets also support their own weight and can be handled more easily. Pellets are produced by placing reactants into a pellet pressing die, which is placed in a hydraulic press and load applied. Higher pressing pressures cause improved density however the process happens with diminishing returns. Eventually, with increasing pressure the pellet undergo failure in the die and cracking occurred. Pellets that have

## Methodology

failed in this way cracked into an hourglass shape. Five grams of reactants in a 15 mm die pressed at 250 MPa (~50 000 N) generally produced high quality, roughly 10 mm tall pellets. Taller pellets often presented pressing problems, if pellets were unwilling to hold together less material was pressed producing shorter, more disk-like pellets, which generally helped. Using 5 g of powder per pellet allowed the 10 g of reactants to produce two pellets, which could be used to either repeat an experiment or test a second variable (e.g. different synthesis conditions).

Pressed pellets were heated in a furnace to allow reaction to occur. Due to the reactive nature of the materials used an inert atmosphere was required, thus tube furnaces were used extensively. Tube furnaces have a long tube which can be sealed at both ends that is placed through a furnace and the centre portion of the tube heated from the outside. In this work 1 m, 50 mm internal diameter Al<sub>2</sub>O<sub>3</sub> tubes were used. An inert atmosphere can be created in two ways. One is to attach a vacuum pump to one end of the tube and deplete the system of air. The other is to have a flow of Ar into one end of the tube and out the other. Both methods were used however the flowing Ar method proved more practical and so was used far more extensively.

Green pellets are normally placed inside a boat while in the furnace. The boat helps in transporting the pellets and in preventing cross contamination to the tube. Al<sub>2</sub>O<sub>3</sub> is generally the material of choice for boats however they are prone to cracking due to thermal shock from exothermic reactions. As a result custom made graphite boats were machined for this work and used extensively.

Heating sequences are determined based on the desired products. Each phase may have its own required reaction temperature and time. In many cases overheating causes decomposition of the target phase, however insufficient temperature does not allow for complete reaction. Temperature is generally a critical variable. In many cases where reaction temperatures had to be kept low because of decomposition issues, the slower diffusion resulted in extended synthesis times. A typical material  $Ti_3SiC_2$ , was synthesised at 1400°C with a 180 min dwell. Heating ramps were generally 5°C/min, a rate determined by  $Al_2O_3$  furnace tubes, which are susceptible to cracking from thermal shock.

Pellets removed from the furnace had generally undergone visible change in both colour and size as well as an obvious change in hardness. Pellets were sectioned (generally in half) on a low speed diamond bladed cut-off saw. A layer of surface oxidation was apparent in the vast majority of samples, however this was generally limited to the outer <1 mm of the pellet. The 5 g samples produced are large enough to safely disregard surface effects. After sectioning one half of each pellet was prepared for X-ray diffraction (XRD) analysis and the other kept for scanning electron microscopy (SEM).

XRD preparation involved first removing the surface by grinding. Once a homogeneous pellet had been obtained it was crushed in a motor and pestle into powder (<100  $\mu m$ ). The crushed powder is then loaded into standard XRD sample holders for XRD analysis. The cut surface of pellets can be directly analysed however the cut surface is not necessarily representative of the bulk and preferred orientation of the plate like MAX phase grains will be considerable, making analysis slightly more complex. When analysing MGA samples cut and lightly polished surfaces were generally used.

## Methodology

Samples underwent XRD analysis for phase identification and also quantitative phase analysis using Rietveld refinement<sup>[1]</sup> to determine the proportions of products produced. The process is explained in more detail although still at an introductory level in the following sections.

SEM preparation involves polishing the cut surface with progressively finer grades of SiC abrasive papers. Normally this process is followed by diamond polishing using a diamond suspension on a cloth polishing pad. Unfortunately the porosity of the MAX phase pellets caused the cloth pads to erode rapidly and fill the pores of the sample with debris. In many cases 1200 grit SiC paper provided a surface that could be adequately imaged in the SEM and so diamond polishing was not required. Alternatively a fracture surface may be viewed which can also give a good representation of the morphology.

### 4.2. X-ray diffraction analysis

An explanation of X-ray diffraction (XRD) relies on some knowledge of crystallography. An exceptionally short overview will be given here mainly to help explain terminology used. In general atoms in a solid are arranged in a regular repeating pattern. The number of available patterns are vast but each is defined by a unit cell of atoms which is the smallest group of atoms that can be repeated through space by translation to make up the infinite crystal. For example three common structures are shown in Figure 11. These are the basic building blocks of crystallography. This building block is a parallelepiped which may have sides of unequal length and unequal angles resulting in 7 different crystal systems from high symmetry cubic systems (all sides equal lengths all angles equal) to triclinic systems (all sides having different lengths and all angles being different). If the

structure has an atom at its corners and another identical atom in the centre of the cell, it is referred to as body-centred. Similar configurations contain an atom in the centre of each face and in the centre of one face (face-centred and base-centred respectively). These more complex units obey all the same rules as a lattice with only atoms at its centre, a so called primitive lattice. The non-primitive cells form what is known as a Bravais lattice and create a total of 14 crystal systems whilst still maintaining the ability for the cell to be repeated through space indefinitely by translation alone.

A more complex unit cell may have one or more different atoms and each type of atom may have multiple positions or sites that it occupies in the cell, in order to create a structure that can be reproduced solely by translation. The arrangement of the atoms in the cell often shows a high symmetry. The positions of a smaller number of atoms can define an asymmetric unit which, along with a set of point group symmetry conditions defines the remaining atoms in the cell. The space group and position of all atoms in a unit cell are required to fully define the crystal structure of a material.

The Bravais lattices are a special case. The face-centred cubic structure for example, can also be made using a rhombohedral cell however it is generally more convenient to use the cubic cell as it more directly indicates the symmetry of the system even though the cubic cell is larger.

The length of the sides of the unit cell are known as lattice parameters and are referred to as  $a$ ,  $b$  or  $c$ . The lattice parameters  $a$ ,  $b$  and  $c$  lie along the unit vectors  $i$ ,  $j$  and  $k$  respectively. The angles between these vectors are;  $\alpha$  (between  $i$  and  $j$  unit vectors,),  $\beta$  (between  $j$  and  $k$  unit vectors,) and  $\gamma$  (between  $i$  and  $k$  unit vectors,). These parameters are used to define the dimensions of the unit cell. In systems with high symmetry these

## Methodology

parameters can be related, cubic materials, for example have lattice parameters equal and angles are  $90^\circ$  so are defined by a single parameter  $a$ . Other crystal systems require more variables to completely define the unit cell shape. The positions of the atoms within the unit cell are also important. Atomic positions are defined as the fractional coordinate along each of the unit vectors ( $i, j$  and  $k$ ) the atom sits. For example the atomic position of the atom in the centre of the body-centred cubic structure could be written as  $(0.5, 0.5, 0.5)$ .

The distance between crystallographically identical planes of atoms are known as d-spacings. These distances are easily measured by X-ray or neutron diffraction. This introduction serves only to explain the terminology that will be used in later sections, and by no means contains a full explanation of the field.

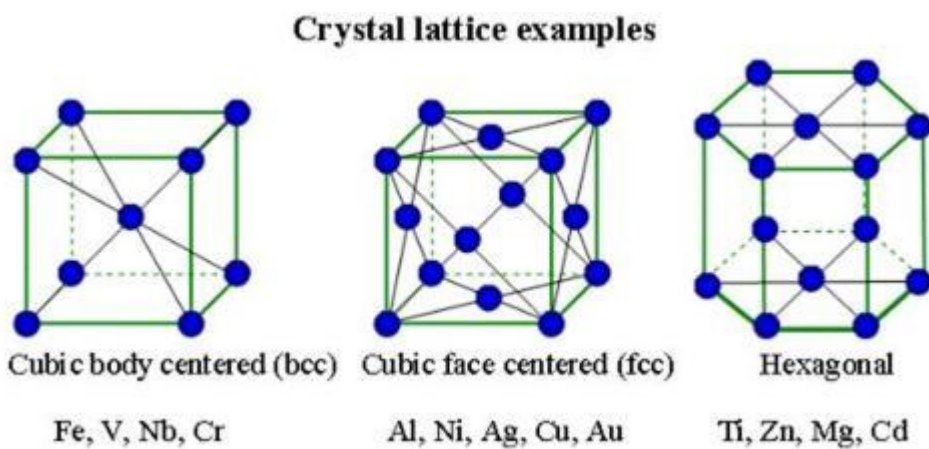
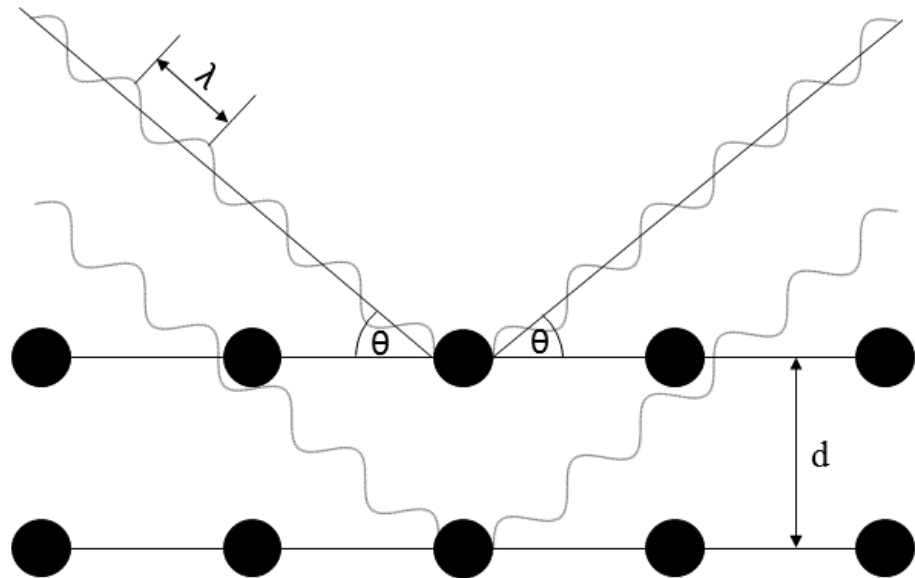


Figure 11 Common metallic crystal lattices.

X-ray diffraction (XRD) and subsequent Rietveld refinements were the main analysis methods used throughout this work. The methods are well established and so the operating principles will be only briefly stated. Powder XRD involves the irradiation of a material with X-rays of a known wavelength. Some X-rays interact with the first crystal plane of atoms in the material and are diffracted, similar to the reflection of a mirror.

However other waves penetrate into the material and interact with subsequent lower planes of atoms as can be seen in Figure 12. In reality many thousands of atomic layers are penetrated up to depths of  $\sim 10 \mu\text{m}$  but two layers serve for explanation.



*Figure 12 Principles of X-ray diffraction*

The waves that strike lower planes travel further than the ones striking higher planes based on the distance between the atoms ( $d$ ) and the incidence angle ( $\theta$ ). Should this difference be equal any integer multiple of the wavelength, constructive interference will occur on the diffracted beam and a significant increase in intensity of the beam will be observed. If the wavelength of the radiation ( $\lambda$ ) and the incidence and diffracted angles are known ( $\theta$ ) the spacing between atoms ( $d$ ), can be determined according to Bragg's law:

$$n\lambda = 2d \sin\theta$$

Eq. 8

## Methodology

If this process is repeated through a range of incidence angles all atomic spacings (d-spacings) can be found. Determining the crystal structure (space group and unit cell) of an unknown material from the d-spacings and intensities of the peaks is possible but non trivial. Fortunately diffraction patterns have been accumulated for >100 000 phases over many decades.

Practically, a material is placed in an X-ray beam and the angle of incidence (and generally the diffracted angle) are varied throughout a range locating all peaks in diffracted intensity, and their relative intensity. The angle locations and intensities of these peaks is compared with a database of known materials to find a match. Should the database contain a phase that has peaks, all of which are present in the XRD pattern and have the corresponding intensities, it is likely that phase is present in the sample. The search-match process is now largely automated by computer software although many of the subtleties still require human interpretation. The PANalytical program *Highscore* and the International Centre for Diffraction Data (ICDD) database were used throughout for the process of phase identification. A typical diffraction pattern with phases identified is shown in Figure 13. The red line represents the measured diffraction intensity data as a function of the incidence and diffracted angle. The peaks in intensity represent constructive interference and thus are indicative of a d-spacing. The vertical lines represent expected peak positions for selected phases, each colour represents a different phase, blue is  $Ti_3SiC_2$  and green is  $TiC$ .

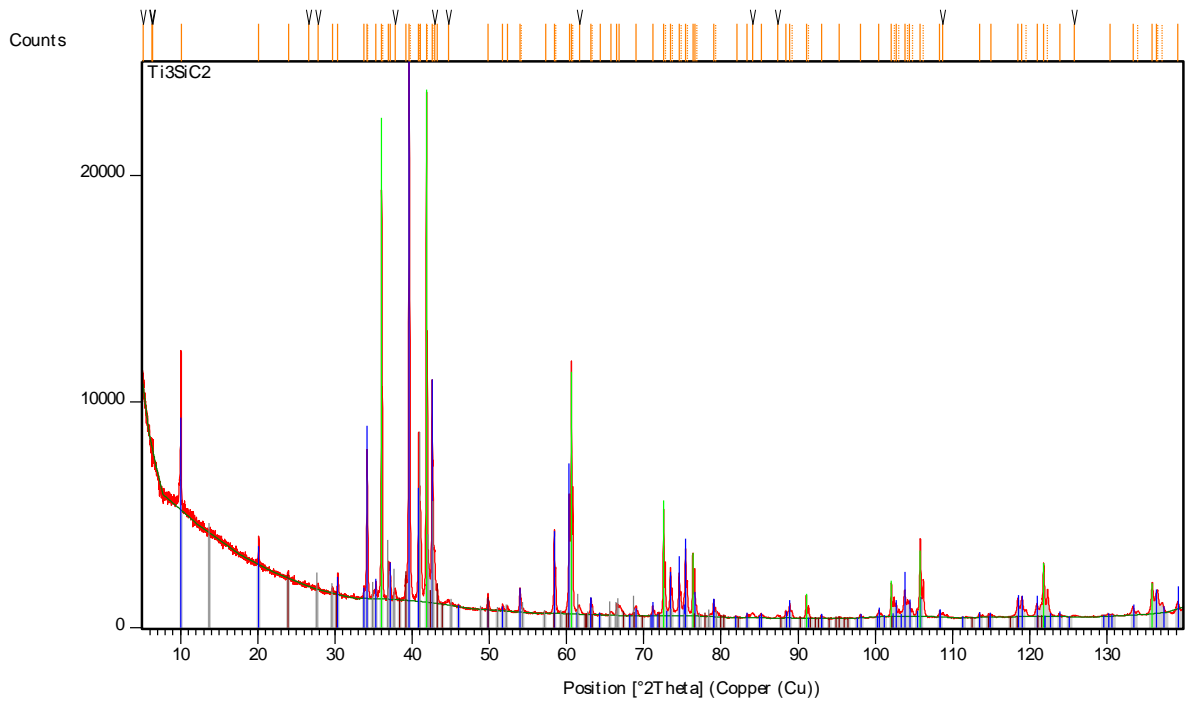


*Figure 13 Typical XRD pattern from the program Highscore for a  $Ti_3SiC_2$  sample. Blue lines represent  $Ti_3SiC_2$  and green lines represent  $TiC$ .*

Phase identification is the first step in any XRD analysis, however more detailed analysis is required to determine variables such as exact crystallographic information and relative phase quantities. For this a process known as Rietveld refinement is used. This is a computational process where a theoretical crystal structure for the targeted phase and a calculated diffraction pattern of this artificial structure is compared to the experimental data. Aspects of the theoretical crystal, along with a scale factor, can then be varied so that the calculated pattern is a better match to the experimental data. When the calculated pattern and the experimental data have a strong match (goodness of fit or minimal least squares error) then the theoretical crystal structure can be said to be representative of the actual crystal that was scanned. A good fit is provided in Figure 14. This method is considerably more complex than the search-match method used for phase identification however it is considerably more powerful allowing virtually every aspect of the crystal to

## Methodology

be examined and refined. The program Rietica was extensively used throughout this thesis and GSAS-II was used occasionally.

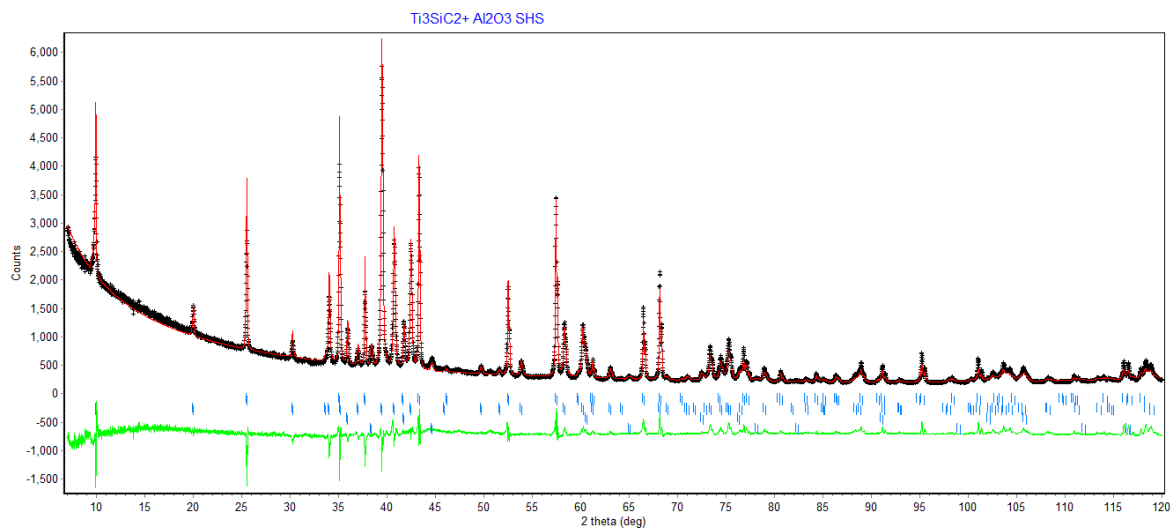


Figure 14 Refined XRD pattern from the program Rietica. Black markers are data, red line is the calculated pattern. The green line is a difference plot between calculated and data. Blue markers are expected peak positions for the phases.

The refinement method can be used on samples with multiple phases and a good fit can be used to determine the relative phase quantities of the phases present according to

$$\text{Quantity Phase A} = \frac{S_A M_A V_A Z_A}{\sum S M V Z} \quad \text{Eq. 9}$$

Where S = scale factor (refined variable), M = mass of unit cell, V = volume of unit cell, Z = the number of formula units in the unit cell.

The machine used to perform XRD in this thesis was a Phillips X’Pert diffractometer. General scan conditions for Rietveld refinement were

*Table 4. Commonly used XRD parameters for refinement*

| <b>Variable</b>      | <b>Typical Value</b>   |
|----------------------|--|
| Radiation wavelength | Cu K <sub>α</sub> (K <sub>α1</sub> = 1.54051 Å, K <sub>α2</sub> = 1.54433 Å) |
| Angle Range          | 5-120° 2θ  |
| Step Size            | 0.013° θ per step  |
| Total Scan Time      | 1 hour   |
| Irradiated Size      | 10 x 10 mm   |
| Power                | 40kV 40 mA   |
| Silts                | Automatic divergence slits   |

Scan parameters are always determined by the specific sample to be tested. For example MAX phases have a large *c*-axis which produces a diffraction peak at ~10° 2θ, thus scan where always started from 5° 2θ. For most materials starting at such a low angle is redundant and that portion of the scan could be omitted without losing information. Phase Identification could easily be done on MAX phase – alumina composites with 10 min scans provided the required angle range, and step size was known, considerably reducing demand on the instrument.

When conducting Rietveld refinement many strategies can be used to ensure convergence. In most cases a suitable order for the introduction of variables into the refinement is to

- 1) Complete phase ID on all phases possible.
- 2) Add these phases into the refinement software (e.g. Rietica) but set scale factor to a small number (setting to zero sometimes causes this parameter to go negative when automatically refined).
- 3) Manually add and refine coefficients of a background. Accuracy here is not required yet.
- 4) Manually increase the scale factor of one of the major phases and confirm a reasonable match to the appropriate peaks in the data.
- 5) Refine the lattice parameters for this phase.

## Methodology

- 6) Refine scale factor for this phase. The scale factor controls the amount of this phase in the sample.
- 7) Refine the zero offset for the system which controls a constant angle shift of the peaks caused by a height error of the tested sample or diffractometer calibration error.
- 8) Repeat steps 4 – 6 for all other major phases.
- 9) For one major phase that fits well, refine the sample dependant peak shape parameters.
- 10) Peaks shapes are the most likely variables to become unstable. Manual refinement may be required until the shape is very close to correct. Knowing the instruments underlying peak shape is generally required. This may be refined from the XRD pattern of a standard (NIST660) LaB<sub>6</sub> sample.
- 11) Perform peak shape refinement on remaining major phases.
- 12) Perform steps 4 – 6 for minor phases.
- 13) Attempting to refine peak shape for minor phases often causes instability. Manual refinement of these variables is generally required. Alternatively they may be fixed at appropriate values from either a similar major phase from the refinement or previously determined values.
- 14) Remaining variables such as atom occupancy, atom positions, preferred orientation and thermal parameters can now be refined if the residual error justifies this step.
- 15) At all times care must be taken to ensure refined values remain physically possible. Negative peak widths, scale factors and thermal parameters are all common issues that can occur none of which are physically possible.

Introducing new variables to the refinement will always reduce the residual error, however this is often only statistical and it is important to ensure there is evidence in the form of identifiable features in the difference plot before refining. To quote John von Neumann “With four parameters I can fit an elephant, and with five I can make him wiggle his trunk.”

In well-known systems the process can become quite efficient however in more complex or unknown systems this process may require very many iterations to determine a suitable fit. Again many aspects of this process can now be automated with software, however many phenomena can be missed by automated processes. Further guidance on the topic of Rietveld refinement can be found in references <sup>[1, 2]</sup>.

#### **4.3. Scanning electron microscope (SEM) analysis**

Whereas XRD is used to give detailed crystallographic information about a material and phases present, SEM is used to see the morphology of a material and to obtain elemental microanalysis. In an SEM electrons are emitted from a source by a thermionic emission process, using a strong bias. Once the electrons have been emitted they are accelerated towards a sample by an accelerating voltage and focused using electromagnetic lenses. The electrons interact with the surface of the material being analysed and are collected, processed and turned into a visible image by scanning the fine electron beam over a portion of the surface of the sample. Three different interactions which can be used for imaging occur when the electrons strike the material summarised in Figure 15.

## Methodology

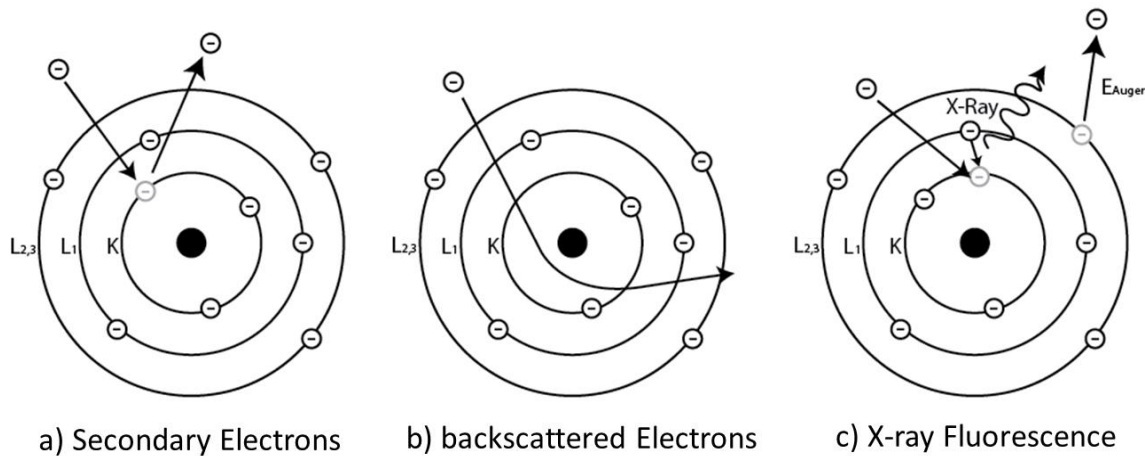


*Figure 15 Electron interactions used for imaging which occur in an SEM*

Secondary electrons (Figure 15a) are of low energy and emitted in all directions. Their intensity at a fixed detector depends on the angle of the emitting surface and so they are used to give topographical details. The backscattered electron (Figure 15b) yield is functional on the average mass of the nuclei in the crystal and so gives contrast based on the elements present (Figure 16). The energy emitted from electrons decaying into lower energy states (Figure 15c) to replace the secondary electron is unique to each element and can be used to determine the elements present. This process is known as energy dispersive spectroscopy (EDS). The EDS signal is processed by an energy sensitive detector and will give chemical analysis of the area illuminated by the electron beam. The beam can be manipulated to remain on a single spot, or scanned across a region. If the information is continuously processed as the beam is scanned across an area an image can be built up of each element present (Figure 17). This process is considerably slower than using backscattered electrons for imaging by at least 2 orders of magnitude. Image quality can be affected by the elements present with (B, C, N etc.) being of lower quality (Figure 17c) at accelerating voltages commonly used for imaging. Overall SEM imaging is a very

useful process for determining morphology and elemental ratios. SEM and XRD together are complementary techniques which allow a complete picture of a material to be created.

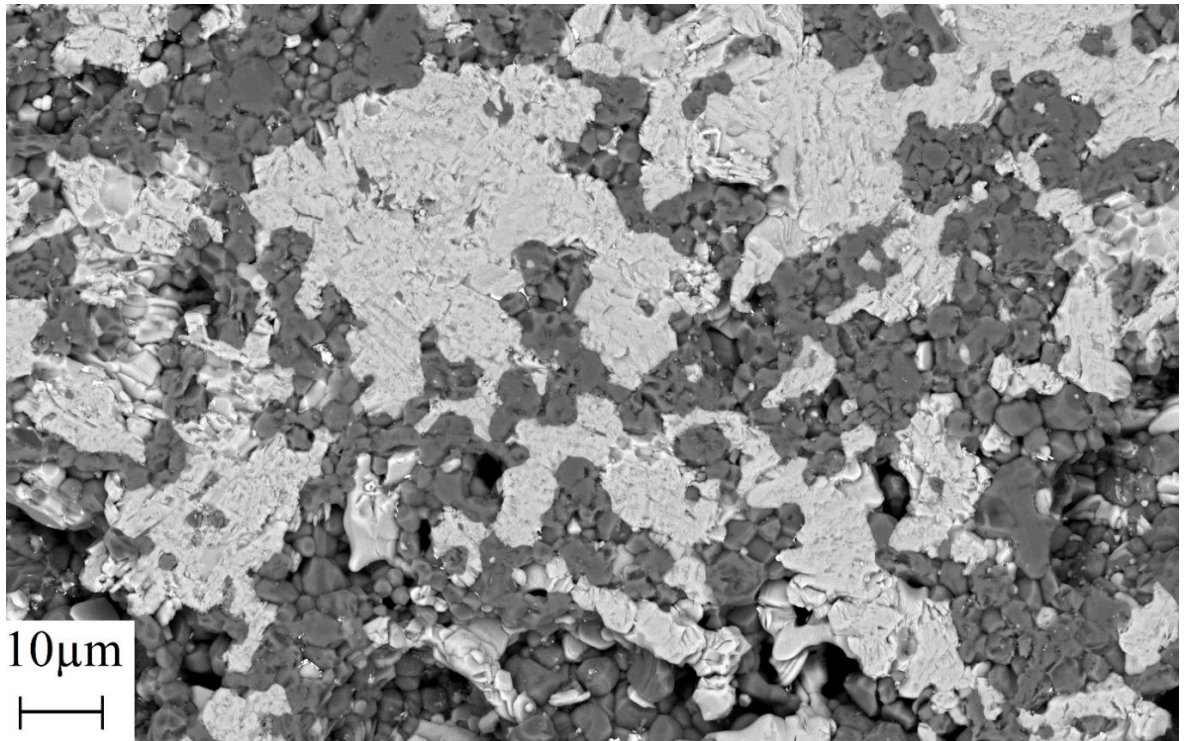


*Figure 16 Backscattered electron SEM image of the microstructure of a  $Ti_3SiC_2 + Al_2O_3$  composite made via an exchange reaction. The MAX phase is the lighter phase and  $Al_2O_3$  the darker.*

## Methodology

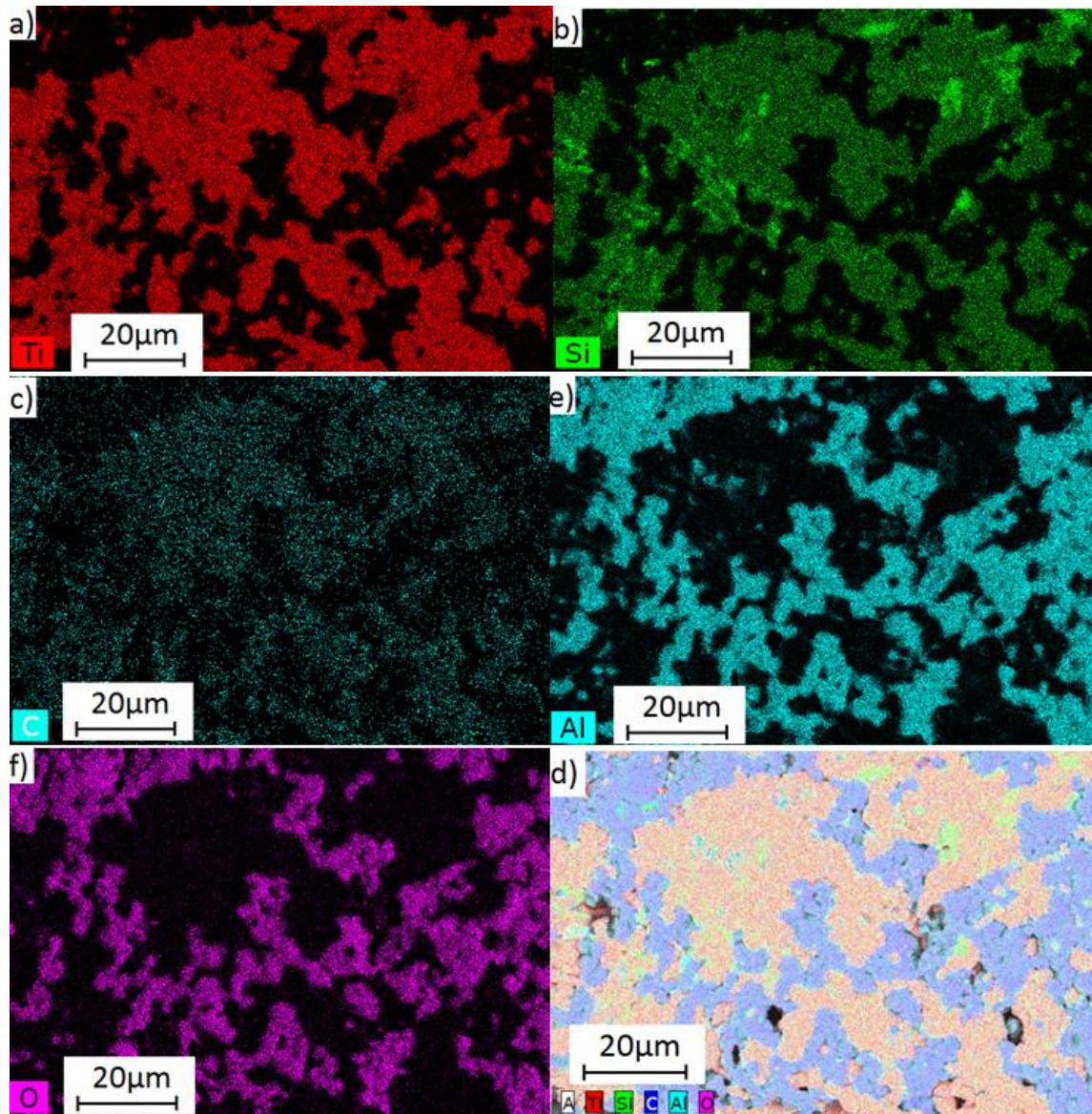


Figure 17 EDS maps of the elements in Figure 16. Individual maps are created for each element and a composite map also created.

#### 4.4. Additional Experimental Methods

Although material synthesis was the main focus of this work material property testing was also performed on a selected subset of the samples made. An overview the testing procedures is included here.

##### 4.4.1. Schottky chamber

The work function of a material is not a property that can be easily measured. ASTM standard F83-71 defines how, from measured field assisted emission currents, the work function of a material can be calculated. The method involves measuring the emitted current from a sample at a known temperature under varying bias voltages. The sample temperature is then changed and the process repeated. Typical results for this type of process are presented in Chapter 12 Publication 8: *Development of a Thermionic Converter for CSP Applications* and repeated here in Figure 18.

To process these data the linear region of each curve in Figure 18 a), (in this case  $\sim 6 V^{0.5}$ ) is fitted with a straight line. The line is extrapolated to the y-intercept to give a value at zero bias voltage. The intercepts are then plotted on (Figure 18 b) against inverse temperature in what is known as a Richardson plot. The gradient of the linear line of best fit through these points gives the work function divided by Boltzmann's constant. It is by this method that all work functions were determined throughout this thesis.

## Methodology

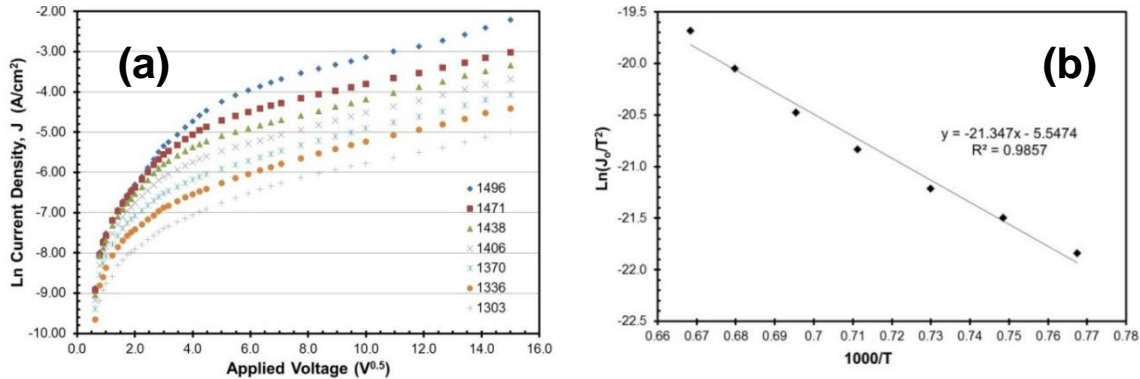
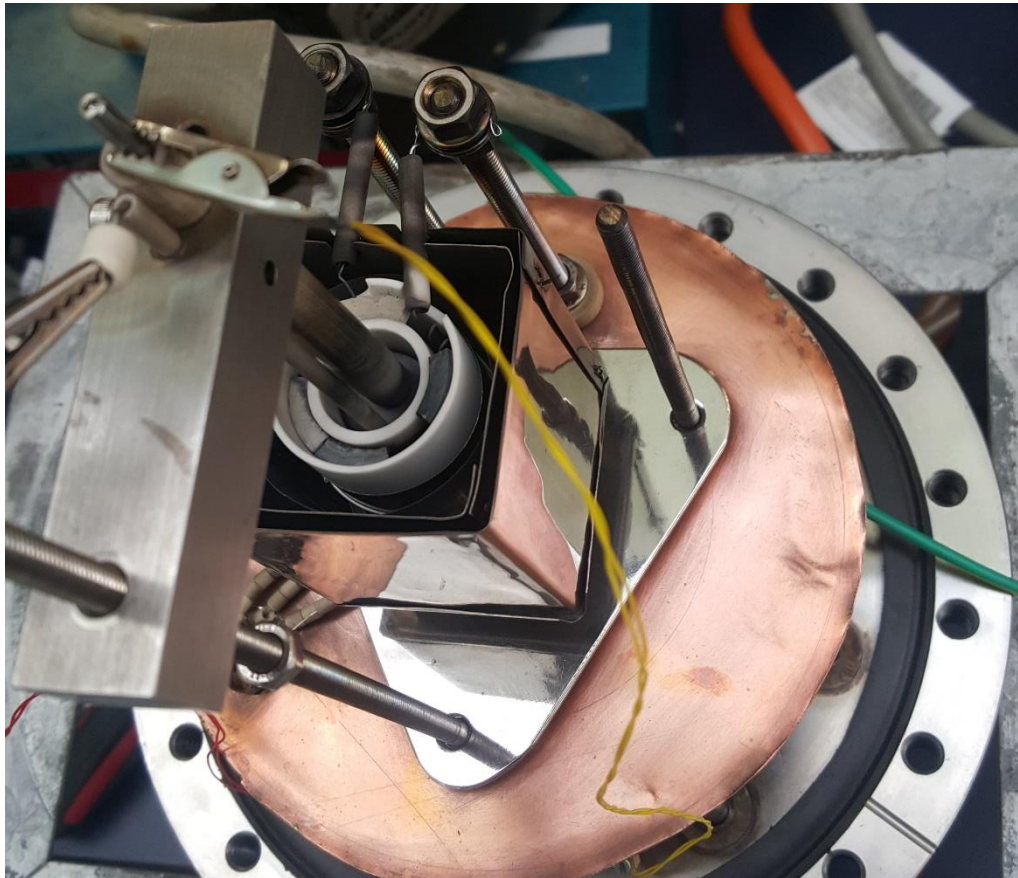


Figure 18. (a) Schottky curves and (b) Richardson plot for GdB<sub>6</sub> alloy.

What is not presented in the papers is that in order for these measurements to be made on our samples a device known as a Schottky chamber had to be constructed. The chamber in Figure 19 was designed, constructed and commissioned as part of the larger thermionic emission project which this thesis contributed to. Dr Heber Sugo was the principal investigator on that project and is responsible for over half the work which went into this aspect of the project.



*Figure 19 Schottky chamber with outer casing and radiation shielding removed. The sample sits inside the innermost alumina crucible.*

The components that make up the Schottky chamber starting from the centre and working outward are:

1. The sample which sits inside the centre alumina crucible.
2. A tantalum heating element, wound into coils, wrapped around the inner crucible. The heating element, shielded by alumina rods, was attached to custom stainless steel feed through.
3. A second alumina crucible enclosed the heating element. A type R thermocouple came directly up the centre of the outer crucible to contact the inner crucible and give sample temperature.
4. Reflective radiation shielding surrounds the outer crucible (upper shielding is removed in Figure 19 to expose the sample).

## Methodology

5. A stainless steel collector rested in the large vertical alumina rod rising from the surface of the sample. This alumina rod and collector were maintained 2 mm clear of the sample. Electrical connection was made through the yellow insulated wire.
6. A bias voltage was applied to the sample through a molybdenum wire in the thinner vertical alumina rod.
7. The internal components were supported on stainless steel threaded rods to minimise conductive heat transfer.
8. Water cooled copper heat sinks where placed below (shown), around and above (removed) the internal components in order to keep the external chamber cool during operation.
9. All electrical and water feedthroughs are made through the base plate, hidden in the image by the bottom copper heat sink.
10. A vacuum chamber was placed over the entire setup and sealed upon the black rubber gasket creating a sealed system. A vacuum port in the chamber was then attached to a vacuum system with backing pump and turbo to achieve a vacuum of  $10^{-3}$  Pa.
11. During operation the temperature was controlled by varying the voltage placed across the heating element. A bias was created between the sample and collector by means of a high voltage power supply.
12. As electrons were emitted from the sample they condensed on the collector. The circuit between the collector and sample (via the bias rod) was completed through a resister. By measuring the voltage across the known resister, the emission current could be determined.

Through this chamber samples could be heated to a selected temperature, have emission current recorded under varying bias voltages and then moved to a new temperature and a new set of emission currents recorded. The data were then used to produce Schottky then Richardson plots from which the work function was determined (Figure 18).

#### **4.4.2. Thermal testing**

Throughout the work on thermal storage MGAs, custom equipment was constructed to measure thermal properties. Thermal conductivity measurements were made as well as differential thermal analysis (DTA) conducted on these material, to observe the absorption and release of heat during the phase change of the MGA. In both cases larger than normal samples were required as the nature of the MGAs prevents samples smaller than ~5 mm from being representative of the bulk. In standard DTA for example only micrograms of material is typically used. As considerably larger samples are needed, custom built equipment was made to analyse samples of 15 – 32 mm in diameter.

##### *Thermal conductivity*

Thermal conductivity was measured through an axial heat flux method. In this case reference samples are placed above and below the sample to be tested according to Figure 20. Measuring the change in temperature ( $\Delta T_1$ ), through a known length ( $\Delta L_1$ ) of a reference sample, of known thermal conductivity, allows for the heat flux ( $Q_1$ ) to be determined. The calculated heat flux can then be used in conjunction with the change in temperature ( $\Delta T_s$ ) and length of the tested sample ( $\Delta L_s$ ), to determine its thermal conductivity. A second reference allows for the heat flux ( $Q_2$ ) to be calculated out of the sample. The difference of the two heat fluxes is the heat lost radially to the environment

## Methodology

and gives an indication of the error. In practice an average of the two ( $Q_1+Q_2/2$ ) is often used as an assumption with less error.

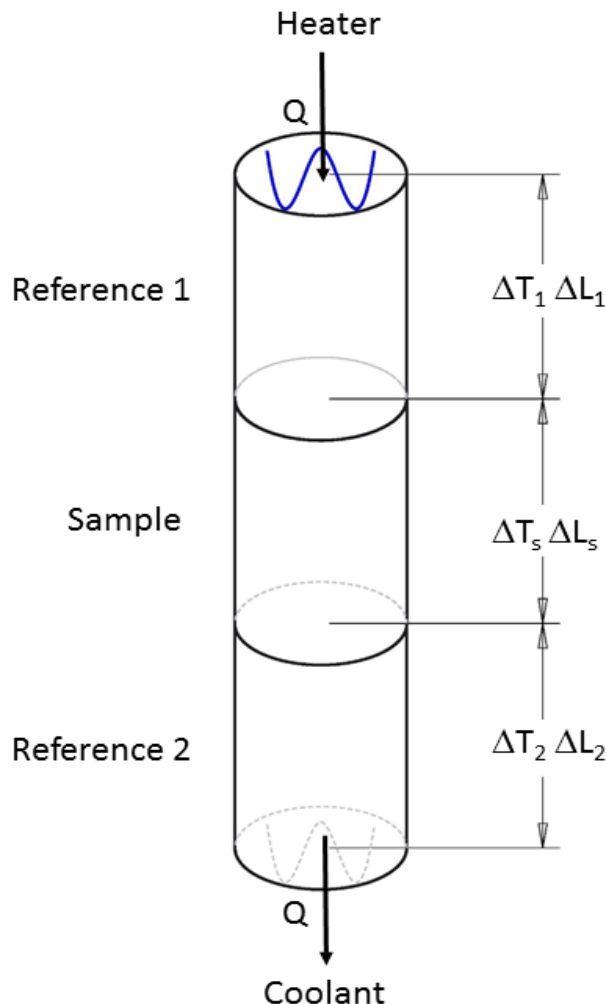


Figure 20 Configuration for measuring thermal conductivity

### Differential thermal analysis (DTA)

DTA experiments compare the temperature of a reference sample with that of the sample to be tested while both are simultaneously heated with the same heat flux. The thermal masses of the materials are generally matched so that they both heat in a similar way. When one sample experiences a phase change there is a thermal arrest while the reference continues to change in temperature. The difference between the two sample

temperatures illustrates the energy being absorbed or released by the phase change.

Typical DTA data repeated from Chapter 11, Publication 6 *High thermal conductivity alloys for thermal storage: Miscibility gap alloys* is shown in Figure 21.

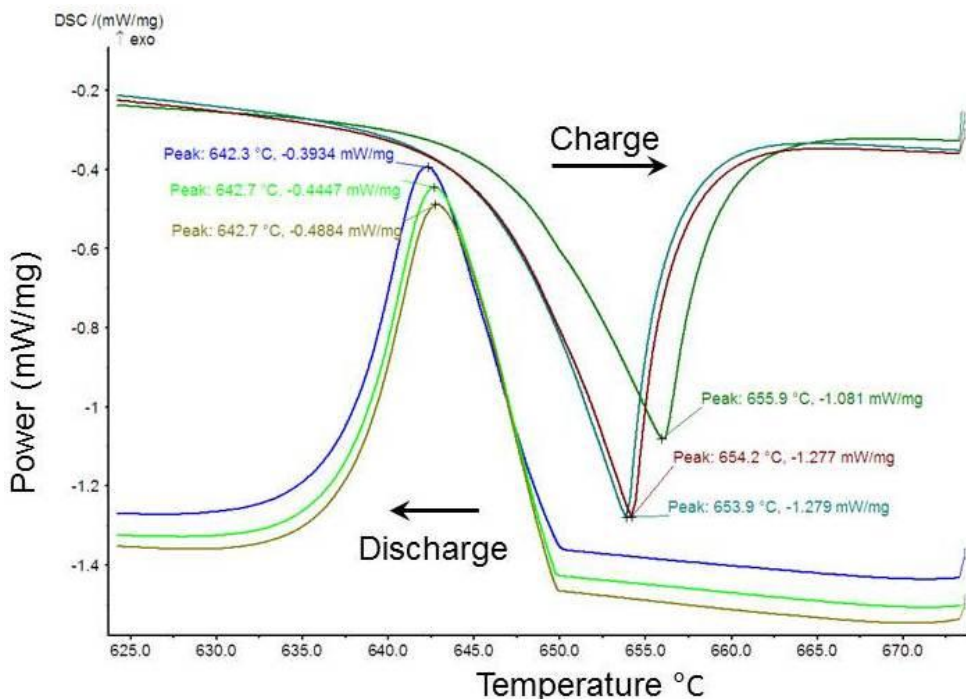


Figure 21 Typical DTA data for an Mg – Fe MGA

## References

1. Howard, C.J. and E.H. Kisi, *Application of powder neutron diffraction*. Oxford series neutron scattering in condensed matter. 2008, Oxford: Oxford university press.
2. Kisi, E.H., *Rietveld analysis of powder diffraction patterns*. Materials forum, 1994. **18**: p. 135-153.

MAX phase - alumina composites *via* exchange reaction in the  $M_{n+1}AlC_n$  systems ( $M=Ti, V, Cr, Nb, or Ta$ )

## 5. Publication 1: MAX phase - alumina composites *via* exchange reaction in the $M_{n+1}AlC_n$ systems ( $M= Ti, V, Cr, Nb, or Ta$ )

Dylan T. Cuskelly<sup>1</sup>, Erich H. Kisi, Heber Sugo

School of Engineering, The University of Newcastle, Callaghan, NSW 2308, Australia

*Journal of Solid State Chemistry*. DOI: 10.1016/j.jssc.2015.10.024

### Abstract

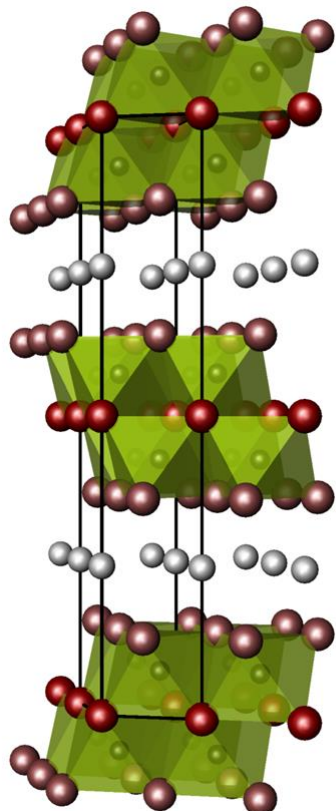
MAX phases have been produced for the first time via an exchange reaction between the  $M$ -element oxide and Al leading to an  $M$ -Al-C – $Al_2O_3$  composite in the V-Al-C, Cr-Al-C, Nb-Al-C and Ta-Al-C systems in addition to the previously known Ti-Al-C system. The reduction reaction was first investigated by forming the binary M-X carbide and then proven to be generic across all  $M$ -Al-C systems with the production of the  $M_2AlC$  phase in each case. The work was extended to the other  $M_3AlC_2$  and  $M_4AlC_3$  phases in the respective systems, and was successful in 4 of the 5 cases with moderate yield.

## 1. Introduction

The MAX phases are an interesting group of ternary carbides and nitrides first discovered in 1963<sup>[1]</sup> and first produced as bulk single phase materials in 1996<sup>[2]</sup>. They have been under intense study ever since due to their interesting material properties<sup>[3-5]</sup>. MAX phases are of the form  $M_{n+1}AX_n$ , where  $M$  is an early transition metal,  $A$  is a group 13 or 14 element,  $X$  is either C or N and  $n$  is an integer either 1, 2 or 3 resulting in what are termed 211, 312 or 413 phases respectively<sup>[2]</sup>. There are in total nine known  $M$ -elements, twelve  $A$ -elements and two  $X$ -elements, as well as three common values of  $n$ <sup>[6]</sup>. The MAX phases have a layered structure comprised of  $MX$  octahedra separated by layers of the  $A$ -element; the integer  $n$  indicates the number of octahedra in each layer. Figure 1 displays the structure of a 312 MAX phase. Not all possible  $M$ - $A$ - $X$  combinations are thermodynamically stable<sup>[7]</sup>. Out of the 216 possible combinations about 90 MAX phases have been discovered so far<sup>[6, 8]</sup>. By far the most commonly studied MAX phases are  $Ti_3SiC_2$ ,  $Ti_3AlC_2$  and  $Ti_2AlC$ . These were some of the first to be synthesised by Barsoum et. al<sup>[2]</sup>.

as monolithic polycrystals and have been the subject of the majority of synthesis investigations and property testing<sup>[9]</sup>. The systems that form *carbide* MAX phases are summarised in Table 1 below<sup>[10]</sup>. It can be seen that there is a strong bias towards: the 211 phases; on Ti as the  $M$ -element (row 1); and Al as the  $A$ -element (column 1).

Figure 1 Structure of a 312 MAX phase. Green octahedra have  $M$  atom corners and  $X$  atom centres, White atoms separating the octahedra are  $A$ -element layers. The two octahedra in each layer indicate this is a  $n=2$  or 312 MAX phase.



MAX phase - alumina composites *via* exchange reaction in the  $M_{n+1}AlC_n$  systems ( $M = Ti, V, Cr, Nb, or Ta$ )

*Table 1 Systematics of MAX phase formation, showing known carbide MAX phases arranged by M and A-element. Higher order phases i.e. 312 and 413 phases are shown in darker grey and can be seen to exclusively occupy the Al column and the Ti row<sup>[10]</sup>.*

| <b>M VS A</b> | <b>Al</b>         | <b>Si</b>  | <b>P</b> | <b>S</b> | <b>Ga</b>         | <b>Ge</b>         | <b>As</b> | <b>Cd</b> | <b>In</b>  | <b>Sn</b>  | <b>Tl</b> | <b>Pb</b> |
|---------------|-------------------|------------|----------|----------|-------------------|-------------------|-----------|-----------|------------|------------|-----------|-----------|
| <b>Sc</b>     |                   |            |          |          |                   |                   |           |           | 211        |            |           |           |
| <b>Ti</b>     | 211<br>312        | 312<br>413 |          | 211      | 211<br>312<br>413 | 211<br>312<br>413 |           | 211       | 211<br>312 | 211<br>312 | 211       | 211       |
| <b>V</b>      | 211<br>312<br>413 |            | 211      |          | 211               | 211               | 211       |           |            |            |           |           |
| <b>Cr</b>     | 211               |            |          |          | 211               | 211               |           |           |            |            |           |           |
| <b>Zr</b>     |                   |            |          | 211      |                   |                   |           |           | 211        | 211        | 211       | 211       |
| <b>Nb</b>     | 211<br>413        |            | 211      | 211      | 211               |                   | 211       |           | 211        | 211        |           |           |
| <b>Mo</b>     |                   |            |          |          | 211               |                   |           |           |            |            |           |           |
| <b>Hf</b>     |                   |            |          | 211      |                   |                   |           |           | 211        |            | 211       |           |
| <b>Ta</b>     | 211<br>312<br>413 |            |          |          | 211               |                   |           |           | 211        |            | 211       |           |

MAX phases have a unique combination of metallic and ceramic properties making them attractive engineering materials<sup>[3]</sup>. Material properties normally associated with ceramics such as high specific stiffness and high temperature oxidation resistance are coupled with the metallic properties of high electrical and thermal conductivity as well as fracture tolerance<sup>[11, 12]</sup>. These properties are present in combination with the ability to be easily machined and are just some of the interesting engineering properties of the MAX phases which have been presented in detail elsewhere<sup>[2-5]</sup>. However, difficulties in the cost effective synthesis of high purity bulk products have severely limited the applications of

## MAX phase - alumina composites *via* exchange reaction in the $M_{n+1}AlC_n$ systems ( $M=Ti, V, Cr, Nb, \text{ or } Ta$ )

MAX phases. Phase stability in these ternary systems is often quite complex with many factors, both thermodynamic and kinetic, influencing the conversion of reactants into particular products [13-15].

In general, ceramic synthesis involves producing large quantities of a phase-pure powdered starting material which is suitable for downstream processing into components by various shaping processes (uniaxial pressing, cold isostatic pressing, extrusion etc.). Shaping is then followed by sintering to produce dense, strong components. Some processes such as hot pressing or hot isostatic pressing combine these two stages into a single step. In other cases, synthesis is combined with the shaping and/or sintering steps (*via* reactive sintering, reactive hot pressing, reactive hot isostatic pressing *etc.*) such that unreacted starting powders undergo solid-state reactions to form the desired ceramic compound. At the same time, plastic flow and sintering act to produce the desired final shape. Current MAX phase synthesis methods are primarily of the latter kind. Methods such as reactive sintering (hot iso-static pressing or hot uni-axial pressing) and pulse discharge sintering are effective in the production of high purity, high density samples [2, 16-19]. These techniques are effective in producing laboratory scale cylindrical samples for mechanical property testing and have been fundamental in understanding the formation mechanisms of MAX phases. However, methods which combine the synthesis and shaping steps are inherently small scale and unsuited to large scale powder production.

Self-propagating high-temperature synthesis (SHS) is an appealing method of producing bulk quantities of powders due to its low input energy and fast reaction times [14, 20]. However SHS is prone to complications due to a lack of control over the reaction parameters. Problems include extreme temperatures which result in unequal vapour phase loss of reactants affecting product stoichiometry in systems that are highly sensitive to minor compositional differences. There is also a propensity for the retention of

MAX phase - alumina composites *via* exchange reaction in the  $M_{n+1}AlC_n$  systems ( $M=Ti, V, Cr, Nb, or Ta$ )

intermediate phases as the rapidly falling post reaction temperature does not allow sufficient time for reactions to reach completion<sup>[21]</sup>.

In an effort to control intermediate phase formation and ultimately prevent unwanted phase retention, non-elemental starting materials are often utilised. MAX phases have been synthesised from,  $AX$  compounds (e.g.  $SiC$ ,  $Al_4C_3$ )<sup>[14, 22, 23]</sup> or  $MX_x$  compounds ( $TiC_x$ )<sup>[24]</sup>. The use of  $AX$  compounds appears beneficial in controlling the release rate of the  $A$ -element, hence reducing sublimation losses before reaction.

Recently  $TiO_2$  was successfully used as an alternative starting material in MAX phase formation. The use of the metal oxide as a starting material is particularly interesting as almost all potential engineering applications of MAX phases are hampered by the high material cost. This is due in part to the synthesis difficulties mentioned above but also to the high cost of metallic starting materials. Specifically all of the  $M$ -elements involved in the formation of MAX phases are difficult to refine and are inherently expensive, compared with the  $M$ -element oxides.

The  $M$ -elements used in MAX phase formation are either found directly as oxides in their ore, or easily refined from the ore into an oxide (e.g.  $TiO_2$  is usually found either as rutile or refined from Ilmenite). Normally the pure element is then produced from this oxide via carbothermal or aluminothermic reduction. Carbothermal reduction is the industry preferred method of refinement as carbon is less expensive than aluminium; however some metals cannot be obtained this way. Aluminothermic reduction is used in the refinement of both  $V$  from the oxide  $V_2O_5$  and  $Cr$  from  $Cr_2O_3$ . In the case of  $Cr$  refinement, carbothermal reduction leads to the formation of  $Cr_2C_3$ , thus aluminothermic reduction is the preferred method. Aluminothermic reduction of  $FeO$  known as a thermite reaction is common in railway track welding.

MAX phase - alumina composites *via* exchange reaction in the  $M_{n+1}AlC_n$  systems ( $M = Ti, V, Cr, Nb, or Ta$ )

It has been demonstrated in the literature that aluminothermic reduction can be modified into an exchange reaction which combines  $M$ -element reduction and carbide formation in a single-step self-propagating high temperature synthesis (SHS) reaction giving TiC and  $Al_2O_3$ <sup>[25]</sup> according to:



Modification of the stoichiometry by the addition of excess Al allowed extension to the SHS production of Ti-Al-C MAX phase- $Al_2O_3$  composites mixed according to Eq.2<sup>[26, 27]</sup>.



In that work, *Chen et al.* were successful in demonstrating that  $Ti_3AlC_2$  can be synthesised via a single step reduction reaction or exchange reaction, and the conversion rate was similar to that often seen in SHS experiments. Products contained both the expected alumina and  $Ti_3AlC_2$  along with TiC. Attempts to avoid TiC formation by modification of reactant ratios was only successful in limiting the TiC to approximately 5%. Additional modification introduced additional phases, primarily  $TiAl_3$ . Nonetheless this process opens a new route for the production of MAX phase powders.

The exchange reaction concept has been extended to the production of  $Ti_3SiC_2 - Al_2O_3$  composites via the reduction of  $TiO_2$  by Al in the presence of Si and C<sup>[28]</sup>. This was an important demonstration that showed the process can be applied to systems where the A-element of the MAX phase and the reducing element are different i.e. the process can potentially be applied to the phases in row 2 of Table 1.

To date no MAX phases outside of the Ti systems have been synthesised via a single step exchange reaction, however  $Al_2O_3$  has a lower Gibbs free energy of formation per oxygen atom than any of the  $M$ -element oxides<sup>[29]</sup> as shown in Table 2, and therefore should be

MAX phase - alumina composites *via* exchange reaction in the  $M_{n+1}AlC_n$  systems ( $M = Ti, V, Cr, Nb, or Ta$ )

capable of reducing all of them. The work presented here expands the concept of the exchange reaction synthesis of  $M_{n+1}AlX_n$  phases to different  $M$ -element oxides using Al as both the reducing agent and as the  $A$ -element. Consequently, this work will investigate column 1 of Table 1. The  $M$ -elements all have multiple oxidation states. In general the highest oxidation state is the most common and was therefore used throughout this work.

*Table 2 Thermodynamic data for the oxides used in this work<sup>[29]</sup>.*

| Oxide     | $\Delta H$ (per O)<br>kJ/mol | $\Delta S$ (per O)<br>J | G at 1500°C (per O) kJ/mol |
|-----------|------------------------------|-------------------------|----------------------------|
| $Al_2O_3$ | -558.7                       | 17                      | -588.8                     |
| $TiO_2$   | -472                         | 25.5                    | -517.2                     |
| $V_2O_5$  | -310.2                       | 26.2                    | -356.6                     |
| $Cr_2O_3$ | -380                         | 27                      | -427.8                     |
| $Nb_2O_5$ | -368.4                       | 15.3                    | -391.3                     |
| $Ta_2O_5$ | -409.2                       | 28.6                    | -459.9                     |

The reduction of the oxide does not necessarily mean that the MAX phase can form under typical conditions of dry-pressed 4-component powders such as these. Formation of MAX phases is quite complex with specific reaction conditions required for each phase. The optimum synthesis conditions range in temperature from 1200°C to 1650°C and times from minutes to many hours, depending on the elements present and the desired  $n$  value. Certain MAX phases also thermally decompose at temperatures which are lower than the synthesis temperatures of other MAX phases<sup>[30, 31]</sup>. For example,  $Ti_2GeC$  decomposes at 1300°C whereas  $Nb_2AlC$  only forms above 1600°C<sup>[32]</sup>. The problem of a stable equilibrium for synthesis is compounded by partial loss of the  $A$ -element due to vapour phase transport<sup>10</sup>. The  $211$  phases generally tolerate the widest range of formation conditions whereas some of the higher order phases require far more specific conditions.

## MAX phase - alumina composites *via* exchange reaction in the $M_{n+1}AlC_n$ systems ( $M = Ti, V, Cr, Nb, or Ta$ )

In many cases stable conditions for the higher order phases have not been found and may not exist. A  $211$  type MAX phase has been reported in all five of the systems investigated here while there are only three  $312$  and three  $413$  phases.

In this paper, all of the carbide MAX phase forming systems in the first column of Table 1 are investigated. Optimisation of the synthesis procedure and phase purity of a single system was not the overall goal in this work. Instead the work is focused on determining whether the exchange reactions occurs in these  $M$ -element systems, and if so, which MAX phases form in a single step pressureless sintering process. Formation of the relevant  $211$  phase was the success criterion used for MAX phase formation however the higher order phases were also investigated to test the generality of the process.

### 2. Method

For all systems identified in column 1 of Table 1, samples were initially made using stoichiometric mixing ratios as described by Eq.3-12. Samples were first made according to Eq's 3, 5, 7, 9 and 11 aimed at producing the binary carbide to determine in the simplest cases, whether the exchange reaction would occur for each  $M$ -element. Following this, compositions intended to produce  $211$  MAX phases, Eq's 4, 6, 8, 10 and 12, were investigated.

Samples were prepared using  $TiO_2$  (+99.9%,  $<5\ \mu m$ ),  $Cr_2O_3$  (+99%,  $<45\ \mu m$ ),  $Nb_2O_5$  (+99.9%,  $<45\ \mu m$ ),  $V_2O_5$  (+99%,  $<45\ \mu m$ ),  $Ta_2O_5$  (99.99%,  $<45\ \mu m$ ),  $Al$  (+99%,  $<45\ \mu m$ ) and graphite (+99.8%,  $<100\ \mu m$ ) powders mixed according to Eqs. 3-12. Due to a number of factors most notably  $A$ -element losses, stoichiometric mixing ratios often lead to poor conversion of the products to MAX phase. In cases where conversion was so poor that MAX phase formation was negligible, or vast improvement could be readily achieved, the initial mixing ratios were varied. In the  $Ta-Al-C$  and  $V-Al-C$  systems the mixing ratio

MAX phase - alumina composites *via* exchange reaction in the  $M_{n+1}AlC_n$  systems ( $M=Ti, V, Cr, Nb, or Ta$ )

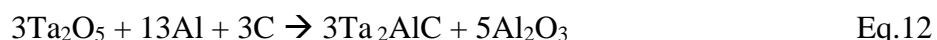
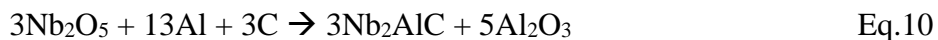
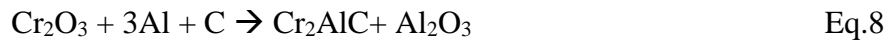
was modified to 100%  $M$ -element oxide, 120% Al and 95% C compared with the stoichiometric quantities in order to produce significant amounts of MAX phase. As this work was focused on assessing the feasibility for the reaction to take place rather than high purity products, further optimisation of starting ratios to produce phase-pure products was generally not pursued.

The  $Cr_2AlC$  system displayed high initial conversion and was selected as a system to undergo optimisation (i.e. no binary carbides or intermetallic compounds present in products). The mixing ratio, 100%  $M$ -element oxide, 115% Al and 100% C of stoichiometric was found to eliminate unwanted binary carbides from the products, however this was at the expense of  $Cr_5Al_8$  formation.

For each composition, 10 g of the reactants were ball milled for 15 minutes (SPEX 8000, steel vial and balls charge ratio 7:1). The powder was halved and uniaxially pressed at 250 MPa into two pellets 15 mm diameter and ~10 mm high. Pellets resting in a graphite boat under flowing argon were heated at 5°C/min to the appropriate sintering temperature and held for the associated time in accordance with Table 3.



MAX phase - alumina composites *via* exchange reaction in the  $M_{n+1}AlC_n$  systems ( $M = Ti, V, Cr, Nb, or Ta$ )



Due to the reasons outlined in §1, a generic firing sequence was not suitable. Instead a heating cycle was determined for each system from the present state of knowledge in the literature using other synthesis methods and the cumulative knowledge gained throughout the work<sup>[31, 33-36]</sup>. As many of these compounds have not been produced via pressureless reactive sintering before, and almost none via an exchange reaction, the sequences used here are not considered to be optimal.

*Table 3 Sintering conditions used for different systems.*

| Systems              | Sintering temperature | Sintering Time |
|----------------------|-----------------------|----------------|
| Ti, V, Cr<br>Eq. 2-7 | 1400°C                | 3 hours        |
| Nb<br>Eq.8 and 9     | 1600°C                | 12 hours       |
| Ta<br>Eq. 10 and 11  | 1550°C                | 0.5 hours      |

The V system was unusual in that the powders reacted in the ball mill before being placed into the furnace. A lower milling time of 3 minutes and lower charge ratio of 3.5:1 was used in subsequent milling to prevent reaction in the mill and allow the reaction to occur in the furnace.

MAX phase - alumina composites *via* exchange reaction in the  $M_{n+1}AlC_n$  systems ( $M=Ti, V, Cr, Nb, \text{ or } Ta$ )

The fired pellets were sectioned and XRD patterns ( $Cu K\alpha$ ) recorded using a Panalytical X'Pert<sup>TM</sup>. XRD data were analysed via the Rietveld method to determine lattice parameters and atomic positions whilst the refined scale factors were used for quantitative phase analysis according to the method given by Hill and Howard<sup>[37]</sup>. In these refinements, the background, zero offset, peak width parameters and scale factors of all phases were refined.

### 3. Results

#### a. Binary carbides

Samples targeting the binary carbides all produced the desired products thus showing the exchange reaction took place in all cases. This was indicated by the joint absence of  $M$ -element oxides and presence of  $Al_2O_3$ . The  $Al_2O_3$  along with the expected carbide formed the major phases in all samples. Smaller amounts of other compounds were found in some samples (most notably  $Cr_3C_7$  and unreacted graphite). Figure 2 contains XRD results for samples made according to Eqs. 3, 5, 7, 9 and 11 highlighting the  $Al_2O_3$  and carbide phases.. Overall the exchange reaction was deemed successful for these systems under the conditions used.

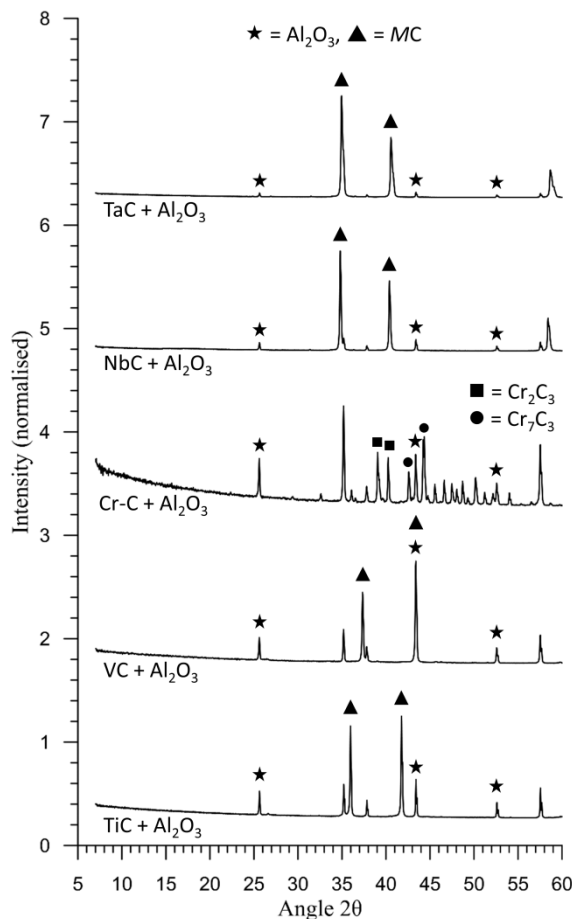


Figure 2 XRD data of the binary carbide systems. Intensity has been normalised in all scans. Only selected signature peaks are marked for each phase although all peaks were identified.

### b. 211 MAX phase formation

It was found that all of the known  $M_2AlC$  MAX phases (i.e. Ti<sub>2</sub>AlC, V<sub>2</sub>AlC, Cr<sub>2</sub>AlC, Nb<sub>2</sub>AlC and Ta<sub>2</sub>AlC) could be successfully synthesised via a single step exchange reaction using the pressureless reactive sintering method. XRD analysis of samples made according to Eqs. 4, 6, 8, 10 and 12 are shown in Figure 3 with the characteristic 211 MAX phase peaks easily seen in the region 12-14° 2θ highlighted by (▼). Along with Al<sub>2</sub>O<sub>3</sub>, many of the systems also produced a mixture of other phases including binary

MAX phase - alumina composites *via* exchange reaction in the  $M_{n+1}AlC_n$  systems ( $M=Ti, V, Cr, Nb, \text{ or } Ta$ )

carbides, intermetallic compounds and/or other MAX phases which are highlighted on each XRD individually.

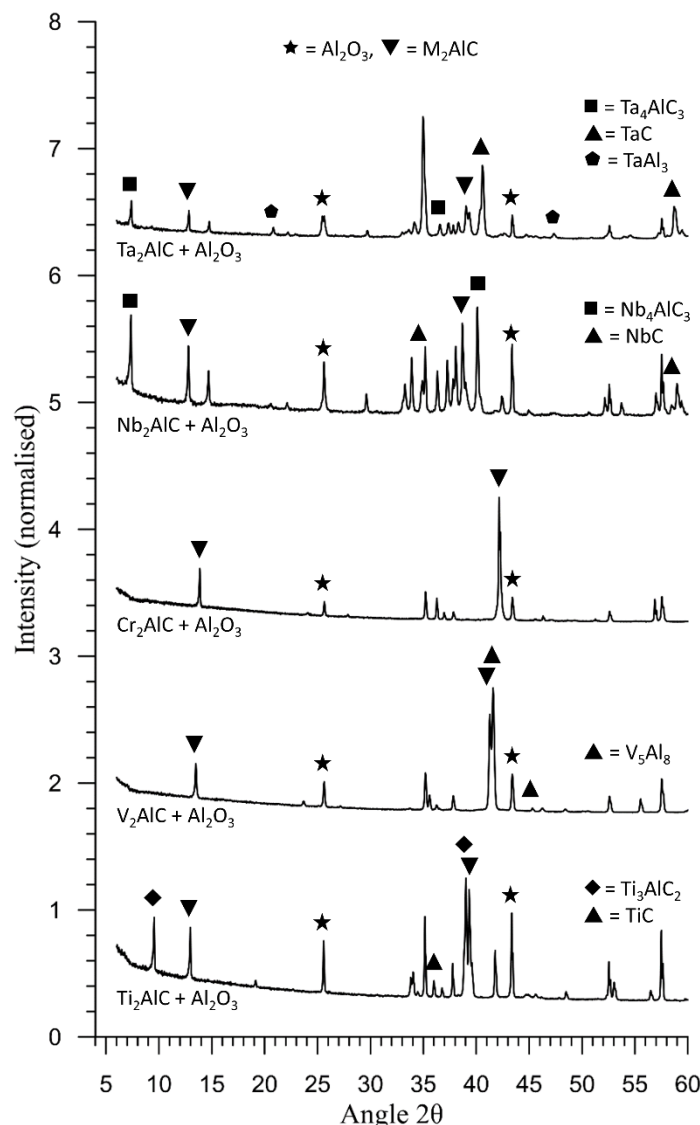


*Figure 3* 211 MAX phase XRD data, higher order phases can also be seen in the Ti-Al-C, Nb-Al-C and Ta-Al-C systems. Each MAX phase can be identified by their characteristic peak in the 5-15° $2\theta$  range. All peaks were identified although only selected peaks are marked.

Rietveld refinements were carried out on all systems to confirm the presence of each MAX phase. An example refinement plot for the optimised  $Cr_2AlC + Al_2O_3$  using the modified mixing ratio 100%  $Cr_2O_3$ , 115% Al and 100% C is shown in Figure 4. The modification was found to have eliminated the large amount of binary carbide  $Cr_3C_2$  which was present in stoichiometric samples. Unfortunately an intermetallic compound,

$Cr_5Al_8$ , had formed as a secondary phase using these modified mixing ratios. Final quantities were determined by Rietveld analysis to be 36 mol%  $Al_2O_3$  and 55 mol%  $Cr_2AlC$ , 9 mol%  $Cr_5Al_8$ , with no other phases found at the detection limit of the XRD for these systems. It is expected there is an optimum mixing ratio between stoichiometric and what was used here, which would result in a minimum of additional phases.

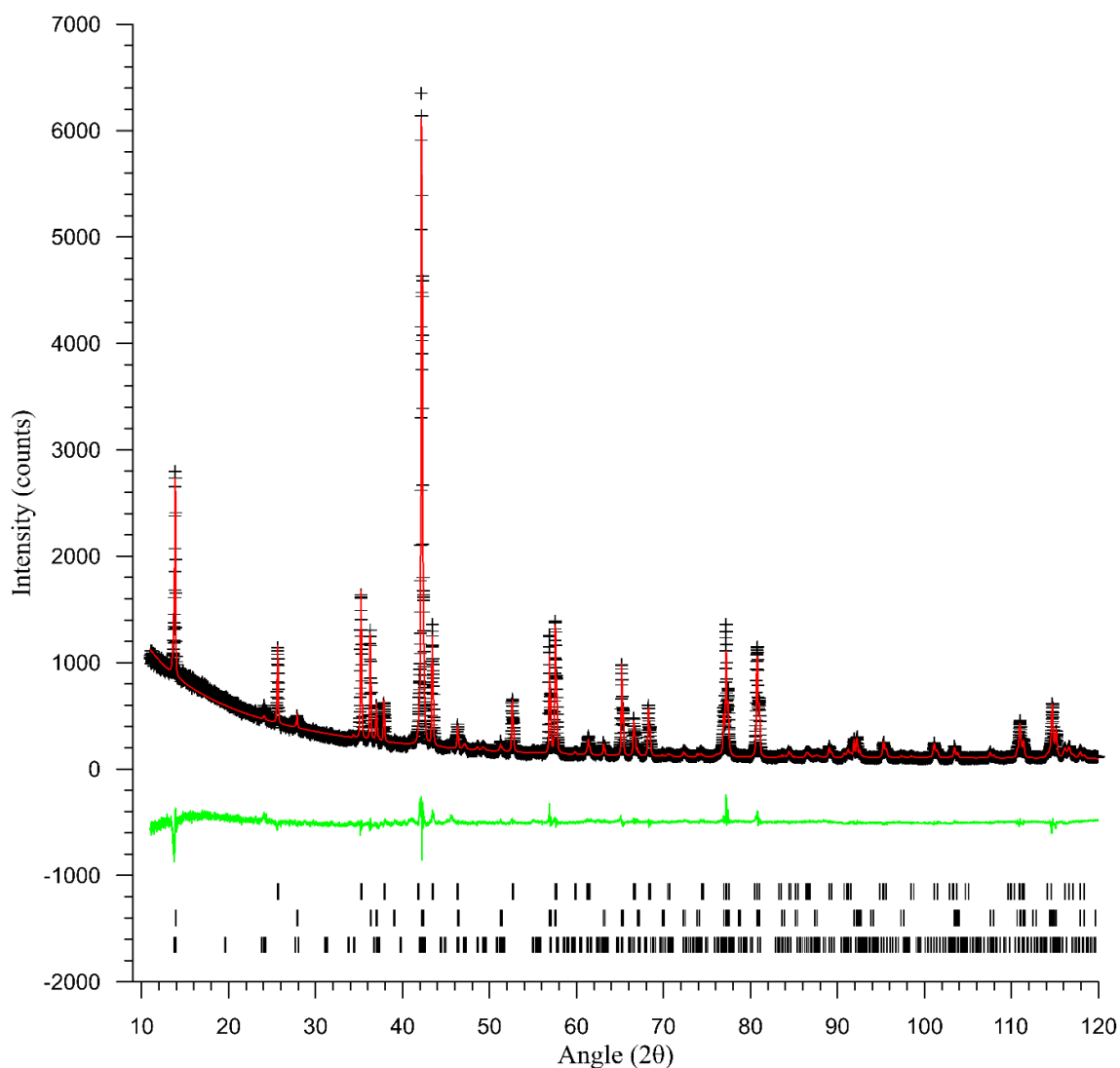


Figure 4 Rietveld refinement of the  $Cr_2AlC$  system. Black '+' represent measured data, the red line is the calculated fit, and the green line is the difference plot. Markers represent expected peak positions from the phases  $Al_2O_3$ ,  $Cr_2AlC$  and  $Cr_5Al_8$  from top to bottom.

### c. 312 and 413 MAX phase formation

MAX phase - alumina composites *via* exchange reaction in the  $M_{n+1}AlC_n$  systems ( $M=Ti, V, Cr, Nb, \text{ or } Ta$ )

A surprisingly large proportion of the known higher order phases (*312* or *413*) are contained within in the *M-Al-C* systems studied here (three of the eight *312* phases, and three of the seven *413* phases). Of the six higher order phases ( $Ti_3AlC_2, V_3AlC_2, V_4AlC_3, Nb_4AlC_3, Ta_3AlC_2, Ta_4AlC_3$ ) five were ultimately formed by exchange reaction,  $Ta_3AlC_2$  being unsuccessful. The phases  $Ti_3AlC_2, Nb_4AlC_3$  and  $Ta_4AlC_3$  all formed within samples formulated to produce the  $M_2AlC$  phase, denoted by the  $\blacklozenge$  and  $\blacksquare$  markers in Figure 2. The  $V_3AlC_2$  and  $V_4AlC_3$  phases were found in a sample originally mixed to form VC and  $Al_2O_3$  as shown in Figure 4. The Cr-Al-C system does not contain any known stable higher order phases. These results show that the exchange reaction can form *312* and/or *413* MAX phases in all systems where such phases are known.

#### d. V-Al-C formation

Contrary to other systems the  $V_2O_5$ , Al and C powders reacted during the milling process. XRD analysis of the milled reactants prepared according to Eq. 6 (Figure 5 lower) proved they had successfully undergone an exchange reaction and produced a significant amount of the desired  $V_2AlC$  MAX phase. The milling time and charge ratio was then lowered for all other samples containing  $V_2O_5$  to prevent reaction in the mill.

Even after milling parameters had been adjusted, visual inspection of a sample mixed according Eq. 5 targeting VC and  $Al_2O_3$ , after firing, indicated that the sample had undergone an SHS reaction in the furnace. XRD analysis of this sample, shown in Figure 5 upper, revealed the intended VC was not produced however it had produced a mixture of 3 MAX phases ( $V_2AlC, V_3AlC_2$  and  $V_4AlC_3$ ) and  $Al_2O_3$ , hence proving that all of these phases can be formed via an exchange reaction (albeit under SHS conditions). Other

MAX phase - alumina composites *via* exchange reaction in the  $M_{n+1}AlC_n$  systems ( $M=$   
Ti, V, Cr, Nb, or Ta)

samples prepared under identical conditions but which did not undergo SHS, produced the intended VC and  $Al_2O_3$ .

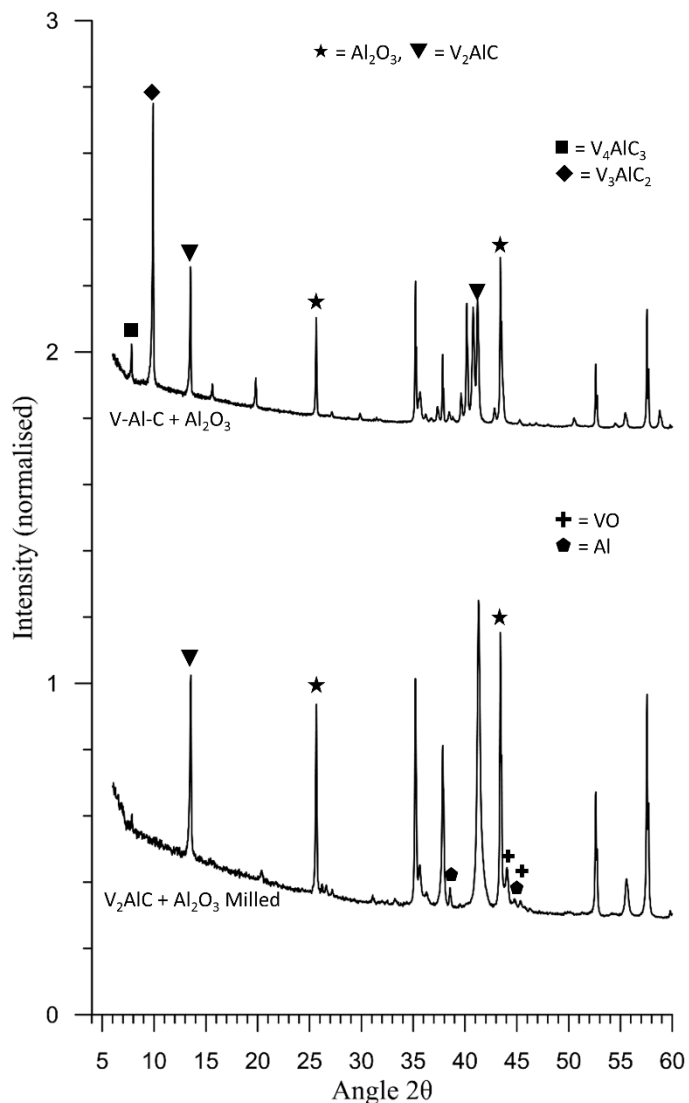


Figure 5 XRD data of the V-Al-C system (top) after SHS in the furnace and (bottom) MASHS within the ball mill. The  $V_3AlC_2$  and  $V_4AlC_3$  phases can be easily identified in the 5-15° $2\theta$  range. Again only selected peaks are marked.

MAX phase - alumina composites *via* exchange reaction in the  $M_{n+1}AlC_n$  systems ( $M=Ti, V, Cr, Nb, \text{ or } Ta$ )

## Discussion

Table 4 presents a summary of the  $M\text{-Al-C}$  MAX phases able to be produced via an exchange reaction in this work. Overall the method is applicable to all systems analysed in this study and indeed almost every composition, indicating the exchange reaction is a very general synthesis technique. The complete absence of the  $Ta_3AlC_2$  phase may be due to the sintering conditions being unsuitable however  $Ta_3AlC_2$  has only ever been synthesised as small single crystals and may not form bulk polycrystals [38]. Given the success of all other systems, and the formation of both  $Ta_2AlC$  and  $Ta_4AlC_3$ , it is unlikely that the exchange reaction methodology is the reason for the failure to produce  $Ta_3AlC_2$ .

*Table 4 Summary table of MAX phase synthesis via exchange reactions. N/A indicates a MAX phase is not known to exist in this system.*

|                | Ti  | V              | Cr  | Nb  | Ta  |
|----------------|-----|----------------|-----|-----|-----|
| Binary Carbide | Yes | Yes            | Yes | Yes | Yes |
| $M_2AlC$       | Yes | Yes            | Yes | Yes | Yes |
| $M_3AlC_2$     | Yes | Yes (SHS only) | N/A | N/A | No  |
| $M_4AlC_3$     | N/A | Yes (SHS only) | N/A | Yes | Yes |

It is qualitatively useful to consider the exchange reactions to proceed via two half reactions although the exact reaction mechanism is likely to be more complex and would

MAX phase - alumina composites *via* exchange reaction in the  $M_{n+1}AlC_n$  systems ( $M = Ti, V, Cr, Nb, or Ta$ )

require extensive rapid *in situ* diffraction studies to observe<sup>1</sup>. The two half reactions comprise  $M$ -oxide reduction by Al oxidation (or oxygen exchange) followed by MAX phase formation. For example in the Ti-Al-C system, Eq. 4 can be written:



For each of the different M-Al-C systems, each half reaction can proceed at its own rate on the proviso that the rate of MAX phase formation cannot exceed the rate of oxygen exchange. The rates are governed by a complicated interplay of many parameters. First, the thermodynamic drive is quite different for each system as may be seen for the oxide decomposition in Table 2. Second, the reactants are in the form of a mixed powder with local variations in composition and the density of inter-particle contacts of a particular type. For example, the oxygen exchange half reactions such as Eq. 13 rely upon direct contact between  $M$ -oxide particles and Al droplets<sup>2</sup>. This microstructural aspect is strongly influenced by the particle size, particle shape green density and the deformability of the particles. Third, there are likely to be highly localised temperature variations due to the liberation of the half-reaction enthalpies at reacting inter-particle contacts. Examination of Table 2 indicates that this is likely to vary widely between the different systems studied. A number of features of the results presented here may be discussed within this qualitative framework.

The formation of mixed MAX phases occurred in every system where more than one MAX phase was available. A-element deficient phases are common in MAX phase production and in standard methods this is normally observed as the  $MX$  binary. However

---

<sup>1</sup> By analogy with other MAX phase synthesis paths, it may be expected that intermediate phases will form as transitional steps between these half-reactions.

<sup>2</sup> Al melts at 660°C on the heating ramp.

MAX phase - alumina composites *via* exchange reaction in the  $M_{n+1}AlC_n$  systems ( $M = Ti, V, Cr, Nb$ , or  $Ta$ )

higher order MAX phases are also *A*-element deficient variants of  $M_2AlC$  phases, having a closer stoichiometry with respect to both the  $M$ - $A$  ratio and the  $M$ - $C$  ratio. *A*-element losses account for both the presence of the higher order phases in the  $211$  formulations of this study and the need to modify starting powder ratios to achieve enhanced yields in some systems. They are believed to be the result of vapour transport.

The equilibrium vapour pressure of Al at the temperatures indicated in Table 3 lies in the moderate range 9.7 Pa ( $M = Ti, V, Cr$ ) to 122 Pa ( $M = Nb$ ). However, as briefly discussed previously<sup>10</sup>, these are far from closed systems. In a reactive sintering experiment such as these, Al vapour is highly mobile and reactive. It is continually flushed from the furnace chamber by the flowing argon atmosphere as well as adsorbing on chamber walls and condensing on cooler parts of the furnace system remote from the hot zone. In a given furnace environment, the degree of *A*-element deficiency observed therefore depends upon a combination of the (overall + local) synthesis temperature as well as the hold time. The temperature, which governs the equilibrium vapour pressure, is constrained by the stability range and formation kinetics of the MAX phase and any intermediate phases which may precede MAX phase formation. In the Ta and V systems, Al losses were so great that very little MAX phase was observed in the products prior to adjustment of the reactant ratios. Although these two systems suffered from the same problem and both benefited from the same remedy, the underlying reasons may be different. Preliminary experimentation in the Ta system with sintering temperatures of 1400°C (not shown in this work) failed to produce any MAX phase. When the temperature was raised to 1550°C synthesis was successful. Conversely, in the V system, the reactivity is so high there was a propensity to undergo spontaneous SHS reaction. This suggests that in the latter system, even under macroscopically non-SHS conditions, locally high temperatures are caused

MAX phase - alumina composites *via* exchange reaction in the  $M_{n+1}AlC_n$  systems ( $M = Ti, V, Cr, Nb, or Ta$ )

by the rapid oxygen exchange reaction and this leads to an excess of Al loss. In the Ta system, it may be that 1550°C is at the upper end of the MAX phase stability range.

In general, optimisation of a MAX phase system is a compromise between the (often unknown) stability range of the desired product phase, the kinetics of MAX phase formation and the kinetics of *A*-element losses. It is managed by adjusting both the ratio of reactants and the reaction conditions. These are related variables whose separation from *ex situ* analysis can be difficult as either can produce the same result – the introduction of additional phases, primarily binary carbides. The experimental method introduces additional variables. Methods such as hot pressing and hot isostatic pressing partially suppress *A*-element losses, by rapidly closing the internal pore structure within the compacted reactants. Spark Plasma Sintering significantly reduces the sintering time and thus would require a different set of optimised parameters.

In stark contrast to the other systems the V-Al-C sample intended to produce VC, in which all of the available Al should have been consumed in the reduction of the  $V_2O_5$ , instead underwent SHS and produced the *A*-element *rich* phases  $V_2AlC$ ,  $V_3AlC_2$  and  $V_4AlC_3$ . The formation of *A*-element rich phases in MAX phase synthesis is very rare. Their formation in the current work is not fully understood, however it is believed to be related to the SHS reaction. Subsequent samples made via reactive sintering using powder from the same batch produced the binary carbide as expected. A possible explanation is that part of the vanadium oxide was reduced by the carbon. Carbothermal reduction is possible for all the *M*-element oxides investigated however aluminothermal reduction is thermodynamically preferred at the firing temperatures used. SHS reactions tend to have very short reaction times and generate high reaction temperatures, as a result the

MAX phase - alumina composites *via* exchange reaction in the  $M_{n+1}AlC_n$  systems ( $M=Ti, V, Cr, Nb, \text{ or } Ta$ )

equilibrium phase may be different at the peak reaction temperature and kinetically accessible intermediate phases can dominate over the equilibrium phases. As such it is possible that some of the vanadium oxide was rapidly reduced by carbon, leaving residual aluminium to partake in MAX phase formation. It is also possible that under the extremely short reaction times characteristic of SHS, the reduction of the vanadium oxide was incomplete and left partially reduced  $V_xO_y$ , which may have then been subsequently reduced by C.

The extreme reactivity of the V-Al-C system was also revealed when high energy ball milling the samples in preparation for reaction. MAX phase synthesis via high energy ball milling has been studied<sup>[39]</sup>, although the milling times and charge ratios used here are comparatively very low. Mechanically Activated SHS (MASHS) was more successful in producing  $V_2AlC$  than pressureless reactive sintering with stoichiometric powder ratios in the V-Al-C system. At these ratios samples synthesised in the furnace produced no  $V_2AlC$ , whereas the MAX phase and  $Al_2O_3$  were the major phases in samples made by MASHS. Unfortunately subsequent firing of samples made by MASHS at 1400°C caused the MAX phase to decompose. Although the milling time was reduced in subsequent samples to prevent reaction in the mill, the powders were still extremely reactive, making them prone to undergo SHS when heated. SHS ignition temperature suppression by mechanical activation is a well-documented phenomenon<sup>[40]</sup>.

The exchange reaction synthesis method for MAX phases is highly appealing from an economic standpoint. Consider the reduction of  $TiO_2$  by Al as described in Eq. 1. Elemental Ti, is considerably more expensive than both  $TiO_2$  and the Al required for reduction. The raw material cost to produce one tonne of  $Ti_3AlC_2$  from elemental reactants is approximately \$11 500. (73.8wt% Ti at \$15000/t, 13.8wt% Al at \$2400/t and

MAX phase - alumina composites *via* exchange reaction in the  $M_{n+1}AlC_n$  systems ( $M = Ti, V, Cr, Nb, or Ta$ )

12.3wt% graphite at \$800/t) whereas an exchange reaction to make the same amount of  $Ti_3AlC_2$  would cost less than half, only \$4350 (60.1wt%  $TiO_2$  at \$2100/t, 33.9wt% Al at \$2400/t and 6.0wt% graphite at \$800/t and accounting for the need to produce 2.05 tonne of composite to yield 1 tonne of MAX phase<sup>[41]</sup>). If separation of the MAX phase is desired, then an associated cost would need to be incorporated nonetheless the savings in raw materials are substantial. In addition, the composite itself may find engineering application<sup>[42]</sup>, removing the need for refinement and greatly increasing yield.

The concept of MAX phase formation via an exchange reaction has two main avenues for extension. Firstly there is the application of Al as a reducing element to other MAX phase systems, primarily the  $TiO_2$ -A-C systems. As the  $Ti_3SiC_2 + Al_2O_3$  composite is already known to form under these conditions the Ti -A-C MAX phases in row 2 of Table 1 ( $A = Al, Si, S, Ga, Ge, Cd, In, Sn, Tl$  and Pb) are the most promising systems. Alternatively the use of a different reducing agent would produce different composites. Choices for a reducing element are limited but Mg, Ca, B and at high temperatures C may all reduce  $M$ -element oxides. These reducing agents are however not free from problems. MgO is likely to form spinels with the A-element (although a MAX phase-spinel composite is possible via this method), Ca is often more expensive than the  $M$ -element, B often results in the formation of very stable  $MB_2$  over MAX phases, and C may only be a suitable reducing agent at temperatures outside that of MAX phase formation. Overall although Al is not the only available reducing agent, finding a different one which still results in MAX phase formation is non-trivial.

An alternative avenue for development is to investigate methods of separating the MAX phase and the  $Al_2O_3$ . The MAX phases are resistant to attack from both acids and bases, but  $Al_2O_3$  is soluble in both HCl and NaOH at elevated temperatures. It is possible that a

MAX phase - alumina composites *via* exchange reaction in the  $M_{n+1}AlC_n$  systems ( $M=Ti, V, Cr, Nb, \text{ or } Ta$ )

method analogous to the Bayer process could dissolve the  $Al_2O_3$  leaving the MAX phase. Alternatively, physical separation of crushed powders of composite using mineral separation techniques could allow for refinement. Simple flotation methods have yielded promising results although still far from producing pure products.

#### 4. Conclusions

The exchange reaction used to produce  $Ti_3AlC_2$  via an SHS reaction mechanism in the past has been investigated here under pressureless reactive sintering conditions. The concept of using an exchange reaction to produce MAX phase –  $Al_2O_3$  composites has been successfully extended to all the of the  $M$ -elements which produce a  $M_2AlC$  phase. Many higher order phases ( $M_3AlC_2$  and  $M_4AlC_3$ ) also exist in these systems and it has been shown that these phases will also form under the conditions used. It was observed that the exchange reaction can also take place during high energy ball milling, successfully producing  $V_2AlC$  and a furnace ignited SHS exchange reaction in the V-Al-C system can produce all three of the  $V_{n+1}AlC_n$  phases. Modification of reactant ratios was shown to be very effective in improving yield of the target phase.

## 5. References

1. Jeitschko, W., H. Nowotny, and F. Benesovsky, *Die H-Phasen  $Ti_2InC$ ,  $Zr_2InC$ ,  $Hf_2InC$  und  $Ti_2GeC$* . Monatshefte für Chemie und verwandte Teile anderer Wissenschaften 1963. **94**(6): p. 1201-1205.
2. Barsoum, M.W. and T. El-Raghy, *Synthesis and Characterisation of a Remarkable Ceramic:  $Ti_3SiC_2$* . Journal American Ceramic Society, 1996. **79**: p. 1953-1956.
3. Barsoum, M.W., *MAX Phases: Properties of Machineable Ternary Carbides and Nitrides*. 2013: Wiley.
4. Barsoum, M.W., *The  $M_{n+1}AX_n$  Phases and their Properties*, in *Ceramics Science and Technology: Materials and Properties*, R. Riedel and I.-W. Chen, Editors. 2010, John Wiley and Sons. p. 299-347.
5. Barsoum, M.W. and M. Radovic, *Elastic and Mechanical Properties of the MAX Phases*. Annual Review of Materials Research, 2011. **41**: p. 195-227.
6. Eklund, P., et al., *The  $Mn + 1AX_n$  phases: Materials science and thin-film processing*. Thin Film Solids, 2010. **518**(8): p. 1851-1878.
7. Keast, V.J., S. Harris, and D.K. Smith, *Prediction of the stability of the  $Mn+1AX_n$  phases from first principles*. Physical Reviews B 2009. **80**: p. 214113.
8. Barsoum, M.W., *The  $M_{n+1}AX_n$  Phases: A New Class of Solids; Thermodynamically Stable Nanolaminates*. Solid State Chemistry, 2000. **28**: p. 201-281.
9. Low, I.M., *Advances in science and Technology of the  $M_{n+1}AX_n$  Phases*. 2012: Woodhead publishing.
10. Cus Kelly, D.T., et al.,  *$Ti_3GaC_2$  and  $Ti_3InC_2$ : First bulk synthesis, DFT stability calculations and structural systematics*. Journal of Solid State Chemistry, 2015. **230**: p. 418-425.
11. Barsoum, M.W., et al., *Fabrication and electrical and thermal properties of  $Ti_2InC$ ,  $Hf_2InC$  and  $(Ti,Hf)2InC$* . Journal of Alloys and Compounds, 2002. **340**: p. 173-179.
12. Bruesewilz, C., et al., *Single Crystal Microcompression tests of the MAX phases  $Ti_2InC$  and  $Ti_4AlN_3$* . Scripta Materialia, 2013. **69**(4): p. 303-306.
13. Ganguly, A., M.W. Barsoum, and J. Schuster, *The 1300°C Isothermal Section in the Ti-In-C Ternary Phase Diagram*. Journal American Ceramic Society, 2005. **88**: p. 1290-1296.
14. Riley, D.P. and E.K. Kisi, *Self-Propagating High-Tempertue Synthesis of  $Ti_3SiC_2$ : 1, Ultra High-Speed Neutron Diffraction Study of the Reaction Mechanism*. Journal American Ceramic Society, 2002. **85**(10): p. 2417-2424.
15. Viala, J.C., et al., *Phase equilibria at 1000C in the Al-C-Si-Ti quaternary system: An experimental approach*. Materials science and engineering, 1997. **A229**: p. 95-113.
16. Li, J.-F., F. Sato, and R. Watanabe, *Synthesis of  $Ti_3SiC_2$  polycrystals by hot-isostatic pressing of the elemental powders*. Journal of Materials Science Letters, 1999. **18**: p. 1595-1597.
17. Sun, Z., H. Hashimoto, and W. Tian, *Synthesis of the MAX Phases by Pulse Discharge Sintering*. International Journal of Applied Ceramic Technology, 2010. **7**: p. 704-718.
18. Zang, Z.F., et al., *Application of pulse discharge sintering (PDS) technique to rapid synthesis of  $Ti_3SiC_2$  from  $Ti/Si/C$  powders*. Journal of the European Ceramic Society, 2002. **22**(16): p. 2957-2961.
19. Zhang, J., et al., *Rapid fabrication of  $Ti_3SiC_2-SiC$  nanocomposite using the spark plasma sintering-reactive synthesis (SPS-RS) method*. Scripta Materialia, 2007. **56**(3): p. 241-244.
20. Goesmann, F., R. Wenzel, and R. Schmid-Fetzer, *Perperation of  $Ti_3SiC_2$  by Electron-Beam-Ignited Solid-State Reaction*. Journal American Ceramic Society, 1998. **81**(11): p. 3025-3028.
21. Kisi, E.H. and D.P. Riley, *Diffraction thermometry and differential thermal analysis*. Journal of Applied Crystallography, 2002. **35**: p. 664-668.
22. El Saeed, M.A., *Optimization of the  $Ti_3SiC_2$  MAX phase synthesis*. Refractory Metals and Hard Materials, 2012. **35**: p. 127-131.

MAX phase - alumina composites *via* exchange reaction in the M<sub>n+1</sub>AlC<sub>n</sub> systems (M= Ti, V, Cr, Nb, or Ta)

23. Wu, E. and E.H. Kisi, *Synthesis of Ti<sub>3</sub>AlC<sub>2</sub> from Ti/Al<sub>4</sub>C<sub>3</sub>/C Studied by In Situ Neutron Diffraction*. Journal of the American Ceramic Society, 2005. **89**(2): p. 710-713.
24. Hwang, S.S., S.W. Park, and T.W. Kim, *Synthesis of the Ti<sub>3</sub>SiC<sub>2</sub> by Solid State Reaction Below Melting Temperature of Si*. Journal of Alloys and Compounds, 2004. **392**(1-2): p. 285-290.
25. Hadadzadeh, H., M. Shafiee Afarani, and M. Ekrami, *Synthesis of Titanium Carbide by the Combustion of TiO<sub>2</sub>-2Mg-C and 3TiO<sub>2</sub>-4Al-3C Systems in a Tubular Furnace*. Iran Journal Chemistry and Chemical Engineering, 2009. **28**: p. 71-76.
26. Hendaoui, A., et al., *A novel method for synthesis of low-cost Ti-Al-C-based cermets*. International Journal of Self-Propagating High-Temperature Synthesis, 2010. **18**(4): p. 267-272.
27. Chen, J., J. Li, and Y. Zhou, *In-situ Synthesis of Ti<sub>3</sub>AlC<sub>2</sub>/TiC-Al<sub>2</sub>O<sub>3</sub> Composite from TiO<sub>2</sub>-Al-C System*. Journal of Materials Science and Technology, 2005. **22**(4): p. 455-458.
28. Yeh, C.L., R.F. Li, and Y.G. Shen, *Formation of Ti<sub>3</sub>SiC<sub>2</sub>-Al<sub>2</sub>O<sub>3</sub> in situ composites by SHS involving thermite reactions*. Journal of Alloys and Compounds, 2009. **478**(1-2): p. 699-704.
29. Aylward, G. and T. Findlay, *SI Chemical Data*. Vol. 6. 2008: Wiley.
30. Pang, W.K., et al., *Comparison of thermal stability in MAX 211 and 312 phases*. Journal of Physics, 2010. **251**(1): p. 012025.
31. Zhang, W., et al., *Reactive Hot Pressing and Properties of Nb<sub>2</sub>AlC*. Journal of the American Ceramic Society, 2009. **92**(10): p. 2396-2399.
32. Etzkorn, J., et al., *Ti<sub>2</sub>GaC, Ti<sub>4</sub>GaC<sub>3</sub> and Cr<sub>2</sub>GaC- Synthesis, crystal growth and structure analysis of the Ga-containing MAX phases M<sub>n=1</sub>GaC<sub>n</sub> with M= Ti, Cr and n= 1, 3*. Journal of Solid State Chemistry, 2009. **182**(5): p. 995-1002.
33. Salama, I., T. El-Raghy, and M.W. Barsoum, *Synthesis and mechanical properties of Nb<sub>2</sub>AlC and (Ti,Nb)2AlC*. Journal of Alloys and Compounds, 2002. **347**(1-2): p. 271-278.
34. Hu, C., et al., *In Situ Reaction Synthesis and Mechanical Properties of V<sub>2</sub>AlC*. Journal American Ceramic Society, 2008. **91**(12): p. 4029-4035.
35. Xiao, L.-O., et al., *Synthesis and thermal stability of Cr<sub>2</sub>AlC*. Journal European Ceramic Society, 2011. **31**(8): p. 1497-1502.
36. Hu, C., et al., *In situ reaction synthesis and decompositioitn of Ta<sub>2</sub>AlC*. International Journal of Materials Reasearch, 2008. **99**: p. 8-13.
37. Hill, R.J. and C.J. Howard, *Quantitative phase analysis from neutron powder diffraction data using the Rietveld method*. Journal of Applied Crystallography, 1987. **20**(6): p. 467-474.
38. Etzkorn, J., M. Ade, and H. Hillebrecht, *Ta<sub>3</sub>AlC<sub>2</sub> and Ta<sub>4</sub>AlC<sub>3</sub> – Single-Crystal Investigations of Two New Ternary Carbides of Tantalum Synthesized by the Molten Metal Technique*. Inorganic Chemistry, 2007. **46**(4): p. 1410-1418.
39. Hendaoui, A., et al., *Synthesis of high-purity polycrystalline MAX phases in Ti-Al-C system through Mechanically Activated Self-propagating High-temperature Synthesis*. Journal of the European Ceramic Society, 2009. **30**(4): p. 1049-1057.
40. Riley, D.P., E.H. Kisi, and D. Phelan, *SHS of Ti<sub>3</sub>SiC<sub>2</sub>: Ignition temperature depression by mechanical activation*. Journal European Ceramic Society, 2004. **26**(6): p. 1051-1058.
41. Inc., I. *InvestmentMine; Mining Markets and Investment*. 2015; Available from: <http://www.infomine.com/investment/metal-prices/>.
42. Wang, H., Z.H. Jin, and Y. Miyamoto, *Effect of Al<sub>2</sub>O<sub>3</sub> on mechanical properties of Ti<sub>3</sub>SiC<sub>2</sub>/Al<sub>2</sub>O<sub>3</sub> composite*. Ceramics International, 2002. **28**(8): p. 931-934.

**6. Publication 2: MAX phase – alumina composites via elemental and exchange reactions in the  $Ti_{n+1}AC_n$  systems ( $A = Al, Si, Ga, Ge, In$  and  $Sn$ ).**

Dylan Cuskelly, Erin Richards, Erich Kisi

School of Engineering, The University of Newcastle, Callaghan, NSW 2308, Australia

*Journal of Solid State Chemistry* DOI: 10.1016/j.jssc.2016.01.04

**Abstract**

Extension of the aluminothermal exchange reaction synthesis of  $M_{n+1}AX_n$  phases to systems where the element ‘A’ is not the reducing agent was investigated in systems  $TiO_2$ - $A$ -Al-C for  $A = Al, Si, Ga, Ge, In$  and  $Sn$  as well as  $Cr_2O_3$ - $Ga$ -Al-C. MAX phase -  $Al_2O_3$  composites were made in all systems except those with  $A=Ga$  or  $In$ . The effectiveness of conversion to MAX phases was generally in the range 63-96% without optimisation of starting ratios. Optimisation in the Ti-Si-C system gave a MAX phase component with >98%  $Ti_3SiC_2$

## 1. Introduction

The  $M_{n+1}AX_n$  or so called MAX phases are an intensely studied set of materials due to their interesting crystal structure and associated material properties<sup>[1-6]</sup>. These materials are comprised of a layered structure of rigid  $MX_6$  octahedra where  $M$  is an early transition metal and  $X$  is either carbon or nitrogen, interleaved by layers of the  $A$ -element. The number of  $MX$  layers between the  $A$ -element is denoted by the integer  $n$  and takes values 1, 2 or 3 giving the compositions  $M_2AX$ ,  $M_3AX_2$  and  $M_4AX_3$  known as 211, 312 or 413 compounds<sup>[7]</sup>. A  $M_3AX_2$  ( $Ti_3SiC_2$ ) structure is shown in Figure 1<sup>[8]</sup>. Due to the rigidity of the  $MX$  bonding, the MAX phases exhibit many properties normally associated with ceramics such as high specific stiffness, resistance to chemical attack and stability at high temperature. However, free electrons in the  $A$  layers ensure good electrical and thermal conductivity, properties more akin to metals<sup>[4]</sup>. The mixed bonding and layered structure also grant peculiar properties such as extremely low coefficient of friction as well as outstanding thermal shock resistance, reasonable fracture toughness and perhaps their most useful trait, ease of machining<sup>[1]</sup>. Difficulties in the manufacture of the MAX phases result in their high cost which has limited their practical application.

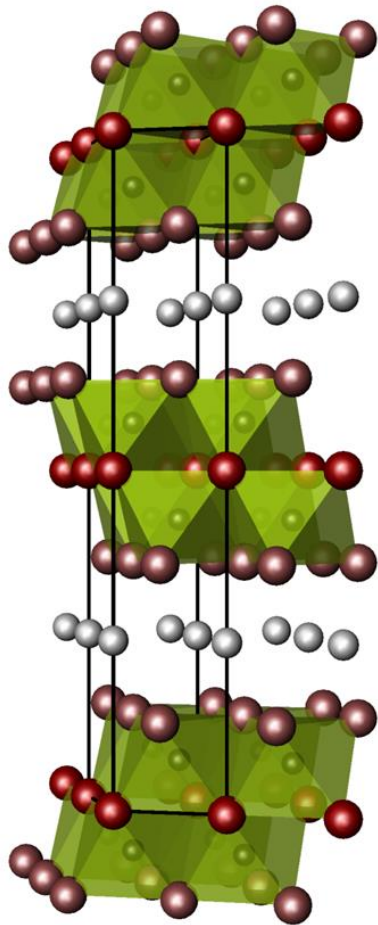


*Figure 1 Structure of a 312 MAX phase<sup>[8]</sup>. Green octahedra have M atom corners and X atom centres, white atoms separating the octahedra are A-element layers. The two octahedra in each layer indicate this is a n = 2 or 312 MAX phase. (For interpretation of the references to colour in this figure legend, the reader is referred to the web version of this article.)*

Manufacturing difficulties have plagued the formation of the MAX phases throughout their short history. The ternary systems involved typically contain many local free energy minima surrounding the MAX phase composition. Taking the Ti-Si-C system as an example,  $Ti_3SiC_2$  formation is competing with the formation of the binary carbides, TiC and SiC as well as multiple Ti-Si intermetallic compounds<sup>[9, 10]</sup>. Any variation from ideal stoichiometry can easily push the equilibrium towards a mixture of these phases, all of which are highly stable. In some M-A-X systems these competing phases are more stable than the potential MAX phase which cannot form<sup>[11]</sup>. Even in systems that will form a

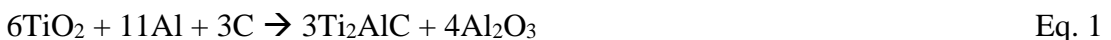
MAX phase, the temperatures required are often high (in the order of 1400°C), and can result in irregular losses of elements, which then move the system away from the required stoichiometry<sup>[12]</sup>. That is to say even if a phase is thermodynamically favourable it still needs to be kinetically accessible. Even small amounts of secondary phases in the bulk of a sample can severely compromise the desired properties. Machinability of Ti<sub>3</sub>SiC<sub>2</sub> for example is heavily compromised by only a few percent of TiC.

The vast majority of literature focus on the manufacture of MAX phases is towards the production of samples for investigations into the formation mechanisms of the MAX phases and subsequent property analysis<sup>[3, 4, 7, 13-24]</sup>. This has led to the manufacturing processes being tailored to extremely high quality samples, at small batch sizes and irrespective of cost. Reactive hot pressing, pulse discharge sintering and thin film methods such as chemical vapour deposition all fall into this category, and although these methods are fundamental to furthering the understanding of MAX phase properties none can be used to produce monolithic MAX phases at batch sizes large enough to be economic. The method of Self-propagating High temperature Synthesis (SHS) is a promising route to low cost MAX phase powder synthesis<sup>[25-28]</sup>. This method requires very little energy input and has much shorter reaction times; overall the method is far more economical. SHS reactions however tend to suffer from higher secondary phase retention than other methods.

The elements from which MAX phases are made are all considered high cost. Of the *M*-elements, Ti or Cr are the cheapest however both are considered in many industrial applications to be uneconomically costly<sup>[29]</sup>. Invariably the MAX phases are eliminated

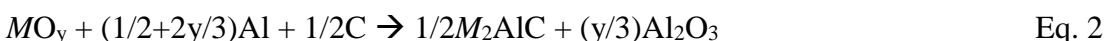
as a suitable material as they are inherently more expensive than the starting materials from which they are comprised. The cost of the elements is generally not a result of rarity, or the cost of the ore but from a high refinement cost, due to the large amount of energy required to obtain the metal from the ore. The use of the *M*-element oxide as a reactant in the MAX phase synthesis could eliminate this costly refinement step, thus making large scale production accessible.

An exchange reaction can be manipulated to produce a MAX phase in the following way<sup>[30, 31]</sup>:



This process was shown to occur under SHS conditions and produced similar levels of secondary phases to elemental reactions i.e. optimised initial mixing ratios still resulted in at least 5% TiC. Attempts to remove the TiC by further modification of mixing ratios introduced new secondary phases such as Ti-Al intermetallic compounds.

In our previous work<sup>[8]</sup>, the process was shown to be generic across the *M*-elements in the *M*-Al-C systems according to the reaction



This drastically increased the number of MAX phases that can be made by this method, yielding the production of 8 phases not previously synthesised by the exchange reaction mechanism. The method so far relies on using Al as both the reducing agent and as the *A*-element of the MAX phase. Attempting to extend the exchange reaction to other *A*-element systems (e.g. Si) with the direct manipulation of Eq. 1 would lead to

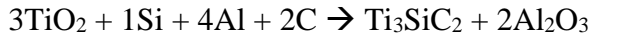


This is where the process hits its first major hurdle, Si is thermodynamically incapable of reducing TiO<sub>2</sub> and Eq. 3 cannot proceed. Unfortunately this is the case for many of the

Publication 2: MAX phase – alumina composites via elemental and exchange reactions in the Tin+1ACn systems (A = Al, Si, Ga, Ge, In and Sn).

MAX phases, the majority of A-elements cannot reduce the corresponding M-element oxide<sup>[32]</sup>.

However the exchange reaction has been applied to the Ti<sub>3</sub>SiC<sub>2</sub> system according to<sup>[28]</sup>:



Eq. 4

Therefore the exchange reaction can be successful in systems where the reducing element is not the A-element of the MAX phase, which broadens the scope of applicable systems considerably.

The MAX phase – Al<sub>2</sub>O<sub>3</sub> composites formed via an exchange reaction may find direct practical applications related to the combination of high hardness from the alumina with damage resistance from the MAX phase. However for the majority of the envisioned applications of the MAX phases, the desired properties such as machinability are severely compromised. Chemical and physical methods for separating the MAX phase from the Al<sub>2</sub>O<sub>3</sub> have been discussed<sup>[8]</sup> and have had initial success. Al<sub>2</sub>O<sub>3</sub> is soluble in both strong acids and bases, and so may be separated by a method similar to the Bayer process, alternatively the difference in surface chemistries may be manipulated for flotation separation.

Many different MAX phases have been synthesised since their original discovery in the 1960's, with the majority since the advent of the hot pressing techniques established in the 1990's<sup>[3]</sup>. The number of M-elements that are known to form MAX phases is now 9, there are 12 A-elements and 2 X-elements. Although this gives over 200 combinations, there are only about 50 combinations of elements from which MAX phases have been successfully synthesised, with many systems shown to be experimentally inaccessible

and/or energetically unfavourable by density functional theory (DFT) analysis. Analysis of the systems that do succeed is useful in determining patterns. Table 1 from our earlier work<sup>[33]</sup> summarises the carbide MAX phases, which will be the focus here. Two main observations are clear.

- i) The  $211$  ( $n=1$ ) MAX phases are by far the most common
- ii) The  $M$  and  $A$ -elements that form the most phases are Ti and Al respectively.

Publication 2: MAX phase – alumina composites via elemental and exchange reactions in the  $Tin_{n+1}AC_n$  systems ( $A = Al, Si, Ga, Ge, In$  and  $Sn$ ).

*Table 1 – Systematics of MAX phase formation. The table shows known carbide MAX phases arranged by M and A-element. Combinations where the higher order phases i.e. 312 and 413 phases occur are shown in darker grey and can be seen to exclusively occupy the Al column and the Ti row<sup>[33]</sup>. Table reproduced from reference 33.*

| M VS A    | Al                | Si | P   | S                 | Ga                | Ge                | As  | Cd  | In         | Sn         | Tl  | Pb  |
|-----------|-------------------|----|-----|-------------------|-------------------|-------------------|-----|-----|------------|------------|-----|-----|
| <b>Sc</b> |                   |    |     |                   |                   |                   |     |     | 211        |            |     |     |
| <b>Ti</b> | 211<br>312<br>413 |    |     | 211<br>312<br>413 | 211<br>312<br>413 | 211<br>312<br>413 |     | 211 | 211<br>312 | 211<br>312 | 211 | 211 |
| <b>V</b>  | 211<br>312<br>413 |    | 211 |                   | 211               | 211               | 211 |     |            |            |     |     |
| <b>Cr</b> | 211               |    |     |                   | 211               | 211               |     |     |            |            |     |     |
| <b>Zr</b> |                   |    |     | 211               |                   |                   |     |     | 211        | 211        | 211 | 211 |
| <b>Nb</b> | 211<br>413        |    | 211 | 211               | 211               |                   | 211 |     | 211        | 211        |     |     |
| <b>Mo</b> |                   |    |     |                   | 211               |                   |     |     |            |            |     |     |
| <b>Hf</b> |                   |    |     | 211               |                   |                   |     |     |            | 211        |     | 211 |
| <b>Ta</b> | 211<br>312<br>413 |    |     |                   | 211               |                   |     |     | 211        |            | 211 |     |

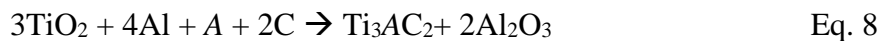
In a previous study, the substitution of different  $M$ -elements into  $M_{n+1}AlC_n$  was successfully carried out by exchange reactions using Al as the reducing agent, i.e. column 1 of Table 1<sup>[8]</sup>. The work presented in this paper complements the previous study by investigating the feasibility of substituting the  $A$ -element in the  $Ti_{n+1}AC_n$  systems i.e. row 2 of Table 1. The focus is on the systems where  $A = Al, Si, Ga, Ge, In$  and  $Sn$ . Systems using both the elemental and exchange reactions will be investigated to give an indication of the relative effectiveness of the exchange reaction in a simple solid state synthesis

methodology. The  $Cr_2GeC + Al_2O_3$  system was also investigated as representative of a MAX phase that contains *neither* Ti as the *M*-element *nor* Al as the *A*-element.

## 2. Method

The  $211$  MAX phase in each system was targeted first in order to establish the applicability of the methodology. The  $211$  phases generally have the widest range of solid state synthesis conditions (temperature and time) as well as better tolerance for composition variations caused either by *A*-element losses or inhomogeneous mixing. The  $Ti-Si-C$  system however is unique among MAX phases as the only system that does not contain a bulk  $211$  phase. In this case the  $312$  phase was targeted. In systems where the  $211$  phase was found to be successful, the exchange reaction was applied to the higher order  $312$  compound. For each MAX phase investigated, samples were made via both an exchange reaction and from elemental starting materials to allow for comparison of the methods.

Samples were prepared using  $Ti (+99\%, <45 \mu m)$ ,  $TiO_2 (+99.9\%, <5 \mu m)$ ,  $Cr_2O_3 (+99\%, <45 \mu m)$ ,  $Al (+99\%, <45 \mu m)$ ,  $Si (+99\%, <45 \mu m)$ ,  $Ga (+99.99\%, ingot)$ ,  $In(+99.999\%, ingot)$ ,  $Ge(+99.99\% \text{ single crystal ingot})$ ,  $Sn (99\%, <45 \mu m)$  and graphite ( $+99.8\%, <100 \mu m$ ) powders mixed according to Eq. 5 and 6 with  $A = Al, Ga, Ge, In$  and  $Sn$  targeting  $211$  phases via both elemental and exchange reaction. Samples made according to Eq. 7 and 8 with  $A = Al, Si, Ge$  and  $Sn$  targeted the  $312$  phases. Lastly samples were made according to Eq. 9 to extend the exchange synthesis to other systems in neither row 2 nor column 1 of Table 1.



For each composition 10 g of high energy ball milled reactants (SPEX 8000, steel vial and balls charge ratio 7:1, 15 min.) were halved and uniaxially pressed into two pellets at 250 MPa producing samples 15 mm diameter and ~10 mm high. Pellets resting in a graphite boat under flowing argon were heated at 5°C/min to the appropriate sintering temperature and held for the times shown in Table 2.

Bulk synthesis is considered a key aspect of this work, as the main application of MAX phase synthesis via exchange reaction is foreseen as a cost effective method for large scale production of powders which can then undergo subsequent processing. For this reason the sample size used was selected, and pressureless reactive sintering chosen as a synthesis method, as both were considered to be amenable to scaling to larger batch sizes. The elements S, Cd, Tl and Pb are potential A-elements however these have boiling temperatures close to or below the formation temperature of typical MAX phases, which makes them unsuitable for the method used here.

Prior to our previous paper<sup>31</sup>, only Ti<sub>3</sub>AlC<sub>2</sub>, Ti<sub>2</sub>AlC and Ti<sub>3</sub>SiC<sub>2</sub> had been produced by an exchange reaction and the earlier work mainly used SHS as a reaction mechanism which does not have reaction parameters that can be translated to pressureless reactive sintering.

Therefore a heating cycle was determined for each system based on other synthesis methods and knowledge gained in previous experiments. These conditions are shown in Table 2 however they are not considered optimal.

*Table 2 Sintering conditions used for different systems.*

| Systems                 | Sintering temperature | Sintering Time |
|-------------------------|-----------------------|----------------|
| $A = \text{Al, Si}$     | 1400°C                | 3 hours        |
| $A = \text{Ga, In, Sn}$ | 1300°C                | 7 hours        |
| $A = \text{Ge}$         | 1225°C                | 12 hours       |
| $\text{Cr}_2\text{GeC}$ | 1300°C                | 6 hours        |

Fired pellets were sectioned and X-ray diffraction (XRD) patterns ( $\text{Cu K}_\alpha$ ) recorded using a Panalytical X’Pert™. XRD data were analysed via the Rietveld method to determine lattice parameters and atomic positions whilst the refined scale factors were used for quantitative phase analysis according to the method given by Hill and Howard<sup>[34]</sup>. In these refinements, the background, zero, peak width parameters and scale factors of all phases were refined.

Following quantitative refinement on initial samples, subsequent samples were prepared in some systems to improve conversion rates. Although not the major focus of this work, it is of interest to produce MAX phases free from secondary phases, specifically TiC. Mixing ratios were varied in these samples generally by the addition of excess A-element and sometimes deficiency of C. Results are only reported where drastic improvements were seen in product conversion.

### 3. Results

#### 3.1 General results

Rietveld analysis of all samples yielded relative phase quantities which are summarised in Table 3. Comparison between the exchange and elemental reactions can be difficult as complete conversion to the expected products in the exchange reaction includes  $\text{Al}_2\text{O}_3$  whereas the elemental systems do not and the 211 systems produce a different amount than the 312 systems. To allow for easier comparison, an ‘effectiveness’ is introduced to describe the conversion of reactants into the desired products for each system.  $\text{Al}_2\text{O}_3$  is removed from the calculation and the desired phase compared to the remaining phases. For example, refinement for samples made according to Eq. 8 with A = Al (Table 3) which contained  $\text{Al}_2\text{O}_3$  along with  $\text{Ti}_3\text{AlC}_2$  as well as some unwanted TiC would become

$$\frac{\text{Ti}_3\text{AlC}_2}{\text{Ti}_3\text{AlC}_2 + \text{TiC}} = \frac{44}{44 + 13} = 77 \text{ mol\%} \quad \text{Eq. 10}$$

An effectiveness is quoted for each system in Table 3.

*Table 3 Products of samples made according to Eq. 5-8. “Other” phases include TiC and unreacted A-element. Elemental methods are reactions according to Eqs. 5 or 7, Exchange methods are reaction according to Eqs. 6 or 8.*

| Target MAX Phase                 | Method    | Al <sub>2</sub> O <sub>3</sub> mol% | Ti <sub>2</sub> AC mol% | Ti <sub>3</sub> AC <sub>2</sub> mol% | Other (Total) mol% | Minor phases | Effectiveness % conversion to desired MAX | Effectiveness % conversion to any MAX phase |
|----------------------------------|-----------|-------------------------------------|-------------------------|--------------------------------------|--------------------|--------------|---|---|
| Ti <sub>2</sub> AlC              | Elemental |                                     | 60                      | 39                                   | 1                  | TiC          | 60  | 99  |
|                                  | Exchange  | 40                                  | 29                      | 26                                   | 6                  | TiC          | 48  | 91  |
| Ti <sub>3</sub> AlC <sub>2</sub> | Elemental |                                     | 84                      |                                      | 16                 | TiC          | 84  | 84  |
|                                  | Exchange  | 43                                  |                         | 44                                   | 13                 | TiC          | 77  | 77  |
| Ti <sub>3</sub> SiC <sub>2</sub> | Elemental |                                     |                         | 47                                   | 53                 | TiC          | 57  | 57  |
|                                  | Exchange  | 58                                  |                         | 40                                   | 1.8                | TiC          | 96  | 96  |
| Ti <sub>2</sub> GaC              | Elemental |                                     | 91                      | 8                                    | 1                  | TiC, Ga      | 91  | 99  |
|                                  | Exchange  | 35                                  |                         |                                      | 65                 | TiC, Ga      | 0   | 0   |
| Ti <sub>2</sub> GeC              | Elemental |                                     | 46                      |                                      | 54                 | TiC, Ge      | 46  | 46  |
|                                  | Exchange  | 45                                  | 2                       | 43                                   | 9                  | TiC, Ge      | 4   | 83  |
| Ti <sub>3</sub> GeC <sub>2</sub> | Elemental |                                     | 4                       | 27                                   | 69                 | TiC, Ge      | 2   | 2   |
|                                  | Exchange  | 31                                  |                         | 2                                    | 68                 | TiC, Ge      | 2   | 2   |
| Ti <sub>2</sub> InC              | Elemental |                                     | 76                      |                                      | 24                 | TiC, In      | 76  | 76  |
|                                  | Exchange  | 29                                  |                         |                                      | 71                 | TiC, In      | 0   | 0   |
| Ti <sub>2</sub> SnC              | Elemental |                                     | 71                      |                                      | 29                 | TiC, Sn      | 71  | 71  |
|                                  | Exchange  | 36                                  | 62                      |                                      | 2                  | TiC, Sn      | 96  | 96  |
| Ti <sub>3</sub> SnC <sub>2</sub> | Elemental |                                     | 25                      | 7                                    | 68                 | TiC, Sn      | 7   | 33  |
|                                  | Exchange  | 38                                  |                         | 39                                   | 22                 | TiC, Sn      | 63  | 63  |

### 3.2. Formation of 211 Phases

XRD analysis (Figure 2) conducted on samples made according to Eq. 5 targeting Ti<sub>2</sub>AC with A = Al, Ge, Ga, In or Sn all indicated a measurable amount of the target phase and thus demonstrate that the sintering conditions used allowed for formation of a MAX phase using stoichiometric elemental starting reactants. Samples made using oxide starting

Publication 2: MAX phase – alumina composites via elemental and exchange reactions in the Tin+1ACn systems (A = Al, Si, Ga, Ge, In and Sn).

materials according to Eq. 6 with A= Al, Ge and Sn, indicate that these systems will *also* form a MAX phase as part of a single step exchange reaction via pressureless reactive sintering. This is the first exchange reaction MAX phase synthesis using either Ge or Sn as an A-element.

In contrast to these successes, the samples made according to Eq. 6 with A = Ga or In both failed to produce any Ti<sub>2</sub>AC. The presence of Al<sub>2</sub>O<sub>3</sub> and absence of any TiO<sub>x</sub> confirms that an exchange reaction took place. However, in these two systems, conversion of the intermediate products into the desired compound failed, resulting in mixtures of TiC and pure Ga or In. Visual inspection of the pellets directly after removal from the furnace showed beads of metallic Ga or In covering the surface. Metal droplets were absent in systems where MAX phase synthesis was successful.

In many systems the samples originally intended to produce the 211 phase instead produced a mixture of both the 211 and the 312 phase. This was apparent using both elemental and oxide starting materials (exchange reactions).

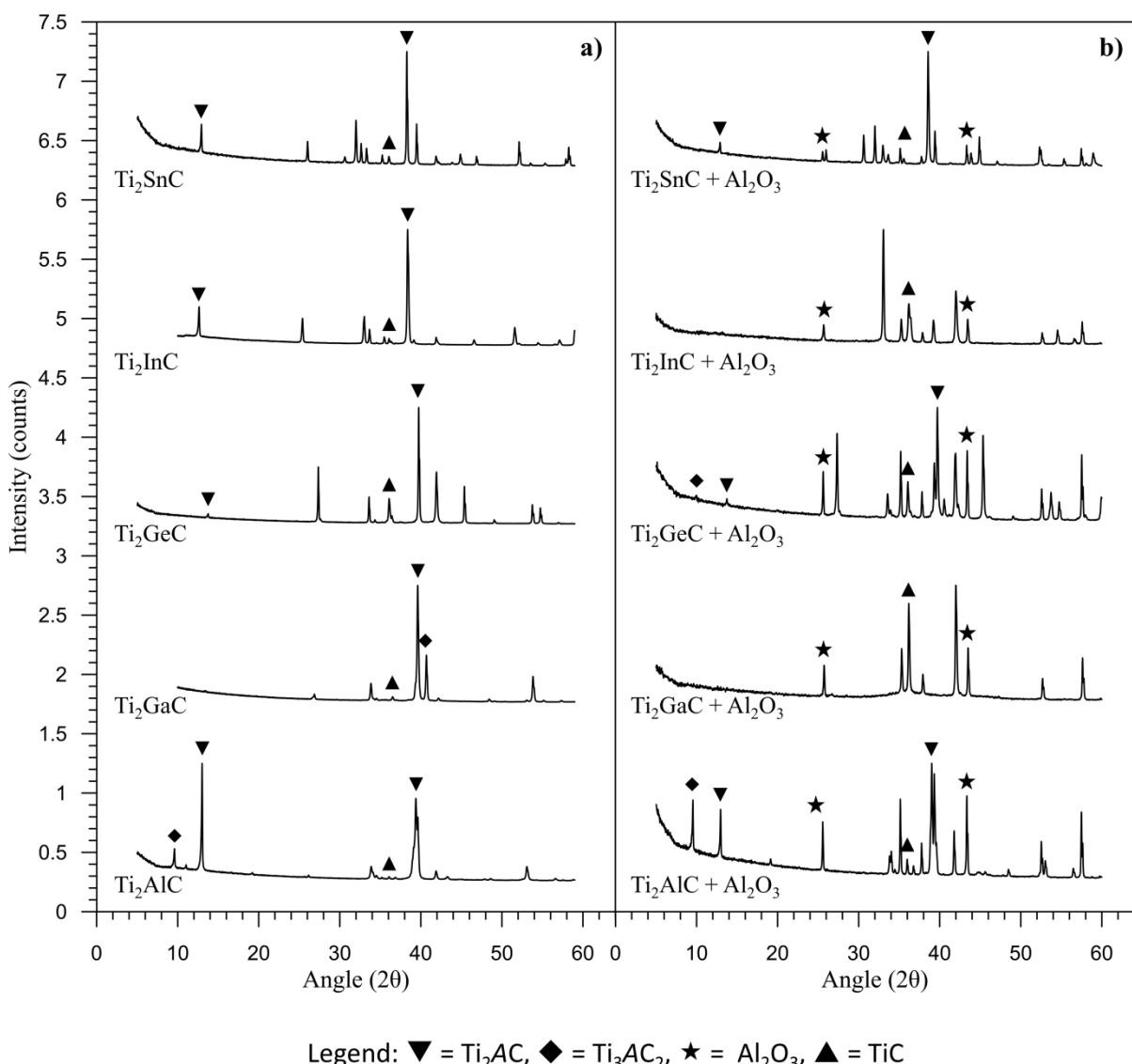
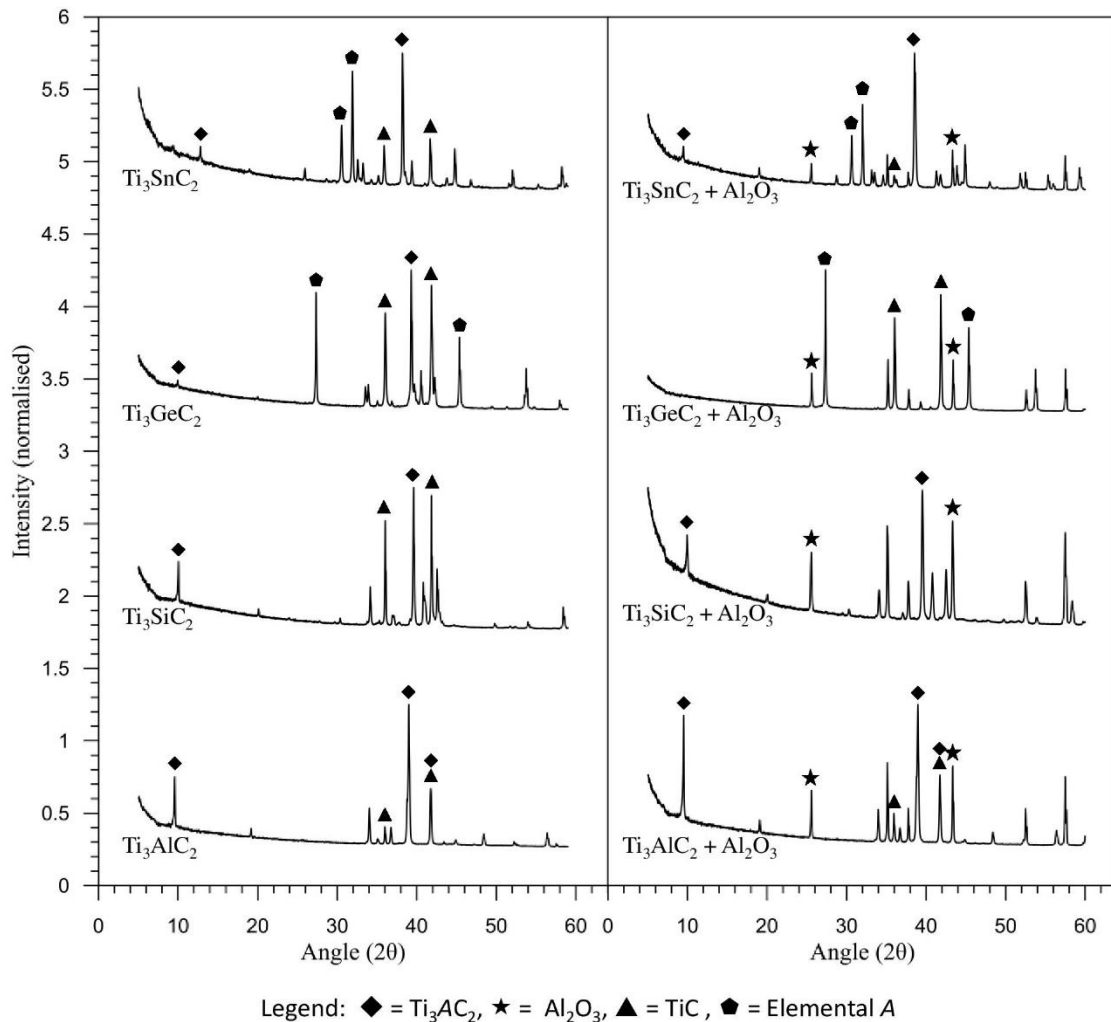


Figure 2 XRD of all 211 systems from elemental reactants (Eq. 5) on the left and exchange reactions (Eq.6) on the right. Systems from bottom to top are A = Al, Ga, Ge, In and Sn. Symbols show selected peaks of the major phases.

### 3.3 Formation of 312 Phases

Samples made according to Eq. 7 targeting the Ti<sub>3</sub>AC<sub>2</sub> phase with A = Al, Si, Ge and Sn also proved successful via elemental reactions, demonstrating the applicability of the sintering conditions and mixing ratios (Figure 3). The exchange reaction was also effective in the Al, Sn and Si systems. Although the Ti<sub>3</sub>GeC<sub>2</sub> phase formed as part of the Ti<sub>2</sub>GeC + Al<sub>2</sub>O<sub>3</sub> sample proving its ability to form as part of an exchange reaction under

the sintering conditions used, the yield was very low using stoichiometric starting mixtures (Eq. 8).



*Figure 3 XRD of all 312 systems with elemental reactions (Eq. 7) on the left and exchange reactions (Eq. 8) on the right. Systems from bottom to top are A = Al, Si, Ge, and Sn. Symbols show selected peaks of the major phases.*

### 3.4 Cr<sub>2</sub>GeC + Al<sub>2</sub>O<sub>3</sub>

The Cr<sub>2</sub>GeC system was selected as an additional system for trial synthesis via an exchange reaction as a system in neither Row 2 nor Column 1 of Table 1. Samples heated to 1225°C, as the successful Ti<sub>2</sub>GeC samples were, failed. They resulted in a mixture of Cr<sub>2</sub>O<sub>3</sub>, Al, Ge and C. Subsequent samples were heated to 1300°C, a temperature closer to that used in the formation of Cr<sub>2</sub>AlC +Al<sub>2</sub>O<sub>3</sub> in previous work, where the exchange reaction is known to take place<sup>[8]</sup>. Samples heated to this higher temperature did react and form the expected products as can be seen in Figure 4. This successful exchange reaction synthesis of Cr<sub>2</sub>GeC + Al<sub>2</sub>O<sub>3</sub> composite which is outside row 2 or column 1 of Table 1 allows the exchange reaction description to be generalised to



given the correct choice of  $M$ ,  $A$ ,  $n$  and synthesis conditions.

Although formation of the MAX phase and the Al<sub>2</sub>O<sub>3</sub> was obvious and elemental Cr and Ge were identified as minor phases, not all peaks could be identified and thus a minor phase is missing. As a result a true quantitative phase analysis was not possible however relative quantities can still be compared. The molar ratio of the Al<sub>2</sub>O<sub>3</sub> to Cr<sub>2</sub>GeC was approximately 1:0.45 when it is expected from Eq. 9 to be 1:1. Thus we can say the unoptimised reaction is about 50% effective.

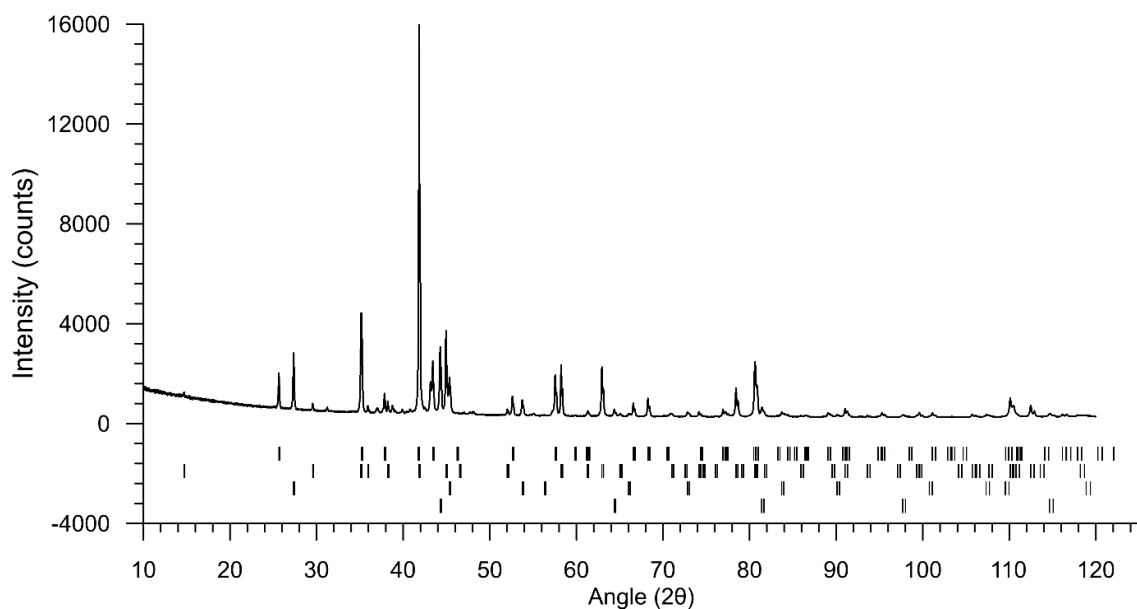


Figure 4 showing XRD data for a sample made according to Eq. 10, demonstrating the formation of  $\text{Cr}_2\text{GeC} + \text{Al}_2\text{O}_3$  composite via an exchange reaction. Markers are shown for  $\text{Al}_2\text{O}_3$ ,  $\text{Cr}_2\text{GeC}$ ,  $\text{Ge}$  and  $\text{Cr}$  (top to bottom).

### 3.5 Optimisation

The  $\text{Ti}_3\text{SiC}_2 + \text{Al}_2\text{O}_3$  system (Eq. 8) was selected to undergo optimisation of starting reactants in an effort to attain complete conversion to the desired products i.e. maximise its effectiveness (Table 1). The reducing agent Al, the A-element Si and the C were all varied independently with respect to the  $\text{TiO}_2$ . Ultimately the optimum ratios were found to be 100%  $\text{TiO}_2$ , 115% Al, 115% Si and 95% C compared with stoichiometric ratios. Rietveld refinement output of the XRD pattern from this material is shown in Figure 5.

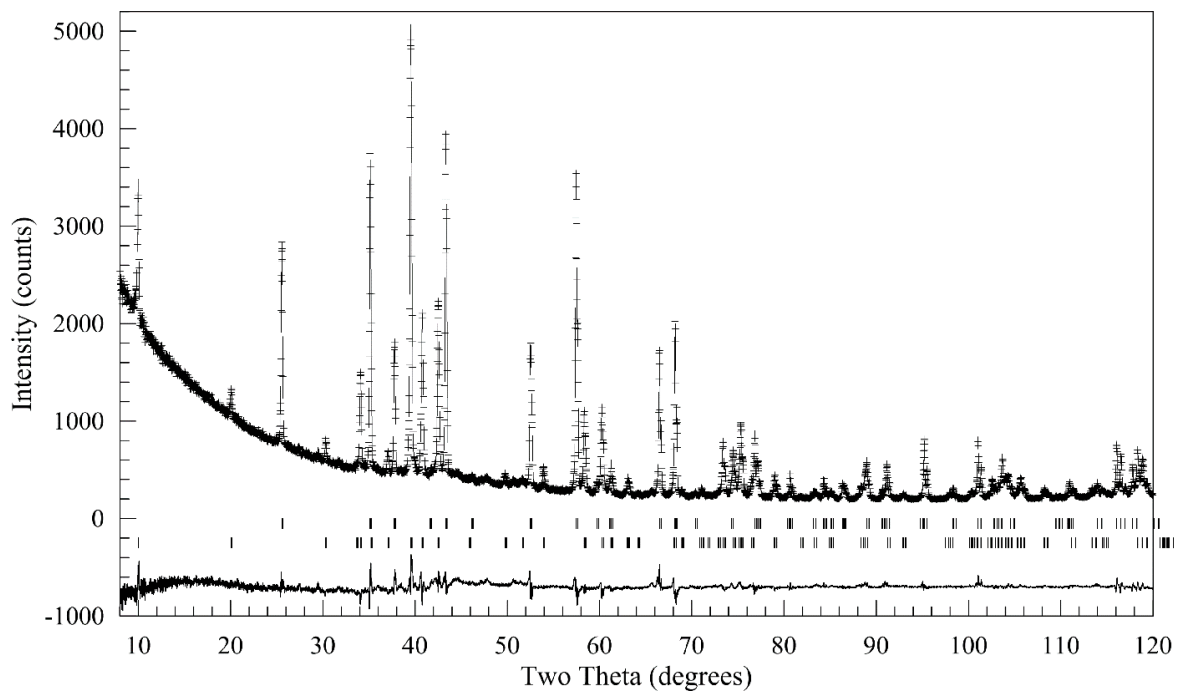


Figure 5  $\text{Cu K}\alpha$  XRD pattern and associated Rietveld refinement for a sample produced by exchange reaction of the optimised starting mixture. Data are given as (+) and the calculated profile as a solid line through them. A difference plot and reflection markers for  $\text{Al}_2\text{O}_3$  (top row) and  $\text{Ti}_3\text{SiC}_2$  (bottom row) are given below the main figure.

#### 4. Discussion

The exchange reaction systems, including: the A-elements studied here (row 2 Table 1), the M-elements (column 1 Table 1) studied elsewhere and the Cr<sub>2</sub>GeC system, have all been successful with the exception of the In and Ga systems. Primarily this confirms the generality of the exchange reaction as a method for producing MAX phases across different M-elements, A-elements and values of n. The successful systems are summarised in Table 2.

*Table 3 Demonstrating which of the carbide MAX phase systems have been successfully synthesised via exchange reaction (light green previous work<sup>[8]</sup>, dark green this work). Systems coloured red did not form MAX phases.*

| M<br>VS A | Al | Si | P   | S   | Ga  | Ge  | As  | Cd  | In  | Sn  | Tl  | Pb  |
|-----------|----|----|-----|-----|-----|-----|-----|-----|-----|-----|-----|-----|
| Sc        |    |    |     |     |     |     |     |     | N/A |     |     |     |
| Ti        | ✓  | ✓  |     | N/A | ✗   | ✓   |     | N/A | ✗   | ✓   | N/A | N/A |
| V         | ✓  |    | N/A |     | N/A | N/A | N/A |     |     |     |     |     |
| Cr        | ✓  |    |     |     | N/A | ✓   |     |     |     |     |     |     |
| Zr        |    |    |     | N/A |     |     |     |     | N/A | N/A | N/A | N/A |
| Nb        | ✓  |    | N/A | N/A | N/A |     | N/A |     | N/A | N/A |     |     |
| Mo        |    |    |     |     | N/A |     |     |     |     |     |     |     |
| Hf        |    |    |     | N/A |     |     |     |     |     | N/A |     | N/A |
| Ta        | ✓  |    |     |     | N/A |     |     |     | N/A |     | N/A |     |

Failure to form MAX phases in the In and Ga systems is believed to be linked to the observation of metallic beads covering the surface of the pellets. Clearly these A-elements do not wet the compounds present in the remainder of the samples. Thus the failure of these systems may be due to physical separation of the A-element from the remaining reactants rather than chemical factors. It is possible that the use of a different synthesis method such as reactive hot pressing or spark plasma sintering, may prevent separation and thus allow for the formation of these phases.

Considering the 211 systems, many samples produced a mixture of the intended 211 MAX phase in addition to a significant amount of the 312 phase. This mix of MAX phases is seen in the Al and Ge systems in both the exchange and elemental reactions. In the elemental reactions dual MAX phase formation also occurs in the Ga and In system. The phenomenon is not limited to these systems having been previously observed in diverse M-Al-C + Al<sub>2</sub>O<sub>3</sub> systems, particularly Nb-Al-C, V-Al-C and Ta-Al-C. The concept of mixed MAX phases was first discussed by Kisi<sup>[35]</sup> with respect to the formation of Ti<sub>3</sub>AlC<sub>2</sub> from the reaction of Ti<sub>2</sub>AlC and TiC.



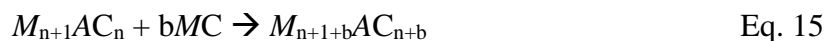
The work here suggests that this process may be extended to a range of A-elements, not just Al and previous work indicates the method is also general for different M-elements, giving



In the case of the Nb-Al-C and Ta-Al-C systems, a 312 phase is not known to exist in the *bulk*, however the 413 phase is known to be stable<sup>[8]</sup>. In the systems where 211 and 413 phases are known to co-exist the reaction may have proceeded in an analogous way



If so, the reaction can be further generalised to



although this cannot easily be proven without *in situ* X-ray or neutron diffraction analysis. This rationale does not explain the failure of the Sn system to form a mixture of MAX phases at any stage despite both a 211 and 312 phase forming in separate samples (Table 3). It is possible that diffusion kinetics play a highly important role and the results presented here are a snapshot within a more complex process.

The mechanism outlined in Eq. 12-15 is particularly interesting as it allows for residual MC that may have formed early during synthesis to be subsequently consumed. MC formation is common in MAX phase synthesis and is often attributed to A-element losses, inhomogeneous mixing and/or incomplete reaction. Examples of TiC contamination is evident in all of the un-optimised 312 systems studied in this work. Even a small amount of TiC in the products can have disastrous effects on some properties. The removal of the MC post reaction is problematic as MC compounds are similar to the MAX phase in the properties normally used for separation such as density or resistance to chemical attack nor can they be removed by melting. However if the MC can be consumed by the mechanism suggested in Eq. 15, a composite consisting of two MAX phases with very similar properties and minimal residual TiC can be formed. As a result a column was added to Table 3 indicating the effective conversion of the products into *any* MAX phase, regardless of the intended product. Extremely high conversion can be seen in the 211 systems which have formed mixed MAX phases as opposed to relatively lower conversion in the systems that did not. Taking the Al containing systems (first 4 rows of Table 3), the ‘Effectiveness % conversion into the desired MAX phase’ is higher in the 312 system for samples produced by either elemental or exchange reaction. However the amount of unwanted TiC in the 211 samples is much smaller due to the formation of mixed MAX phases, which is reflected by the ‘Effectiveness % conversion to any MAX

phase' column. Systems which did not form a mixture of MAX phases were generally the higher order phases where this mechanism is not available.

Optimisation of the initial mixing ratios has also proved to be highly successful in the reduction of TiC and other unwanted phases. The effectiveness in the optimised  $Ti_3SiC_2 + Al_2O_3$  system was seen to be very high at 98% and thus it can be said that the exchange reaction does not inhibit the formation of high purity MAX phases. However it should be noted that the method of varying mixing ratios will always be susceptible to binary carbide formation as the process is scaled up to larger batch sizes. The optimised mixing ratios are also sample and sintering condition specific i.e. the optimised mixing ratios used here may not be applicable to other systems, nor even to this exact system made via an alternative synthesis method such as reactive hot pressing, known to be less susceptible to  $A$ -element losses.

With the extension of the exchange reaction to the  $Ti_{n+1}AC_n$  phases and the  $Cr_2GeC$  phase the reaction mechanism can be seen to be quite general. The production of the  $Cr_2GeC$  phase indicates the exchange reaction may be applicable to many of the other MAX phases. Using Table 1, the most likely candidates are those involving elements already known to successfully partake in exchange reactions  $M = Ti, V, Cr, Nb$  or  $Ta$  and  $A = Al, Si, Ge$ , or  $Sn$ , the untested phases of these combinations are  $V_2GeC$  and  $Nb_2SnC$ . The  $M$ -elements *not* studied previously ( $M = Sc, Zr, Mo$  and  $Hf$ ) were omitted from that investigation only as they do not form phases where  $A = Al$ , however this requirement has now been proven redundant by the current work. All of the  $M$ -elements are capable of being reduced by  $Al$ , and so are all strong contenders for formation via an exchange reaction. The primary point of concern will be the temperature at which reduction occurs and whether that is below the decomposition temperature of the MAX phases. Provided

Publication 2: MAX phase – alumina composites via elemental and exchange reactions in the Tin+1ACn systems (A = Al, Si, Ga, Ge, In and Sn).

suitable synthesis conditions exist the Zr<sub>2</sub>SnC and Hf<sub>2</sub>SnC systems become possible. By far the greatest number of systems become available if Ga and In could be utilised as A-elements with 5 Ga containing compounds (V<sub>2</sub>GaC, Cr<sub>2</sub>GaC, Nb<sub>2</sub>GaC, Mo<sub>2</sub>GaC and Ta<sub>2</sub>GaC) and 4 In containing compounds (Sc<sub>2</sub>InC, Zr<sub>2</sub>InC, Nb<sub>2</sub>InC and Ta<sub>2</sub>InC). However a better understanding of the reaction mechanism is needed before the synthesis of these phases can be realised.

## 5. Conclusions

The solid state synthesis of  $Ti_{n+1}AX_n$  phase -  $Al_2O_3$  composites directly from  $TiO_2$  via an exchange reaction has been successful in the  $Ti_2AC$  ( $A = Al, Ge$  and  $Sn$ ) and  $Ti_3AC_2$  ( $A = Al, Si, Ge$  and  $Sn$ ) systems. Extension of the process to  $Cr_2GeC$  when considered with its generality for  $M-Al-C$  systems demonstrates the general exchange reaction equation  $\alpha MO_x + \beta A + \delta C \rightarrow \varepsilon M_{n+1}AC_n + \phi Al_2O_3$  for  $n=2$  or  $3$  to be true. In systems where MAX phases were formed, the effectiveness of the exchange reaction was generally found to be comparable to similarly un-optimised reactive sintering from  $M$ -elemental reactants. A number of systems produced a mixture of both  $211$  and  $312$  MAX phases with a significant reduction in  $TiC$  formation. The mechanism for this  $TiC$  reduction appears to be its reaction with the  $211$  MAX phase to form a higher order MAX phase as originally proposed in the  $Ti-Al-C$  system<sup>34</sup>. That reaction type appears to be far more general than first thought and to proceed according to  $M_{n+1}AC_n + bMC \rightarrow M_{n+1+b}AC_{n+b}$ .

## Acknowledgments

The first author gratefully acknowledges the support provided by the Australian Renewable Energy Authority and an Australian Postgraduate Award. We also thank the staff of the Electron Microscopy and X-ray Unit of the University of Newcastle for the continued use of their facilities and expertise.

## References

1. Barsoum, M.W., *The  $M_{n+1}AX_n$  Phases and their Properties*, in *Ceramics Science and Technology: Materials and Properties*, R. Riedel and I.-W. Chen, Editors. 2010, John Wiley and Sons. p. 299-347.
2. Barsoum, M.W., *MAX Phases: Properties of Machineable Ternary Carbides and Nitrides*. 2013: Wiley.
3. Barsoum, M.W. and T. El-Raghy, *Synthesis and Characterisation of a Remarkable Ceramic:  $Ti_3SiC_2$* . Journal American Ceramic Society, 1996. **79**: p. 1953-1956.
4. Barsoum, M.W. and M. Radovic, *Elastic and Mechanical Properties of the MAX Phases*. Annual Review of Materials Research, 2011. **41**: p. 195-227.
5. Jeitschko, W., H. Nowotny, and F. Benesovsky, *Die H-Phasen  $Ti_2InC$ ,  $Zr_2InC$ ,  $Hf_2InC$  und  $Ti_2GeC$* . Monatshefte für Chemie und verwandte Teile anderer Wissenschaften 1963. **94**(6): p. 1201-1205.
6. Low, I.M., *Advances in science and Technology of the  $M_{n+1}AX_n$  Phases*. 2012: Woodhead publishing.
7. Eklund, P., et al., *The Mn + 1AXn phases: Materials science and thin-film processing*. Thin Film Solids, 2010. **518**(8): p. 1851-1878.
8. Cuskelly, D.T., E.H. Kisi, and H. Sugo, *MAX phase - alumina composites via exchange reaction in the Mn+1AlCn systems (M= Ti, V, Cr, Nb, or Ta)*. Journal of Solid State Chemistry, 2015. **223**: p. 150-157.
9. Ganguly, A., M.W. Barsoum, and J. Schuster, *The 1300°C Isothermal Section in the Ti-In-C Ternary Phase Diagram*. Journal American Ceramic Society, 2005. **88**: p. 1290-1296.
10. Viala, J.C., et al., *Phase equilibria at 1000C in the Al-C-Si-Ti quaternary system: An experimental approach*. Materials science and engineering, 1997. **A229**: p. 95-113.
11. Keast, V.J., S. Harris, and D.K. Smith, *Prediction of the stability of the Mn+1AXn phases from first principles*. Physical Reviews B 2009. **80**: p. 214113.
12. Kisi, E.H. and D.P. Riley, *Diffraction thermometry and differential thermal analysis*. Journal of Applied Crystallography, 2002. **35**: p. 664-668.
13. Bruesewilz, C., et al., *Single Crystal Microcompression tests of the MAX phases  $Ti_2InC$  and  $Ti_4AlN_3$* . Scripta Materialia, 2013. **69**(4): p. 303-306.
14. El Saeed, M.A., *Optimization of the  $Ti_3SiC_2$  MAX phase synthesis*. Refractory Metals and Hard Materials, 2012. **35**: p. 127-131.
15. Etzkorn, J., M. Ade, and H. Hillebrecht, *Ta<sub>3</sub>AlC<sub>2</sub> and Ta<sub>4</sub>AlC<sub>3</sub> – Single-Crystal Investigations of Two New Ternary Carbides of Tantalum Synthesized by the Molten Metal Technique*. Inorganic Chemistry, 2007. **46**(4): p. 1410-1418.
16. Etzkorn, J., et al., *Ti<sub>2</sub>GaC, Ti<sub>4</sub>GaC<sub>3</sub> and Cr<sub>2</sub>GaC- Synthesis, crystal growth and structure analysis of the Ga-containing MAX phases  $M_{n=1}GaC_n$  with M= Ti, Cr and n= 1, 3*. Journal of Solid State Chemistry, 2009. **182**(5): p. 995-1002.
17. Goesmann, F., R. Wenzel, and R. Schmid-Fetzer, *Perperation of  $Ti_3SiC_2$  by Electron-Beam-Ignited Solid-State Reaction*. Journal American Ceramic Society, 1998. **81**(11): p. 3025-3028.
18. Hfgberga, H., et al., *Growth and characterization of MAX-phase thin films*. Surface & Coatings Technology, 2005. **193**: p. 6-10.
19. Li, J.-F., F. Sato, and R. Watanabe, *Synthesis of  $Ti_3SiC_2$  polycrystals by hot-isostatic pressing of the elemental powders*. Journal of Materials Science Letters, 1999. **18**: p. 1595-1597.
20. Lin, T.-C. and M.-H. Hon, *Synthesis and microstructure of the  $Ti_3SiC_2$  in SiC matrix grown by chemical vapor deposition*. Ceramics International, 2008. **34**(3): p. 631-638.
21. Sun, Z., H. Hashimoto, and W. Tian, *Synthesis of the MAX Phases by Pulse Discharge Sintering*. International Journal of Applied Ceramic Technology, 2010. **7**: p. 704-718.

Publication 2: MAX phase – alumina composites via elemental and exchange reactions in the Tin+1ACn systems (A = Al, Si, Ga, Ge, In and Sn).

22. Zang, Z.F., et al., *Application of pulse discharge sintering (PDS) technique to rapid synthesis of Ti<sub>3</sub>SiC<sub>2</sub> from Ti/Si/C powders*. Journal of the European Ceramic Society, 2002. **22**(16): p. 2957-2961.
23. Zhang, J., et al., *Rapid fabrication of Ti<sub>3</sub>SiC<sub>2</sub>-SiC nanocomposite using the spark plasma sintering-reactive synthesis (SPS-RS) method*. Scripta Materialia, 2007. **56**(3): p. 241-244.
24. Zhang, W., et al., *Reactive Hot Pressing and Properties of Nb<sub>2</sub>AlC*. Journal of the American Ceramic Society, 2009. **92**(10): p. 2396-2399.
25. Riley, D.P. and E.K. Kisi, *Self-Propagating High-Tempertue Synthesis of Ti<sub>3</sub>SiC<sub>2</sub>: 1, Ultra High-Speed Neutron Diffraction Study of the Reaction Mechinism*. Journal American Ceramic Society, 2002. **85**(10): p. 2417-2424.
26. Riley, D.P., E.H. Kisi, and D. Phelan, *SHS of Ti<sub>3</sub>SiC<sub>2</sub>: Ignition temperature depression by mechanical activation*. Journal European Ceramic Society, 2004. **26**(6): p. 1051-1058.
27. Hendaoui, A., et al., *Synthesis of high-purity polycrystalline MAX phases in Ti-Al-C system through Mechanically Activated Self-propagating High-temperature Synthesis*. Journal of the European Ceramic Society, 2009. **30**(4): p. 1049-1057.
28. Yeh, C.L., R.F. Li, and Y.G. Shen, *Formation of Ti<sub>3</sub>SiC<sub>2</sub>-Al<sub>2</sub>O<sub>3</sub> in situ composites by SHS involving thermite reactions*. Journal of Alloys and Compounds, 2009. **478**(1-2): p. 699-704.
29. Inc., I. *InvestmentMine; Mining Markets and Investment*. 2015; Available from: <http://www.infomine.com/investment/metal-prices/>.
30. Chen, J., J. Li, and Y. Zhou, *In-situ Synthesis of Ti<sub>3</sub>AlC<sub>2</sub>/TiC-Al<sub>2</sub>O<sub>3</sub> Composite from TiO<sub>2</sub>-Al-C System*. Journal of Materials Science and Technology, 2005. **22**(4): p. 455-458.
31. Hendaoui, A., et al., *A novel method for synthesis of low-cost Ti-Al-C-based cermets*. International Journal of Self-Propagating High-Temperature Synthesis, 2010. **18**(4): p. 267-272.
32. Aylward, G. and T. Findlay, *SI Chemical Data*. Vol. 6. 2008: Wiley.
33. Cuskelly, D.T., et al., *Ti<sub>3</sub>GaC<sub>2</sub> and Ti<sub>3</sub>InC<sub>2</sub>: First bulk synthesis, DFT stability calculations and structural systematics*. Journal of Solid State Chemistry, 2015. **230**: p. 418-425.
34. Hill, R.J. and C.J. Howard, *Quantitative phase analysis from neutron powder diffraction data using the Rietveld method*. Journal of Applied Crystallography, 1987. **20**(6): p. 467-474.
35. Kisi, E.H., et al., *Inter-Conversion of M<sub>n+1</sub>AX<sub>n</sub> Phases in the Ti-Al-C system*. Journal American Ceramic Society, 2007. **90**(6): p. 1912-1916.

## **7. Publications 3: Single step carbothermal synthesis of high purity MAX phase powders**

Dylan T. Cuskelly\*, Erich H. Kisi

School of Engineering, the University of Newcastle, Callaghan NSW 2308, Australia

*Journal of the American Ceramic Society* JACERS-37809.R1

### **Abstract**

The MAX phases Cr<sub>2</sub>GeC and Cr<sub>2</sub>GaC were synthesised with high phase-purity directly from Cr<sub>2</sub>O<sub>3</sub>; Ge or Ga; and C starting materials using a single step carbothermal reduction. XRD and SEM analysis of the materials shows them to be >99 mol% Cr<sub>2</sub>GeC and 92 mol% Cr<sub>2</sub>GaC respectively. Extension to non-Cr systems is briefly demonstrated by applying the method to the synthesis of V<sub>2</sub>GeC.

## Introduction

$M_{n+1}AX_n$  (MAX) phases, extensively studied, over the past two decades need little introduction<sup>[1, 2]</sup>. Due to their unusual combination of properties many potential uses for monolithic MAX phases have been identified<sup>[1]</sup>, however these have been largely frustrated by a number of synthesis, production and economic concerns. Thin film methods<sup>[3]</sup> have been relatively successful however these cannot produce monolithic pieces. Direct laboratory scale synthesis of monolithic MAX phases has been demonstrated for many systems using reactive hot-pressing or reactive hot isostatic pressing (HIP)<sup>[4]</sup>. The production of larger volumes of product has been demonstrated by Self-propagating High Temperature Synthesis (SHS)<sup>[5]</sup> and pressureless reactive sintering<sup>[6]</sup> which are suitable for subsequent grinding followed by hot pressing, HIP or Spark Plasma Sintering (SPS) treatments to make larger samples<sup>[7]</sup>. These methods generally suffer from excessive retention of unwanted secondary phases. Consequently, commercial production of either monolithic MAX phase ceramics or low cost starting powders has not become widespread.

In contrast to most other ceramic materials, synthesis of MAX phases is usually described as commencing from elemental reactants (e.g.  $3Ti + Si + 2C \rightarrow Ti_3SiC_2$ ) or from a binary compound intended to suppress loss of the A-element by slowing its release (e.g.  $3Ti + SiC + C \rightarrow Ti_3SiC_2$ )<sup>[5]</sup> Irregular losses result in the formation of secondary compounds (e.g.  $3Ti + (1-x)Si + 2C \rightarrow (1-x)Ti_3SiC_2 + xTiC$  where  $x =$  lost Si) which may adversely affect the physical properties of the desired material. Excess A-element can reduce this effect and most successful MAX phase synthesis uses off stoichiometric starting ratios. Localised variations still result in the formation of TiC and large excess A-element results in either *M-A* intermetallic or *AX* formation.

In either case, the true synthesis and economic chain is more correctly described as commencing with ores, generally oxides. A substantial amount of processing has already been applied to the oxides in order to produce the usual elemental starting materials. Although ores of metals such as iron and aluminium are readily reduced, the ores of the MAX phase *M*-elements are difficult to reduce making the pure metal expensive. MAX phase production would therefore be greatly simplified if a processing route commencing with *M*-element oxides was available.

MAX phase formation via aluminothermic reduction (where  $\text{TiO}_2$  is reduced by Al in the presence of C) has been previously explored and shown to be applicable in the formation of  $\text{Ti-Al-C} + \text{Al}_2\text{O}_3$ <sup>[8]</sup> and  $\text{Ti-Si-C} + \text{Al}_2\text{O}_3$ <sup>[9]</sup> products. The aluminothermic method can be extended to many  $\text{Ti-A-C} + \text{Al}_2\text{O}_3$  systems, all  $M\text{-Al-C} + \text{Al}_2\text{O}_3$  systems and to  $\text{Cr}_2\text{GeC} + \text{Al}_2\text{O}_3$ <sup>[6]</sup>. Therefore Al is a fairly universal reducing agent in these systems. These MAX  $\text{Al}_2\text{O}_3$  products may be useful as composites or alternatively may be concentrated by physical or chemical means (e.g. adaptation of the Bayer process). In cases where the pure MAX phase is desired, it would be greatly advantageous to avoid  $\text{Al}_2\text{O}_3$  formation through the use of an alternative reducing agent.

Finding a reducing element to replace Al is difficult as the *M*-element oxides have very high enthalpy of formation. Candidates with oxides more readily removed than  $\text{Al}_2\text{O}_3$  include Mg, Ca and B. Unfortunately, reduction by B results in the formation of  $MB_2$  as the diboride is more stable than the MAX phase. Similarly,  $\text{MgO}$  can react with MAX phases to form an  $MX + \text{Mg-A-O}$  spinel composite.

The use of C as a reducing agent (carbothermal reduction) of *M*-element ores to metals or for the production of  $MC$  compounds is well known. The replacement of Al with C as reducing agent in MAX phase synthesis offers a number of advantages. Carbon is

abundant, inexpensive and the oxide reaction product would be gaseous potentially giving direct impurity-free synthesis.

Consultation of the relevant Ellingham diagram demonstrates that  $C + 1/2 O_2 \rightarrow CO$  is a viable reduction reaction for all oxides, however very stable oxides require very high temperatures.  $Cr_2O_3$  for example can be reduced by carbon at  $1225^\circ C$  while in pure systems  $TiO_2$  cannot be readily reduced below  $1650^\circ C$ .

One prior attempt at carbothermal synthesis of a MAX phase has been located in the literature<sup>[10]</sup>. Therein thermodynamic calculations were used to isolate promising conditions for co-reduction of  $TiO_2$  and  $SiO_2$  by C leading to formation of  $Ti_3SiC_2$ . Experimental implementation was partially successful, initially producing primarily TiC with trace amounts of  $Ti_3SiC_2$ . Optimisation gave a maximum yield of 31wt% (~12 mol%)  $Ti_3SiC_2$ .

Here we report the successful production of  $Cr_2GeC$  and  $Cr_2GaC$  at high levels of phase purity in a single step carbothermal reduction of  $Cr_2O_3$ . Adaptation to non-Cr systems is demonstrated by synthesis of  $V_2GeC$  by direct carbothermal reduction of  $V_2O_5$ .

## Experimental

Samples were prepared from  $Cr_2O_3$  (+99%, <45 µm),  $V_2O_5$  (+99%, <45 µm), Ga (+99.99%, ingot), Ge(+99.99%, single crystal ingot) and C (+99.8%, <100 µm), mixed initially in stoichiometric ratios according to Eqs. 1- 3. Five gram aliquots of mixed powders were high energy ball milled in a SPEX 8000 mill for 7min at a charge ratio of 14:1 and subsequently pressed into 15mm diameter pellets ~10mm high. As the major

impurity in stoichiometric Cr<sub>2</sub>GaC samples was a Cr-Ga intermetallic compound, the effect of increasing starting C was investigated. In the Cr-Ga-C system the initial C content was systematically increased to 105%, 110% and 115% of the stoichiometric amount while in the Cr-Ge-C system it was increased to 110% C. Optimisation of the V<sub>2</sub>GeC system was not attempted.



Pressed pellets in a graphite boat were heated to 1225°C at 5°C/min under flowing argon and held for 12 hours. Pellets were sectioned and a segment crushed for X-ray diffraction (XRD) (Cu K<sub>α</sub>) using a Panalytical X'Pert™. Rietveld analysis was conducted on all XRD data for Quantitative Phase Analysis (QPA)<sup>[11]</sup> and refined crystal structures.

## Results and Discussion

Analysis using XRD showed that stoichiometric samples in all systems were immediately successful resulting in the first majority MAX phase samples directly synthesised by carbothermal reduction. Rietveld refinement based QPA revealed that initial conversion was as high as 86 mol% in the Cr<sub>2</sub>GaC system. Interestingly the principal secondary phase was the intermetallic compound Cr<sub>3</sub>Ga at 14 mol% accompanied by <1 mol% of Cr<sub>7</sub>C<sub>3</sub>. Figure 1 shows the effect of varying the initial carbon content on the proportion converted into Cr<sub>2</sub>GaC.

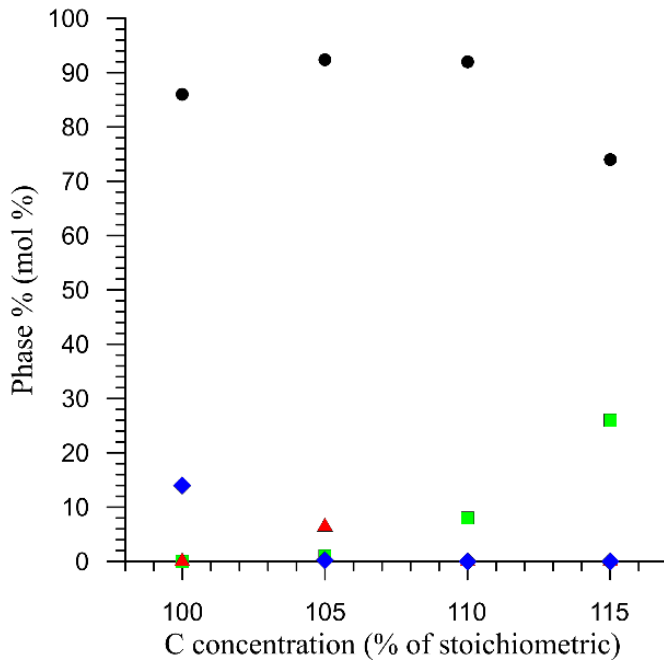


Figure 1 – Phase composition of Cr-Ga-C system shown in mol% of  $\text{Cr}_2\text{GaC}$  (●),  $\text{Cr}_3\text{C}_2$  (■),  $\text{Cr}_7\text{C}_3$  (▲),  $\text{Cr}_3\text{Ga}$  (◆) determined by Rietveld refinement as the initial carbon concentration was varied.

As the carbon concentration was increased, the secondary phase changed from the C deficient phase  $\text{Cr}_3\text{Ga}$  to chromium carbides, principally  $\text{Cr}_3\text{C}_2$ , indicating that after reaction the system is no longer C deficient. The highest conversions, ~92 mol%, were found at 105% and 110% of the stoichiometric C content. Therefore the optimum initial C concentration lies between 105% and 110% for this experimental arrangement. The exact proportion is most likely specific to elemental ratios, sample size, experimental arrangement and firing sequence and as such, further optimisation was not deemed necessary in this work. The XRD pattern for a sample formulated with 110% of the stoichiometric C concentration is shown in Figure 2a).

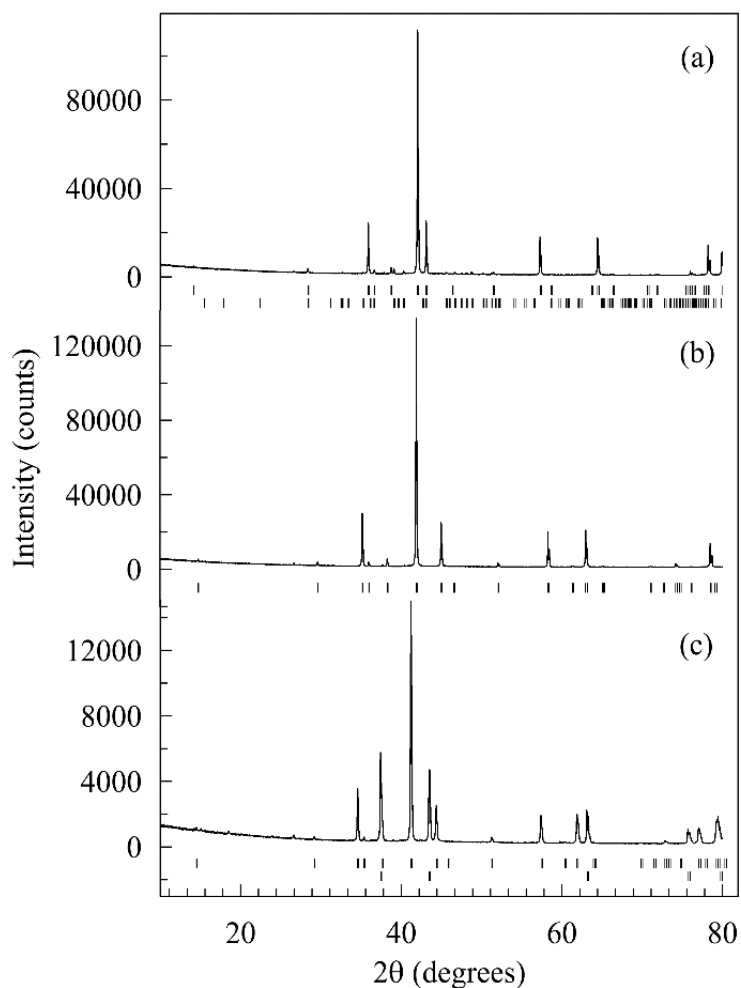
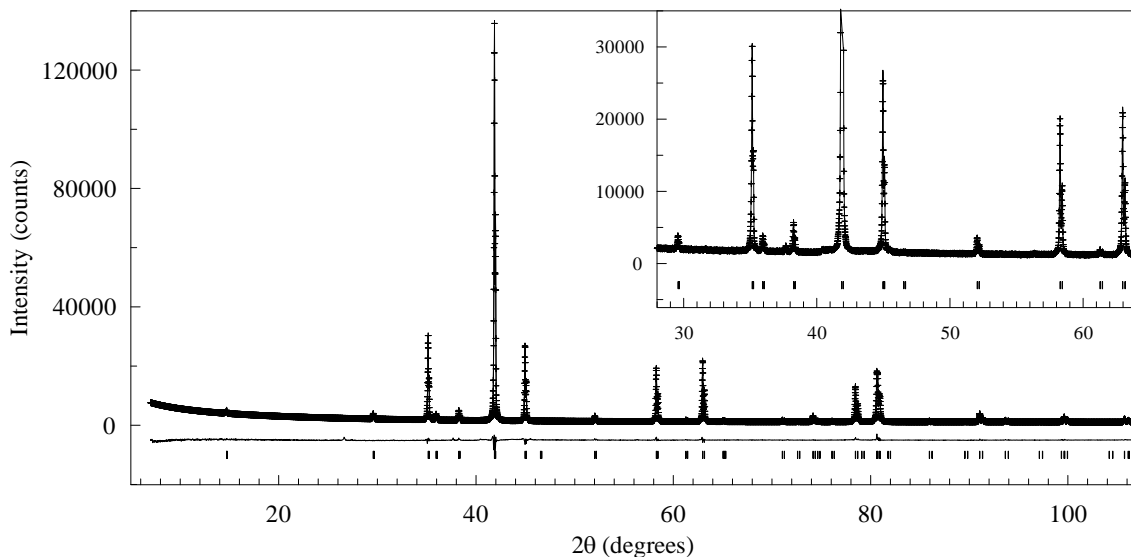


Figure 2 – XRD data for three systems a) optimised  $\text{Cr}_2\text{GaC}$  ( $\text{Cr}_3\text{C}_2$  as secondary phase), b) optimised  $\text{Cr}_2\text{GeC}$  and c) un-optimised  $\text{V}_2\text{GeC}$  ( $\text{VC}$  as secondary phase). Reflection markers show the peak positions for the MAX phase and major secondary phase.  $\text{Cr}_2\text{GeC}$  has no detectable secondary phases.

Samples produced in the  $\text{Cr}_2\text{GeC}$  system with excess C content (110% of the stoichiometric) also showed a strong increase in conversion to the MAX phase. Indeed, the product was > 99 mol%  $\text{Cr}_2\text{GeC}$  with no other phases detected via XRD analysis. The X-ray diffraction data are shown in Figure 2b) and a portion of the Rietveld analysis fit is shown in Figure 3. The high conversion seen here is extremely desirable as even small quantities of impurity phases have a drastic effect on properties. The conversion rate here is as good as high quality reactive hot pressed samples and far higher than normally seen in pressureless reactive sintering.

X-ray data for the un-optimised V<sub>2</sub>GeC material is given in Figure 2c). Its phase composition was found to be 33 mol% (56 wt%) V<sub>2</sub>GeC and 67 mol% (44 wt%) VC. Both the level of conversion and the secondary carbide phase seen are typical of un-optimised MAX phase syntheses.

The refined structure parameters and agreement indices are given in Table 1. Lattice parameters are all within 0.3% of the values originally published by Nowotny et.al.<sup>[12]</sup> The M atomic positions were not refined in earlier work and we believe are reported here for the first time.



*Figure 3 – Rietveld refinement using Cu K $\alpha$  XRD data (+) for an optimised Cr<sub>2</sub>GeC sample. The calculated profile is a solid line and a difference plot and reflection markers are given below. Inset shows the range in which secondary phases to be free from unidentified peaks other than at  $\sim 37.8^\circ 2\theta$  where the K $\beta$  peak corresponding to the large peak at  $42^\circ$  is visible.*

*Table 1 – Refined structure parameters and agreement indices for Cr<sub>2</sub>GeC, Cr<sub>2</sub>GaC and V<sub>2</sub>GeC. Figures in parentheses are the standard deviation in the last digit.*

|                           | Cr <sub>2</sub> GeC | Cr <sub>2</sub> GaC | V <sub>2</sub> GeC |
|---------------------------|---------------------|---------------------|--------------------|
| <i>a</i> (Å)              | 2.95368(2)          | 2.89214(1)          | 2.99864(5)         |
| <i>c</i> (Å)              | 12.10933(7)         | 12.60293(7)         | 12.2623(3)         |
| <i>zM</i>                 | 0.0872(1)           | 0.0855(1)           | 0.0887(1)          |
| <i>R<sub>wp</sub></i> (%) | 4.9                 | 6.2                 | 8.87               |
| <i>GOF</i>                | 5.7                 | 7.5                 | 3.9                |
| <i>R<sub>B</sub></i> (%)  | 2.2                 | 4.1                 | 2.9                |

Pellets removed from the furnace after firing had undergone visible shrinkage and some showed laminar cracking indicative of pressing faults, although they contained no macroscopic pores. From this it seems the reaction is reasonably slow. If it had proceeded at the speed of an SHS reaction, the volume of gas produced would cause gross deformation of the pellets and macroscopic pores, always present in pellets reacted under SHS conditions. Representative SEM images are shown in Figure 4. Crystal size in the Cr<sub>2</sub>GaC system (Figure 4a) ranged from ~100 nm up to ~5μm and were more equi-axed than often seen in MAX phases. No obvious evidence of a secondary phase was seen in the SEM although the fine grain size makes energy dispersive X-ray spectroscopy (EDS) difficult.

The V-Ge-C pellet surface in Figure 4b) shows the microscopic void structure left by the escape of CO. No voids significantly larger than those shown appeared elsewhere on the sample surface. Crystals were plate-like but quite small, only 0.8μm to 3μm in width and 0.2 to 0.4 μm thick. In this un-optimised system, VC is obvious as the ~200nm equi-axed crystals. EDS spot analysis confirmed the presence of Ge in the MAX phase crystals and its absence in the clusters of VC crystals.

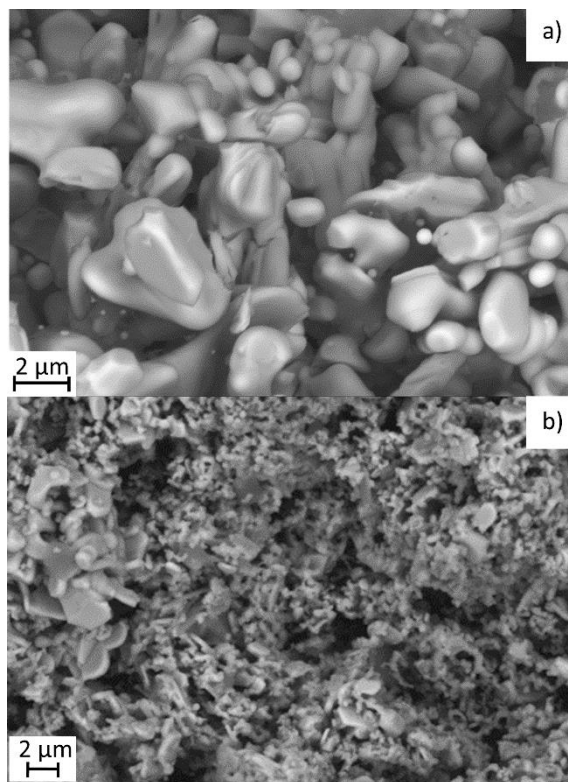


Figure 4 - Backscattered electron images showing a) high purity Cr<sub>2</sub>GaC powder, b) an overview of the structure of a V<sub>2</sub>GeC pellet.

The successful production of phase-pure MAX phases by carbothermal reduction of *M*-oxides opens the field of MAX phase synthesis to a new range of options. It promises the ability to produce large quantities of pure MAX phase powders with no need for refinement prior to downstream processing into monolithic ceramic components; an outcome long sought after. It also promises a significant cost saving compared with conventional synthesis of the *same* MAX phases from elemental starting materials and additionally a decreased material cost of the reducing agent. However, some caution must be exercised.

In some cases, the carbothermal reduction temperature of the oxide may be above the practical sintering temperature of the MAX phase. Taking for example the 18 Ti containing phases, generally 1650°C is required for carbon reduction of TiO<sub>2</sub>, a temperature which causes significant vaporisation loss of typical *A*-elements and

ultimately a poor MAX phase yield in a pressureless reactive sintering environment. Cetinkaya and Eroglu<sup>[10]</sup> have shown that intensive sample preparation can allow some successful conversion to  $Ti_3SiC_2$  at 1527°C in a system containing both  $SiO_2$  and  $TiO_2$  however yield, scalability and losses are still a major concern.  $M$  oxides that have high reduction temperatures (Nb, Zr Ti etc.) are only applicable if the decomposition temperatures of the MAX phase is also very high.  $Nb_2SnC$  for example has been shown to be stable at high temperatures and may resist the 1500-1700°C required for  $Nb_2O_5$  reduction. Alternatively the  $A$ -element of the MAX phase may preferentially reduce the  $M$ -oxide, as is the case with the 11 Al-containing MAX phases. Overall this limits the number of systems available for carbothermal reduction. Nonetheless, systems such as those studied here are very amenable to the technique. The most promising systems for expansion are  $M = Cr$  or  $V$  of which is  $V_2GaC$  the most likely due to success with both  $V_2GeC$  and  $Cr_2GaC$ .

## Conclusions

A simple reactive sintering process can convert  $Cr_2O_3$  – Ge – C mixtures into commercially pure (>99 mol%)  $Cr_2GeC$ . This is the first successful demonstration of single step carbothermal synthesis of a MAX phase from the corresponding  $M$  oxide. The methodology is not unique to this system as it was also readily shown that >92 mol%  $Cr_2GaC$  can be produced in this way. The method was shown to be adaptable to  $V_2GeC$  and a number of promising additional systems were identified.

## Acknowledgements

The first author gratefully acknowledges support from the Australian Renewable Energy Authority and an Australian Postgraduate Award. We also thank the staff of the Electron

Microscopy and X-ray Unit of the University of Newcastle for continued use of their facilities and expertise.

## References

1. Barsoum, M.W., The  $M_{n+1}AX_n$  Phases and their Properties, in Ceramics Science and Technology: Materials and Properties, R. Riedel and I.-W. Chen, Editors. 2010, John Wiley and Sons. p. 299-347.
2. Barsoum, M.W. and T. El-Raghy, Synthesis and Characterisation of a Remarkable Ceramic:  $Ti_3SiC_2$ . *J. Am. Ceram. Soc.*, 1996. 79: p. 1953-1956.
3. Eklund, P., et al., The  $M_{n+1}AX_n$  phases: Materials science and thin-film processing. *Thin Film Solids*, 2010. 518(8): p. 1851-1878.
4. Li, J.-F., F. Sato, and R. Watanabe, Synthesis of  $Ti_3SiC_2$  polycrystals by hot-isostatic pressing of the elemental powders. *J. Mater. Sci. Lett.*, 1999. 18: p. 1595-1597.
5. Riley, D.P. and E.K. Kisi, Self-Propagating High-Temperature Synthesis of  $Ti_3SiC_2$ : 1, Ultra High-Speed Neutron Diffraction Study of the Reaction Mechanism. *J. Am. Ceram. Soc.*, 2002. 85(10): p. 2417-2424.
6. CusKelly, D.T., E.H. Kisi, and H. Sugo, MAX phase - alumina composites via exchange reaction in the  $M_{n+1}AlC_n$  systems (M= Ti, V, Cr, Nb, or Ta). *J. Solid State Chem.*, 2015. 223: p. 150-157.
7. Zhang, J., et al., Rapid fabrication of  $Ti_3SiC_2$ -SiC nanocomposite using the spark plasma sintering-reactive synthesis (SPS-RS) method. *Scr. Mater.*, 2007. 56(3): p. 241-244.
8. Chen, J., J. Li, and Y. Zhou, In-situ Synthesis of  $Ti_3AlC_2/TiC-Al_2O_3$  Composite from  $TiO_2$ -Al-C System. *J. Mater. Sci. Technol.*, 2005. 22(4): p. 455-458.
9. Yeh, C.L., R.F. Li, and Y.G. Shen, Formation of  $Ti_3SiC_2-Al_2O_3$  in situ composites by SHS involving thermite reactions. *J. Alloy. Comp.*, 2009. 478(1-2): p. 699-704.
10. Cetinkaya, C. and S. Eroglu, Synthesis and reaction mechanism of  $Ti_3SiC_2$  ternary compound by carbothermal reduction of  $TiO_2$  and  $SiO_2$  powder mixtures. *Ceram. Int.*, 2012. 38: p. 6445-6453.
11. Hill, R.J. and C.J. Howard, Quantitative phase analysis from neutron powder diffraction data using the Rietveld method. *J. of Appl. Crystallogr.*, 1987. 20(6): p. 467-474.
12. Nowotny, H., W. Jeitschko, and F. Benesovsky, Kohlenstoffhaltige ternäre Verbindungen(V-Ge-C, Nb-Ga-C, Ta-Ga-C, Ta-Ge-C, Cr-Ga-C und Cr-Ge-C). *Monatshefte für Chemie und verwandte Teile anderer Wissenschaften*, 1963. 94(5): p. 844-850.

## 8. Publication 4: Ti<sub>3</sub>GaC<sub>2</sub> and Ti<sub>3</sub>InC<sub>2</sub>: first bulk synthesis, DFT stability calculations and structural systematics

Dylan T. Cuskelly<sup>1\*</sup>, Erin R. Richards<sup>1</sup>, Erich H. Kisi<sup>1</sup>, Vicki J. Keast<sup>2</sup>

<sup>1</sup> School of Engineering, The University of Newcastle, Callaghan, NSW 2308, Australia

<sup>2</sup> School of Mathematical and Physical Sciences, The University of Newcastle, Callaghan, NSW 2308, Australia

*Journal of Solid State Chemistry* DOI:10.1016/j.jssc.2015.07.028

### Abstract

A simple methodology for identifying possible higher order M<sub>n+1</sub>AX<sub>n</sub> phases (n≥2) from the chemical characteristics of known phases was developed. The method was used to identify two potential M<sub>3</sub>AC<sub>2</sub> phases Ti<sub>3</sub>GaC<sub>2</sub> and Ti<sub>3</sub>InC<sub>2</sub>. After verifying that the n=1 MAX phases in these systems could be synthesised in bulk using a simple pressureless reactive sintering process, the new phases were synthesised using the same method. DFT calculations were used to test the thermodynamic stability of the new phases against the known competing phases within the same ternary systems. Both were found to be stable although Ti<sub>3</sub>InC<sub>2</sub> only marginally so. Crystal structure refinements and comparison to other MAX phases revealed a linear increase in the c-axis length as a function of the atomic radius of the A-element.

## 1. Introduction

The  $M_{n+1}AX_n$  (MAX) phases are a group of ceramics with a remarkable set of properties making them interesting for both scientific study and materials engineering. MAX phases are comprised of an early transition metal  $M$ , a group IIIA or IVA-element  $A$ , and  $X$  is either C or N. The index  $n$  takes the value 1, 2 or 3<sup>[1]</sup> and the resulting phases are commonly referred to as ‘211’, ‘312’ and ‘413’ type respectively. Since their discovery in the 1960’s over 60 different MAX phases have been found. However, production of bulk single phase samples was possible only after the development of the reactive hot pressing technique in the 1990’s by Barsoum and El Raghay<sup>[2]</sup>. MAX phases possess a nanolayered crystal structure where covalently bonded  $MX$  carbides or nitrides are interleaved with metallically bonded  $A$ -element layers. Much of the research on MAX phases has been motivated by their rare and sometimes unique set of properties, which arise from a combination of metallic, covalent and weak ionic bonding in the unit cell. MAX phases display properties typical of both metals and ceramics such as: good electrical and thermal conductivity; resistance to thermal shock; machinability; oxidation resistance; modest density; high strength and stiffness at elevated temperatures<sup>[13]</sup>.

Whilst they possess this desirable combination of properties, MAX phases have complex formation paths, which cause well documented difficulties during synthesis. These complexities can lead to the retention of intermediate or impurity phases, most commonly binary carbides (e.g. TiC) which possess some drastically different physical properties to the parent MAX phase. These unwanted phases are often difficult to remove due to their chemical stability and affinity to the MAX phases<sup>[5]</sup>. The major focus of synthesis research has therefore been the production of pure and fully dense monolithic ceramic bodies from a relatively small number of MAX phases (such as Ti<sub>3</sub>SiC<sub>2</sub>, Ti<sub>3</sub>AlC<sub>2</sub> and

Ti<sub>2</sub>AlC) by methods such as hot isostatic pressing, pulse discharge sintering or spark plasma sintering<sup>[4, 7, 14-17]</sup>. Less attention has been paid to the synthesis of new examples of MAX phases and the difficult problem of predicting which of the possible M-A-X systems actually produce MAX phases and which type, 211 and/or 312 and/or 413, is formed. Recently thin film processes such as chemical vapour deposition and magnetron sputtering have been gaining traction in the production of MAX phases. Some of the new MAX phases discovered in this way have been found only in thin films or have been present as small single crystals in a sample of which the majority is a separate non-MAX phase<sup>[18]</sup>. Our work is concerned primarily with the synthesis and stability of *bulk* quantities of new MAX phases, with the focus on the carbides which are currently more numerous than the nitrides.

Bulk synthesis can only occur if the target phase is both thermodynamically stable and kinetically accessible. Taking the thermodynamic perspective first, there are combinations of elements known individually to be present in some MAX phases, which will nonetheless not combine to form a new MAX phase. For example, both V<sub>3</sub>AlC<sub>2</sub> and Ti<sub>3</sub>SiC<sub>2</sub> exist however V<sub>3</sub>SiC<sub>2</sub> does not. In other cases, elements known to form a MAX phase at one value of *n*, will not combine in phases with a different value of *n*, regardless of the synthesis conditions. The absence of a bulk Ti<sub>2</sub>SiC phase in the Ti-Si-C system is one such thermodynamically prohibited example.<sup>[19]</sup> From a kinetic perspective, reaction pathways on the ternary diagrams of MAX phase systems tend to involve the production of intermediate compounds. The free energy surface of these systems is deeply pitted with local minima and these often require extremes of temperature, pressure and time to overcome. Synthesis difficulties have been primarily attributed to phase diagram complexity leading to many competing compounds and partial loss of the *A*-element at

high temperature.<sup>[20, 21]</sup> This is exacerbated by the extremes of temperature and time required.

Density functional theory (DFT) has been successfully used to predict or verify the energetic stability of selected MAX phases when compared to the available competing phases<sup>[19, 22-28]</sup>. Such calculations represent the system energy at 0 K and, as such, neglect the electronic and vibrational entropic contributions. However, a recent study has verified that inclusion of such effects does not significantly influence the outcome of the calculated formation energies<sup>[29]</sup> and confirm that DFT calculations at 0 K are a useful tool in determining which MAX phases can be expected to be the thermodynamically favourable. However, whilst DFT calculations for a single target MAX phase are now relatively straight forward, their application to all of the phases in all permutations of all the M-A-X ternary systems which could potentially contain MAX phases is still a daunting task. Fortunately the systematics of known MAX phases can provide some guidance to the selection of promising systems.

## 1.2 Analysis of M-A-C Systems

Of the elements known to form MAX phases, only a subset of the many possible permutations have been synthesised so far. The systems which are known to form bulk quantities of carbide MAX phases are displayed in Table 1. There are 216 combinations, but only about 50 discrete M-A-X systems. Of the MAX phases that have been reported, over forty five (approximately 80%) are 211 phases compared with only six 312 and seven 413 phases (about 10% each). Of the higher order ( $n = 2$  or 3) MAX phases that have been synthesised, all appear to meet the following two conditions.

- i) They contain either Ti as the *M*-element or Al as the *A*-element or both.

ii) All higher order phases so far discovered also have a bulk *211* counterpart, with the notable exception of Ti<sub>3</sub>SiC<sub>2</sub>.

*Table 1 – Systematics of MAX phase formation. The table shows known carbide MAX phases arranged by M and A-element. Combinations where the higher order phases i.e. 312 and 413 phases occur are shown in darker grey and can be seen to exclusively occupy the Al column and the Ti row.*

| M VS A    | Al                | Si         | P   | S   | Ga                | Ge                | As  | Cd  | In         | Sn         | Tl  | Pb  |
|-----------|-------------------|------------|-----|-----|-------------------|-------------------|-----|-----|------------|------------|-----|-----|
| <b>Sc</b> |                   |            |     |     |                   |                   |     |     | 211        |            |     |     |
| <b>Ti</b> | 211<br>312        | 312<br>413 |     | 211 | 211<br>312<br>413 | 211<br>312<br>413 |     | 211 | 211<br>312 | 211<br>312 | 211 | 211 |
| <b>V</b>  | 211<br>312<br>413 |            | 211 |     | 211               | 211               | 211 |     |            |            |     |     |
| <b>Cr</b> | 211               |            |     |     | 211               | 211               |     |     |            |            |     |     |
| <b>Zr</b> |                   |            |     | 211 |                   |                   |     |     | 211        | 211        | 211 | 211 |
| <b>Nb</b> | 211<br>413        |            | 211 | 211 | 211               |                   | 211 |     | 211        | 211        |     |     |
| <b>Mo</b> |                   |            |     |     | 211               |                   |     |     |            |            |     |     |
| <b>Hf</b> |                   |            |     | 211 |                   |                   |     |     |            | 211        |     | 211 |
| <b>Ta</b> | 211<br>312<br>413 |            |     |     | 211               |                   |     |     | 211        |            | 211 |     |

The search for new 312 phases was limited to those systems which meet the two conditions above (Ti as an *M*-element or Al as an *A*-element; and a corresponding *211* phase). The, non-Ti, *M*<sub>3</sub>AlC<sub>2</sub> systems that have not yet been reported have *M*= Cr or Nb. DFT calculation has indicated that Cr<sub>3</sub>AlC<sub>2</sub> is unstable<sup>[19]</sup> and Nb<sub>3</sub>AlC<sub>2</sub> has presented experimental difficulties. The Ti<sub>3</sub>AC<sub>2</sub> systems yet to be reported have *A*= S, Ga, Cd, In,

Pb and Tl. Ga was considered a strong contender as it is known to form both a *413* and a *211* phase. Considering elements in both the same rows of the periodic table as Ge and Sn and the same column as Al (which are each involved in known *312* phases), the Ti-In-C and Ti-Ga-C systems were identified as the best candidates for further investigation into the synthesis of a new *312* phase.

There have been no previous reports of the Ti<sub>3</sub>InC<sub>2</sub> phase, making this system a novel one, and there is only one previous report of Ti<sub>3</sub>GaC<sub>2</sub> as a very minor phase within a predominantly Ti<sub>6</sub>Al<sub>10</sub>Ga<sub>5</sub>C sample. The phase suspected of being Ti<sub>3</sub>GaC<sub>2</sub> was present as isolated crystals approximately 100μm in size. Energy dispersive X-ray spectroscopy (EDS) analysis also revealed that the crystal contained Sn with an estimated composition of Ti<sub>3</sub>Ga<sub>0.85</sub>Sn<sub>0.15</sub>C<sub>2</sub>.<sup>[18]</sup> The single crystals allowed micro hardness testing to be conducted, however methods of producing bulk polycrystalline samples were not reported. The corresponding *211* phases have both been reported<sup>[30, 31]</sup> but have not been previously synthesised using simple pressureless reactive sintering.

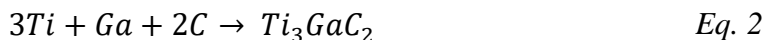
In this paper we report the first ever synthesis of bulk polycrystalline Ti<sub>3</sub>InC<sub>2</sub> and Ti<sub>3</sub>GaC<sub>2</sub> by a simple pressureless reactive sintering method. This was preceded by a proof of concept syntheses of the known *211* phases Ti<sub>2</sub>GaC and Ti<sub>2</sub>InC via the same method. DFT was used to confirm that the total energy of the MAX phases is lower than the competing phases in these systems. Refined crystal structures (lattice dimensions and atomic positions) for both Ti<sub>3</sub>GaC<sub>2</sub> and Ti<sub>3</sub>InC<sub>2</sub> are also presented and compared with the structural systematics of all the Ti<sub>n+1</sub>AC<sub>n</sub> MAX phases.

## 2. Method

### 2.1. Sample Preparation and Analysis

Powders of titanium (180µm, 99.3%) and graphite (<100 µm, 99.8%) were mixed in stoichiometric molar ratios with liquid gallium (99.99%) or indium ingot (99.995%). Powders were high-energy ball milled for 15 minutes with steel balls in a SPEX 8000 using a hardened steel vial with a ball-to-powder mass charge ratio of 7:1. The powders were then uni-axially pressed into 15 mm diameter pellets, each weighing approximately 4 g. The pellets, contained in graphite sample holders, were fired in an argon atmosphere with a heating ramp of 5°C/min to 1300°C and held for 7 hours to produce optimal products. Experiments investigating the effect of sintering time (3h, 7h and 12h holds) and temperature (1250°C, 1300°C, 1350°C and 1400°C) were conducted. A hold of 7 hours at 1300°C was found to give the highest conversion rates.

Four sample types were studied according to Eqs. 1-4. Formulations targeting Ti<sub>2</sub>GaC and Ti<sub>2</sub>InC (Eqs. 1 and 3) were used to verify that the reactive sintering method could produce bulk quantities of these known MAX phases in the systems of interest. Formulations targeting Ti<sub>3</sub>GaC<sub>2</sub> and Ti<sub>3</sub>InC<sub>2</sub> (Eqs. 2 and 4) were attempts to synthesise monolithic samples of new MAX phases.



Sintered pellets were abraded before analysis with Cu K<sub>α</sub> X-Ray Diffraction (XRD) on a Panalytical X'Pert™ diffractometer. Rietveld refinements allowed for determination of lattice parameters and atomic positions whilst the refined scale factors were used for quantitative phase analysis according to the method given by Hill and Howard<sup>[11]</sup>. In these refinements, the background, zero, peak width parameters and scale factors of all phases were refined. The microstructure of the resulting MAX phases was studied uncoated using a Zeiss Sigma VP FESEM scanning electron microscope (SEM) operated at 3 and 15 keV, in backscattered electron (BSE) and secondary electron (SE) imaging mode. Energy dispersive X-ray spectroscopy (EDS) spectra were obtained using a Bruker thin window spectrometer.

## 2.2 DFT Analysis

Potential ternary phase diagram plots were determined on the basis of the binary phase diagrams and the known ternary phases in the ICSD<sup>[32]</sup>. A high temperature ternary diagram for Ti-In-C has also been derived previously<sup>[33]</sup>. The position of the MAX phases in the ternary diagram was determined and the possible competing phases identified from the nearby stable points on the diagram. A simplex linear optimisation procedure was used to determine the most competitive combination of competing phases<sup>[22]</sup>. One possible competing phase for Ti<sub>2</sub>InC is a disordered compound Ti<sub>56</sub>In<sub>44</sub>, which cannot be easily modelled computationally and was not observed experimentally, so it has not been included here. There are a large number of Ti-Ga intermetallic phases, many with complex and disordered structures and the Ti<sub>2</sub>GaC phase has been shown to be thermodynamically stable experimentally. For these reasons DFT stability calculations were performed on the 312 and 413 phases in this ternary system and it was assumed that Ti<sub>2</sub>GaC and TiC were the competing phases.

Initial crystal structures were chosen on the basis of experimental structures from the ICSD or from structural details generated by Rietveld refinements using high resolution X-ray diffraction patterns. In the case of the n = 3 phase, a best first estimate was used, based on parameters for similar MAX phases and the n = 2 and n = 3 phases. Structural relaxations were performed for all crystal structures including lattice parameters and internal coordinates (where applicable). This is necessary so that the energy calculations between different phases are consistent, particularly when considering phases which have not yet been observed experimentally. The final lattice parameters and atom positions derived from DFT are usually systematically slightly different from those observed experimentally. The exceptions here are Ti<sub>3</sub>InC<sub>2</sub> and Ti<sub>8</sub>In<sub>5</sub> where the optimized structures have a significantly lower energy than the structure with the experimental lattice parameters.

The DFT calculations were performed using the (linearized) augmented plane wave plus local orbitals method (L/APW+lo) within the WIEN2K software package<sup>28</sup>. The generalised gradient approximation (GGA) was used for the exchange-correlation potential<sup>[34]</sup>. The plane-wave cut-off, defined by the product of the smallest atomic sphere radius times the magnitude of the largest reciprocal-lattice vector  $R_{MT}K_{max}$ , was set to 7.0 and a  $G_{max}$  (magnitude of the largest vector in the charge-density Fourier expansion) of 12 was used for all calculations. The atomic sphere radii (in Bohr) were taken as: Ti = 2.1; In = 2.3 and C = 1.7. They were kept constant for all calculations to ensure comparisons of total energy between different structures remained valid. Spin polarization was not included. The number of  $k$ -points in the irreducible Brillouin zone was in the range of 20-150 during structural relaxations, depending on the size of the

crystal cell. The number of  $k$ -points was increased for the final energy calculations and the total energies are converged with respect to the number of  $k$ -points.

### 3. Results

#### 3.1 XRD

Figure 1 shows the XRD data, Rietveld analysis and refined fit for the Ti-Ga-C samples (Eqs. 1 and 2) and Figure 2 the same information for the Ti-In-C samples (Eqs. 3 and 4). All 4 systems produced the desired phase with varying levels of effectiveness. The relative quantities of the phases, determined by Rietveld refinement, are summarised in Table 2. All MAX phases occupy the space group P  $6_3/mmc$  and the general atomic positions for the 211 and 312 MAX phases are summarised in Table 3. Refined structural parameters for all systems studied are included in Table 4.

*Table 2 Relative phase quantities determined by Rietveld analysis for samples made to eq. 1-4.*

| Eq.#     | System        | TiC<br>(wt%) | Ti <sub>2</sub> GaC<br>(wt%) | Ti <sub>3</sub> GaC <sub>2</sub><br>(wt%) | Ti <sub>2</sub> InC<br>(wt%) | Ti <sub>3</sub> InC <sub>2</sub><br>(wt%) | In<br>(wt%) |
|----------|---------------|--------------|------------------------------|---|------------------------------|---|-------------|
| <b>1</b> | 2Ti + Ga + C  | -            | 91                           | 9   | -                            | -   |             |
| <b>2</b> | 3Ti + Ga + 2C | 4            | -                            | 96  | -                            | -   |             |
| <b>3</b> | 2Ti + In + C  | 11           | -                            | -   | 85                           | -   | 4           |
| <b>4</b> | 3Ti + In + 2C | 19           | -                            | -   | 37                           | 39  | 4           |

Table 3 General atomic positions of the MAX phases

211 Atomic       $x$        $y$        $z$

Positions

|            |     |     |          |
|------------|-----|-----|----------|
| $M$        | 1/3 | 2/3 | $M_z$    |
| $A$        | 1/3 | 2/3 | 3/4      |
| $X$        | 0   | 0   | 0        |
| 312 Atomic |     |     |          |
| Positions  |     |     |          |
| $M(1)$     | 0   | 0   | 0        |
| $M(2)$     | 2/3 | 1/3 | $M(2)_z$ |
| $A$        | 0   | 0   | 1/4      |
| $X$        | 1/3 | 2/3 | $X_z$    |

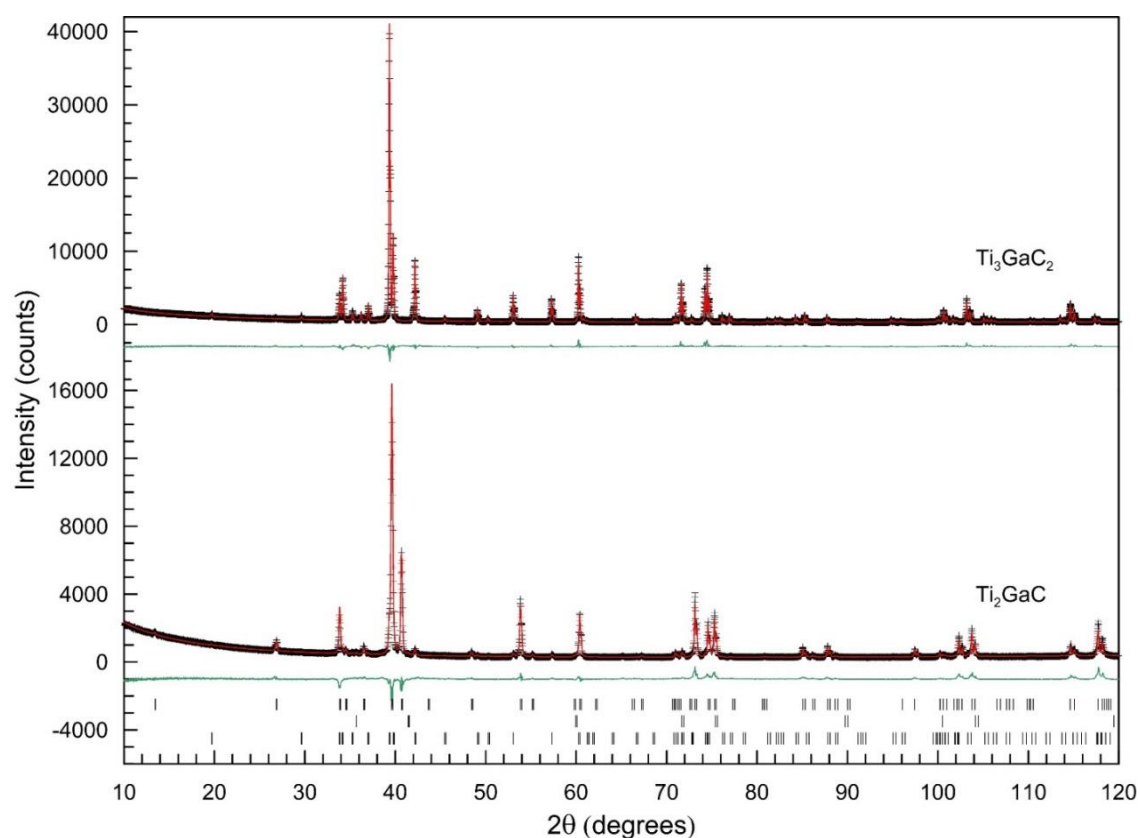
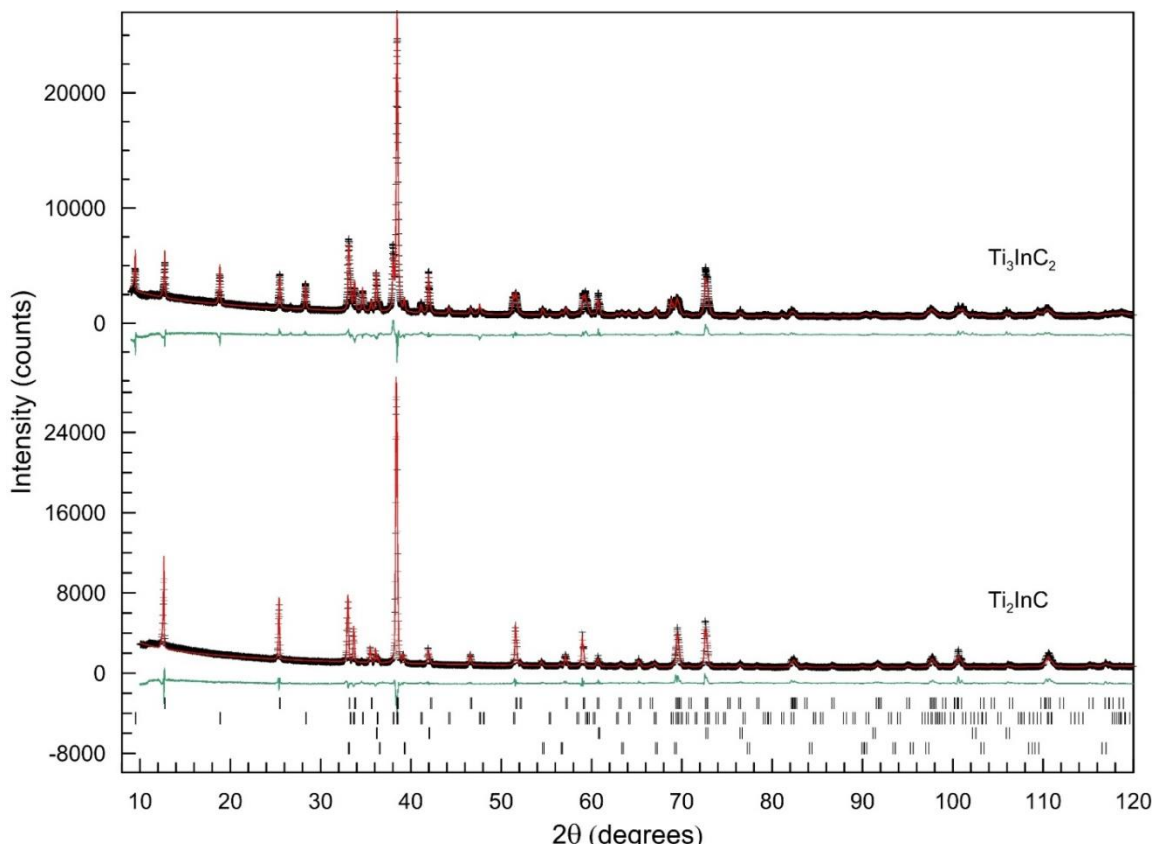


Figure 1. Ti-Ga-C XRD Rietveld analysis. Typical sample made according to Eq.1 (lower) with main phase Ti<sub>2</sub>GaC, and typical sample from Eq.2 (upper) with main phase Ti<sub>3</sub>GaC<sub>2</sub>. Black '\*' represent measured data, the red line is the calculated fit, and the green line is the difference plot. Markers represent expected peak positions from the phases Ti<sub>2</sub>GaC, TiC and Ti<sub>3</sub>GaC<sub>2</sub> from top to bottom

*Table 4 Refined structural parameters of the phases investigated in this work. Structural information is only reported for the major phase in each sample.*

| Structural parameters    | Ti <sub>2</sub> GaC | Ti <sub>3</sub> GaC <sub>2</sub> | Ti <sub>2</sub> InC | Ti <sub>3</sub> InC <sub>2</sub> |
|--------------------------|---------------------|----------------------------------|---------------------|----------------------------------|
| a                        | 3.0713(1)           | 3.08162(1)                       | 3.13220(5)          | 3.1212(8)                        |
| c                        | 13.353(4)           | 18.2447(1)                       | 14.0427(3)          | 19.0030(5)                       |
| Ti <sub>z</sub> (211)    | 0.0859(1)           | -                                | 0.07963(8)          | -                                |
| Ti(2) <sub>z</sub> (312) | -                   | 0.12981 (3)                      | -                   | 0.1182(1)                        |
| C <sub>z</sub> (312)     | -                   | 0.0691(2)                        | -                   | 0.0536(4)                        |



*Figure 2 Ti-In-C XRD Rietveld analysis. Typical sample made according to Eq.3 (lower) with main phase Ti<sub>2</sub>InC, and typical sample from Eq.4 (upper) with main phase Ti<sub>3</sub>InC<sub>2</sub>. Black '\*' represent measured data, the red line is the calculated fit, and the green line is the difference plot. Markers represent expected peak positions from the phases Ti<sub>2</sub>InC, Ti<sub>3</sub>InC<sub>2</sub>, TiC and metallic In from top to bottom*

### 3.2 Scanning electron microscopy

SEM analysis was conducted on all samples to investigate their morphology. Both backscattered (BSE) and secondary (SE) electrons were used however in general there was limited BSE contrast.

### 3.2.1 Ti-Ga-C system

The uniformity of the Ti<sub>2</sub>GaC MAX phase made according to Eq. 1 may be seen in the SEM images in Figure 3a) and b), with no evidence of TiC inclusions. The grains were seen to be very fine, approximately 1-2  $\mu\text{m}$  and roughly cuboid. Minor contrast was observed in some MAX phase grains which could be attributed to the slightly Ga depleted Ti<sub>3</sub>GaC<sub>3</sub> phase. However, the grains were too small and isolated to be reliably analysed (interaction volume of the electron beam is approximately 1  $\mu\text{m}^3$ ). Close inspection of certain grains in Figure 3b) does show some of the layered features characteristic of MAX phase microstructures.

Figure 3c) and d) show SEM micrographs of the new phase Ti<sub>3</sub>GaC<sub>2</sub>. Crystals in this system were again very fine but more plate-like, being ~0.5  $\mu\text{m}$  thick and up to 6  $\mu\text{m}$  wide. This aspect ratio in the order of 1:10 is more typical of MAX phase grains. No TiC crystals were observed and overall the sample appeared phase-pure. The titanium to gallium ratio in Figure 3d) was 3Ti : 0.96Ga determined by spot EDS analyses which corresponds well with both the XRD results and the stoichiometric composition of Ti<sub>3</sub>GaC<sub>2</sub>.

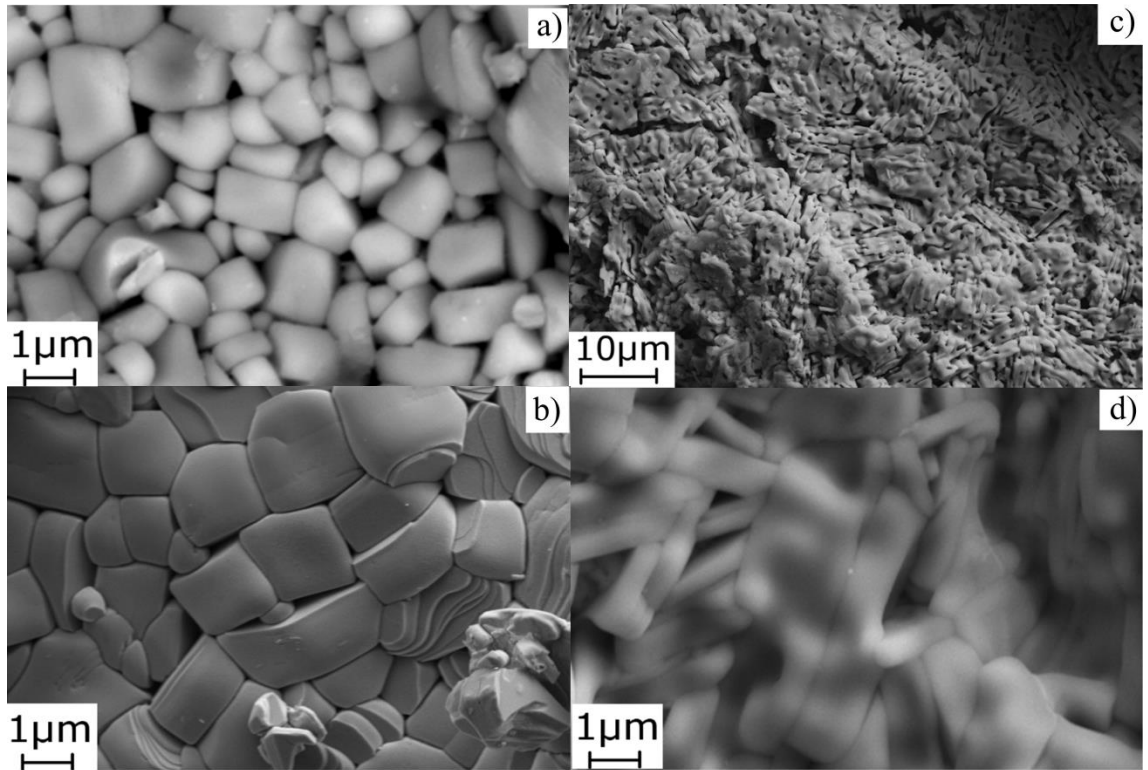


Figure 3. SEM images of the samples in the Ti-Ga-C system. a) (BSE) and b) (SEI) show the Ti<sub>2</sub>GaC system while c) and d) (SEI) show the Ti<sub>3</sub>GaC<sub>2</sub> system. No crystals that obviously belong to another phase were seen in either system.

### 3.2.2 Ti-In-C system

The microstructure of the Ti<sub>2</sub>InC in Figure 4a) and b) shows two distinct regions. The samples primarily comprised grains similar to those seen in Figure 4a), which were relatively large, 10 μm by 1 μm, MAX phase grains. These regions also were phase-pure with no contaminant crystals to be seen. Regions such as that shown in Figure 4b) were seen as isolated pockets. Crystals in this region were on the order of 250 nm making EDS spot analysis on a single grain impossible. However, high contrast can be seen in backscattered electron images indicating what are likely to be regions containing TiC crystals imbedded in an indium matrix.

SEM investigation of a sample targeting Ti<sub>3</sub>InC<sub>2</sub> (Eq. 4) can be seen in Figure 4c) and d).

Although XRD demonstrated that the sample is a composite of 4 phases, minimal backscattered electron contrast could be seen over large areas. Regions of typical MAX phase grains similar in appearance to the Ti<sub>2</sub>InC crystals seen in Figure 4a) were seen in Figure 4c) however in other regions cubic crystals were observed. Closer inspection of these crystals, shown in Figure 4d) using secondary electrons, indicate the crystal displaying the layered nature commonly associated with MAX phases. The tabular crystals appear to be approximately 70 nm thick and 2μm wide. Crystals of about 200nm were also commonly seen.

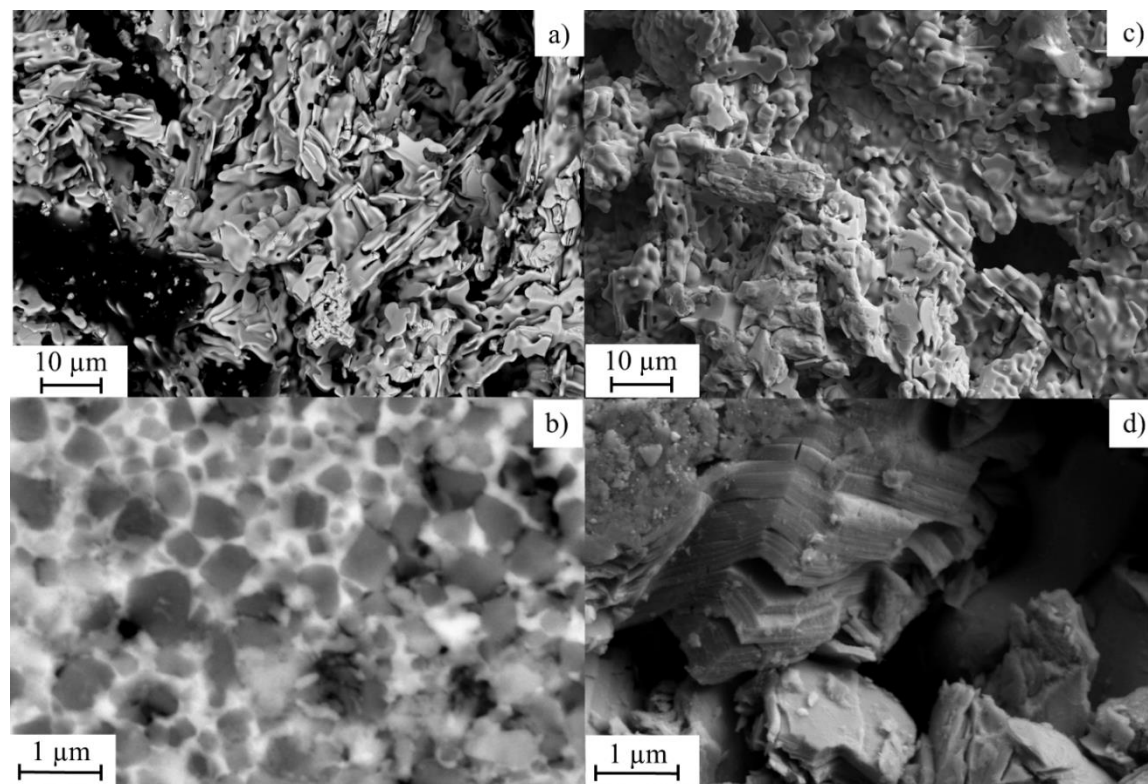


Figure 4. SEM images of the samples in the Ti-In-C system showing distinct regions. a) and b) (BSE) show the Ti<sub>2</sub>InC system while c) and d) (SEI) show the Ti<sub>3</sub>InC<sub>2</sub> system.

### 3.3 DFT Calculations

Calculations showed that when starting from stoichiometric elemental ratios, all the 211 and 312 MAX phases analysed in this paper are energetically stable. The results are given in Table 5 where the most energetically favourable options for the possible competing phases are shown. Two cases were considered, one where the higher order phases were included as a competing phase, and one where they were not. Optimised structural parameters were calculated and the total energy (per formula unit) calculated. The data in Table 5 gives the energy difference (eV) between the product phase ( $E_{MAX}$ ) and the lowest energy set of competing phases ( $E_{CP}$ ).  $\Delta E < 0$  suggests the MAX phase is energetically stable and  $\Delta E > 0$  suggests that the competing phases would form instead. The second column indicates energies calculated using the optimised structural parameters, whereas the third column indicates energies calculated using the experimental structural parameters. In all cases the optimised structural parameters indicate that the MAX phase is the stable state, with the exception of Ti<sub>4</sub>InC<sub>3</sub> which would likely decompose. Imposing experimental lattice parameters determined from X-ray diffraction also indicated three of the four MAX phases studied in this paper (Ti<sub>2</sub>GaC, Ti<sub>3</sub>GaC<sub>2</sub> and Ti<sub>2</sub>InC) are stable, however the calculated energy for Ti<sub>3</sub>InC<sub>2</sub> suggests instability.

*Table 5 Summary of energy differences from DFT calculations used to test stability of the MAX phases in the Ti-Ga-C and Ti-In-C systems compared with competing phases. Energies calculated using both the theoretical (column 2) and experimental (column 3) lattice parameters are given.*

| Balance Equations   | $\Delta E = E_{MAX} - E_{CP}$<br>(eV) | $\Delta E = E_{MAX} - E_{CP}$<br>(eV) (exp.) |
|---|---------------------------------------|--|
| Ti <sub>3</sub> GaC <sub>2</sub> ↔ Ti <sub>2</sub> GaC + TiC  | -0.163                                | -0.150                                       |
| Ti <sub>3</sub> GaC <sub>2</sub> ↔ $\frac{1}{2}$ Ti <sub>2</sub> GaC + $\frac{1}{2}$ Ti <sub>4</sub> GaC <sub>3</sub>                                       | -0.079                                | -  |
| Ti <sub>4</sub> GaC <sub>3</sub> ↔ Ti <sub>3</sub> GaC <sub>2</sub> + TiC   | -0.004                                | -  |
| Ti <sub>4</sub> GaC <sub>3</sub> ↔ Ti <sub>2</sub> GaC + 2TiC   | -0.166                                | -  |
| Ti <sub>2</sub> InC ↔ $\frac{3}{8}$ Ti <sub>3</sub> InC + $\frac{1}{8}$ Ti <sub>2</sub> In <sub>5</sub> + $\frac{5}{8}$ TiC                                 | -0.706                                | -0.710                                       |
| Ti <sub>2</sub> InC ↔ $\frac{3}{13}$ Ti <sub>3</sub> InC + $\frac{1}{13}$ Ti <sub>2</sub> In <sub>5</sub> + $\frac{5}{13}$ Ti <sub>3</sub> InC <sub>2</sub> | -0.373                                | -0.816                                       |
| Ti <sub>3</sub> InC <sub>2</sub> ↔ Ti <sub>2</sub> InC + TiC  | -0.162                                | <b>+0.989</b>                                |
| Ti <sub>3</sub> InC <sub>2</sub> ↔ $\frac{1}{2}$ Ti <sub>2</sub> InC + $\frac{1}{2}$ Ti <sub>4</sub> InC <sub>3</sub>                                       | -0.090                                | -  |
| Ti <sub>4</sub> InC <sub>3</sub> ↔ Ti <sub>3</sub> InC <sub>2</sub> + TiC   | <b>+0.019</b>                         | -  |

### 3.4 Analysis of structural systematics

Given the observation from Table 1 of the systematic chemical similarities between systems that form higher order MAX phases, it is of interest to consider whether this is accompanied by systematic structural features. Of the twelve possible A-elements known to form Ti<sub>n+1</sub>AC<sub>n</sub> MAX phases (Al, Si, P, S, Ga, As, Ge, Cd, In, Sn, Tl and Pb), nine form Ti<sub>2</sub>AC phases (Al, S, Ga, Ge, Cd, In, Sn, Tl and Pb) and, until this paper, four (Al, Si, Ge and Sn) were known to form bulk Ti<sub>3</sub>AC<sub>2</sub> phases. With the addition of Ti<sub>3</sub>GaC<sub>2</sub> and Ti<sub>3</sub>InC<sub>2</sub>, a sufficient number of MAX phases have now been synthesised, and subjected to accurate determination of structural parameters via Rietveld refinement, to allow for meaningful analysis of unit cell dimensions and bondlengths.

The *c* parameter of the unit cell is strongly affected by the ground state atomic radius of the *A*-element as displayed in Figure 5a). The refined values for both Ti<sub>3</sub>GaC<sub>2</sub> and Ti<sub>3</sub>InC<sub>2</sub> are shown as the, green diamond and green star respectively, and conform well to the overall trend. In order to give an indication of the variance of data, all the lattice parameter data for Ti<sub>3</sub>AlC<sub>2</sub> reported in the ICSD<sup>[32]</sup> are shown (at 1.43Å).

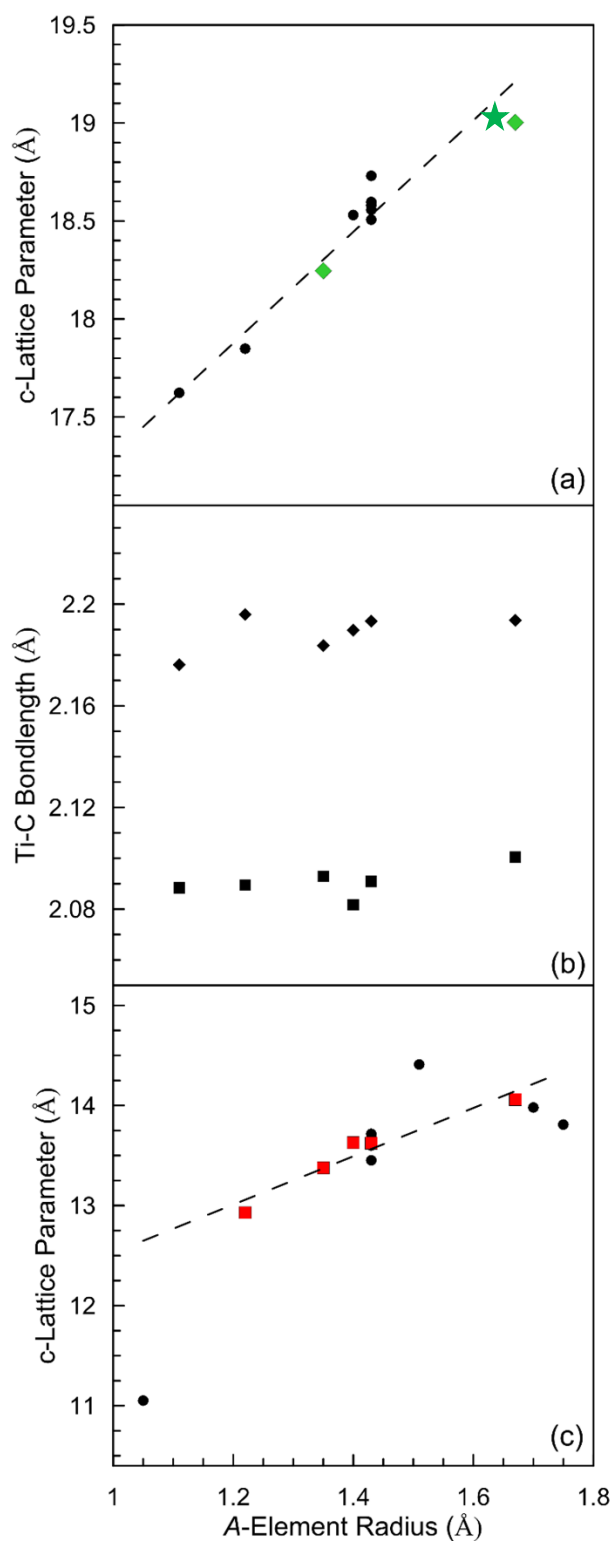


*Figure 5 a) The lattice parameter  $c$  plotted against A-element atomic radius in the 312 phases. The new MAX phases  $Ti_3GaC_2$  and  $Ti_3InC_2$  are represented by green diamonds and star respectively. b) TiC bondlengths in the  $Ti_3AC_2$  MAX phases; diamonds representing  $Ti_1$ -C and squares representing  $Ti_2$ -C. c) The  $c$  lattice parameter of the  $Ti_2AC$  MAX phases plotted against the atomic radius of the A-element. A-elements that have both a  $Ti_2AC$  and  $Ti_3AC_2$  phase are represented by red squares. The line of best fit through the red squares is primarily drawn as a guide for the eye.*

The MAX phase crystal structure can be regarded as having two regions, the *MX* octahedra, in this case TiC, and the *A*-element layers between them. Figure 5b) shows the interatomic distances within the TiC octahedra. In Figure 5, Ti<sub>1</sub> is the titanium atom bound between 2 carbons and Ti<sub>2</sub> is situated at the edge of the TiC blocks between a carbon and the *A*-element. These two distinct bondlengths were first discussed in relation to Ti<sub>3</sub>SiC<sub>2</sub><sup>[35]</sup> but can now be seen to be quite general and relatively constant.

With the exception of Ti<sub>3</sub>SiC<sub>2</sub>, all of the Ti<sub>3</sub>AC<sub>2</sub> MAX phases have a corresponding bulk Ti<sub>2</sub>AC phase. The *c* lattice parameter for all known Ti<sub>2</sub>AC MAX phases is shown in Figure 5c) plotted against the atomic radius of the *A*-element similar, to Figure 5a). Those systems which also form a Ti<sub>3</sub>AC<sub>2</sub> phase are highlighted with red squares. The main observation is that the *A*-elements that form both Ti<sub>2</sub>AC and Ti<sub>3</sub>AC<sub>2</sub> phases maintain their strong linear relationship between *A*-element atomic radius and the *c* lattice parameter which appears to be absent in some of the other systems.

#### 4. Discussion

In Table 1, a methodology for identifying potential higher order MAX phases from the chemical characteristics of known phases was developed and used to identify the Ti-Ga-C and Ti-In-C systems as candidates for having 312 MAX phases. Preliminary experiments using the stoichiometric mixtures in equations 1 and 3 clearly demonstrated that simple reactive sintering, not previously used to synthesize Ti<sub>2</sub>GaC or Ti<sub>2</sub>InC, readily produces bulk samples containing a majority of the target phases. A demonstration of stability does not equate with the ready production of phase-pure products. Commonly in MAX phase synthesis, *A*-element deficient phases form as an unwanted microstructural constituent. The *A*-element deficient phases can be the corresponding *MX* phase (e.g. TiC)

which is detrimental to properties. In rare cases another MAX phase is the A-element deficient product, for example when a 211 ceramic also includes the corresponding 312 phase. Pressureless reactive sintering is a synthesis method very susceptible to losses of the A-element due to uncontrolled vaporisation because it involves high temperatures, long sintering times and a relatively open system. Even elements with high boiling points such as Si, suffer losses. Reasons why a stable partial pressure is never attained include: continual depletion of the evaporated species due to adsorption or reaction with surroundings; as well as the flowing argon or vacuum environments that are commonly used to prevent oxidation. During this type of synthesis, common MAX phases such as Ti<sub>3</sub>AlC<sub>2</sub> or Ti<sub>3</sub>SiC<sub>2</sub> generally form with a fraction of TiC in the order of 10-15 wt%. Rates of conversion observed in this work (Table 2) were generally comparable to this and much better in the Ti-Ga-C system. The worst conversion to MAX phases here was 76%, albeit with only 37% of the target phase in the Ti<sub>3</sub>InC<sub>2</sub> case.

Samples made according to Eq. 1 produced a large amount of the desired phase Ti<sub>2</sub>GaC, and a smaller amount of the A-element deficient phase (in this context) Ti<sub>3</sub>GaC<sub>2</sub>. This is particularly interesting as a secondary phase for two reasons. Firstly it proved that Ti<sub>3</sub>GaC<sub>2</sub> is stable and could be formed under the conditions used. Secondly Ti<sub>3</sub>GaC<sub>2</sub> is a MAX phase which has very similar properties to the target Ti<sub>2</sub>GaC and will not result in the same level of detriment to physical properties that TiC does. The production of TiC-free Ti-A-C MAX phase samples is an area of intense study and, although not the direct focus of this work, makes Ti<sub>2</sub>GaC a strong candidate for further investigation. The morphology revealed by SEM indicated that the Ti<sub>2</sub>GaC comprised mainly cuboid grains. Cuboid grains are uncommon in MAX phases, typically crystals grow much faster in the *a-b* plane than along the *c* direction, resulting in plate-like morphology with a high aspect

ratio. The cuboid morphology may also make this material less susceptible to the extreme texturing observed in hot-pressed Ti<sub>3</sub>AlC<sub>2</sub> and Ti<sub>3</sub>SiC<sub>2</sub>.<sup>[36]</sup>

Following the success in the Ti<sub>2</sub>GaC system, the same method was also able to synthesise bulk samples of the Ti<sub>3</sub>GaC<sub>2</sub> for the first time (Figure 1, Table 2) confirming the expectations derived from Table 1. This first bulk synthesis of Ti<sub>3</sub>GaC<sub>2</sub> can be considered an unqualified success. XRD phase analysis showed that the samples had experienced a high conversion rate yielding 96% by mass of Ti<sub>3</sub>GaC<sub>2</sub> and only 4% of TiC, the A-element deficient phase. This low level of TiC is attributed to the lower synthesis temperature, 1300°C compared with 1400°C – 1600°C for Ti<sub>3</sub>AlC<sub>2</sub> or Ti<sub>3</sub>SiC<sub>2</sub><sup>[1, 4]</sup>. Conversion of over 95 wt% of the reactants into the desired product via a simple reactive sintering technique strongly suggests that not only is Ti<sub>3</sub>GaC<sub>2</sub> a stable MAX phase, it can be made in the bulk and the method may be suitable for scale up, allowing bulk property testing and engineering applications.

The bulk synthesis of Ti<sub>2</sub>InC was also successful. The conversion rate into the desired Ti<sub>2</sub>InC was approximately 85 wt% in samples made according to Eq. 3. This may not be the highest conversion into Ti<sub>2</sub>InC yet observed<sup>[37]</sup> but it is nonetheless a high yield for un-optimised pressureless reactive sintering. The presence of residual In implies two things. Firstly, the lower sintering temperatures of the In and Ga systems result in reduced A-element losses. Secondly, the presence of both TiC and In in the reactants implies an incomplete reaction. It is likely that the TiC<sub>x</sub> imbedded in the In may have reached a stoichiometric amount of carbon (x = 1) early in the process, which leads to stagnation of the reaction even in the presence of In. Rietveld refinements suggested the TiC was not

substoichiometric, supporting this theory but this cannot be confirmed without *in-situ* diffraction experiments.

Samples made according to Eq. 4 had the lowest conversion ratio to the desired phase but converted into the most interesting products. The analysis shown in Table 2 indicate 39 wt% of the previously undiscovered phase Ti<sub>3</sub>InC<sub>2</sub>. The sample also contained three other phases including 37 wt% of the Ti<sub>2</sub>InC MAX phase giving a total MAX phase content of 76%. The remainder was TiC and metallic In, again implying that the reaction may not have proceeded to completion. In an effort to increase conversion, sintering times were varied, sintering temperature was varied and crushing repressing and refiring pellets was also tried. No improvement in conversion was achieved. As with Ti<sub>2</sub>InC, it may be that any TiC<sub>x</sub> that attains the fully stoichiometric composition is unable to react with free In to form a MAX phase at this temperature.

Some regions were found in the Ti-In-C system where the morphology was similar in samples mixed according to both equation 3 and equation 4 as visible in Figures 4a) and 4c). Other regions of the samples were quite distinct such as Figure 4b) which shows a TiC-In mixture. In addition, MAX phase regions with a distinct morphology from that of Figure 4c) were found in samples prepared according to Equation 4 and one is illustrated in Figure 4d). Plate like crystals can be seen on 2 scales, Figure 4c) showing large crystals and Figure 4d) showing much smaller crystals. It is possible that the different sized grains belong to the two different MAX phases. The similarity between Figure 4a) and Figure 4c) strongly suggests that the large crystals in both systems are Ti<sub>2</sub>InC and thus the smaller crystals are Ti<sub>3</sub>InC<sub>2</sub>. Interaction volumes in the electron microscope were too

large and the variation in elemental ratios too small to use EDS to conclusively determine this.

Additional experimentation was conducted to determine the effects of the sintering conditions in both the Ti-Ga-C and Ti-In-C systems, time and temperature being the tested variables. Both systems behaved in a similar manner. Lower sintering times and temperatures (e.g. 3h hold and 1250°C) resulted in higher amounts of TiC and unreacted A-element in the products, which was interpreted as incomplete reaction. Higher temperatures were more interesting, 1350°C resulted in the formation of more of the 211 phase and TiC in the samples at the expense of the 312 phase. This decomposition of 312 MAX phases at high temperature into the 211 and TiC has been reported in other MAX phase systems<sup>[38]</sup>. Sintering temperature of 1400°C and over caused even the 211 phase to decompose leaving mainly TiC in its place. Clearly loss of the A-element was significant at these temperatures.

In addition to the implied stability due to successful synthesis, DFT calculations (Table 5) showed that Ti<sub>3</sub>GaC<sub>2</sub> is stable relative to mixtures of TiC and the 211 or 413 MAX phases in the same system. The DFT calculations for Ti<sub>3</sub>InC<sub>2</sub> showed one unusual aspect. The compound was found to be relatively stable, with a similar energy difference to that of Ti<sub>3</sub>GaC<sub>2</sub> for the scenario of degradation into the corresponding 211 compound and TiC. However, this was only the case when the relaxed (theoretical) lattice parameters were used. Although relaxation during DFT always changes the lattice parameters slightly, in the Ti<sub>3</sub>InC<sub>2</sub> system the relaxation was far greater than usual. The increased relaxation may indicate that the structure is non ideal and may be suffering from slightly non-stoichiometric composition or less likely some solid state substitution. Further, when

the unrelaxed experimental lattice parameters from Rietveld refinements of the XRD patterns (Tables 3 and 4), were imposed on the DFT calculation, Ti<sub>3</sub>InC<sub>2</sub> was no longer the most energetically stable state, instead the competing two-phase mixture of Ti<sub>2</sub>InC and TiC was found to have significantly lower energy (large positive energy difference in column 3 of Table 5). This indicates that although the bulk Ti<sub>3</sub>InC<sub>2</sub> phase has been proven to exist experimentally, its stability may be marginal, explaining why it had not been discovered before and had a lower phase proportion in the synthesis here.

Concerning Figure 5, with the inclusion of the Ti<sub>3</sub>GaC<sub>2</sub> and Ti<sub>3</sub>InC<sub>2</sub> phases, it seems reasonable to say that a correlation exists between the *211* phases which conform to the straight line relationship on the figure and the successful synthesis of the corresponding *312* phases. Although the origins of the correlation are not yet fully understood, taken in conjunction with Figure 5, these results suggest an important role for structural factors in determining stability.

## 5. Conclusions

Analysis of the systematic features of MAX phase systems highlighted the possibility of two new *312* MAX phases in the Ti-Ga-C and Ti-In-C systems. Both were subsequently synthesised. Their ability to be synthesised by simple pressureless reactive sintering at 1300°C, as well as energies calculated by DFT being lower than the energy of competing combinations of phases, strongly suggest that both are stable phases; Ti<sub>3</sub>InC<sub>2</sub> less so than Ti<sub>3</sub>GaC<sub>2</sub>. The related *211* phases in the same systems were also able to be synthesised in the bulk by pressureless reactive sintering.

## References

1. Barsoum, M.W., *The Mn<sub>n+1</sub>AX<sub>n</sub> Phases and their Properties*, in *Ceramics Science and Technology: Materials and Properties*, R. Riedel and I.-W. Chen, Editors. 2010, John Wiley and Sons. p. 299-347.
2. Barsoum, M.W. and T. El-Raghy, *Synthesis and Characterisation of a Remarkable Ceramic: Ti<sub>3</sub>SiC<sub>2</sub>*. Journal American Ceramic Society, 1996. **79**: p. 1953-1956.
3. Eklund, P., et al., *The Mn + 1AXn phases: Materials science and thin-film processing*. Thin Film Solids, 2010. **518**(8): p. 1851-1878.
4. Li, J.-F., F. Sato, and R. Watanabe, *Synthesis of Ti<sub>3</sub>SiC<sub>2</sub> polycrystals by hot-isostatic pressing of the elemental powders*. Journal of Materials Science Letters, 1999. **18**: p. 1595-1597.
5. Riley, D.P. and E.K. Kisi, *Self-Propagating High-Tempertue Synthesis of Ti<sub>3</sub>SiC<sub>2</sub>: 1, Ultra High-Speed Neutron Diffraction Study of the Reaction Mechinism*. Journal American Ceramic Society, 2002. **85**(10): p. 2417-2424.
6. Cuskelly, D.T., E.H. Kisi, and H. Sugo, *MAX phase - alumina composites via exchange reaction in the Mn+1Al/Cn systems (M= Ti, V, Cr, Nb, or Ta)*. Journal of Solid State Chemistry, 2015. **223**: p. 150-157.
7. Zhang, J., et al., *Rapid fabrication of Ti<sub>3</sub>SiC<sub>2</sub>-SiC nanocomposite using the spark plasma sintering-reactive synthesis (SPS-RS) method*. Scripta Materialia, 2007. **56**(3): p. 241-244.
8. Chen, J., J. Li, and Y. Zhou, *In-situ Synthesis of Ti<sub>3</sub>AlC<sub>2</sub>/TiC-Al<sub>2</sub>O<sub>3</sub> Composite from TiO<sub>2</sub>-Al-C System*. Journal of Materials Science and Technology, 2005. **22**(4): p. 455-458.
9. Yeh, C.L., R.F. Li, and Y.G. Shen, *Formation of Ti<sub>3</sub>SiC<sub>2</sub>-Al<sub>2</sub>O<sub>3</sub> in situ composites by SHS involving thermite reactions*. Journal of Alloys and Compounds, 2009. **478**(1-2): p. 699-704.
10. Cetinkaya, C. and S. Eroglu, *Synthesis and reaction mechinism of Ti<sub>3</sub>SiC<sub>2</sub> ternary compound by carbothermal reduction of TiO<sub>2</sub> and SiO<sub>2</sub> powder mixtures*. Ceramics International, 2012. **38**: p. 6445-6453.
11. Hill, R.J. and C.J. Howard, *Quantitative phase analysis from neutron powder diffraction data using the Rietveld method*. Journal of Applied Crystallography, 1987. **20**(6): p. 467-474.
12. Jeitschko, W., H. Nowotny, and F. Benesovsky, *Die H-Phasen Ti<sub>2</sub>InC, Zr<sub>2</sub>InC, Hf<sub>2</sub>InC und Ti<sub>2</sub>GeC*. Monatshefte für Chemie und verwandte Teile anderer Wissenschaften 1963. **94**(6): p. 1201-1205.
13. Barsoum, M.W. and M. Radovic, *Elastic and Mechanical Properties of the MAX Phases*. Annual Review of Materials Research, 2011. **41**: p. 195-227.
14. Hfgberga, H., et al., *Growth and characterization of MAX-phase thin films*. Surface & Coatings Technology, 2005. **193**: p. 6-10.
15. Lin, T.-C. and M.-H. Hon, *Synthesis and microstructure of the Ti<sub>3</sub>SiC<sub>2</sub> in SiC matrix grown by chemical vapor deposition*. Ceramics International, 2008. **34**(3): p. 631-638.
16. Sun, Z., H. Hashimoto, and W. Tian, *Synthesis of the MAX Phases by Pulse Discharge Sintering*. International Journal of Applied Ceramic Technology, 2010. **7**: p. 704-718.
17. Zang, Z.F., et al., *Application of pulse discharge sintering (PDS) technique to rapid synthesis of Ti<sub>3</sub>SiC<sub>2</sub> from Ti/Si/C powders*. Journal of the European Ceramic Society, 2002. **22**(16): p. 2957-2961.
18. Kotzott, D., *Synthese und Charakterisierung von neuen und bekannten Hartstoffen und die technische Relevanz von Härtewerten* in Faculty of Chemistry and Pharmacy. 2009, THE ALBERT - LOUIS - UNIVERSITY.
19. Keast, V.J., S. Harris, and D.K. Smith, *Prediction of the stability of the Mn+1AXn phases from first principles*. Physical Reviews B 2009. **80**: p. 214113.

20. Viala, J.C., et al., *Phase equilibria at 1000C in the Al-C-Si-Ti quaternary system: An experimental approach*. Materials science and engineering, 1997. **A229**: p. 95-113.
21. Goesmann, F., R. Wenzel, and R. Schmid-Fetzer, *Perperation of Ti<sub>3</sub>SiC<sub>2</sub> by Electron-Beam-Ignited Solid-State Reaction*. Journal American Ceramic Society, 1998. **81**(11): p. 3025-3028.
22. M., D., B. Alling, and J. Rošen, *Stability trends on M A X phases from first principles*. Physical Reviews B 2010. **81**: p. 220102.
23. Eklund, P., et al., *Discovery of the ternary nanolaminated compound Nb<sub>2</sub>GeC by a systematic theoretical-experimental approach*. Physical Review Letters, 2012. **109**(3): p. 035502.
24. Fang, C.M., R. Ahuja, and O. Eriksson, *Perdiction of MAX phases VN=1SiCn (N= 1,2), from first principles theory*. Journal of Applied Physics, 2007. **101**: p. 013511.
25. Grechnev, A., et al., *Layered compound Nb<sub>3</sub>SiC<sub>2</sub> predicted from first-principles theory*. Applied Physics Letters, 2004. **85**: p. 3071-3073.
26. Palmquist, J.-P., et al., *Mn+1ACn phases in the Ti-Si-C system studied by thin film synthesis and ab initio calculations*. Physical Reviews B 2004. **70**: p. 165401.
27. Wang, J., Y. Zhou, and H. C, *Phase stability, electronic structure and mechanical properties of tenary-layered carbide Nb<sub>4</sub>AlC<sub>3</sub>: An ab initio study*. Acta Materialia 2008. **56**: p. 1511-1518.
28. *Advances in Science and Technology on M<sub>n+1</sub>AX<sub>n</sub> Phases*, ed. I.M. Low. 2012, Woodhead publishing, Sawston, Cambridge: Woodhead Publishing.
29. Thore, A., et al., *Temperature dependent phase stability of nanolaminated ternaries from first-principles calculations*. Computational Materials Science 2014. **91**: p. 251-257.
30. Etzkorn, J., et al., *Ti<sub>2</sub>GaC, Ti<sub>4</sub>GaC<sub>3</sub> and Cr<sub>2</sub>GaC- Synthesis, crystal growth and structure analysis of the Ga-containing MAX phases M<sub>n=1</sub>GaC<sub>n</sub> with M= Ti, Cr and n= 1, 3*. Journal of Solid State Chemistry, 2009. **182**(5): p. 995-1002.
31. Bruesewilz, C., et al., *Single Crystal Microcompression tests of the MAX phases Ti<sub>2</sub>InC and Ti<sub>4</sub>AlN<sub>3</sub>*. Scripta Materialia, 2013. **69**(4): p. 303-306.
32. Moran, M. and H. Shapiro, *Fundamentals of engineering thermodynamics*. 1993, USA: Wiley and Sons.
33. Ganguly, A., M.W. Barsoum, and J. Schuster, *The 1300°C Isothermal Section in the Ti-In-C Ternary Phase Diagram*. Journal American Ceramic Society, 2005. **88**: p. 1290-1296.
34. Perdew, J.P., S. Burke, and M. Ernzerhof, *Generalized Gradient Approximation Made Simple*. Physical Review Letters, 1996. **77**: p. 3865-3868.
35. Kisi, E.H., et al., *Inter-Conversion of M<sub>n+1</sub>AX<sub>n</sub> Phases in the Ti-Al-C system*. Journal American Ceramic Society, 2007. **90**(6): p. 1912-1916.
36. Zang, J.F., E.H. Kisi, and O. Kirstan, *Quantitative Neutron Diffraction Texture Measurement Applied to  $\alpha$ -phase Alumina and Ti<sub>3</sub>AlC<sub>2</sub>*. Journal of Applied Crystallography, 2011. **44**: p. 1062-1070.
37. Barsoum, M.W., et al., *Fabrication and electrical and thermal properties of Ti<sub>2</sub>InC, Hf<sub>2</sub>InC and (Ti,Hf)2InC*. Journal of Alloys and Compounds, 2002. **340**: p. 173-179.
38. Pang, W.K., et al., *Comparison of thermal stability in MAX 211 and 312 phases*. Journal of Physics, 2010. **251**(1): p. 012025.

## 9. Publication 5: Miscibility gap alloys with inverse microstructures and high thermal conductivity for high energy density thermal storage applications

Heber Sugo, Erich Kisi\*, Dylan Cuskelly

School of Engineering, the University of Newcastle, Callaghan NSW 2308 Australia

*Applied Thermal Engineering* DOI:10.1016/j.applthermaleng.2012.11.029

### Abstract

New high energy-density thermal storage materials are proposed which use miscibility gap binary alloy systems to operate through the latent heat of fusion of one component dispersed in a thermodynamically stable matrix. Using trial systems Al-Sn and Fe-Cu, we demonstrate the development of the required inverse microstructure (low melting point phase embedded in high melting point matrix) and excellent thermal storage potential. Several other candidate systems are discussed. It is argued that such systems offer enhancement over conventional phase change thermal storage by using high thermal conductivity microstructures (50-400 W/m.K); minimum volume of storage systems due to high energy density latent heat of fusion materials (0.2-2.3 MJ/L); and technical utility through adaptability to a great variety of end uses. Low (<300°C), mid (300-400°C) and high (600-1400°C) temperature options exist for applications ranging from space heating and process drying to concentrated solar thermal energy conversion and waste heat recovery.

## 1. Introduction

The global momentum to develop renewable sources of energy that do not overly disrupt the natural environment has been building for some decades. The IEA World Energy Outlook 2009 [1] indicates that a speedy transition is required to stabilise the concentration of greenhouse gases at 450 ppm. Delays in the implementation of renewable and carbon neutral energy sources not only narrows the window for action but also increases the cost of transforming the energy sector by US\$ 500 billion per year [1]. With the exception of geothermal and hydroelectricity all other forms of renewable energy suffer from intermittency. Diurnal cycle and weather excursions directly affect solar generation but wind and wave sources are also intermittent.

Energy storage by chemical, electrochemical or mechanical means are all subject to conversion losses in the storage-recovery cycle additional to those associated with eventual energy utilisation. For thermal sources of energy, direct Thermal Energy Storage (TES) can be made almost lossless, suffering only environmental losses through the insulation envelope. For example, the sensible heat based Concentrated Solar-Thermal plants which use thousands of tonnes of molten  $\text{KNO}_3/\text{NaNO}_3$  salt for sensible heat storage, through careful attention to insulation, can return in the order of 99% of the heat stored (known as the return efficiency) [2].

The application of efficient thermal energy storage (TES) systems to capture heat from renewable sources like solar or waste heat from existing industries can offer significant savings and reduction in the emission of greenhouse gases. It is estimated that in 2008 the USA consumed  $33.5\text{EJ}$  ( $10^{18}\text{J}$ ) as *heat* for applications at temperatures below  $300^\circ\text{C}$  [3]. Approximately 50% was consumed by residential space heating applications with the

Publication 5: Miscibility gap alloys with inverse microstructures and high thermal conductivity for high energy density thermal storage applications

remainder being utilized by industry for low-temperature steam generation and process drying. Concentrating solar thermal (CST) technologies such as trough collectors and tower receivers are well advanced and could potentially replace combustion of fossil fuels for these applications provided efficient TES systems are developed to overcome intermittency of supply due to the daily solar cycle and weather excursions. If effective thermal storage solutions are developed, the range of applications is not limited to renewable energy sources. The technology can also be used for load shifting applications and thermal inertia/overload protection in electric motors or even micro-electronics<sup>[4]</sup>.

Various thermal storage options have been previously discussed in the literature e.g.<sup>[5]</sup> and include direct storage as sensible heat due to temperature rise or latent heat due to a phase change. Over the last 20 years there has been extensive research into both forms of TES which has resulted in widespread publication of thermophysical data for organic materials, inorganic salts and some metallic systems<sup>[5-8]</sup>. It is clear that the phase change systems exhibit the highest storage density. The key design parameters for deployment of TES are based on the energy density *per unit volume*, time delay between recharge-discharge and costs. Hence research work has also extended to the development of mathematical models for predicting input and extraction rates of energy from various systems<sup>[4]</sup>. If we only consider high energy density Phase Change Material (PCM) based TES, the state of the art technology is considered to be NaNO<sub>3</sub>/KNO<sub>3</sub> eutectic salts or paraffin products combined with heat transfer enhancement technologies. These are necessary to improve the poor thermal conductivity of organic/inorganic salts which are in the order of 0.22-0.75 W/m/K respectively<sup>[4, 9]</sup>.

Numerous heat transfer enhancement techniques have been developed. For paraffin based systems; metallic particulates, foams and fins or expanded graphite particulates are used [4]. For NaNO<sub>3</sub>/KNO<sub>3</sub> eutectics, the use of expanded graphite particulates, fibres or fins have been reported [6]. Design of TES systems vary but generally resemble conventional finned-coil heat exchangers circulating either a heat transfer fluid or steam during the charge/discharge cycle [10].

Metallic systems have also been employed as PCM thermal storage systems. Several candidates were reported by Sharma [5] and Kenisarin [6]. The authors highlight the suitability of metals as PCM due to their high temperature phase change, good thermal stability and reliability, and large heats of fusion on a mass basis. Detailed data of the performance over 1000 heating/cooling cycles of an Al-Mg-Zn eutectic alloy was described by Sun et.al. [7]. The overall performance was very promising, however a slight reduction in phase transition temperature of 3-5.3°C after 1000 cycles with an accompanying reduction of 11.1% in the latent heat of fusion was reported. Microstructural investigations indicated a change in the morphology of the eutectic phase with some additional microconstituents being formed, possibly as a result of the interaction with the stainless steel containment vessel. Maruoka et.al. [11] carried out an energy density and cost benefit analysis for potential PCM aimed at waste heat recovery between 927 and 1527°C and found copper to be an ideal candidate. Copper balls were initially coated with nickel to act as an encapsulant and catalyst for hydrogen reforming. Failure of the nickel coating was observed during experimentation and to resolve the problem a layer of carbon or ruthenium was introduced at the copper/nickel interface. Whilst not directly identified by Maruoka et.al. the failure mechanism of the nickel coating can be attributed to the complete solid-solubility of nickel in copper. The carbon

or ruthenium layer acted as a diffusion barrier to hinder the solution of these completely miscible metals.

In this paper we indicate how thermodynamically stable miscibility gap binary metallic systems that operate through the latent heat of fusion of the dispersed component delivered through a high thermal conductivity matrix phase have thermal conductivity, energy density and temperature tunability advantages over both sensible heat and conventional phase change materials.

## 2. Conceptual development

When two metals are mixed in a fixed ratio in the liquid state and allowed to solidify, broadly speaking they may form a solid solution by mixing randomly, an intermetallic compound by mixing in an ordered structure or, if are immiscible, they de-mix and solidify as a mixture of two distinct solid phases. The overarching idea for this research is that high temperature thermal storage is most efficient and compact using thermodynamically stable two phase mixtures in which the active phase that undergoes melting and solidification during charge-discharge cycle, is present as discrete particles fully enclosed within a dense, continuous, thermally conductive matrix. We also postulate that the best way to construct such a microstructure is to exploit miscibility gaps in the phase diagrams of some alloys. The inherent immiscibility of the dispersed phase coupled with the high thermal conductivity metal matrix overcome the shortcomings of many current TES systems. By constructing an *inverse* microstructure in which the active (melting) phase is present as micro-particles, during discharge, these will release intense bursts of latent heat locally during solidification which is then conducted away by the

surrounding matrix phase (and *vv* during charging). The conceptual advantages of such a material include:

- i) High energy density per unit volume by capitalising on the high latent heat of fusion per unit volume of metals.
- ii) A range of melting temperatures for active phases are available and therefore the materials may be individually matched to useful operating temperatures: 250°C for space heating, 600°C for steam turbine electricity generation and 1400°C for high temperature industrial processes.
- iii) Latent heat is delivered (or accepted) over a narrow temperature range allowing more precise control of process parameters and, in terms of steam generation, would allow for easier matching of turbine-generator.
- iv) Since the heat is delivered and retrieved from the active phase by conduction alone, there is no need to transport the molten phase around the system and very high heat transfer rates are possible.
- v) No special containment is necessary as the matrix phase remains solid at all times and encapsulates the active phase.
- vi) Chemical reactions between component materials are avoided as the two materials are thermodynamically stable and immiscible.

These characteristics avoid the major difficulties with many PCM systems published to date including corrosion and degradation of metallic components in salt-based phase change materials, low heat transfer rates and low energy density.

In Table 1 a few of the candidate systems are listed. The key variables are firstly, the melting temperature of the active phase which determines the charge-discharge

Publication 5: Miscibility gap alloys with inverse microstructures and high thermal conductivity for high energy density thermal storage applications

temperature and hence the suitability of a material for a given application; and secondly, the energy density in MJ/litre which determines the overall size of thermal storage infrastructure. In order to allow comparison with two state of the art phase change systems, data for an organic PCM Paraffin (PCM-1) and a molten salt PCM  $\text{KNO}_3\text{-NaNO}_3$  eutectic (PCM-2) are given at the top of the table. Similarly, a comparison with sensible heat storage is enabled by the sixth column which indicates the temperature rise in each system to store, as sensible heat, an equivalent amount of energy to the latent heat. It may be readily seen from the table that the two trial systems chosen in this study, Al-Sn and Fe-Cu, have significantly greater energy density and perhaps more significantly, thermal conductivity approximately two orders of magnitude greater than conventional PCMs. In addition to these qualities, the two systems have been chosen as they have useful operating temperatures for space-heating applications (Al-Sn) and steam turbine electricity generation (Fe-Cu), are abundant, have established refinement and processing technologies, and are readily recycled.

*Table 1 - Candidate thermal storage systems compared with state of the art PCM (rows 1,2)*

| System           | Fusible Phase                                       |                    |  |   |   | Thermal Conductivity of Matrix<br>$\left( \frac{W}{mK} \right)$ |
|------------------|---|--------------------|--|---|---|---|
|                  | Phase Name  | Melting Point (°C) | Heat of Fusion<br>$\left( \frac{kJ}{kg} \right)$ | Energy Density<br>$\left( \frac{MJ}{L} \right)$ | Equivalent Temperature Range of Sensible Heat |   |
| PCM-1<br>Organic | Paraffin C <sub>20-33</sub><br>[5]                  | 50                 | 189  | 0.17  | 76  | <1  |
| PCM-2<br>Salt    | KNO <sub>3</sub> -NaNO <sub>3</sub><br>eutectic [9] | 221                | 100  | 0.204   | 70  | <1  |
|                  |   |                    |  |   |   |   |
| Al-Sn            | Sn  | 232                | 59   | 0.43  | 257   | 237   |
| Al-Bi            | Bi  | 271                | 52   | 0.51  | 433   | 237   |
|                  |   |                    |  |   |   |   |
| Fe-Mg            | Mg  | 650                | 346  | 0.60  | 590   | 80  |
| Fe-Cu            | Cu  | 1085               | 205  | 1.84  | 526   | 80  |
|                  |   |                    |  |   |   |   |
| SiC-Si           | Si  | 1414               | 1926   | 4.49  | 2713  | 200   |

Immiscible binary alloy systems sourced from <sup>[12]</sup>, enthalpy data from <sup>[13]</sup>.

In order to realise the potential shown by these materials, the active thermal storage phase needs to be fully encapsulated within a dense, highly conductive matrix phase. This microstructure is the opposite of that expected for a two phase alloy solidifying from the melt and therefore, the means by which this microstructure can be formed is a central problem addressed in the experimental component of this paper. For example, referring to Figure 1, on cooling a Sn-Al alloy containing 50 wt% Sn from 600°C to 230°C,

Publication 5: Miscibility gap alloys with inverse microstructures and high thermal conductivity for high energy density thermal storage applications

relatively pure solid aluminum and a tin-rich liquid will co-exist. Natural cooling below 228°C produces a continuous Sn-rich matrix as shown by the mid-gray phase in Figure 2, with encapsulated Al particles (the dark phase). We desire the *inverse* microstructure comprising a continuous, highly conductive, Al matrix with Sn-rich particles fully encapsulated within it. How then do we obtain such a microstructure? To do this, two methods from standard metallurgical practice are available. In the first, which is applicable to systems with slow diffusion kinetics for de-mixing, precipitation of the low melting temperature phase may be suppressed by rapid cooling to form an unstable solid solution (e.g. if our 50% Sn alloy could be quenched to room temperature at a sufficient rate). The active phase may then be formed by solid-state precipitation and growth upon re-heating the material within the range below the melting temperature of the active phase (e.g. below 228°C in our example). For systems with rapid diffusion kinetics, the powder metallurgy techniques of pressing and sintering, routinely used in industry for producing a range of solid engineering components, are applicable. In this process solid state diffusion causes the matrix material to become fused into a continuous body, completely encapsulating the active phase.

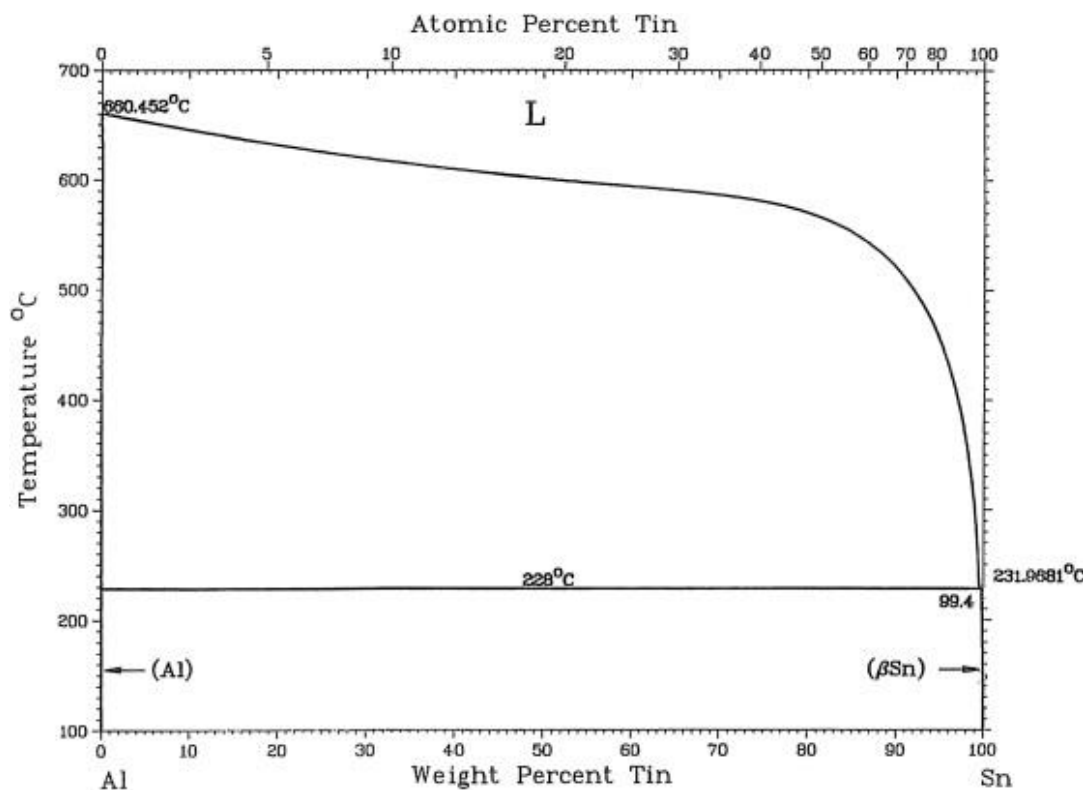


Figure 1 - Al-Sn phase diagram<sup>[11]</sup> illustrating the immiscibility of molten tin and solid aluminium.

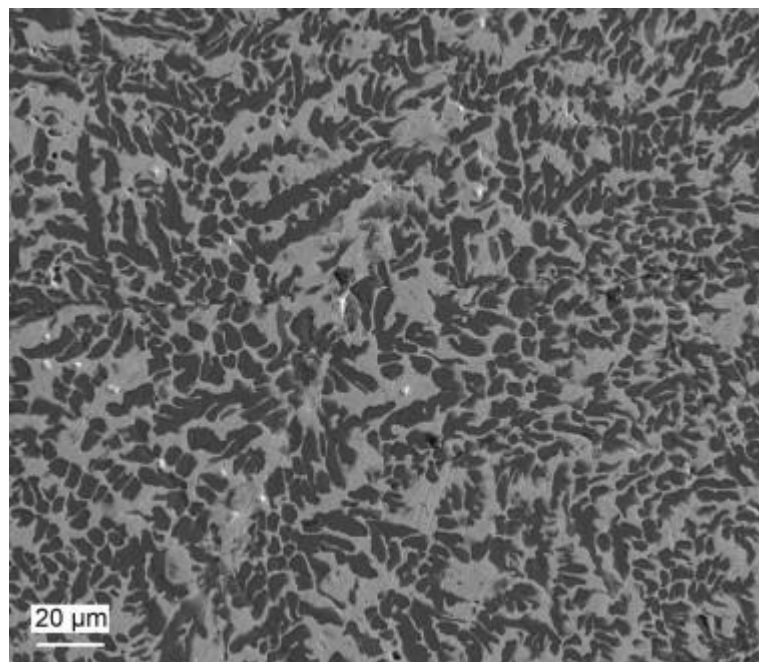


Figure 2 – Scanning electron micrograph of an Al-Sn alloy cast and allowed to air cool. The dark grey phase is Al and the mid-grey phase Sn.

### 3. Experimental methods

Two prototype thermal storage alloys were produced using the powder starting materials; Sn (Towson & Mercer Distributors, London, <200 mesh), Al (Alloys International, Australasia, <75 µm), Fe (International Nickel Company, London) and Cu spheres (MicroMet, GmbH, <80 µm). Samples comprising 35 vol% Sn in Al and 35 vol% Cu in Fe were made by simple powder metallurgy in the form of mixing, uniaxial pressing in a 16mm die at 300MPa and subsequent sintering at 500°C (Sn-Al) or 1000°C (Cu-Fe) in an inert argon atmosphere. Sintered samples were dressed and polished for Metallurgical examination using optical and Scanning Electron Microscopy (SEM). The phase identity was established and contaminant phases searched for using X-ray diffraction (XRD). Samples were then studied using a simple Differential Thermal Analysis (DTA) arrangement and the raw signal Fourier filtered to remove high frequency noise. Rather than the tiny samples typically used for such measurements, DTA in this instance was based around the entire 30g samples in order to give a more realistic result in the context of larger thermal storage applications. The pure matrix phase, Al was used as the reference material in the Al-Sn case and a low carbon steel (>99% Fe) in the Fe-Cu case.

#### 4. Results and discussion

##### 4.1 Microstructural and XRD Analysis

Figure 3 shows the microstructure of an Al-Sn prototype thermal storage material made in this way. Note the complete isolation of the Sn regions (pale phase) from each other. This has two major consequences; it prevents draining and loss of the molten phase at the elevated temperature and it ensures continuous heat transfer paths from the phase undergoing melting (solidification) to the exterior during charging (discharging). The distribution of Sn in Figure 3 is not uniform and will require processing adjustments if further testing demonstrates a link between Sn distribution and performance. Note also

that, since the sintering was pressureless, a small fraction of unfilled cavities remain in the material - again giving scope for improvements in fabrication. The corresponding X-ray Diffraction pattern is shown in Figure 4. It is essentially free from peaks associated with contaminants or intermetallic compounds, containing very strong diffraction peaks from the Al and Sn phases.

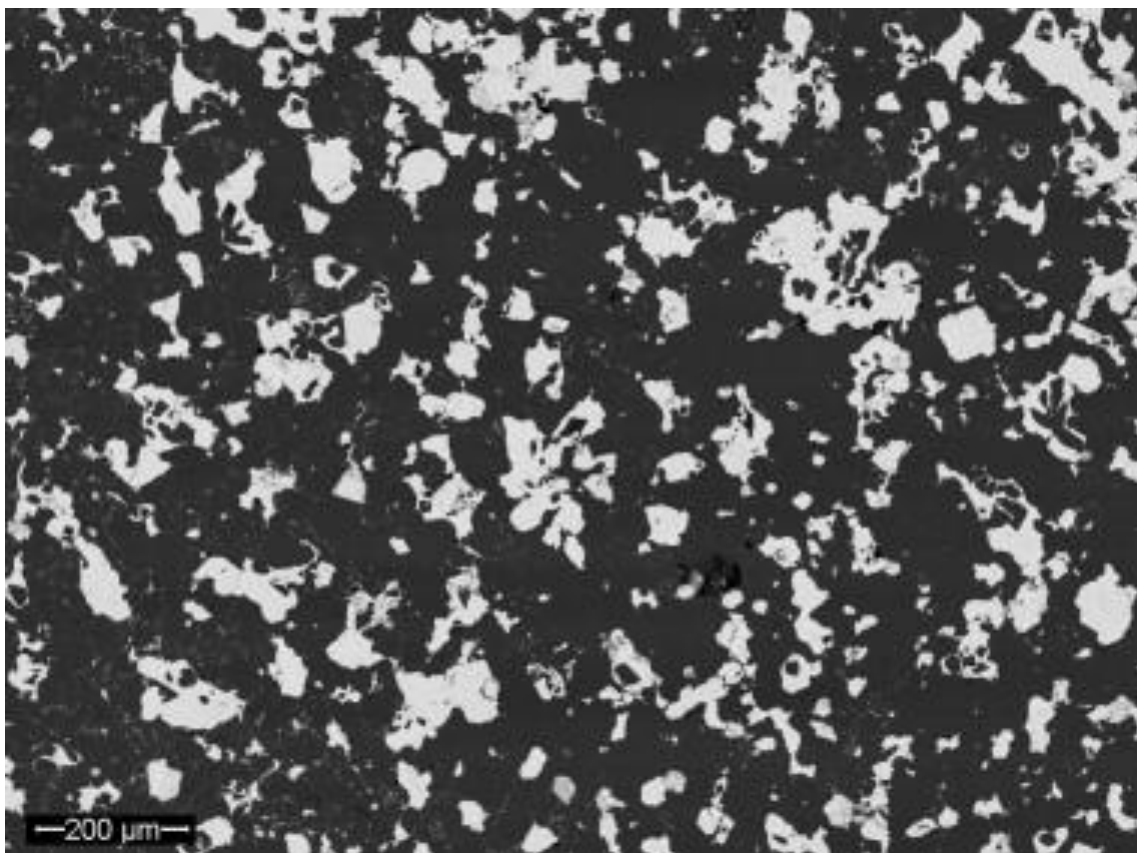


*Figure 3 – Secondary electron image of an Al- 35 vol %Sn thermal storage alloy demonstrating the inverse microstructure. The dark grey phase is Al and the brighter phase Sn, now reversed in distribution with respect to Figure 2.*

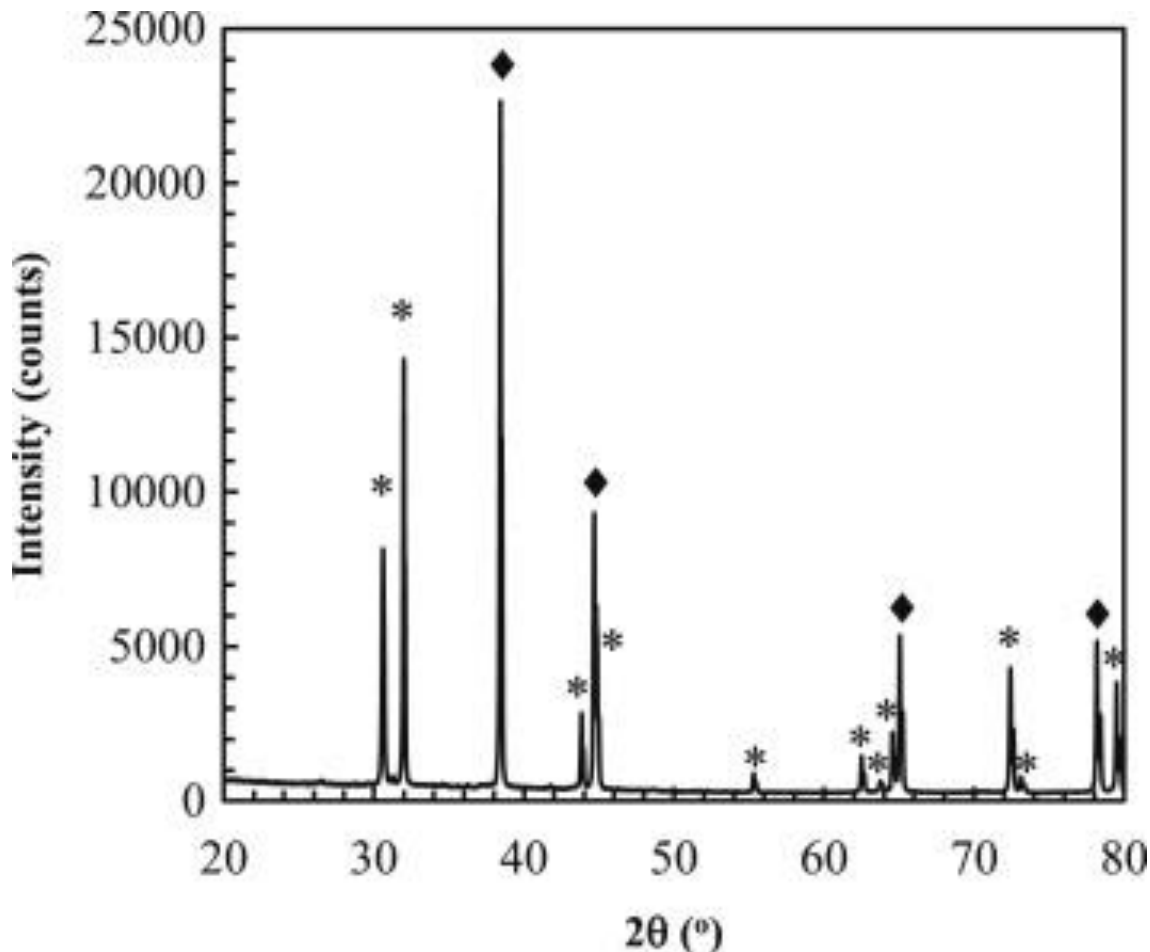
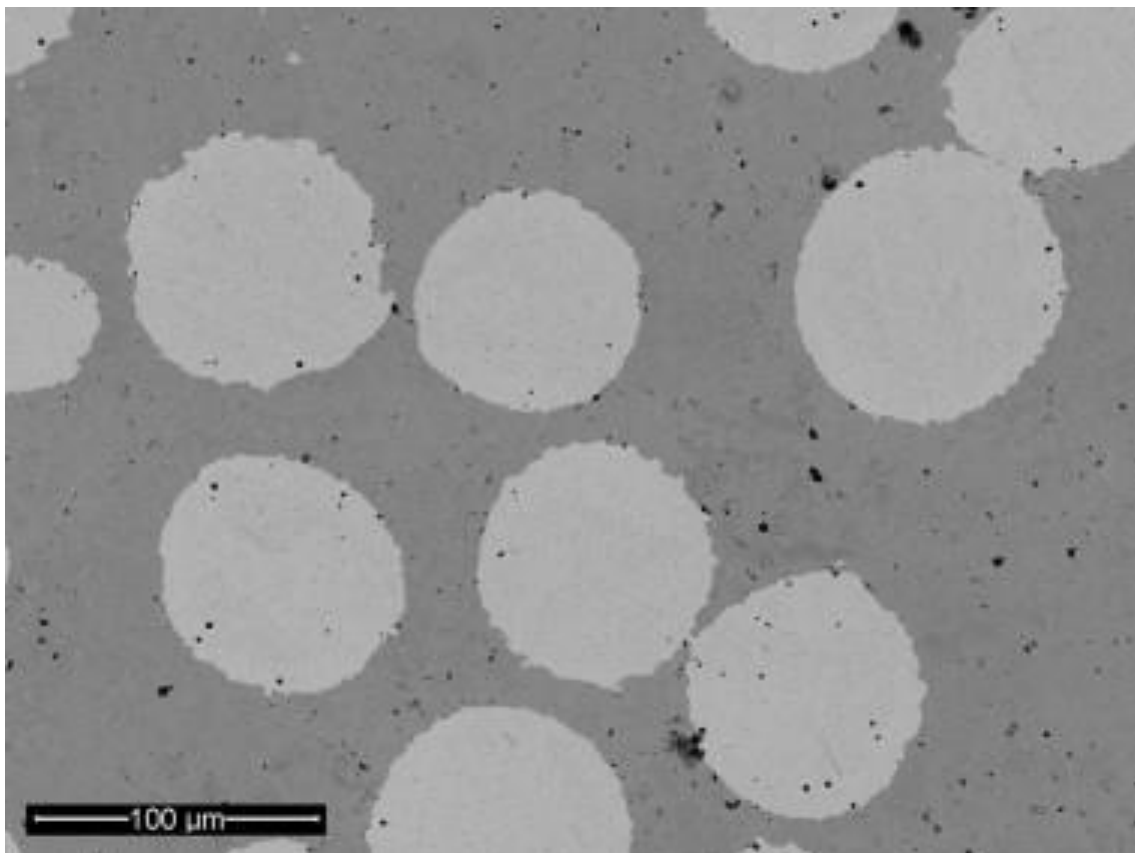


Figure 4 - Cu K $\alpha$  XRD pattern of the Al-Sn alloy demonstrating only Al and Sn as major phases. Al peaks are marked with a diamond (◆) and Sn peaks are marked with an asterisk (\*).

The microstructure of the Fe-Cu system is shown in Figure 5. In this case, the sintering temperature of the matrix was lower than the melting temperature of the active phase (Cu) and so the Cu spheres have kept their shape very well with little agglomeration. This was most likely assisted by the particle size of the Fe powder being smaller than the Cu spheres and gives us some indications of optimum manufacturing processes. At higher magnification than Figure 5, small Fe nuclei within the Cu particles could be observed. These are formed from the limited solubility of Fe in Cu (2-4%) in the 1000-1200°C temperature range and the nearly complete insolubility at room temperature. Note that in

Publication 5: Miscibility gap alloys with inverse microstructures and high thermal conductivity for high energy density thermal storage applications

the operational range of the Cu-Fe storage system 1000-1200°C once the Cu phase is saturated with Fe, no further dissolution of Fe will occur. An X-ray diffraction pattern from the Fe-Cu system, shown in Figure 6, contains the expected peaks representing Fe and Cu confirming that no reactions have occurred.



*Figure 5 - Backscattered electron image of Fe-Cu thermal storage alloy demonstrating the inverse microstructure. The brighter circular phase is Cu and the darker matrix is Fe.*

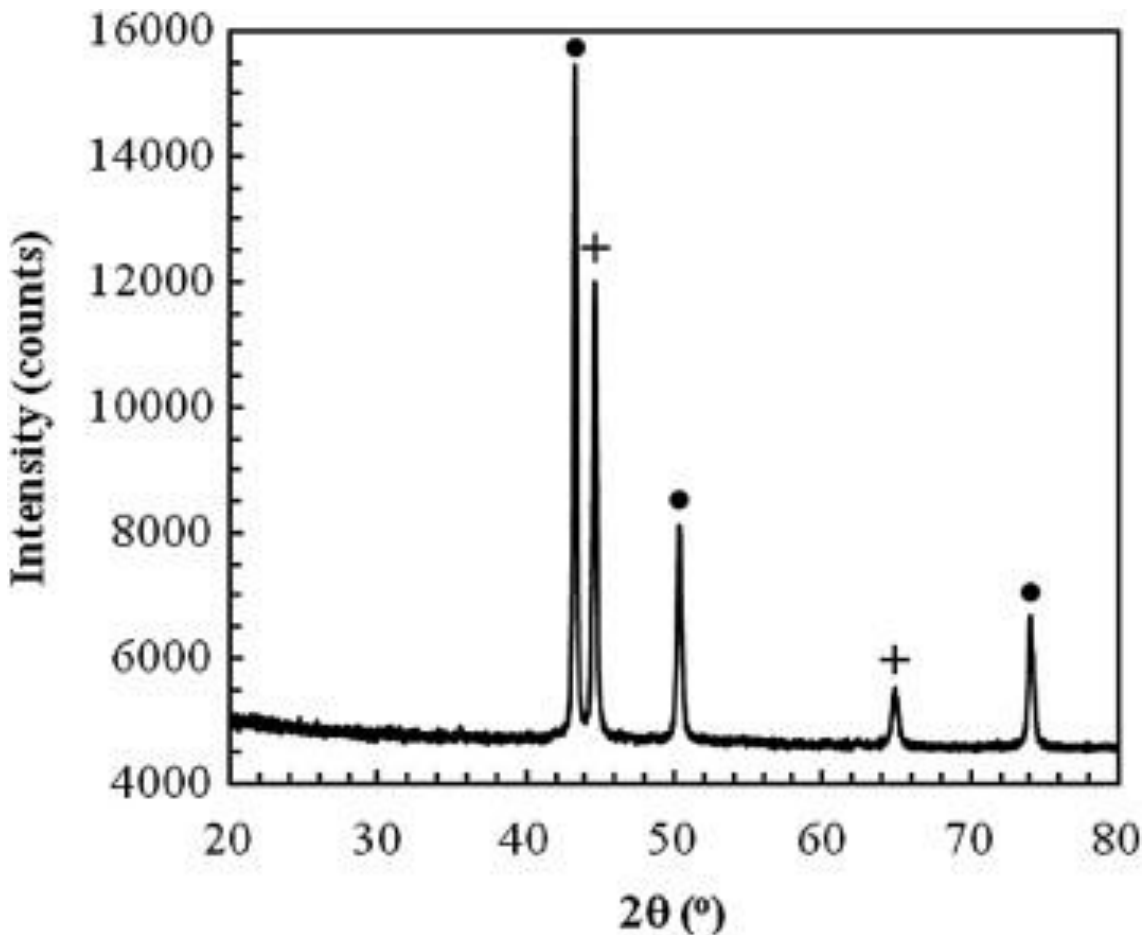


Figure 6 - Cu K $\alpha$  XRD pattern of the Fe-Cu alloy demonstrating only Fe and Cu as major phases. Fe peaks are marked with a plus sign (+) and Cu peaks are marked with a filled circle (•).

In summary, the metallographic examination shown in Figures 3 and 5 of the Al-Sn and Fe-Cu alloys indicate that the desired ‘inverse’ microstructures have been obtained with the active phase being encapsulated by the higher melting point matrix. The dispersion of Cu in Fe is very regular whereas that of Sn in Al is not even and could be improved by the use of more regular shaped particles as starting material (similar to the Cu spheres) or if the sintering temperature was reduced to below the melting point of Sn (<232°C). Only two significant micro-constituents can be observed in each system with no intermetallic compounds being formed. This is confirmed by the XRD patterns in Figures 4 and 6.

One advantage of containing the active phase within an immiscible (or largely immiscible) matrix is demonstrated by the micrographs and XRD plots. Contamination of the active phase with constituents from the containment vessel, like those experienced by Sun et.al. [6], are eliminated. Therefore, no reduction in melting temperature or latent heat of fusion is anticipated although further testing is evidently required.

## 4.2 Charge-Discharge Cycles and Energy Density

Thermal cycling around the melting point of the active phase demonstrates the charge-discharge behaviour of each system. Figure 7 shows the behaviour of the Al-Sn system over 3 consecutive cycles in a sample previously cycled approximately 30 times. It is clear that although there is some smearing and hysteresis of the solid-liquid-solid transition, the entire charge-discharge cycle occurs within a 22°C range (224-246°C) allowing for relatively constant temperature heat delivery during discharge from larger volumes of material. On heating, melting typically begins at 228°C in agreement with the phase diagram. Solidification at 232°C during the cooling stage. The freezing curve rises extremely sharply with a trailing edge conforming to Newton's law of cooling. In the raw data, only 4s elapse before the temperature excursion permeates the entire sample. This extreme rate can be attributed to the very high thermal conductivity of the Al matrix. Over the 3 charge-discharge cycles no significant changes in the onset of melting or solidification can be observed. The tight grouping of the heating/cooling curves implies that no measurable reduction in energy capacity (storage/release) occurred over this small test series however this will need to be validated by further testing.

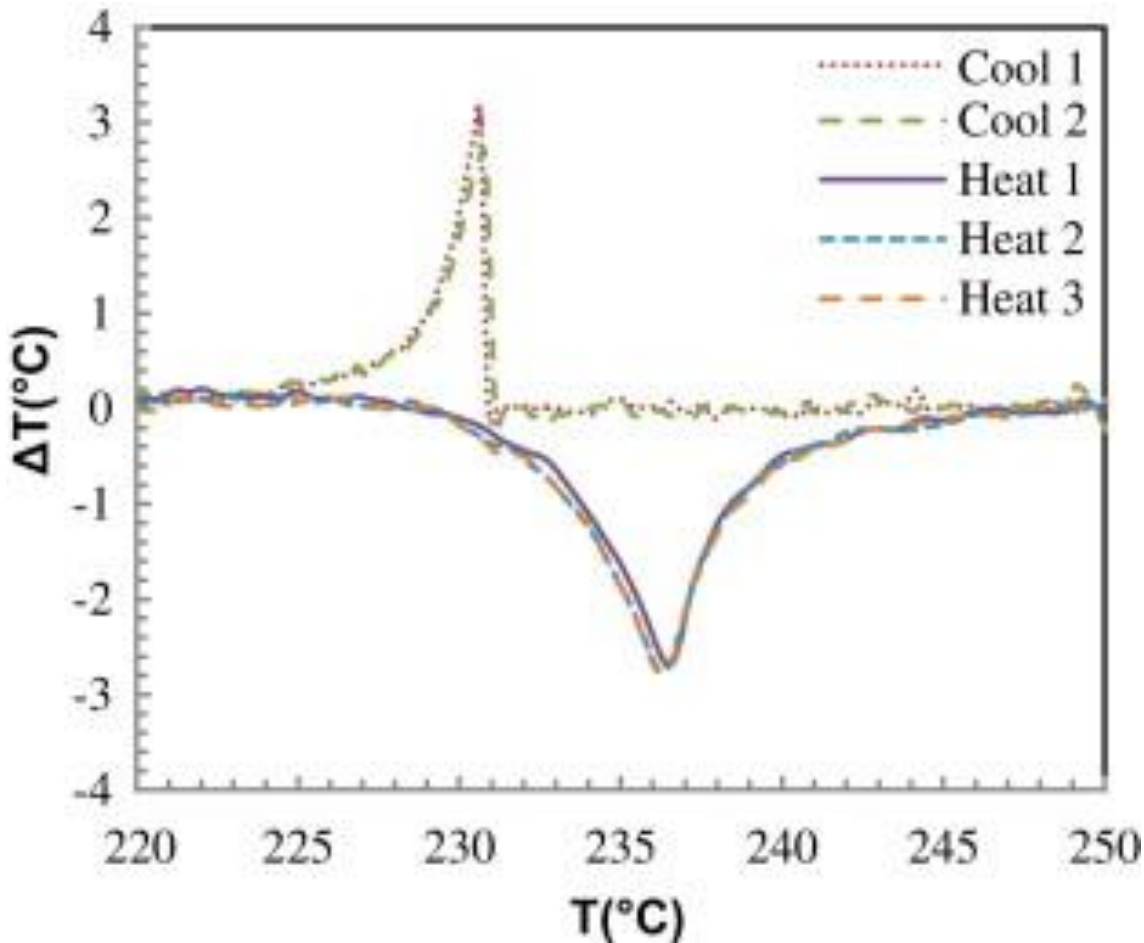


Figure 7 - DTA curves illustrating the uptake and delivery of heat in the Al-Sn alloy. Note the steep temperature rise on cooling as latent heat is released followed by cooling according to Newton's law of cooling.

Similar behaviour is demonstrated by the Cu-Fe system shown in Figure 8. Again three heating/cooling cycles are shown. Unlike the Al-Sn system, these were the initial 3 cycles and a shift in the heating curve of  $1.9^{\circ}\text{C}$  was observed between the first and second endotherms and a further  $1.5^{\circ}\text{C}$  between the second and third. This is due to the effect of the confinement due to the surrounding matrix which provides a large isostatic pressure and increases the melting temperature of Cu. After the first two cycles, there has been sufficient time for creep relaxation to occur and accommodate most of the volume change on melting and the thermal expansion difference. The higher energy density of the Cu active phase is evident by the stronger endotherms and exotherms. For these systems the energy density was  $151\text{kJ/L}$  and  $641\text{kJ/L}$  for the Al-Sn and Fe-Cu respectively.

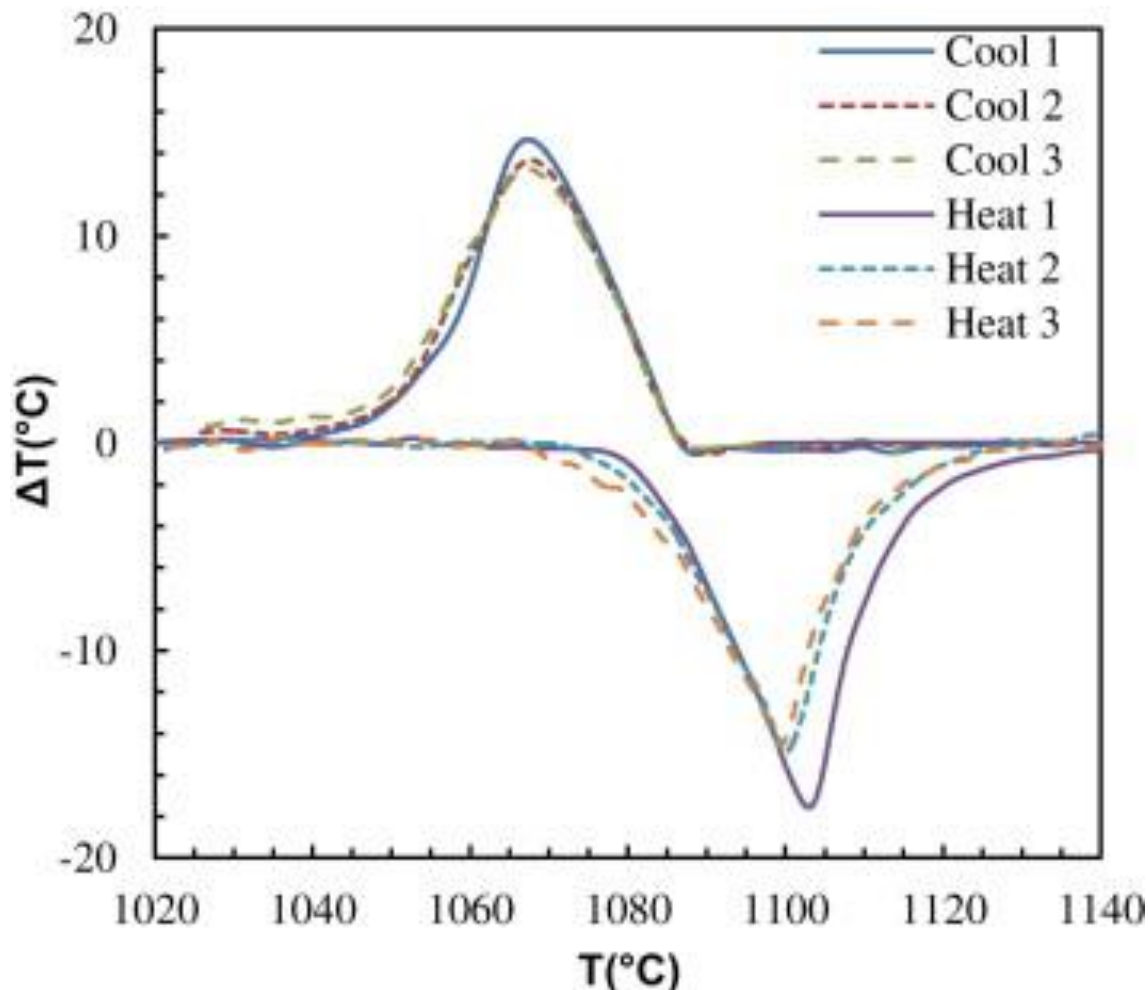


Figure 8 - DTA curves illustrating the uptake and delivery of heat in the Fe-Cu alloy for the first three thermal cycles. Note the shift in peak temperature between the first and subsequent heating runs.

Even higher energy density is possible by either increasing the volume fraction of the active phase or by selecting systems with a higher latent heat of fusion. Considering the first strategy – increased volume fraction, the maximum volume fractions for discrete active phase spherical particles dispersed in a continuous matrix is limited by the percolation limit of  $\approx 70\%$  by volume. At this volume fraction continuous paths connecting the active phase particles would be expected to allow draining of the molten phase at high temperatures. In the second strategy, systems with higher latent heats of fusion are sought. Table 1 is only a brief extract to demonstrate the application of

immiscibility systems for TES. The maximum energy density achieved by the Al-Sn alloys is about 2 times greater than that of pure paraffin or NaNO<sub>3</sub>/KNO<sub>3</sub> eutectic salt and that for the Cu-Fe system is approximately 8 times greater. From the data in Table 1, the energy density of a material containing 50% vol. Si active phase in a SiC matrix would store about 2.24 MJ/litre or 13.2 times greater than the maximum possible using state-of-the-art PCM. Additional benefits are also incurred due to the higher storage temperature and associated efficiency increase of the subsequent conversion process. Significant improvements in the time for charge-discharge cycles are also anticipated due to the higher conductivity of the matrix phase. No effort has been undertaken to optimize this parameter in Table 1 yet values range 80-237 W/m.K compared with <1 W/m.K for existing technologies. This not only speeds the cycle but also eliminates the need to incorporate heat transfer enhancement elements within the storage tank.

#### **4.3 Adaptability to Renewable or Waste Heat Recovery Technologies.**

The use of thermodynamically stable immiscible materials presents a new direction for developing efficient TES using the latent heat of fusion. Material systems can be selected to match the desired working temperature. No external confinement is required as the matrix phase is solid at all times and remains self-supporting. This simplifies the design and improves the safety aspects of large PCM storage tanks as hydraulic pressures are never developed and volume changes on freezing/melting are restricted to within the volume of small active phase particles.

Worldwide demand for thermal storage is enormous, being measured in units of 10<sup>18</sup>J per annum in the USA alone [3]. The class of miscibility gap alloys discussed here have the capability to considerably reduce demand for conventional forms of energy through the

use of concentrated solar radiation or industrial waste heat recovery and utilisation. This will by definition reduce demand for fossil fuel generated energy leading to substantial environmental gains. In space heating applications, the need for gas or electric heating can be greatly reduced by efficient storage and recovery of surplus heat or solar radiation as appropriate. With the optimisation of our moderate and high temperature storage materials, concentrated solar thermal base load electricity generation becomes increasingly feasible as the intermittency problem due to weather and the diurnal cycle is overcome in a way that allows the use of conventional steam turbine technology. If the solar input is fed directly into the storage block and the heat always extracted via the storage block, then the system can seamlessly continue generating long after the sun has set. The manufacturing methods to be used here are suitable for the incorporation of heat exchanger elements directly into the storage material further enhancing its applicability.

## 5. Conclusion

New metallic phase-change thermal storage materials with a tailored microstructure have been proposed. The low melting point high energy density phase is trapped as small particles within a high thermal conductivity metal matrix that can deliver heat rapidly over large distances. The two prototype systems tested, Al-Sn and Fe-Cu seem to live up to expectations upon short-term testing. The new systems have the potential to overcome the conductivity, energy density, corrosion and instability problems of conventional phase change systems.

## References

- [1] OECD/IEA, (2009), "World energy Outlook, 2009". Accessed online January 2011 – <http://www.worldenergyoutlook.org/2009.asp>
- [2] J. Pacheco, R. Bradshaw, D. Dawson, W. De La Rosa, R. Gilbert, S. Goods, M.J. Hale, P. Jacons, S. Jones, G. Kolb, M. Prairie, H. Reilly, S. Showalter and L. Vant-Hull, Final test and evaluation results from the Solar Two project, Solar Thermal Technology Dept., Sandia national Laboratories NM Tech. Rep. SAND2002-120, [http://www.osti.gov/bridge/product.biblio.jsposti\\_id=793226](http://www.osti.gov/bridge/product.biblio.jsposti_id=793226)
- [3] D.B. Fox, D. Sutter, J.W. Tester, The thermal spectrum of low-temperature energy use in the United States, Proc. 36<sup>th</sup> Workshop on Geothermal Reservoir Eng., University of Stanford, California Jan 31-Feb 2, 2011.
- [4] B. Zalba, J.M. Marin, L.F. Cabeza, H. Mehling, Review on thermal energy storage with phase change: materials, heat transfer analysis and applications, Applied Thermal Engineering 23 (2003) 251-283.
- [5] A. Sharma, V.V. Tyagi, C.R. Chen, D. Buddhi, Review on thermal energy storage with phase change materials and applications, Renewable and Sustainable Energy Reviews 13 (2009) 318-345.
- [6] M. Kenisarin, High-temperature phase change materials for thermal energy storage, Renewable and Sustainable Energy Reviews, 14 (2010) 955-970.
- [7] J.Q. Sun, R.Y. Zhang, Z.P. Liu, G.H. Lu, Thermal reliability test of Al–34%Mg–6%Zn alloy as latent heat storage material and corrosion of metal with respect to thermal cycling, Energy Conversion and Management 48 (2007) 619-624.
- [8] T. Nomura, N. Okinaka, T. Akiyama, Technology of Latent Heat Storage for High Temperature Application: A Review, ISIJ International 50, 9, (2010) 1229-1239.
- [9] A. Sari, A. Karaipekli, Thermal conductivity and latent heat thermal energy storage characteristics of paraffin/expanded graphite composite as phase change material, Applied Thermal Engineering 27 (2007) 1271-1277.
- [10] R. Bayón, E. Rojas, L. Valenzuela, E. Zarza, J. León, Analysis of the experimental behaviour of a 100 kWth latent heat storage system for direct steam generation in solar thermal power plants, Applied Thermal Engineering 30 (2010) 2634-2651.
- [11] N. Maruoka, K. Sato, J. Yagi, T. Akiyama, Development of PCM for recovering high temperature waste heat and utilization for producing hydrogen by reforming reaction of methane, ISIJ International, 42, 2, (2002), 215-219.
- [12] H. Baker editor, ASM Metals Handbook, 10th Edition, Volume 3 *Phase Diagrams* ASM International, Ohio, 1992.
- [13] G. Aylward, T. Findlay, SI Chemical Data, 5<sup>th</sup> edition, Wiley Brisbane, 2002.

## **10. Publication 6: High conductivity phase change materials for thermal energy storage – miscibility gap alloys**

**Heber Sugo, Dylan Cuskelly, Anthony Rawson and Erich Kisi**

The University of Newcastle, Callaghan, NSW 2308, Australia.

*Conference proceedings, Solar 2014 Conference and Expo, Melbourne Australia.*

### **Abstract**

Thermal storage has been identified as a major roadblock for the effective implementation of base load electricity derived from concentrated solar power plants. This research outlines the novel concept of utilizing specific combinations of metallic alloys that exhibit a miscibility gap. This allows the realization of high energy density-high conductivity thermal storage blocks. Energy is stored through the latent heat of fusion of the low melting phase which is dispersed in a higher melting point matrix. The rigid matrix provides containment of the fusible phase at all times forming a thermodynamically stable encapsulant for the phase change material. Nearly constant delivery temperatures ranging from 230-1400°C are possible depending on the choice of miscibility gap alloy (MGA) system. This report outlines the special microstructural requirements of MGA storage blocks and presents typical systems with thermal conductivities (80-200 W/m.K) and potential energy densities between 0.2-2.2 MJ/L respectively.

## 1. Introduction

The Sun delivers  $2.7 \times 10^{18}$  MJ per annum to the Earth's surface making this a significant renewable energy source <sup>[1]</sup>. The attraction for using solar energy is challenged by its dilute dosage (peaking at  $\approx 1$  kW/m<sup>2</sup>) and its intermittent nature due to diurnal cycles and cloud induced events. This intermittency has been identified as the key factor which must be overcome for the effective deployment of PV based renewable energy <sup>[2]</sup>. Concentrated Solar Thermal (CST) plants which incorporate thermal storage have the potential to reduce these intermittency effects allowing for more effective demand management.

Coal which is the current primary fossil fuel for electricity generation is very energy dense, releasing on average ~25 MJ/kg when burnt. To compete with this energy density, solar based electricity production requires the construction of large-scale concentrating plants, using troughs such as Andasol 1 or heliostat fields as in the case of Gemasolar. These plants use thermal energy storage (TES) to increase the dispatchability and improve the electricity MWh market value. TES systems have been developed based on *sensible* heat capacity or the *latent heat of fusion* involving a solid-liquid transition <sup>[3]</sup>. Over the last 20 years there has been extensive research into both forms of TES which has resulted in widespread publication of thermophysical data for organic materials, inorganic salts and some metallic systems <sup>[4-7]</sup>. The key material characteristics for usage in TES systems are the energy density *per unit volume*, thermal diffusivity ( $\alpha$ , ability of a material to conduct heat relative to its capacity to store thermal energy) and costs.

The Andasol 1 and Gemasolar examples rely on *sensible heat storage* using the specific heat capacity and temperature rise of the molten NaNO<sub>3</sub>/KNO<sub>3</sub> salt. One disadvantage is that the tanks and piping must be maintained at at least 260°C to

minimize the risk of the salt freezing. A further disadvantage is the low thermal conductivity ( $k=0.75$  W/m.K) and low thermal diffusivity of the salt ( $\alpha=0.2\times10^{-6}$  m<sup>2</sup>/s) requires large heat exchange surface areas and high salt throughputs to transfer the heat to the steam working fluid. In the case of Andasol 1 the parasitic pumping losses consume about 5% of output <sup>[8]</sup>. Special high-temperature concretes are also being developed to use as a sensible heat storage material in the 400-500°C range <sup>[9]</sup>. This represents an improvement in both thermal conductivity (1.5 W/m.K) and diffusivity ( $0.5\times10^{-6}$  m<sup>2</sup>/s). However, this requires close spacing of heat exchanger piping due to the low transient heat transfer rates realized within the concrete. This adds to the infrastructure costs and parasitic losses during plant operation.

In terms of sensible heat storage media, graphite has good thermal conductivity (90 W/m.K), moderate thermal diffusivity ( $33\times10^{-6}$  m<sup>2</sup>/s) and does not have an upper temperature limitation like molten slat or concrete. It is the medium of choice for Graphite Energy's CST plant at Lake Cargelligo in NSW and has been the subject of a preliminary engineering evaluation for the HELSOLAR project <sup>[10]</sup>. Its main limitation is that it requires a protective envelope from atmospheric oxygen.

TES systems based on *latent heat*, (e.g. solid-liquid transition), have also been developed and offer the advantage of a near isothermal heat delivery temperature and high energy density. For high temperature and high density TES, phase change materials (PCM) based on the NaNO<sub>3</sub>/KNO<sub>3</sub> eutectic salt are considered to be the state of the art system <sup>[11]</sup>. The energy density for the NaNO<sub>3</sub>/KNO<sub>3</sub> eutectic salt is 0.20 MJ/L. The relatively low cost of the NaNO<sub>3</sub>/KNO<sub>3</sub> base material has been an important factor in its usage as a PCM. However, the very low thermal conductivity (0.75 W/m.K) limits the ability to extract energy during power generation and it has been necessary to include heat transfer enhancement elements to increase the rate of

energy exchange [7, 8, 12]. The introduction of these elements increases the complexity of the design and manufacturing costs. The accompanying volume loss of PCM and hence latent heat capacity necessitates larger storage vessels to be constructed. A further disadvantage of the NaNO<sub>3</sub>/KNO<sub>3</sub> eutectic systems is the relatively low heat delivery temperature of 221°C.

Metals are excellent thermal conductors; Sharma [5] and Kenisarin [7] have identified several metallic PCM candidates due to their high melting point, good thermal stability and large heats of fusion on a mass basis. Sun et.al. [13] reported detailed data on the storage performance over 1000 heating/cooling cycles for a Al-Mg-Zn eutectic alloy. A reduction in the latent heat of fusion of 11.1% was observed and was attributed to contamination from the stainless steel containment vessel. In a separate study for a waste heat recovery application, Maruoka et.al. [14] performed a cost benefit analysis and found copper to be an ideal candidate as a high-temperature PCM. Copper balls were initially coated with nickel to simultaneously act as an encapsulant and catalyst for the hydrogen reforming process. Partial melting of the medium was observed due to the complete solid-solubility (miscibility) of nickel in copper forming an alloy with a reduced melting point. Therefore, it would appear that metals are ideal PCM for thermal storage applications if their tendency to form low melting point alloys or to react with the containment vessel could be reduced or eliminated.

The low thermal conductivity and energy density of sensible media, like molten salt or concrete and the effective encapsulation requirements for metallic PCM have been recently overcome through the innovative use of miscibility gap binary metallic systems [15, 16]. A description of this technology together with typical properties and experimental results are provided in this manuscript.

## 2. Miscibility Gap Alloy Thermal Energy Storage Systems

Miscibility Gap Alloys (MGA) offer many advantages for thermal energy storage applications. MGA thermal storage media rely on the latent heat of fusion of a low melting point fusible phase distributed as isolated particles within a higher melting point crystalline matrix. The alloy components are thermodynamically stable with respect to each other, with the higher melting point constituent acting as an encapsulant for the fusible phase. Thermal energy is primarily stored through the latent heat of fusion of the dispersed phase with a smaller component of sensible heat being available due to the high volumetric heat capacity of the metallic components. Thermal conductivities of MGA range from 80-200 W/m.K and systems with potential energy densities between 0.2 and 2.2 MJ/L have been identified [15, 16]. Selection of the MGA will dictate the heat delivery temperature, energy density and effective thermal conductivity of the system. The immiscibility criteria and special microstructural requirements for MGA are described in the following sections.

### 2.1 Microstructural Requirements for MGA Systems

The solidification products of a molten mixture of two metals, A and B, with fixed composition may include a solid solution (random mixture of A+B atoms), an intermetallic compound (ordered mixture in a fixed atomic ratio e.g. AB<sub>2</sub>) or if immiscible, they de-mix and solidify as two separate and distinct phases A and B forming a miscibility gap (i.e. immiscibility).

Miscibility gaps are observed when the free energy of the two solid phases, A and B, is lower than the free energy of a single phase of intermediate composition (either as a mixture or intermetallic compound). In these systems, there is no driving

force for chemical reactions between A and B components; the thermodynamically preferred state is the two separate phases. MGA therefore resolve the encapsulation requirements for metallic PCM, however a further point regarding the microstructural arrangement of the A and B phases needs to be considered for successful storage media.

This is demonstrated in the example given in Figure 1 which represents the microstructure evolution for a 60:40 wt% Sn:Al alloy on cooling. Note that the Al-Sn phase diagram indicates that these two metals are miscible in the liquid state and are essentially immiscible in the solid state. The maximum solubility of Sn in Al is <0.01% and 0.5% for Al in Sn at 230°C. Nucleation of Al crystals will commence at  $T_1$ , 595°C and continue to develop as indicated by the microstructures at  $T_2$  and  $T_3$ . On reaching 228°C the remaining liquid Sn phase will solidify. The final microstructure consists of discrete Al grains in a Sn matrix as shown at  $T_4$ .

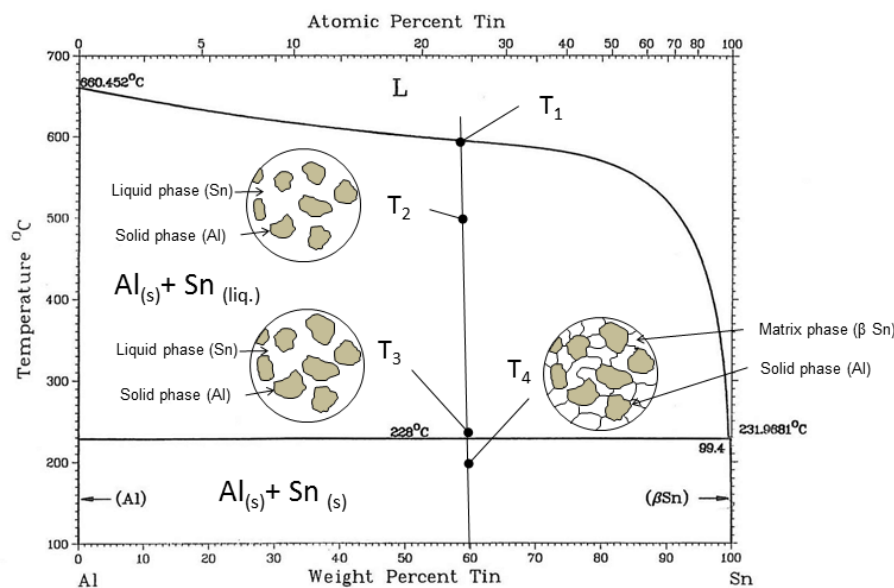


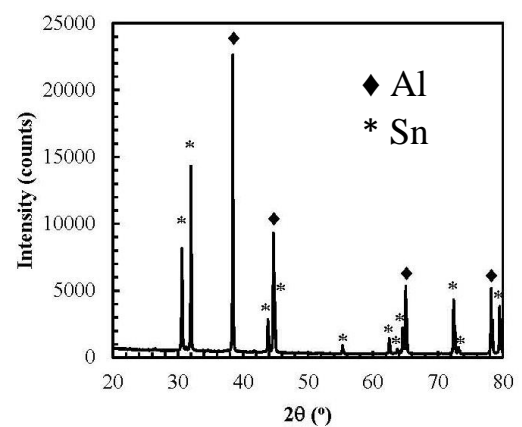
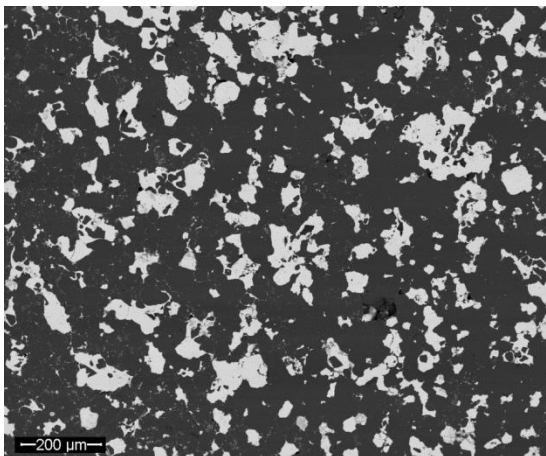
*Figure 1. The Al-Sn phase diagram and microstructure evolution during cooling from the melt for a 60:40 wt% Sn:Al alloy. Adapted from [17].*

This microstructure obtained through the normal cooling sequence is not suitable for thermal storage medium since the Sn fusible phase will melt during the charging process resulting in loss of integrity. For an effective storage medium, the inverse microstructure is required, where the fusible phase is dispersed in the solid, higher melting point matrix. It is possible to fabricate these ‘inverted’ structures through conventional powder metallurgy techniques – mixing of powdered components, pressing into shape, sintering at elevated temperature to obtain a dense and continuous matrix.

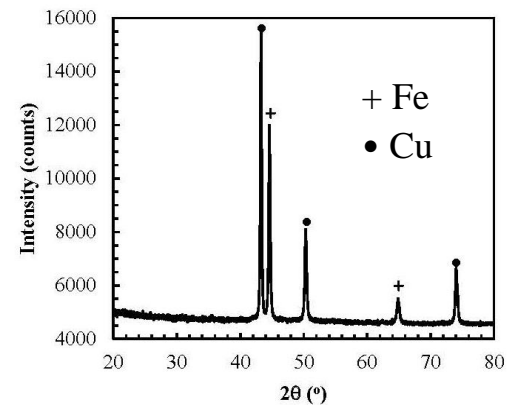
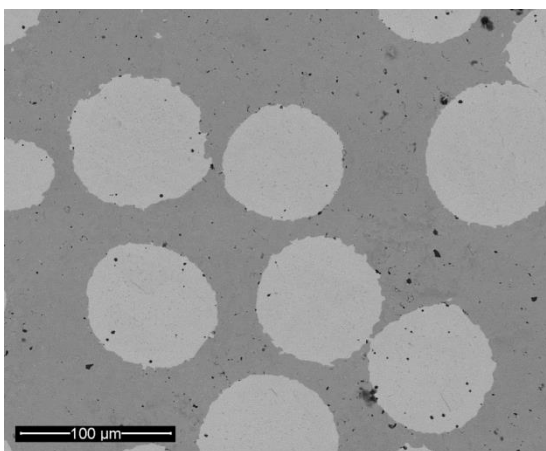
A further microstructural requirement is that the fusible phase should be present as discrete particles. Interconnected particles will contribute to gravity induced drainage of the fusible phase if rupture of the matrix were to occur. To minimize this risk, the volume fraction of the fusible phase should be kept below the percolation limit which is approximately 70% for equally sized spherical inclusions. Generally speaking the fusible phase may not be spherical and a conservative limit of 50% loading (by volume) of fusible phase has been adopted.

## 2.2 Examples of MGA Systems and Charge-Discharge Behaviour

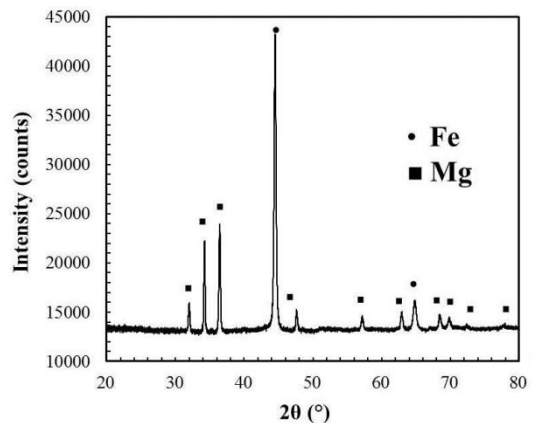
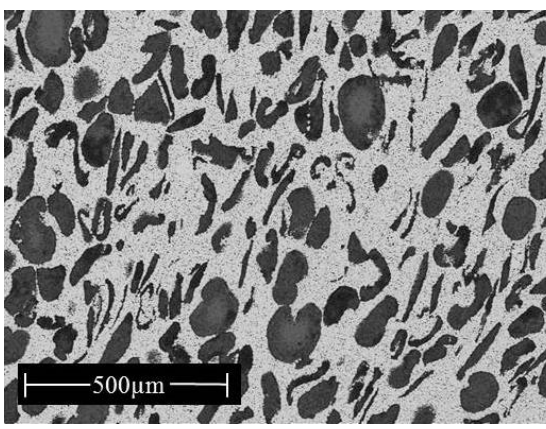
MGA samples of Al-Sn, Fe-Cu and Fe-Mg (fusible-matrix phase) systems have been produced successfully in the laboratory with fusible phase loadings of 35 and 50% by volume. Typical microstructures and phase identification using X-ray diffraction for these systems are presented in Figure 2. Note that as predicted by the corresponding phase diagram, only two metallic phases are present in each system.



(a) 35% vol Sn particles (light) dispersed in Al matrix (dark)



(b) 35% vol Cu microspheres dispersed in Fe matrix



(c) 50% vol Mg particles (dark) dispersed in Fe matrix (light)

Figure 2. Inverted microstructure of three different MGAs (back scattered electron images) indicating the different morphologies of the fusible phases and

*accompanying X-ray diffraction pattern indicating the presence of only two metallic phases in each system.*

The resultant morphology of the fusible phase is dependent on the initial shape of the powdered components and sintering temperature during densification. For the Al-Sn system (Figure 3(a)), sintering was carried out at 500°C, above the melting point of the fusible phase and the Sn material has flowed into the void space between Al particles resulting in a highly irregular morphology. For the Fe-Cu and Fe-Mg systems, sintering has been carried out below the melting point of the fusible phase (at 1000°C and 600°C respectively) and the initial morphology of the fusible material has been maintained.

The cyclic charge-discharge behaviour for the Fe-Mg system was investigated using differential scanning calorimetry (DSC). Figure 3 shows three heating and cooling cycles carried out at 10°C/min with a 37 mg sample mass. Changes in heat capacity start at 635°C, with the melting peak being observed at 656°C for the first cycle and 654°C in the subsequent cycles. The charging stage is fully complete by 668°C. The 1°C displacement of the first cycle is attributed to residual stress from the compaction process and is relieved in the initial melting process with the subsequent heating and cooling cycles converging to near identical temperature profiles. Discharge occurs as the fusible phase starts to solidify at 650°C and is completed by 630°C for all three cycles. This highlights the near constant delivery temperature of these alloys,  $\Delta T = 20^\circ\text{C}$  for the entire latent heat load.

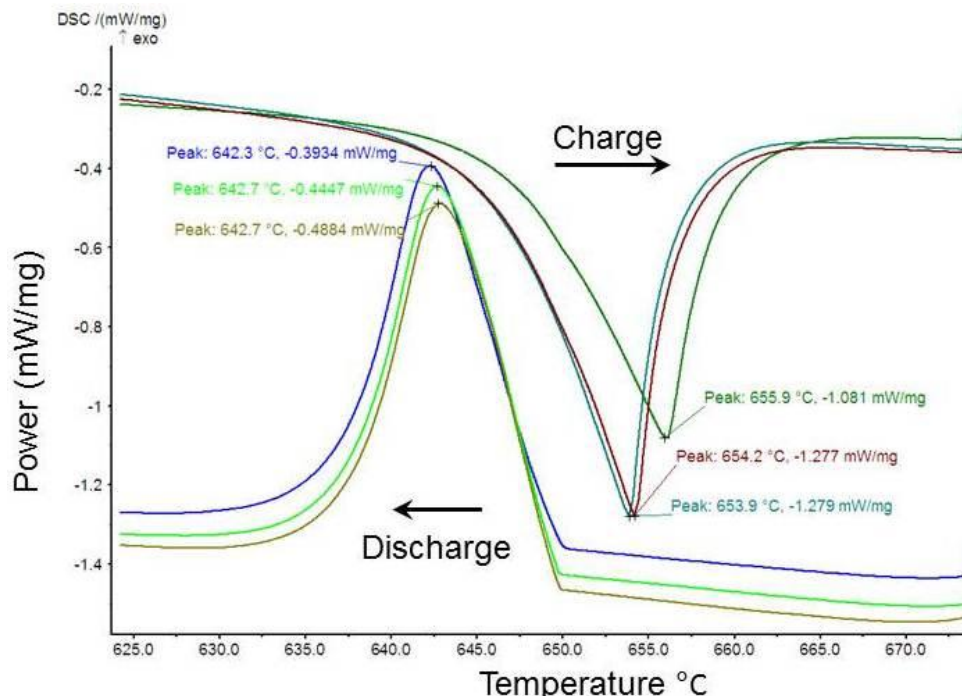


Figure 3. DSC plot of Fe-Mg MGA undergoing charge-discharge cycling demonstrating energy storage through the latent heat of fusion.

These charge-discharge characteristics are similar to those observed in larger, 30 g samples for the Al-Sn and Fe-Cu systems carried out over a larger number of cycles in a laboratory furnace [15]. The tight grouping of the heating/cooling curves implies that the MGA exhibit good energy storage/release capabilities over this small trial and further testing, over many cycles is warranted.

### 3. Thermal Properties of MGA Thermal Storage Systems

Options for large scale thermal storage systems are limited to *pumped fluid storage* or *stationary block storage*. The media options range from sensible heat storage in low cost materials (e.g. molten salt, concrete) to latent heat storage through PCM. A comparison of the thermal properties for conventional sensible and phase change storage media and selected MGA is provided in Table 1. The key advantages

for the MGA are the significant improvements in thermal conductivity, volumetric energy density and maximum service temperature. For MGA, a sensible heat component should also be included in the volumetric energy density. A sensible component equivalent to 100 °C has been added to the latent energy density and the combined values are plotted in Figure 4

*Table 1 – Comparisons of Thermal Storage Media.*

| <b>(a) Sensible Heat Storage</b>   |                          |  |   |                                      |                          |
|--|--------------------------|--|---|--------------------------------------|--------------------------|
| Medium   | Thermal cond.<br>(W/m.K) | Vol. Specific Heat Capacity<br>(kJ/(L.°C)) | Mass Specific Heat Capacity<br>(kJ/(kg.°C)) | Energy Density for 100°C rise (MJ/L) | Maximum Temperature (°C) |
| KNO <sub>3</sub> - NaNO <sub>3</sub> (molten)  | 0.6-0.8                  | 2.93                                       | 1.5   | 0.293                                | 580 <sup>2</sup>         |
| Concrete <sup>[9]</sup>  | 1.2-1.5                  | 1.62-2.36                                  | 0.72-1.05                                   | 0.16-0.24                            | 450-500                  |
| Graphite   | 90 <sup>1</sup>          | 1.53                                       | 0.71  | 0.153                                | >1100                    |
| <b>(b) Latent Heat Storage – conventional media</b>                                  |                          |  |   |                                      |                          |
| Medium   | Thermal cond.<br>(W/m.K) | Melting Temperature (°C)                   | Heat of Fusion (kJ/kg)                      | Latent Heat Energy Density (MJ/L)    | Maximum Temperature (°C) |
| KNO <sub>3</sub> NaNO <sub>3</sub> eutectic  | 0.6-0.8                  | 221  | 100   | 0.204                                | 580 <sup>2</sup>         |
| <b>(c) Latent Heat Storage – Selected MGA media for steam generation<sup>3</sup></b> |                          |  |   |                                      |                          |
| Medium   | Thermal cond.<br>(W/m.K) | Melting Temperature (°C)                   | Heat of Fusion (kJ/kg)                      | Latent Heat Energy Density (MJ/L)    | Maximum Temperature (°C) |
| Al-Sn  | 237                      | Sn 232                                     | 59  | 0.215                                | 400                      |
| Fe-Cu  | 80                       | Cu 1085                                    | 205   | 0.92                                 | 1150                     |
| Fe-Mg  | 112                      | Mg 649                                     | 370   | 0.32                                 | 850                      |
| C-Cu   | 200                      | Cu 1085                                    | 205   | 0.92                                 | >1200                    |

<sup>1</sup> Graphite is a highly anisotropic material hence an average thermal conductivity is reported here. Thermal conductivity can vary from 26 W/(m.K) across the basal plane to >500 W/(m.K) along the plane.

<sup>2</sup> The salt mixture will start to decompose through the formation of NO<sub>2</sub><sup>-</sup> ions

which is suppressed by using an oxygen atmosphere.

<sup>3</sup> The latent heat energy density for MGA metals is quoted for a 50% volume fraction of fusible phase.

Inspection of the micrographs presented in Figure 2 indicates the complex nature of determining the effective conductivity of MGA. The effective conductivity of the alloy will be influenced by the morphology, distribution, volume fraction as well as the magnitude of the thermal conductivity of the fusible/matrix phases. This has been the subject of a detailed study by Rawson et.al. who developed a technique involving Lattice Monte Carlo modelling combined with the evaluation of physical microstructures to determine effective thermal conductivity of these alloys <sup>[18]</sup>.

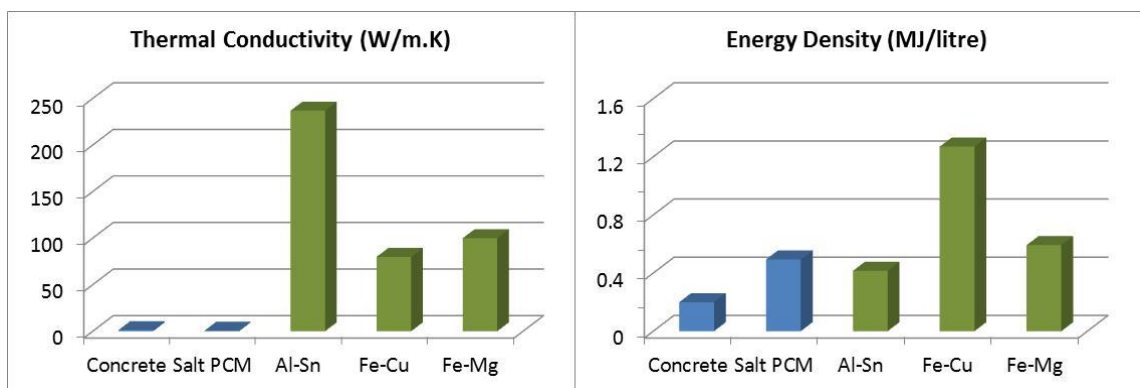


Figure 4. Thermal characteristics of conventional (blue) and selected MGA thermal storage materials (green). Note that the sensible heat component equivalent to  $\Delta T=100^{\circ}\text{C}$  used for concrete has been added to the latent energies density for Salt PCM and MGA .

Rawson<sup>3</sup> et.al. has also carried out an extensive evaluation of conventional and MGA storage media in terms of thermal properties and cost estimates of

---

<sup>3</sup> Refer to “Characterising Thermal Properties of Miscibility Gap Alloys for Thermal Storage Applications” by Rawson, Sugo and Kisi also in these Proceedings.

infrastructure and material for MGA technology [19]. Preliminary estimates indicate that MGA represent promising storage media for high temperature applications. The lack of known chemical drivers for reactions between the matrix and fusible phases offer MGA the additional potential of long-term operation with minimal maintenance and operational costs.

Over 90 MGAs suitable for safe thermal storage have been identified and nearly constant delivery temperatures ranging from 230-1400°C and potential energy densities of 0.2 to 2 MJ/L are possible depending on the choice of miscibility gap alloy (MGA) system [1]. Typically, thermal conductivities range from 80 to +200 W/m.K and depend on MGA system, volume fraction, morphology and distribution of fusible and matrix phases.

#### **4. Future Evaluations of MGA Thermal Storage Systems**

An analytical and experimental programme to further explore the suitability of MGA for high temperature storage in solar thermal or waste heat recovery applications is underway in the School of Engineering at the University of Newcastle. The analytical component is aimed at developing robust procedures to determine the physical properties derived from morphology, volume fractions and distribution of the microconstituents coupled with the intent of being able to accurately predict the charge-discharge behaviour of MGA media at the prototype level. The experimental component is directed at refining manufacturing techniques and quantifying the materials thermal and microstructural properties over short and long cycling periods.

At the fundamental level, a detailed study involving neutron diffraction imaging has been developed to evaluate the state of charge of MGA. For sensible storage media, the state of charge can be evaluated by knowing the representative

temperature of the storage medium. For MGA, like any other PCM, the state of charge can only be predicted by knowing the relative molten/solid proportions of the fusible phase content. Since the latent heat is delivered at a relatively constant temperature; simple temperature measurements are insufficient to determine the state of charge. The capacity of neutrons to penetrate deep into materials is being utilized to carry out a series of in-situ neutron experiments on small-scale storage devices to ascertain relative volumes and distribution of fusible phase as a function of energy input/output. This hard data will be used to verify numerical models relating the state of charge to the solidification front moving through the composite microstructure.

To date, limited funding for the development of MGA has only allowed analytical studies and laboratory studies, bringing the Technology Readiness Level (TRL) index<sup>4</sup> to 3. The research aspects mentioned above are the subject of funding requests made to ARENA and ARC Discovery Projects. If successful, this will allow further development and application of these novel storage media.

## 5. Conclusions

Metallic phase change materials have excellent energy density and thermal conductivity compared to conventional thermal storage media but are difficult to contain due to their reactivity with their containment vessel or affinity for the encapsulation material. These shortcomings can be overcome by using metals that are immiscible in the solid state and processed to give a dispersion of fusible phase particles encapsulated in a highly conducting solid metallic matrix. The thermal storage capability of this miscibility gap alloy (MGA) technology has been described together with useful examples and thermal characteristics. Over 90 MGA suitable for

---

<sup>4</sup> Refer to ARENA TRL Rating Scale at <http://arena.gov.au/resources/readiness-tools/>

safe thermal storage have been identified and details of current and future studies have been presented.

## Acknowledgements

The authors would like to acknowledge the financial contributions to the project by the University of Newcastle and its affiliate Newcastle Innovation. The authors also would like to thank the University of Newcastle and ARENA through the sponsorship of a PhD. Scholarship for Mr Anthony Rawson. Finally, we would like to thank the assistance provided by the Laboratory Staff of the Discipline of Mechanical Engineering and, Electron Microscope and X-ray Unit

## References

1. Smil, V., ‘Energy at the cross-roads: global perspectives and uncertainties’. MIT Press, Cambridge, 2003.
2. Sayeef, S., Heslop, S., Cornforth, D., Moore, T., Percy, S., Ward, J., Berry, A. and Daniel R. ‘Solar Intermittency: Australia’s clean energy challenge – Characterising the effect of high penetration solar intermittency on Australian electricity networks’. CSIRO Energy Transformed Flagship, June 2012.
3. Lovegrove, K., Watt, M., Passey, R., Pollock, G., Wyder, J. and Dowse, J. ‘Realising the potential of Concentrating Solar Power in Australia.’ ASI, May 2012, [www.australiansolarinstitute.com.au](http://www.australiansolarinstitute.com.au) accessed Dec 2012.
4. Medrano, M., Gil, A., Martorell, I., Potau, X. and Cabeza, L. ‘State of the art on high-temperature thermal energy storage for power generation. Part 2-Case studies.’ Renewable and Sustainable Energy Reviews **14** (2010) 56-72.
5. Sharma, A., Tyagi, V.V., Chen, C.R., Buddhi D. ‘Review on thermal energy storage with phase change materials and applications’. Renewable and Sustainable Energy Reviews **13** (2009) 318-345.
6. Abhat, A., ‘Low temperature latent heat thermal energy storage. Heat storage.’ Solar Energy, **30**, 4, (1983), 313-31.
7. Kenisarin, M., ‘High-temperature phase change materials for thermal energy storage.’ Renewable and Sustainable Energy Reviews, **14** (2010) 955-970.
8. Tamme, R., ‘IEA ECES Annex 19 – Optimised Industrial Process Heat and Power Generation with Thermal Energy Storage.’ Final Report, July 2010, IEA, [http://www.iea-eces.org/files/annex\\_19\\_finalreport-07-2010.pdf](http://www.iea-eces.org/files/annex_19_finalreport-07-2010.pdf) accessed Jan. 2013.
9. Laing, D., Bahl, C., Bauer, T. and Fiss, M., ‘High-Temperature Solid-Media Thermal Energy Storage for Solar Thermal Power Plants.’ Proc IEEE 100 (2012) 516-524.
10. Villarroel, E., Fernandez-Pello, C., Lenartz, J., Parysek, K., “High Efficiency Thermal Storage System for Solar Plants (HELSOLAR) – Research Performance

Publication 6: High conductivity phase change materials for thermal energy storage – miscibility gap alloys

- Final Report.” February 2013, <http://www.osti.gov/scitech/biblio/1068058> accessed online February 2013.
11. Bayón, R., Rojas, E., Valenzuela, L., Zarza, E., León, J. “Analysis of the experimental behaviour of a 100 kWth latent heat storage system for direct steam generation in solar thermal power plants”. *Applied Thermal Engineering* 30 (2010) 2634-2651.
  12. Zalba, B., Marin, J.M., Cabeza, L.F., Mehling, H., “Review on thermal energy storage with phase change: materials, heat transfer analysis and applications.” *Applied Thermal Engineering* 23 (2003) 251-283.
  13. Sun, J.Q., Zhang, R.Y., Liu, Z.P., Lu, G.H. “Thermal reliability test of Al–34%Mg–6%Zn alloy as latent heat storage material and corrosion of metal with respect to thermal cycling.” *Energy Conversion and Management* 48 (2007) 619-624.
  14. Maruoka, N., Sato, K., Yagi, J. and Akiyama T., ‘Development of PCM for recovering high temperature waste heat and utilization for producing hydrogen by reforming reaction of methane.’ *ISIJ International*, 42, 2, (2002), 215-219.
  15. Sugo, H., Kisi, E. and Cuskelly, D. ‘Miscibility gap alloys with inverse microstructures and high thermal conductivity for high energy density thermal storage applications.’ *Applied Thermal engineering* 51 (2013) 1345-1350.
  16. Australian Patent Application No. 2012904737.
  17. Baker, H. editor, *ASM Metals Handbook*, 10th Edition, Volume 3 Phase Diagrams, ASM International, Ohio, 1992.
  18. Rawson, A., Kisi, E., Sugo, H. and Fiedler, T., “Effective Conductivity of Cu-Fe and Sn-Al Miscibility Gap Alloys.” Accepted for publication *Intl. J. Heat and Mass Transfer*, February 2014.
  19. Rawson, A., Sugo, H. and Kisi, E., “Characterising Thermal Properties of Miscibility Gap Alloys for Thermal Storage Applications.” Submitted for publication *Proc. of Solar 2014*, Australian Solar Council, Melbourne, Australia, May 8-9th, 2014.

## **11. Publication 7: Development of a thermionic converter for CSP application**

Heber Sugo, Dylan Cuskelly, Muhammad Hasan and Erich Kisi

The University of Newcastle, Callaghan, NSW 2308, Australia.

*Conference proceedings, Solar 2014 Conference and Expo, Melbourne Australia.*

### **Abstract**

The direct conversion of thermal energy to electricity is possible via thermoelectric, thermionic or combinations of these phenomena. These methods are ideally suited for concentrated solar thermal applications as they can utilize the entire solar spectrum once it is converted to heat. The development of a high temperature thermionic device has been undertaken at the University of Newcastle, School of Engineering with funding from the Australian Renewable Energy Agency. This report provides a brief introduction to thermionic emission, the synthesis and characterisation of emissive materials, designing of the device and results from preliminary testing.

## 1. Introduction

Concentrated solar thermal power production is one of the foremost methods of renewable energy generation. A huge amount of research is invested every year into the field of concentrated solar power (CSP). Sunlight can be concentrated in a three main ways, either by trough collectors, standalone parabolic dish or power tower arrangement using an array of mirrors. In conjunction with solar concentration, thermal storage technologies have been developed to overcome the intermittency of sunlight as a power source. This is normally achieved by storage of heat in molten salts, thermal oils, solid sensible storage media or phase change materials. The in-depth research in these fields has led to increased scientific discovery and subsequent development of these technologies [1]. However, CSP still relies on steam generators to convert thermal into electrical energy using technology evolved from the combustion of fossil fuels. This imposes a series of limitations of CSP derived generation:

- 1) The efficiency of steam generators is only ~35%. Although almost all of the energy in solar radiation can be converted into heat only about a third of the energy can be converted into electricity. The entire concept of steam generation is limited by the maximum working temperature of the pressure pipe and turbine machinery components, which in turn lowers the Carnot efficiency of the system. A standard steam turbine running off 600°C-200°C steam cannot run better than 66% efficiency.
- 2) Thermal storage media, needed to overcome the intermittency factor of solar power generation, is also limited to a maximum working temperature and for sensible storage media a decline in the steam delivery temperature will occur as the block is discharged. These factors will also contribute to reduced efficiency.

3) A steam generation system involves a large and complex support system, heat exchangers, pumps and long lengths of piping which add to both the initial outlay of the system as well as the ongoing running costs. Thermal storage systems utilizing media with low thermal diffusivity will further exacerbate these infrastructure and operational costs.

Steam generation is not the only form of power conversion. Stirling engines or organic Rankine cycles can also be used with potentially higher Carnot efficiencies but these technologies still require additional infrastructure. An alternative approach is to use a direct energy conversion process such as thermionic emission. In a thermionic converter electrons are ‘boiled off’ the surface of an emitter material (1000-1600°C) and condensed on the surface of the collector. In comparison to existing Rankine or Brayton cycles, thermionic energy conversion technology is not as advanced but the reduced infrastructure and potentially lower operating costs combined with high conversion efficiency due to the higher operating temperatures warrants the investigation of this technology.

The mechanisms of thermionic emission and thermionic energy conversion are complex. A large amount of theoretical study is required to fully understand the process and in-depth discussions are presented elsewhere [2-4]. This report is designed to focus on the engineering of a thermionic energy conversion device and only a brief discussion of the operating principals, material properties and operational criteria is presented. An outline of the work undertaken to synthesise and characterise electron emissive materials, the design of the high temperature vacuum housing, converter assembly and results from preliminary trials are presented.

## 2. Thermionic Processes and Thermionic Energy Conversion

When a metal atom is heated, thermal energy is imparted to the electrons. If the temperature is high enough some of the conduction band electrons (those at the Fermi level) can gain enough energy to overcome the attractive forces from the array of positively charged nuclei and leave the surface. This energy is known as the surface work function or work function ( $\phi$ ) and is defined as the latent heat of evaporation required by an electron to permit its escape at 0K [2]. The work function is unique to each material and is a critical parameter for thermionic emission.

The saturated thermionic current from the surface of a material into a vacuum varies exponentially with temperature and is described by the Richardson-Dushman equation (Eqn. 1). This equation identifies another material related property, the Richardson emission constant ( $A$ ) although the exponential term ( $-\phi/kT$ ) remains the governing factor.

$$(1) \quad J = AT^2 \exp[-\frac{\phi}{kT}]$$

where:

$J$  = saturated emission current density (Amp/cm<sup>2</sup>)       $\phi$  = work function, (eV)

$A$  = Richardson emission constant (max. 120 Amp/cm<sup>2</sup>.K<sup>2</sup>)       $T$  = temperature (Kelvin)

$k$  = Boltzmann constant, (8.617x10<sup>-5</sup> eV/K)

A schematic of a possible thermionic device using concentrated solar energy (heat) and associated electron potential diagram is shown in Figure 1. At the hot cathode (emitter), the free valence electrons with sufficient thermal (kinetic) energy are able to leave the surface. The electrons traverse across the vacuum gap to the cooler anode (collector) and through the external load, return to the emitter. The difference between the work functions of the collector and the emitter generate a voltage (V) that can be dropped across a load generating useable power. Within each stage of the circuit there are impediments to the flow of electrons. The primary concern is the build-up of electrons within the vacuum gap (space charge) which generates a repulsive force field hindering the emission and flow of electrons away from the emitter surface. Two strategies have been developed to minimise the space-charge barrier. The first one relies on the introduction of an ionisable gas (caesium vapour) to the converter where positively charged particles are able to cancel out the build-up of electrons allowing the device to operate with a wide gap (1-2 mm)<sup>[2]</sup>. The second approach is the close-spaced converter. In this case, much smaller emitter-collector gaps (typically <25 µm) are required to reduce the space-charge effects. Due to the safety and containment issues associated with handling caesium vapour, a close-spaced converter was considered in this project.

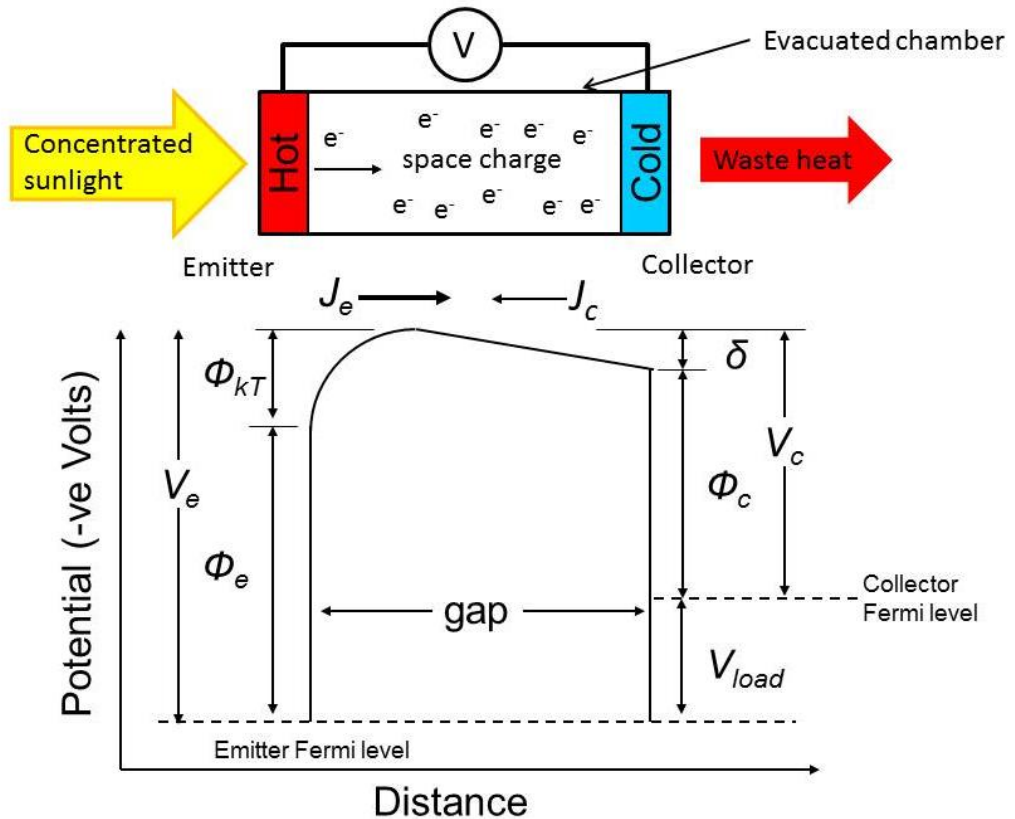


*Figure 1. Schematic of a thermionic convertor (above) and electron potential diagram (below).*

The conversion process of a thermionic converter can be interpreted in terms of electron flow due to changes in potential. The electron current leaving the heated emitter surface ( $J_e$ ) consists of electrons with a combined potential equivalent to both the work function of the emitter ( $\phi_e$ ) and the kinetic component ( $\phi_{kT}$ ). As they traverse through the gap, the work done against the space-charge decrease their potential by the term  $\delta$ . A further reduction in potential occurs as the electrons enter the conduction band of the collector material which is equivalent to the collector work function ( $\phi_c$ ). This energy combined with any residual kinetic energy is transferred to the collector as redundant heat. An opposing electron current arising from the collector ( $J_c$ ) may also contribute to the space charge. In practice, back

emission is avoided by operating the collector at a sufficiently low temperature so that the  $J_c$  term is negligible.

The voltage output is the difference between  $V_e$  and  $V_c$ , which essentially consists of the difference in emitter/collector work functions. The current output will be the proportion of electrons of the saturated emission current that have sufficient initial velocities to overcome the net retarding potential ( $V_c + V_{load} - \phi_e$ ).

For maximum converter efficiency the design considerations include:

- selecting emitter materials with low Fermi levels and collector materials with higher Fermi levels
- correspondingly, the emitter work function should be higher than that of the collector
- selection of emitter materials with high emission constant values,  $A$
- maximising the emitter temperature
- minimizing collector temperature to minimise back emission
- minimizing the potential difference between the kinetic  $\phi_{kT}$  potential and space charge loss  $\delta$ , to allow the maximum possible fraction of the saturated emitter current to reach the collector.

The above analysis is a simplified description of the theory behind thermionic converter. The primary material properties are the work function of the emitter and collector and the Richardson emission constant for the emitter. Operational aspects involve:

- maximising the emitter temperature (1200-1600°C)
- minimizing the collector temperature

- maintaining a close-spaced arrangement to reduce space-charge barrier (distance approaching 25 µm)
- maintaining ultra-high vacuum conditions,  $<10^{-5}$  mBar.

In practice, it is unlikely that all these requirements can be met in a single design cycle. Therefore an additional design criterion was added; to allow the converter assembly to have test-bed capacity by being demountable, enabling various emitter, collector and gap thicknesses to be evaluated.

### **3. Synthesis and Characterisation of Emissive Materials**

Several types of emissive materials were synthesised during the project. This includes refractory metal-emissive oxide composites e.g. W-BaHfO<sub>3</sub> and Ni-(BaO.SrO) and rare-earth hexaborides e.g. LaB<sub>6</sub>, GdB<sub>6</sub> and BaB<sub>6</sub>. Emissive oxides were firstly synthesised by calcining stoichiometric mixtures of BaCO<sub>3</sub> and HfO<sub>2</sub> or BaCO<sub>3</sub> SrCO<sub>3</sub> at 1100°C for 4 h to form the desired phases followed by milling to reduce particle size, mixing with the appropriate refractory metal and firing to promote sintering under 95%Ar-5%H<sub>2</sub> atmosphere. Sintering temperatures were adjusted to suit the system, 1600°C for W-BaHfO<sub>3</sub> and 900°C for Ni-(BaO.SrO). A 4h sintering period being found to be adequate to produce dense compacts. X-ray Diffraction (XRD) and Scanning Electron Microscopy (SEM) were carried out at each step to monitor sample purity and particle size and morphology. Typical electron micrographs for the refractory metal-emissive oxide composites are given in Figure 2.

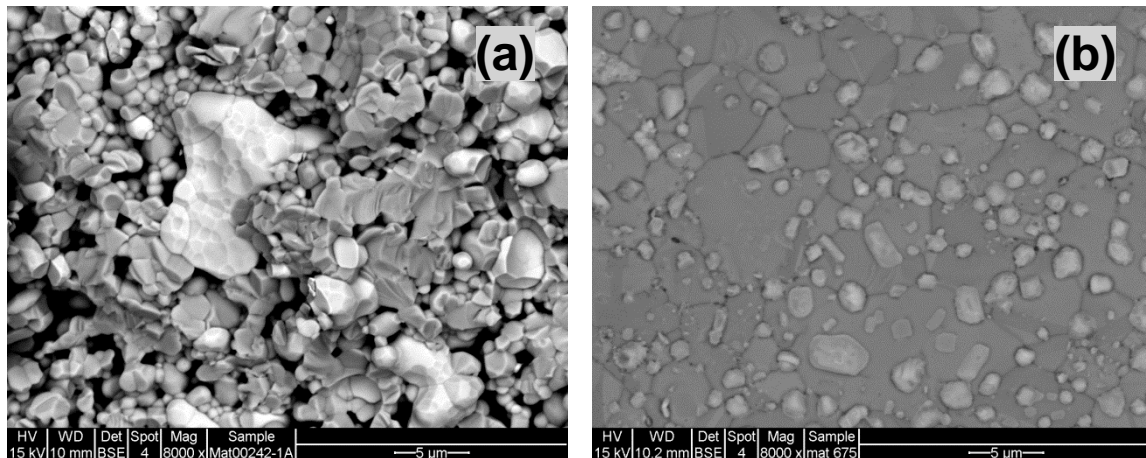


*Figure 2. Backscattered electron micrographs of refractory-emissive oxide composites (a) W grains (light) dispersed in BaHfO<sub>3</sub> matrix and (b) Ni matrix (dark) with partial cover of BaO.SrO (light phase).*

Rare-earth hexaborides especially LaB<sub>6</sub> are frequently used in electron sources due to its moderate work function ( $\approx 2.7$  eV) combined with its high temperature stability and low vapour pressure. Conventional solid-state production routes are difficult due to the high synthesis temperature (1500-1700°C). Low temperature synthesis routes, 1250-1450°C have been developed by Hasan et.al. producing high purity LaB<sub>6</sub> and other rare-earth hexaborides including CeB<sub>6</sub>, GdB<sub>6</sub> and BaB<sub>6</sub>. This is described in detail elsewhere<sup>5</sup> [5,6].

Following synthesis and microstructural characterisation, the thermionic work function ( $\phi_R$ ) and Richardson constant ( $A$ ) were evaluated using standard techniques [7,8]. Schottky plots were generated at temperatures ranging from 1200 to 1500°K under bias conditions between 0-300 Vdc. The current densities at zero fields were used to determine the work function and emission constant using the Richardson line method. Figure 3 shows the Schottky and Richardson plots for a GdB<sub>6</sub> alloy. The

---

<sup>5</sup> Refer to “Synthesis of Thermionic Materials for Solar Energy Conversion” by Hasan, Sugo, and Kisi in these proceedings.

Richardson work function was found to be 1.8 eV with the emission constant 104 A/cm<sup>2</sup>.

#### 4. Gap Materials

The function of the gap material is to maintain a small separation between the emitter and collector to minimise the space charge barrier. The material must also provide electrical isolation between the two electrodes. Therefore, the desired material properties are high dielectric strength, low thermal conductivity and dimensional stability under high temperature-high vacuum conditions. An additional requirement is that the material must be chemically inert with respect to both the emitter and collector.

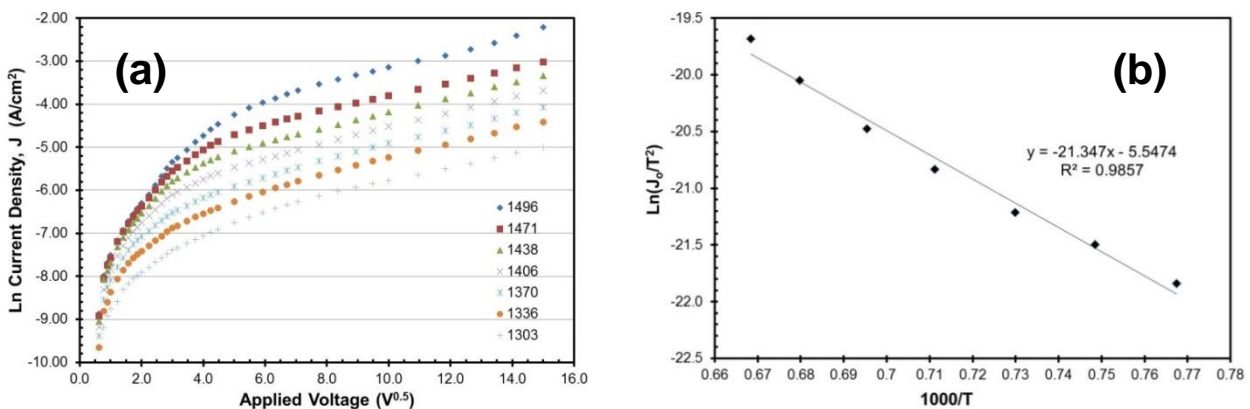


Figure 3. (a) Schottky curves and (b) Richardson plot for GdB<sub>6</sub> alloy.

Numerous high band-gap refractory materials were considered e.g. Al<sub>2</sub>O<sub>3</sub>, MgO, SiC and BN. Chemical compatibility tests were conducted by mixing these materials with LaB<sub>6</sub> and firing the mixtures to 1400°C under vacuum followed by XRD. Reaction by-products were observed in all cases and after several trial and error attempts an oxide mixture was found to be chemically stable. Large compacts

of this material were synthesised and cut into C-shaped disks. These were then ground to 55 µm thick spacers to be used in the device.

## 5. Development and Testing of Thermionic Device

### 5.1 Device Design and Vacuum Stability Tests

Basic design criteria and operational considerations for the device are reported in Table 1. This consists of a high temperature - high vacuum enclosure, a collector support arrangement and provisions to maintain adequate vacuum, cooling and electrical continuity.

A commercial grade Fe-Cr alloy was selected as enclosure material due to its high-temperature oxidation resistance and adequate creep strength at 1400°C. In terms of shape, a closed-end tube arrangement was chosen allowing this sealed end to be exposed to radiant heat whilst provisions for vacuum, electrical and water feedthroughs was provided at the cold end. The ability to be disassembled, for test bed capacity, whilst making a reusable ultra-high vacuum seal was obtained using standard 113.5 mm Conflat vacuum flanges and a copper gasket sealing the system. A 3D CAD design of the device assembly is presented in Figure 4(a) and the housing, as manufactured, in Figure 4(b).

The emitter/collector position can be seen in the sectioned view in Figure 4(a). Provision for cooling of the collector is made via the device base, where the collector support is composed of a dual tube arrangement to allow for water circulation. The collector support is also protected from circumferential radiant heat by a nest of concentric molybdenum shields. (Note that for clarity these have been omitted in Figure 4(a)). The finished assembly, showing water inlet/outlet from the

central collector support and vacuum point (KF25 fitting) are displayed in Figure 4(b).

*Table 1. Design Criteria for Thermionic converter*

| Operational Criteria  | Comments   |
|---|--|
| External Housing High Temperature Properties:<br>Oxidation Resistance<br>Creep<br>Vacuum Stability<br>Low thermal conduction  | 1400°C<br>1400°C<br>$<10^{-5}$ mbar @ 1300°C<br>$<20$ Watts at $\Delta T=1300^{\circ}\text{C}$ |
| Collector Support Structure:<br>Accommodate Thermal movements to maintain gap<br>Adequate Radiation shielding<br>Provide electrical and thermal contacts<br>Adequate cooling capacity                                     | ✓<br>✓<br>✓<br>$\approx 220$ Watts at $\Delta T=1300^{\circ}\text{C}$                          |
| Emitter/Collector Requirements:<br>Emitter – moderate work function ( $\varnothing_R=2.6\text{-}2.8$ eV)<br>Collector – lower work function<br>Gap material – chemical inertness<br>Gap material – thickness requirements | ✓<br>$<2.0$ eV<br>✓<br>tested 55 $\mu\text{m}^*$ ✓   |
| Test bed capacity:<br>Ability to accept different emitter/collector pairs and gap materials   | ✓  |

\* Techniques to reduce the thickness to 30  $\mu\text{m}$  have been developed

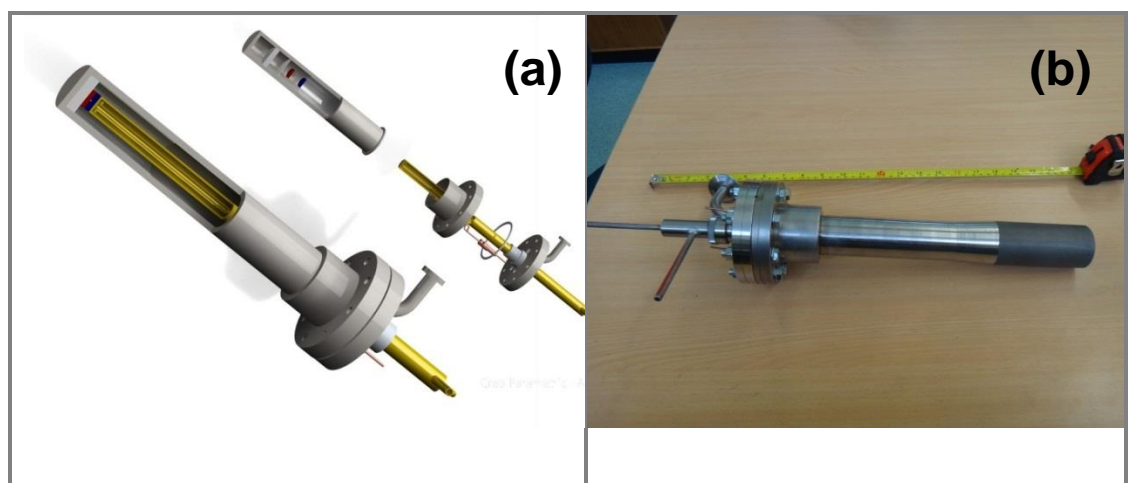


*Figure 4. (a) Design concept of converter and (b) fabricated unit.*

To ensure the vacuum seals are maintained within their operating temperature, a plate-type heat exchanger was mounted to the conflat base to remove the thermal energy

conducted down the external tube. Thermal losses via the collector support and external tube were monitored using the flow rate and temperature rise of the water in each part of the circuit. Water temperatures were monitored using PT100RTD connected to a DT80 Datataker. The enclosure undergoing vacuum testing with the close-end being exposed to radiant heat inside a muffle furnace at 1400°C is shown in Figure 5(a) whilst Figure 5(b) shows the hot-face of the external housing after heating indicating negligible oxidation of the surface after the test.

The vacuum tightness of the enclosure is given in Figure 6 which shows the vacuum (in mbar) during heating of the chamber to 1205°C and holding for 20 min. As expected an increase in temperature causes the pressure to rise due to outgassing however the vacuum improves during the temperature arrest. The stepped nature of the plot is caused by the resolution of the vacuum gauge.

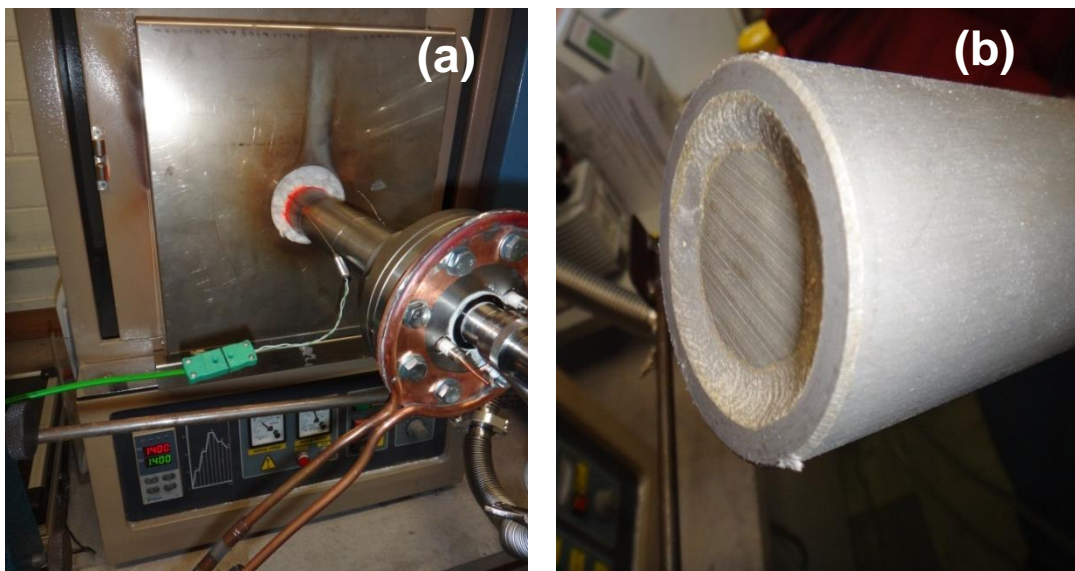


Figure 5. (a) Converter enclosure undergoing initial trials at a working temperature of 1400°C and (b) external converter surface after 4h showing negligible oxidation.

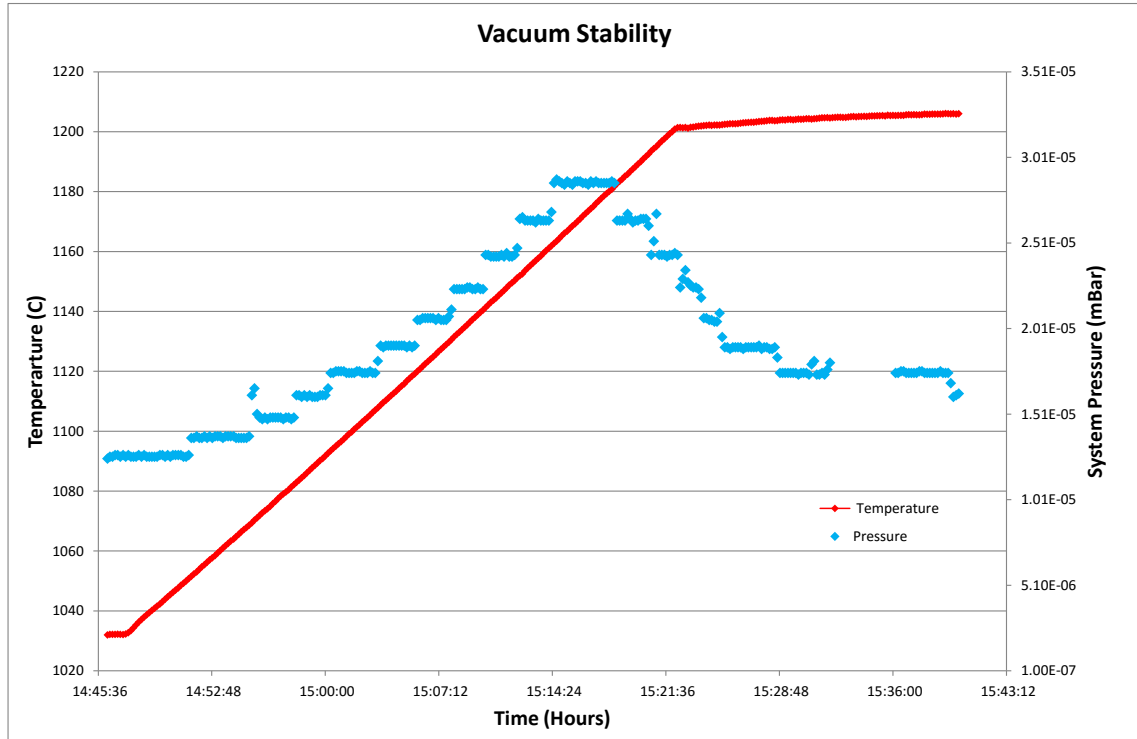


Figure 6. Vacuum stability during heating ramp and temperature soak.

## 5.2 Emission Testing

The device with a blended-LaB<sub>6</sub> emitter and a pure LaB<sub>6</sub> collector and a 55μm thick gap was assembled and fully instrumented for measurement of cell voltage and current. The hot-face was again placed through an orifice into the muffle furnace and output current was logged over the complete temperature range during heating to 1300°C at 300°C/h and whilst at 1300°C. Five different load resistors were used to evaluate current output. A small but stable thermionic emission current (+/- 5%) was observed from the device over periods of several hours. The maximum observed current was 42 mA representing a power output of 0.186 mW.

The thermal conditions, cooling requirement and thermal conduction losses through the device walls are demonstrated in Figure 7(a). The collector support is exposed to both radiation and conduction across the emitter/collector gap and these losses are in

the order of 220 W at 1300°C. The predominant heat transfer of the external enclosure is via conduction which equates to ~20W at 1300°C. The power output is indicated in Figure 7(b). The increase in output current (and power) is due to the reduction of the external circuit resistance. Further reductions in load resistance were not possible due to the configuration of the device at the time of testing. Upon disassembly the emitter, collector and gap material had remained discrete (i.e. no diffusion bonding or chemical reaction had occurred), they were intact, in good condition and reusable.

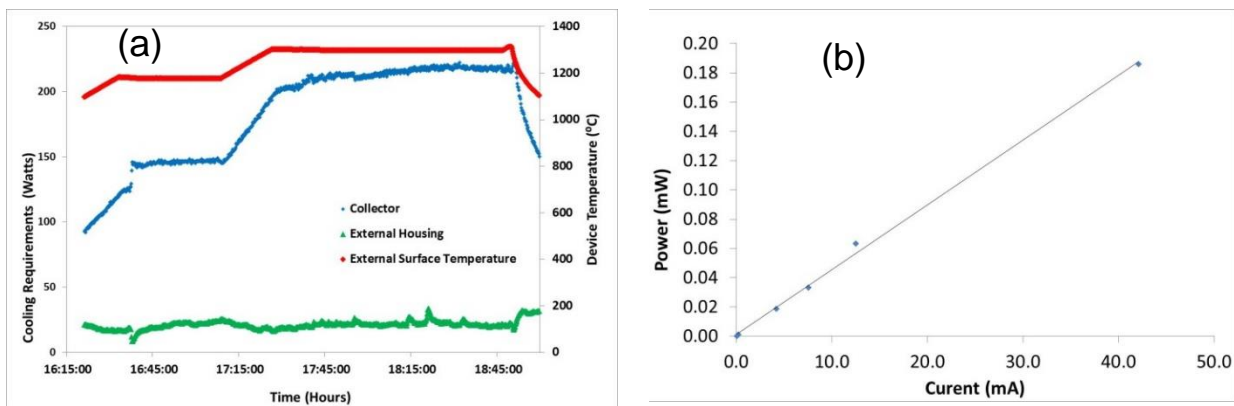


Figure 7. (a) Cooling requirements for the device and (b) device output at 1300°C.

The output of the device was very low given the high working temperature and potentially high Carnot Efficiency. It is likely that this has been caused by a series of factors:

1. Poor thermal contact between emitter and hot face and/or collector and cooling plate, thereby reducing the temperature and emissive capacity of the emitter and potentially allowing the collector to back emit.
2. Space charge effects caused by the gap thickness (55 µm) being greater than 25 µm. This may have been aggravated by distortion of the gap thickness induced by non-uniform temperature gradients.

3. Incompatibility in the selection of emitter/collector pair in terms of voltage output.

These results highlight some of the difficulties encountered in translating technologies with high theoretical efficiencies into practice. Since the device exhibited an output, this indicated that the emitter was sufficiently hot to undergo thermionic emission and the emitter/collector gap had been maintained at elevated temperatures. However, the conditions were not optimum to yield worthwhile conversion efficiencies.

### **5.3 Future Optimization of Device Output**

The thermionic prototype device has been demonstrated to be an excellent test-bed for evaluating emitter-gap-collector combinations due to the ease of disassembly and robust construction. The low output is attributed to a combination of design and emitter/collector material factors. Design improvements include further reductions in load resistance by excluding the outer housing from the current loop and closing the gap to  $<30\text{ }\mu\text{m}$  to further reduce space charge effects. Improvements to the thermal coupling between the emitter/hot-face and collector/cooling plate should also improve the output. Material factors include the improvement to collector-emitter pairs by broadening the focus from work function alone to include the influence of the collector Fermi-level on the device current. As most advanced materials have unknown Fermi levels, this would involve Density Functional Theory (DFT) modelling with subsequent experimental verification.

## 6. Conclusions

Thermionic energy conversion is a direct process of converting thermal energy to electricity. The high temperature requirements for this process combined with the high theoretical efficiency and the capacity to utilize the entire solar spectrum makes it an ideal candidate for CSP applications. The necessary synthesis and characterisation of electron emissive material and advances in the low-temperature synthesis of high-purity emissive boride materials has been described. Design considerations for the development of a prototype thermionic device have been outlined and the results of initial testing indicate a low but stable output. Recommendations for improvements in design and materials are presented.

## Acknowledgements

The authors would like to acknowledge the financial contribution to the project made by ARENA under grant 1-A065 ‘Fabrication of Thermionic Devices Using Directional Solidification/Sintering Processes for High Temperature CST Applications’ and by the University of Newcastle. The authors also would like to thank the University of Newcastle and ARENA through the sponsorship of PhD Scholarship for Mr Muhammad Hasan and Mr Dylan Cuskelly. Finally, we would like to thank the Laboratory Staff of the Discipline of Mechanical Engineering and, Electron Microscope and X-ray Unit for their assistance.

## References

1. Tamme, R. (2010). Optimised Industrial Process heat and Power Generation with Thermal Energy Storage *IEA* (Vol. 19): ECES.
2. Angrist, S.W. (1982). Direct Energy Conversion, 4<sup>th</sup> ed. Allyn and Bacon, Boston MA.
3. Hatsopoulos, G.N. (1973). Thermionic energy conversion. MIT Press, Cambridge.
4. Nottingham, W.B. (1959). Thermionic Diode as a Heat-to-Electrical-Power Transducer, *J. App. Phys.* 30, **3**, 413-17.
5. Hasan, M., Sugo, H. and Kisi, E. (2104). Synthesis of Thermionic Materials for Solar Energy Conversion. *Proc. Solar 14*, Melbourne 8-9 May.
6. Hasan, M., Sugo, H. and Kisi, H. (2013). Low temperature carbothermal and boron carbide reduction synthesis of LaB<sub>6</sub>. *JALCOM* 578,176–182
7. ASTM F83 - 71(2013). Standard Practice for Definition and Determination of Thermionic Constants of Electron Emitters, ASTM International.
8. Cronin, J.L., (1981). Modern dispenser Cathodes, *IEE Proc.* 128, **1**, 19-31.

Publication 8: Low temperature synthesis of low thermionic work function  
 $(\text{La}_x\text{Ba}_{1-x})\text{B}_6$ .

## 12. Publication 8: Low temperature synthesis of low thermionic work function $(\text{La}_x\text{Ba}_{1-x})\text{B}_6$ .

M. M. Hasan\*, D. Cuskelly, H. Sugo and E.H. Kisi

School of Engineering, the University of Newcastle, Callaghan NSW 2308, Australia

*Journal of Alloys and Compounds* DOI:10.1016/j.jallcom.2015.02.105

### Abstract

This study presents investigations of the microstructure, morphology and emission properties of the promising thermionic material  $(\text{La}_x\text{Ba}_{1-x})\text{B}_6$ . The material was synthesised by solid-state reaction without post-synthesis purifications. Powder X-ray diffraction revealed that samples prepared at a temperature  $\geq 1500$  °C had formed a significant proportion of solid solution (above 54 mass%). Subsequent sintering at 1950 °C caused the formation of a mixture of three solid solutions with the dominant phase being  $(\text{La}_{0.31}\text{Ba}_{0.69})\text{B}_6$  ~85% (by mass). The Richardson work function and emission constant for this boride mixture were found to be 1.03 eV and  $8.44 \times 10^{-6}$  A.cm.K<sup>-2</sup> respectively.

## 1. Introduction

Thermionic cathodes are widely used in a variety of thermal emission and field emission devices including cathode ray tubes, sensors and electron microscopes. Each application utilises materials tuned for the specific mode of operation (DC, pulsed *etc.*) and required emission current. Recently, the potential of thermionic energy conversion for concentrated solar electricity generation or industrial waste heat recovery has caused a revival of interest in thermionic emitters for long-term stable DC emission. In terms of material properties, the voltage and power output of a thermionic converter can be maximised by selecting an emitter (cathode) with a moderate work function and high emission constant to yield an appropriate current at the operating temperature. The collector material (anode) should possess a low work function and low emission constant to minimize back emission of electrons. Other properties of the emitter includes high melting temperature, low vapour pressure and high electrical conductivity to sustain high emission currents; properties not often available in a single phase. A case in point are the rare-earth hexaborides ( $\text{REB}_6$ ) which have outstanding thermal stability in vacuum as well as moderate work function (2.5~3 eV).

Numerous pure and mixed hexaborides have been investigated for thermionic or field emission properties including ( $\text{LaB}_6$  and other  $\text{REB}_6$ ) <sup>[1]</sup>,  $(\text{La}_x\text{RE}_{1-x})\text{B}_6$  <sup>[1]</sup>,  $(\text{La}_x\text{Gd}_{1-x})\text{B}_6$  <sup>[2]</sup>,  $(\text{La}_x\text{Ce}_{1-x})\text{B}_6$  <sup>[3]</sup>,  $(\text{Nd}_x\text{Gd}_{1-x})\text{B}_6$  <sup>[4]</sup>, and  $(\text{La}_x\text{Ba}_{1-x})\text{B}_6$  <sup>[6,7,8]</sup>. Due to the good emission characteristics and low evaporation rate at higher temperatures,  $\text{LaB}_6$  has been identified to be the best thermionic emitter <sup>[1,2]</sup> however, barium compounds are often used to reduce the work function of different cathode materials through the formation of a barium monolayer <sup>[5, 6]</sup>. As a consequence, the possibility of enhanced thermionic emission properties in lanthanum hexaborides by forming solid-solutions or mixed boride compounds with the general formulae  $(\text{La}_x\text{Ba}_{1-x})\text{B}_6$  has also been explored <sup>[6,7,8]</sup>. More

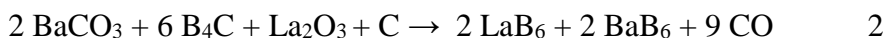
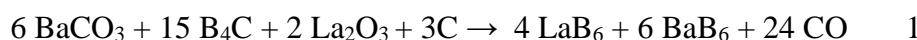
Publication 8: Low temperature synthesis of low thermionic work function  
( $\text{La}_x\text{Ba}_{1-x}\text{B}_6$ ).

recent studies have involved the preparation of ( $\text{La}_x\text{Ba}_{1-x}\text{B}_6$ ) using mixtures of lanthanum and barium hydrides with boron followed by processing using spark plasma sintering [7, 8] or the aluminium flux method [11]. Zhou *et al.* [7] reported on a boride mixed in the proportions ( $\text{La}_{0.6}\text{Ba}_{0.4}\text{B}_6$ ). The Richardson work function ( $\varnothing_R$ ) was determined to be 1.95 eV and the Richardson emission constant ( $A_R$ ) = 1.07  $\text{Acm}^{-2}\text{K}^{-2}$ . These properties were determined using a cathode area of 0.64 mm<sup>2</sup> under pulsed emission current conditions of 20  $\mu\text{s}$  at 120 Hz between 1500°K and 1873°K. An improvement of ~34% at 1873°K was noted in the emission properties of the ( $\text{La}_{0.6}\text{Ba}_{0.4}\text{B}_6$ ) mixture compared to pure  $\text{LaB}_6$  prepared using the spark plasma sintering [7].

Observation of the XRD plot reported by Zhou *et al.* [7] does not reveal the formation of any significant level of solid-solution between the two compounds. Most likely, this is a the result of the very short sintering time (5 min) of the spark plasma sintering technique. Kiparisov *et al.* [6] using the borothermal reduction method prepared solid-solutions of ( $\text{La}_x\text{Ba}_{1-x}\text{B}_6$ ) (where  $x = 0.6-0.7$ ) and reported an improvement of the emission characteristics. In order to explore any possible further enhancement of the emission properties by barium substitution into  $\text{LaB}_6$ , at higher Ba ratios, attempts to synthesize ( $\text{La}_x\text{Ba}_{1-x}\text{B}_6$ ) solid-solutions using the boron carbide solid-state reduction method are reported in the present work. ( $\text{La}_x\text{Ba}_{1-x}\text{B}_6$ ) cathode materials were fabricated through mechanical milling, pressing, firing and sintering. This work describes the structural, chemical and thermionic properties of the resultant mixed and solid solution boride materials.

## 2. Experimental details

Samples were prepared using: barium carbonate (BaCO<sub>3</sub>, May & Baker Ltd., UK, 99.5 wt% purity), La<sub>2</sub>O<sub>3</sub> (Sigma-Aldrich Co., USA, 99.9% purity, particle size 1-3 µm), boron carbide (Alfa Aesar Co. UK, 99+% purity, particle size <10 µm) and graphite (Sigma-Aldrich Co., USA, 99.99% purity, particle size <150 µm) powders. Mixed borides of LaB<sub>6</sub> and BaB<sub>6</sub> were prepared by reducing La<sub>2</sub>O<sub>3</sub> and BaCO<sub>3</sub> with boron carbide and graphite using the boron carbide reduction method [11]. Stoichiometric amounts of these raw materials sufficient for samples of ~5 g were mixed to produce LaB<sub>6</sub>-BaB<sub>6</sub> in 50:50 or 40:60 (La:Ba) molar proportions as given by Equation 1 and Equation 2 respectively.



Three basic variations of the method were used. In Method A, the effects of sintering time at a temperature of 1400°C were evaluated. The starting materials were milled for 20 min using zirconia media in a SPEX8000 mixer mill with a ball-to-powder ratio of 5:1. This corresponds to the lower end of the high-energy milling range. Milled powders were pressed into 19 mm diameter pellets for firing in a moderate vacuum under conditions set out in Table 1.

In Method B the effects of pre-milling the starting oxide and carbonate (La<sub>2</sub>O<sub>3</sub> and BaCO<sub>3</sub>) were investigated. The oxide/carbonate reactants were pre-milled in order to begin solid solution formation in the precursor material. Following this pre-milling, B<sub>4</sub>C and C were added and a further milling period was conducted. Subsequently, pellets were pressed and fired under the conditions shown in Table 1.

In Method C, the effects of secondary high temperature treatment was evaluated. The pre-fired pellets prepared using Method B were re-ground, milled for 1 h, pressed and refired at 1950°C for 1 h using a high-vacuum tantalum furnace. Characterisation was carried out on both pellets and crushed powders. Prior to characterisation, all pellet samples were abraded by 0.2-0.5 mm to remove any possible surface contaminants due to the prevailing conditions in the furnaces.

*Table 1. Material preparation conditions.*

| Material | Ba:La Ratio | Method | Sintering T (°C) | Sintering Time (h) | Milling Time                  |
|----------|-------------|--------|------------------|--------------------|-------------------------------|
| 1        | 01:01       | A      | 1400             | 2                  | 20 min                        |
| 2        | 01:01       | A      | 1400             | 4                  | 20 min                        |
| 3        | 01:01       | A      | 1400             | 14                 | 20 min                        |
| 4        | 06:04       | B      | 1400             | 4                  | Pre-mill 1 h, co-mill 20 min  |
| 5        | 06:04       | B      | 1400             | 4                  | Pre-mill 24 h, co-mill 20 min |
| 6        | 06:04       | A      | 1500             | 2                  | 20 min                        |
| 7        | 06:04       | B      | 1500             | 2                  | Pre-mill 4 h, co-mill 20 min  |
| 8        | 06:04       | C      | 1950             | 1                  | Sample 7 re-milled 1 h        |

The phases present in the mixed borides were analysed by X-ray diffraction (Philips 1710 and Panalytical X'pert MPD) using  $\text{CuK}\alpha$  radiation ( $\lambda=0.15406$  nm), operating at an accelerating voltage of 40 kV, an emission current of 40 mA and a scanning rate of 0.025°/s over the  $2\theta$  range 20-80°. Phase identification utilized the International Centre for Diffraction Data (ICDD) database. Standard structural models of  $\text{BaB}_6$ ,  $\text{LaB}_6$  and  $\text{La}_{0.5}\text{Ba}_{0.5}\text{B}_6$  (seen in Table 2) were utilised to confirm the phase identification for quantitative phase analysis of all samples using Rietveld refinement and the method of Hill and Howard [9].

*Table 2. Standard structural models of BaB<sub>6</sub>, LaB<sub>6</sub> and (La<sub>x</sub>Ba<sub>1-x</sub>)B<sub>6</sub>.*

|                                      | <b>BaB<sub>6</sub></b>          | <b>LaB<sub>6</sub></b>          | <b>(La<sub>x</sub>Ba<sub>1-x</sub>)B<sub>6</sub></b> |
|--------------------------------------|---------------------------------|---------------------------------|--|
| <b>Crystal System</b>                | Cubic                           | Cubic                           | Cubic  |
| <b>Space Group</b>                   | Pm3m                            | Pm3m                            | Pm3m   |
| <b>lattice Parameters,<br/>a (Å)</b> | 4.2615                          | 4.157                           | 4.2  |
| <b>Boron Position</b>                | x = 0.5, y = 0.5,<br>z = 0.2054 | x = 0.5, y = 0.5,<br>z = 0.1975 | x = 0.5, y = 0.5,<br>z = 0.202                       |

The surface morphology of the as-fired, abraded and post-emission pellets was characterized using secondary electron and backscattered electron imaging, and the chemical composition of samples was investigated by means of energy dispersive X-ray analysis (EDX) using a ZEISS Sigma VP FESEM equipped with a Bruker light element Silicon strip detector (SSD) and operated at accelerating voltages of 3-25 kV.

Thermionic emission to evaluate the emission constants was performed on abraded samples in a Schottky device in the temperature range of 1400-1540°K using a 3 mm gap between the emitter and the collector. The collector itself had a rectangular shape 2.5 by 4.5 mm. Vacuum was maintained at  $<1 \times 10^{-3}$  Pa during testing and prior to data collection the samples were activated for 1 hour at the highest operating temperature. DC emission testing was carried out by applying accelerating voltages in the range of 0-300 V during a series of constant temperature holds. Schottky and Richardson plots were used to find the Richardson work function of the sample sintered at 1950°C in accordance with ASTM Standard F83-71 <sup>[10]</sup>.

### 3. Results and discussion

Materials prepared using Method A with a 50:50 La:Ba compositional ratio represent a coherent set investigating the influence of sintering time on the formation of the boride solid solution. XRD patterns from these samples are shown in Figure 1. The major peaks belong to cubic  $\text{BaB}_6$  and  $\text{LaB}_6$  as indicated by the arrows. The sample fired for 2 h also shows the presence of the intermediate  $\text{BaB}_2\text{O}_4$  phase, unreacted boron carbide and BaO. The pronounced intensity saddle between the  $\text{LaB}_6$  and  $\text{BaB}_6$  peaks indicates that a solid solution ( $\text{La}_x\text{Ba}_{1-x}\text{B}_6$ ) has formed in addition to the pure boride phases. There is little apparent improvement in the proportion of the boride solid solution after heating to 1400°C for 14 h instead of 4 h or even 2 h. Therefore, whereas the individual borides were readily synthesised at this temperature, solid solution formation halted quite early in the process.

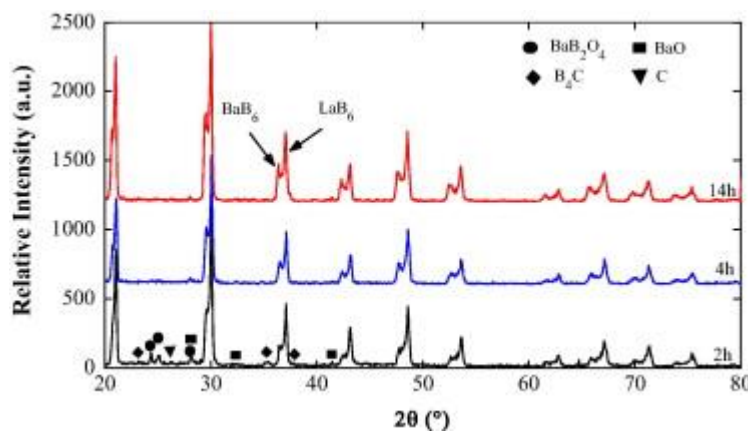
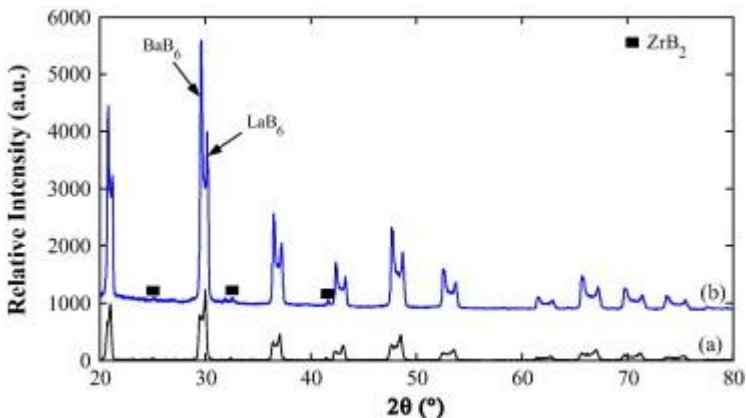


Figure 1 – Effect of time at 1400 °C on XRD patterns for  $\text{BaB}_6\text{-LaB}_6$  (molar ratio 50:50) produced by Method A.

In Figure 2, XRD patterns for materials prepared using Method B and fired at 1400 °C for 4 h show that this procedure also resulted in a two boride mixture with some solid solution. The sample milled for 24 h displays some  $\text{ZrB}_2$  as the milling was performed in a zirconia ball and vial system. It also shows a larger particle size (narrower

peaks) as well as approximately the same degree of solid solution compared to those produced by Method A. The relative peak height ratios of  $\text{LaB}_6$  and  $\text{BaB}_6$  show that now the proportion of  $\text{BaB}_6$  is greater than  $\text{LaB}_6$  in agreement with the 40:60 (La:Ba) starting ratio.



*Figure 2. Effect of pre-milling  $\text{La}_2\text{O}_3$  and  $\text{BaCO}_3$  for (a) 1 h and (b) 24 h on XRD patterns for the  $\text{BaB}_6\text{-LaB}_6$  (40:60 La:Ba) fired at 1400 °C for 4 h using Method B.*

To highlight the influence of firing temperature, Figure 3 shows XRD patterns for samples prepared using Methods A and B, but fired at 1500°C for 2 h. The presence of  $\text{LaAlO}_3$  in one sample is thought to be due to slight evaporation of aluminium from the alumina tube furnace. Figure 3 shows the appearance of a set of middle peaks between the two major peaks of the single borides. These can be thought of as the significant formation of a solid solution  $(\text{La}_x\text{Ba}_{1-x})\text{B}_6$  or perhaps a discrete intermediate compound  $\text{LaBaB}_{12}$  although these are indistinguishable using standard XRD due to the very similar X-ray scattering power of Ba and La which are adjacent in the periodic table.

As shown in Figure 3b, material number 7 in Table 1, is expected to have the highest amount of solid solution due to the distinct ‘middle’ peaks belonging to the solid solution. This sample was selected to be sintered at 1950°C for 1 h with the expectation that further solid solution would form at the higher temperature. Prior to sintering, it was

milled for 1 h to facilitate better contact among single borides and refinement of particle size. The XRD pattern belonging to the sintered pellet (Figure 3c) was found to have a series of unique broadened peaks at regular intervals. Those peaks (I, II and III as shown by arrows) can be thought of as the evolution of three different solid solutions:

- i) Peak I, a barium-rich  $(\text{La}_x\text{Ba}_{1-x})\text{B}_6$ ,
- ii) Peak II, approximately equi-molar  $(\text{La}_{0.5}\text{Ba}_{0.5})\text{B}_6$  and
- iii) Peak III, a lanthanum-rich  $(\text{La}_x\text{Ba}_{1-x})\text{B}_6$ .

In terms of minor phases, only  $\text{ZrB}_2$  (shown by ‘▼’ in the figure) was found to be present due to 1 h milling in addition to 4 h milling in a zirconia vessel during the initial synthesis investigation.

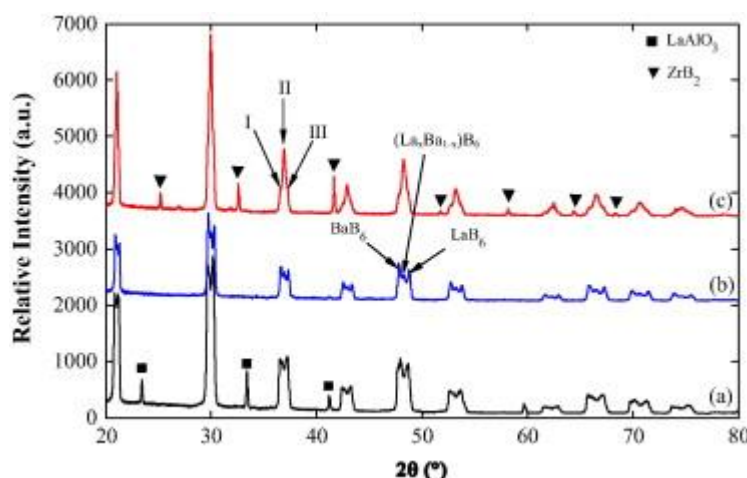


Figure 3 XRD patterns for the  $\text{BaB}_6\text{-LaB}_6$  (60-40%) samples prepared at  $1500\text{ }^\circ\text{C}$  for 2 h (a) Method A, (b) Method B and (c) sample “b” fired at  $1950\text{ }^\circ\text{C}$  for 1 h (Method C).

Table 3 shows the phase proportions and lattice constants derived via the Rietveld refinement for  $\text{BaB}_6$ ,  $\text{LaB}_6$  and their solid solution for the materials prepared with 50:50  $\text{BaB}_6\text{-LaB}_6$ . Samples prepared using Method A and fired for 4 h and 14 h at  $1400\text{ }^\circ\text{C}$  were

found to have the same proportion of  $\text{La}_{0.5}\text{Ba}_{0.5}\text{B}_6$  (34.2% by mass). The proportion of  $\text{BaB}_6$  compared with  $\text{LaB}_6$  increases throughout the series. This effect is not understood at this stage however the rates of formation would depend on the respective diffusion coefficients of La and Ba in the individual phases. For Method A, the lattice constants for the solid solution are observed to be the same as the value for  $\text{La}_{0.5}\text{Ba}_{0.5}\text{B}_6$  (4.200 Å) reported by Bliznakovet *et al.*<sup>[14]</sup>. Therefore, it appears that approximately one third of the material has converted into the intended mixed boride solid solution of  $(\text{La}_{0.5}\text{Ba}_{0.5}\text{B}_6)$ .

*Table 3. Quantitative phase analysis and lattice parameters from Rietveld refinement for the mixed boride materials having  $\text{LaB}_6-\text{BaB}_6$  (50:50 La:Ba) molar*

| Temperature-Firing Time | % By Mass      |                |  | Lattice Constant (Å) |                |  |
|-------------------------|----------------|----------------|--|----------------------|----------------|--|
|                         | $\text{BaB}_6$ | $\text{LaB}_6$ | $\text{Ba}_x\text{La}_{1-x}\text{B}_6$ | $\text{BaB}_6$       | $\text{LaB}_6$ | $\text{Ba}_x\text{La}_{1-x}\text{B}_6$ |
| 1400–2 h                | 18             | 59             |  | 23                   | 4.2373(7)      | 4.1691(4)                              |
| 1400–4 h                | 29.5           | 36.4           |  | 34.2                 | 4.2514(1)      | 4.1721(1)                              |
| 1400–14 h               | 32.7           | 33.1           |  | 34.2                 | 4.2486(1)      | 4.1707(1)                              |

Rietveld refinement results for the mixed boride samples with 40:60 (La:Ba) molar ratios of  $\text{BaB}_6-\text{LaB}_6$  are given in Table 4. The table shows the effect of temperature and milling duration on the formation of the solid solutions  $(\text{La}_x\text{Ba}_{1-x})\text{B}_6$ . It may be seen that pre-milling the starting oxide-carbonate mixture (Method B) is only mildly effective in increasing the yield of solid solution if followed by firing at 1400°C. Its effectiveness is more apparent in samples fired at 1500°C where a yield of 54% was attained compared with only 43% using Method A. This is the lowest known preparation temperature to yield a material the majority of which is a hexa-boride solid solution. The highest yield by far (84%) is from the material produced using Method C (sintered at 1950°C). This trend is shown in Figure 4.

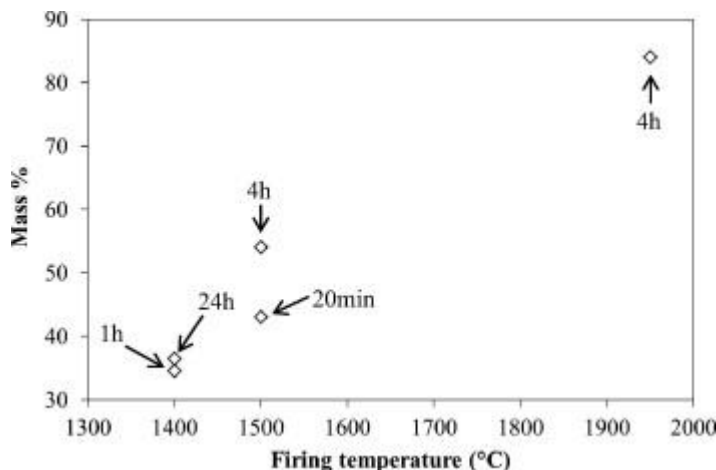


*Figure 4 Variation in mass % of  $(\text{La}_x\text{Ba}_{1-x})\text{B}_6$  solid solution with firing temperatures. Arrows show pre-milling times.*

A comparison of the lattice constants for Method A reported in Table 3 and those for Methods B and C conveyed in Table 4 indicate that the lattice parameter  $a$  for all three phases has increased marginally with the higher Ba molar fraction, the change being more noticeable for the 40:60 (La:Ba) molar  $(\text{La}_x\text{Ba}_{1-x})\text{B}_6$  compound. The relationship between the calculated lattice constants shown in Table 4 and those previously reported in the literature are shown in Figure 5. The lattice parameters for the 40:60 (La:Ba) molar  $(\text{La}_x\text{Ba}_{1-x})\text{B}_6$  solid solution phase (central peaks in Figures 1-3) were found to be very consistent with a mean value of approximately 4.2218(3) Å. This is larger than the literature value for  $\text{La}_{0.5}\text{Ba}_{0.5}\text{B}_6$  (4.200 Å)<sup>[14]</sup>, indicating that the molar proportion of Ba is higher for the  $(\text{La}_x\text{Ba}_{1-x})\text{B}_6$  solid solution *i.e.* a barium rich solid solution has been formed. By fitting a quadratic to the literature lattice parameters for pure  $\text{BaB}_6$ ,  $\text{Ba}_{0.5}\text{La}_{0.5}\text{B}_6$  and pure  $\text{LaB}_6$ <sup>6</sup>, it was possible to estimate the  $\text{BaB}_6$  fraction  $f(\text{Ba})$  of the main solid solution to be 0.69. Similarly, the lattice constants for the  $\text{LaB}_6$  rich phase is quite different to the lattice parameter for the standard NIST  $\text{LaB}_6$  (4.15689(8) Å)<sup>[15]</sup> and

<sup>6</sup>  $a=0.037f(\text{Ba})^2 + 0.0675f(\text{Ba}) + 4.157$  where  $f(\text{Ba})$  is the molar fraction of  $\text{BaB}_6$  in the mixture.

its  $f(\text{Ba})$  may be estimated to be 0.28. It is also worth noting that although the mean lattice constant of the  $\text{BaB}_6$ -rich phase ( $4.2555(3)$  Å) is offset from the standard value in ICDD card no. 65-1833 ( $4.2680$  Å), this amounts to only a small degree of solid solution ( $f(\text{Ba}) = 0.97$ ). In summary all three of the boride phases are solid solutions. Given the relative time insensitivity of the phase composition, considerable control may be exercised over the relative proportions of these phases *via* the sintering temperature thereby allowing tuneable thermionic properties.

*Table 4. Quantitative phase analysis and lattice parameters from Rietveld refinement for the mixed boride samples having  $\text{LaB}_6-\text{BaB}_6$  (40:60 La:Ba) molar*

| Temperature-Firing Time     | % By Mass      |                |  | Lattice Constant (Å) |                |  |
|-----------------------------|----------------|----------------|--|----------------------|----------------|--|
|                             | $\text{BaB}_6$ | $\text{LaB}_6$ | $\text{Ba}_x\text{La}_{1-x}\text{B}_6$ | $\text{BaB}_6$       | $\text{LaB}_6$ | $\text{Ba}_x\text{La}_{1-x}\text{B}_6$ |
| <b>1400–4 h<sup>A</sup></b> | 19.9           | 45.5           | 34.6                                   | 4.2566(1)            | 4.1822(1)      | 4.2241(3)                              |
| <b>1400–4 h<sup>B</sup></b> | 40.3           | 23.2           | 36.5                                   | 4.2576(1)            | 4.1761(1)      | 4.2195(2)                              |
| <b>1500–4 h</b>             | 19.7           | 37.2           | 43.1                                   | 4.2602(1)            | 4.1841(2)      | 4.2287(3)                              |
| <b>1500–4 h<sup>C</sup></b> | 26.5           | 19.4           | 54.1                                   | 4.2556(1)            | 4.1747(1)      | 4.2214(2)                              |
| <b>1950–1 h</b>             | 8.4            | 7.6            | 84                                     | 4.2555(3)            | 4.1757(3)      | 4.2137(3)                              |

<sup>A</sup> the starting oxides milled for 1 h

<sup>B</sup> the starting oxides milled for 24 h

<sup>C</sup> the starting oxides milled for 4 h

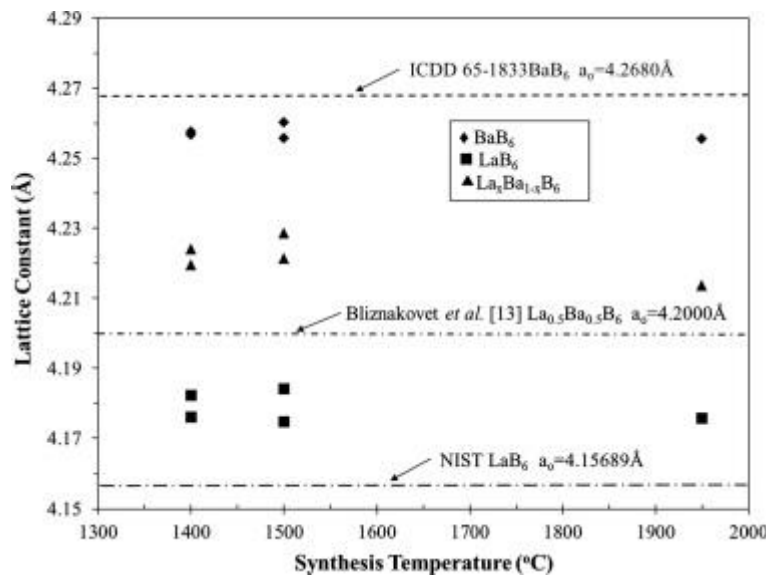


*Figure 5 Relationship between the measured lattice parameters and standard values for mixed boride samples having BaB<sub>6</sub>-LaB<sub>6</sub> (40:60 La:Ba) molar proportions prepared at different temperatures.*

Figure 6 shows secondary electron images for the mixed boride samples 7 and 8 prepared at 1500 and 1950°C using 4 h milled starting blends. The microstructure of both samples contains crystallites with cubic morphology. Large sintered and inter-grown crystals were found to form in the sample prepared at 1500°C. Through EDS spot analysis, some areas could be identified to comprise of BaB<sub>6</sub> (with nominal compositions of 17.0 at% Ba and 83.0 at% B, labelled as 1), LaB<sub>6</sub> regions (2) and (La<sub>x</sub>Ba<sub>1-x</sub>)B<sub>6</sub> solid solution consisting of 17.2 at% La, 33.7 at% Ba and 49.1 at% B (region 3). The sample sintered at 1950°C was found to be dense and compact with large grains (shown by arrows) and some pores. From EDS spectra and elemental maps, some areas were found to have zirconium (ZrB<sub>2</sub>) and only few small areas had iron (possibly FeB) present.

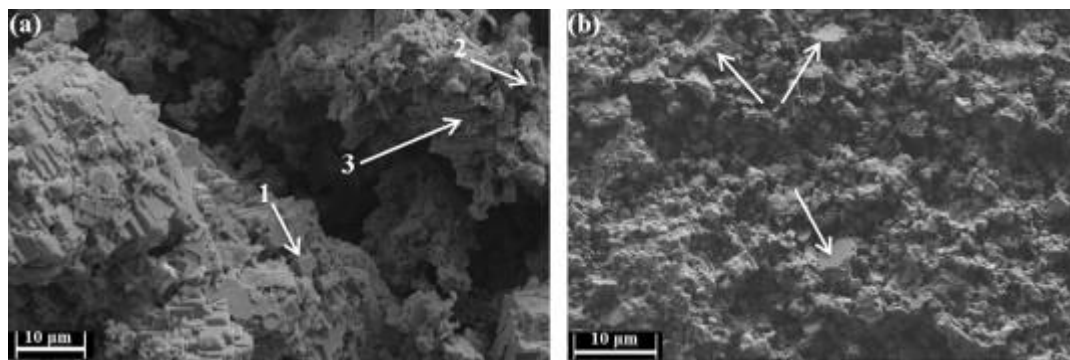


Figure 6 Secondary electron images for the  $\text{BaB}_6\text{-LaB}_6$  (40:60 La:Ba) samples prepared from 4 h milled starting blends (a) Method B firing at  $1500^\circ\text{C}$  for 2 h and (b) Method C firing at  $1950^\circ\text{C}$  for 1 h.

Samples of  $\text{BaB}_6\text{-LaB}_6$  prepared using Method C had sintered to a density of 59% of the combined theoretical density during vacuum heating at  $1950^\circ\text{C}$  for 1 hour. Figure 7 shows the Schottky and Richardson plots for that material. The Richardson work function and emission constant were evaluated to be 1.03 eV and  $8.44 \times 10^{-6} \text{ Acm}^{-2}\text{K}^2$  respectively. This Richardson work function is very much smaller than the value (1.95 eV) reported for the mixed boride of composition  $(\text{La}_{0.6}\text{Ba}_{0.4})\text{B}_6$  prepared by spark plasma sintering [7]. Therefore, it can be seen that barium enrichment and solid solution formation contributes to a spectacular decrease in work function. In contrast to the findings by [7], the very low emission constant is accompanied by a very small current density. This may be a result of the high proportion of divalent Ba cations in the  $(\text{La}_{0.31}\text{Ba}_{0.69})\text{B}_6$  structure, imparting semiconductor properties to the hexaboride solid solution [7,16]. The metallic/semiconductor properties of this mixed boride should be investigated further. The low work function and low DC current output of this boride mixture indicate that this material may be better suited for use as a collector rather than an emitter in thermionic energy converter applications, or as an emitter in traditional AC or pulsed thermionic devices. Alternatively, it may be possible to blend this  $(\text{La}_x\text{Ba}_{1-x})\text{B}_6$  solid solution with  $\text{LaB}_6$  to impart metallic conduction to the cathode whilst still obtaining the benefit of a

reduced work function from the Ba rich solid solution. Further experimental and DFT modelling in this area is being undertaken.

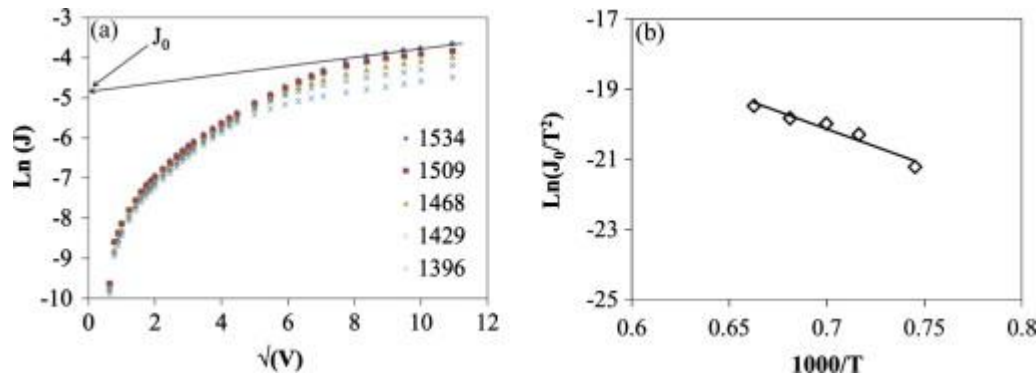


Figure 7(a) Schottky plots at different temperatures (in Kelvin) and (b) Richardson plot for a typical  $(\text{La}_x\text{Ba}_{1-x})\text{B}_6$  cathode prepared using Method C.

After the emission runs, the sample appears to have a similar proportion of solid solution.  $\text{ZrB}_2$  was found to be still present although new contaminant phases  $\text{LaAlO}_3$  and possibly some  $\text{La}_3\text{BO}_6$  had formed as shown in Figure 8. Aluminium and oxygen contamination are most likely to have occurred due to the alumina sample environment in the Schottky chamber. The role of these impurities during emission testing is unknown however the minimum work function ( $\phi_R$ ) for the  $\text{LaB}_6\text{-ZrB}_2$  system has been reported to be 2.86 eV for a 50:50 molar ratio [17].

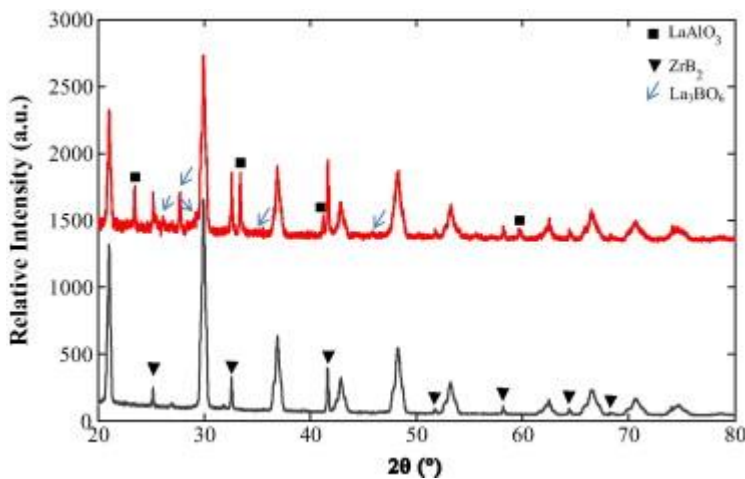


Figure 8 XRD patterns for Method C cathode (a) before and (b) after emission tests.

Representative secondary and backscattered electron images for samples before and after emission runs are shown in Figure 9. After emission testing, the large crystals (shown by arrows) can be seen more clearly on the emission surface. It is also noted that emission tests generate many micro-pores (one shown as a red arrow in Figure 9(d)) across the sample surface. From EDS analysis, the sample was found to have a very small amount of oxygen, aluminium, zirconium; and yttrium in trace amounts. Elemental mapping showed that the large particles (Figure 9 (d)) are LaAlO<sub>3</sub> and some of the long crystals contain yttrium. The contamination by yttrium originates from wear particles of the yttria partially stabilized zirconia milling vial and media during sample preparation. It is expected that the level of impurity arising from the milling process may be decreased through adjustment of the ball to powder ratio and milling time.

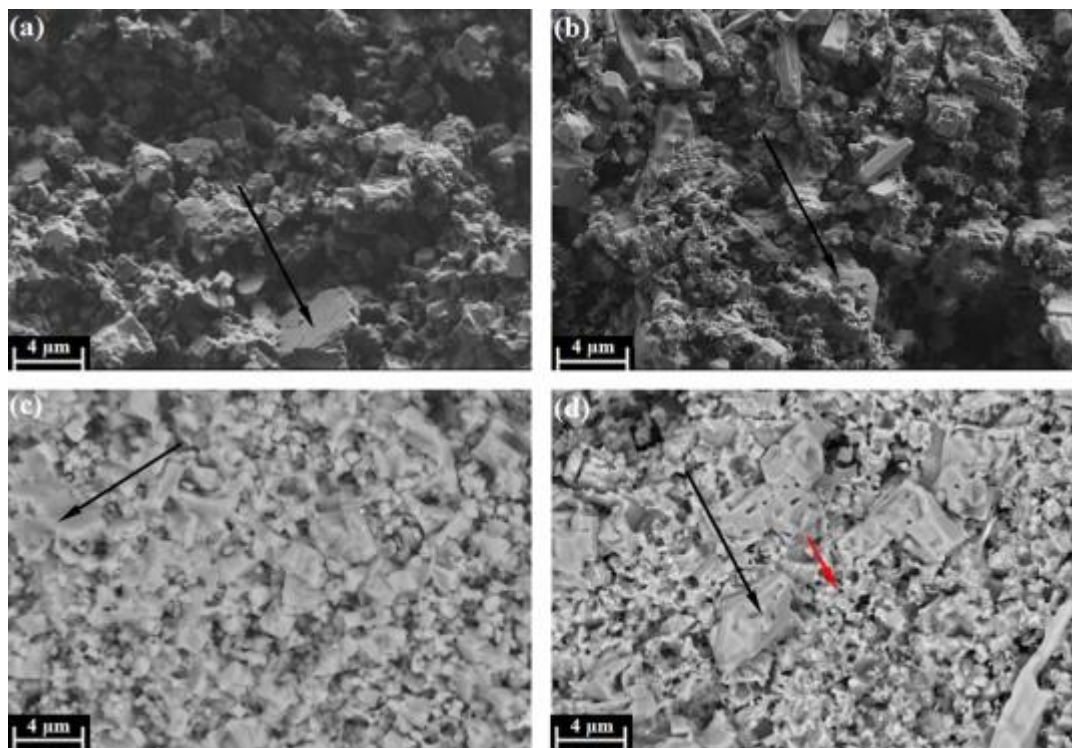


Figure 9. Secondary and backscattered electron images for  $(\text{La}_x\text{Ba}_{1-x})\text{B}_6$  (40:60 La:Ba) sample prepared at 1950 °C for 1 h before emission tests (a) and (c) and afterwards (b) and (d).

#### 4. Conclusion

Mixed  $(\text{La}_x\text{Ba}_{1-x})\text{B}_6$  having a significant proportion of dual boride solid-solution were prepared at relatively low temperature using solid-state reactions via the boron carbide method. Notably, substantial solid solution (36.5% by mass) formed in  $(\text{La}_{0.5}\text{Ba}_{0.5})\text{B}_6$  even at 1400°C and the remaining borides, also with some level of solid solution, coexisted separately as  $\text{LaB}_6$ -rich and  $\text{BaB}_6$ -rich phases. Sintering at around 1950°C for 1 h produced a majority (~85%) of the solid solution  $(\text{La}_{0.31}\text{Ba}_{0.69})\text{B}_6$  from a starting composition of 40:60 (La:Ba) molar ratio. This boride mixture had an exceptionally low work function,  $\phi_R$  1.03 eV. Despite this low Richardson work function, the mixed boride solid solution yielded a very low emission constant ( $A_R$ ) of  $8.44 \times 10^{-6} \text{ A/cm}^2\text{K}^2$  producing low direct current outputs. The reason for the low emission constant is not clear but may

be due to the semiconducting nature of divalent Ba hexaboride. The low work function indicates the potential application for this material to be used as a collector rather than an emitter in thermionic energy converter applications. Alternatively, it may be possible to blend this Ba rich  $(\text{La}_x\text{Ba}_{1-x})\text{B}_6$  solid solution with  $\text{LaB}_6$  to impart metallic conduction to the cathode and increase the emission constant whilst maintaining the benefit of low work function opening the potential for tuneable thermionic properties. Further work on the semiconducting nature of the  $(\text{La}_x\text{Ba}_{1-x})\text{B}_6$  mixed boride and  $\text{LaB}_6-(\text{La}_x\text{Ba}_{1-x})\text{B}_6$  alloy blends is being undertaken.

### Acknowledgements

The authors gratefully acknowledge the financial support given for this work by the Australian Renewable Energy Agency (ARENA, Grant No.1-A065) as well as an Australian Postgraduate Award and Tuition Fee Scholarship for the principal author. The authors also acknowledge help and support from David Phelan and Jennifer Zobec from the University of Newcastle Electron Microscope & X-ray Unit and from Anthony Rawson of the Structure of Advanced Materials Group.

## References

- [1] J.M. Lafferty, Boride Cathodes, *J. Appl. Phys.* 22 (1951) 299-309.
  - [2] M. Futamoto, M. Nakazawa, U. Kawabe, Thermionic emission properties of hexaborides, *Surf. Sci.* 100 (1980) 470-80.
  - [3] L.H. Bao, Z. Jiu-Xing, Z. Ning, L. Xiao-Na, Z. Shen-Lin, In situ (La<sub>x</sub>Gd<sub>1-x</sub>)B<sub>6</sub> cathode materials prepared by the spark plasma sintering technique, *Physica Scripta* 85 (2012) 035710.
  - [4] Menaka, R. Patra, S. Ghosh, A.K. Ganguli, Novel borothermal route for the synthesis of lanthanum cerium hexaborides and their field emission properties, *J. Solid State Chem.* 194 (2012) 173-8.
  - [5] J.X. Zhang, L.H. Bao, S.L. Zhou, Tegus, Synthesis, thermionic emission and magnetic properties of (Nd<sub>x</sub>Gd<sub>1-x</sub>)B<sub>6</sub>, *Chin. Phys. B* 20 (2011) 058101.
  - [6] S.S. Kiparisov, T.P. Tsypysheva, N.A. Iofis, Issledovanie uslovij polucheniya dvojnykh boridov redkozemel'nykh i shchelochnozemel'nykh metallov (On conditions of producing double borides of rare-earth and alkali-earth metals), *Izvestiya Vysshikh Uchebnykh Zavedenij. Tsvetnaya Metallurgiya* 6 (1976) 76-80; (in Russian).
  - [7] S.L. Zhou, J.X. Zhang, L.H. Bao, X.G. Yu, Q.L. Hu, D.Q. Hu, Enhanced thermionic emission properties in textured two-phase LaB<sub>6</sub>-BaB<sub>6</sub> system prepared by spark plasma sintering, *J. Alloy Compd.* 611 (2014) 130-4.
  - [8] J.X. Zhang, S.L. Zhou, D.M. Liu, L. H. Bao, Y.F. Wei, R.G. Ma, Q.Z. Huang, Synthesis, characterization and properties of nanostructured (LaxBa<sub>1-x</sub>)B<sub>6</sub> cathode materials by liquid phase reactive spark plasma sintering. 8th International Vacuum Electron Sources Conference and Nanocarbon (IVESC 2010) 2010, 175-7.
  - [9] I. Brodie, Emission Fluctuations of Tungsten-Based Barium Dispenser Cathodes, *J. Appl. Phys.* 32 (1961) 2039-46.
  - [10] R.O. Jenkins, A Review of Thermionic Cathodes, *Vacuum* 19 (1969) 353-9.
  - [11] M. Hasan, H. Sugo, E. Kisi, Low temperature carbothermal and boron carbide reduction synthesis of LaB<sub>6</sub>, *J. Alloy Comp.* 578 (2013) 176-82.
  - [12] R.J. Hill, C.J. Howard, Quantitative phase analysis from neutron powder diffraction data using the Rietveld method, *J. Appl. Crystallogr.* 20 (1987) 467-74.
  - [13] ASTM F83-71(2013), Standard Practice for Definition and Determination of Thermionic Constants of Electron Emitters, ASTM International, West Conshohocken, PA, 2013, www.astm.org
  - [14] G. Bliznakov, I. Tsolovski, P. Peshev, *Revue Internationale des Hautes Temperatures et des Refractaires* 6 (1969) 159-164.
  - [15] SRM (2010) 660b; Lanthanum Hexaboride Powder Line Position and Line Shape Standard for Powder Diffraction ; National Institute of Standards and Technology; U .S. Department of Commerce: 449 Gaithersburg, MD.
  - [16] K. Maiti, V.R.R. Medicherla, S. Patil, R.S. Singh, Revelation of the Role of Impurities and Conduction Electron Density in the High Resolution Photoemission Study of Ferromagnetic Hexaborides, *Phys. Rev. Lett.* 99 (1-4) (2007) 266401-4.
  - [17] E.K. Storms, Thermionic emission and vaporization behavior of the ternary systems of lanthanum hexaboride containing molybdenum boride, molybdenum diboride, zirconium diboride, gadolinium hexaboride, and neodymium hexaboride, *J. Appl. Phys.* 54(2) (1983) 1076-81..
1. Futamoto, M., M. Nakazawa, and U. Kawabe, *Thermionic emission properties of hexaborides*. Surface Science, 1980. **100**(3): p. 470-480.

Publication 8: Low temperature synthesis of low thermionic work function  
(LaxBa<sub>1-x</sub>)B<sub>6</sub>.

2. Bao, L.-H., et al., *In situ (La<sub>x</sub>Gd<sub>1-x</sub>)B<sub>6</sub> cathode materials prepared by the spark plasma sintering technique*. Physica Scripta, 2012. **85**(3): p. 035710.
3. Menaka, et al., *Novel borothermal route for the synthesis of lanthanum cerium hexaborides and their field emission properties*. Journal of Solid State Chemistry, 2012. **194**: p. 173-178.
4. Zhang, J.X., et al., *Synthesis, thermionic emission and magnetic properties of (Nd(x)Gd(1-x))B(6)*. Chinese Physics B, 2011. **20**(5).
5. Brodie, I., *Emission Fluctuations of Tungsten-Based Barium Dispenser Cathodes*. Journal of Applied Physics, 1961. **32**(10): p. 2039-2046.
6. Jenkins, R.O., *A Review of Thermionic Cathodes*. Vacuum, 1969. **19**(8): p. 353-359.
7. Zhou, S.L., et al., *Enhanced thermionic emission properties in textured two-phase LaB<sub>6</sub>-BaB<sub>6</sub> system prepared by spark plasma sintering*. Journal of Alloys and Compounds, 2014. **611**(0): p. 130-134.
8. Zhang, J.X., et al. *Synthesis, characterization and properties of nanostructured (LaxBa<sub>1-x</sub>)B<sub>6</sub> cathode materials by liquid phase reactive spark plasma sintering*. in *Vacuum Electron Sources Conference and Nanocarbon (IVESC), 2010 8th International*. 2010.
9. Hill, R.J. and C.J. Howard, *Quantitative phase analysis from neutron powder diffraction data using the Rietveld method*. Journal of Applied Crystallography, 1987. **20**(6): p. 467-474.
10. F83, A.S., *Definition and determination of thermionic constants of electron emitters*. 2013.

## 13. Additional results

As a result of the condensed nature of the publications many of the findings obtained through the thesis have yet to be presented in their entirety and the discussions have been limited to the length suitable for a paper. There were a great number of additional investigations undertaken in order to more fully understand the systems studied and a selection of that supplementary material is presented here to facilitate a more complete discussion.

### 13.1. Separation of $\text{Ti}_3\text{SiC}_2 - \text{Al}_2\text{O}_3$ composites

The exchange reaction has been shown through this research to be capable of producing phase pure MAX phase –  $\text{Al}_2\text{O}_3$  composites in a number of systems such as the  $\text{Ti}_3\text{SiC}_2$  system. The high conversion rate to the MAX phase, and thus lack of additional phases like TiC in these systems is important as even a small amount of TiC can compromise desirable MAX phase properties as has been discussed. Unfortunately the aluminothermic exchange reaction, by definition, produces a sample of which approximately half is  $\text{Al}_2\text{O}_3$  having a considerable effect on the properties. In an effort to obtain phase pure MAX phases, separation of  $\text{Ti}_3\text{SiC}_2 - \text{Al}_2\text{O}_3$  mixtures was investigated. Chemical digestion was considered as  $\text{Al}_2\text{O}_3$  is soluble in both strong acids and bases as used in the Bayer process. This process needs to be performed at high temperature ( $\sim 200^\circ\text{C}$ ) and consequently under high pressure to prevent boiling of the solution. This experimental setup was investigated but deemed too complex and dangerous to pursue. Instead physical separation was investigated by means of sedimentation experiments.

Sedimentation separation is used commonly in the refining of ores such as magnetite. In this process a mixture of two (or more) constituents is added to a liquid and allowed to settle. In its absolute simplest form, if one constituent was to sink and the other float, separation would occur directly based on density. Unfortunately many common mixtures ( $Ti_3SiC_2$  and  $Al_2O_3$  included) cannot easily be separated this way due to their high densities (~4.5 g/cm<sup>3</sup> and 4 g/cm<sup>3</sup> respectively) without the use of a high density liquid, a process known as heavy medium separation. Unfortunately the infrastructure required can be complex and the high density liquids are often hazardous. Materials can also be separated in large columns of liquid of lower density based on how fast they sink.

Spherical particles fall according to Stoke's law

$$V = \frac{2(\rho_p - \rho_f)}{9\mu} g R^2 \quad Eq. 3$$

Where V is the terminal velocity,  $\rho_p$  is the density of the particle,  $\rho_f$  is the density of the fluid,  $\mu$  is the viscosity of the fluid, g is the acceleration due to gravity and R is the radius of the particle. The similar densities and particle sizes in these mixtures still make it difficult to directly separate this way. However the surface chemistries of  $Ti_3SiC_2$  and  $Al_2O_3$  are different and this may allow for a chemical flocculent or dispersant to adhere to the surface of one of the constituents, affecting its properties, either keeping it in suspension for longer or causing it to settle out faster, allowing for separation.

The chemical ammonium polyacrylate (NHPA) is a known dispersant in the ceramics industry and is used to keep  $Al_2O_3$  in suspension for long periods. It was decided to create a 1:1 mixture of pure  $Ti_3SiC_2$  and pure  $Al_2O_3$  by mass and suspend in a solution of 0.1 wt % (NHPA). The suspension was given time to settle and the top 90% of solution was removed. The remaining sediment was then analysed by quantitative Rietveld refinement of the XRD data to determine the new  $Ti_3SiC_2:Al_2O_3$  ratio. Figure 22 shows the refined

## Additional results

XRD of the mixture before separation and after allowing 60 min of settling time. A clear decrease in the amount of  $\text{Al}_2\text{O}_3$  can be seen. Indicative peaks are the pair at  $\sim 35^\circ 2\theta$  and  $\sim 44^\circ 2\theta$ . The peak at higher angle represents the  $\text{Al}_2\text{O}_3$  in both pairs.

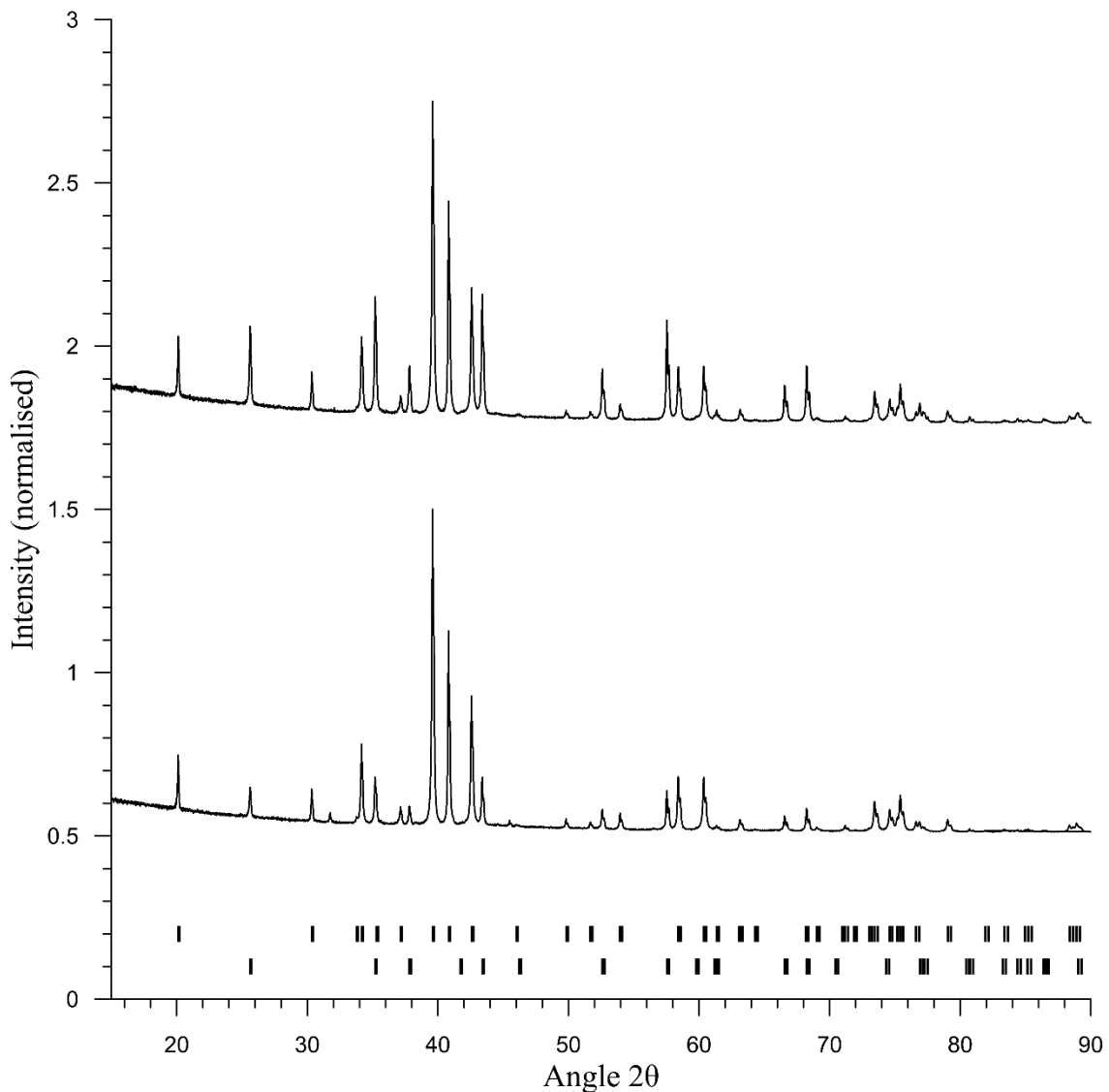


Figure 22 XRD data of  $\text{Ti}_3\text{SiC}_2 - \text{Al}_2\text{O}_3$  mixtures before (top) and after separation (bottom). Markers represent  $\text{Ti}_3\text{SiC}_2$  (upper) and  $\text{Al}_2\text{O}_3$  (lower).

Initial separation experiments were shown to be sensitive to settling time. Short settling times did not give enough time for the MAX phase to settle out of suspension, excessively long settle times allowed a considerable amount of the  $\text{Al}_2\text{O}_3$  that was held in suspension

to eventually settle. The time dependence of on the mass % of MAX phase in the sediment can be seen in Figure 23.

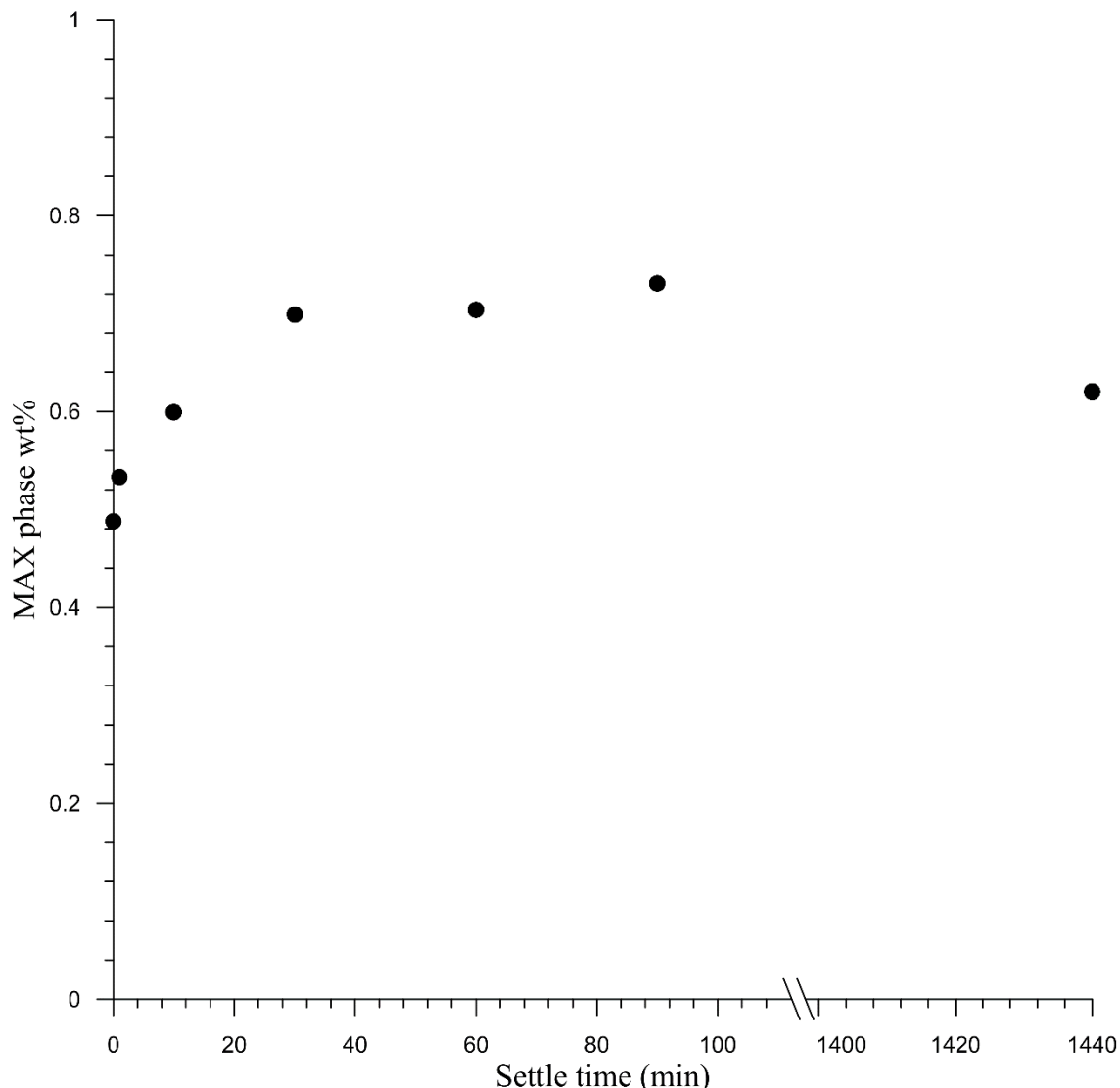


Figure 23 Relative fraction of  $Ti_3SiC_2$  in the sample after separation.

Despite initial improvement in the proportion of  $Ti_3SiC_2$  further improvements could not be reliably made. Taking the sediment and re-suspending in an attempt to separate more  $Al_2O_3$  proved unsuccessful. It is believed that the particle size of the powder plays a key role in the process. If average particle size and the distribution of particles sizes could be reduced the process is expected to be considerably improved.

### 13.2. *In situ* neutron diffraction of $\text{Ti}_3\text{SiC}_2$ - $\text{Al}_2\text{O}_3$ composite formation

The  $\text{TiO}_2 + \text{Al} + \text{Si} + \text{C}$  system was investigated under *in situ* neutron diffraction to investigate the reaction mechanism of the  $\text{Ti}_3\text{SiC}_2 - \text{Al}_2\text{O}_3$  composite. These experiments involved the use of the high intensity powder diffractometer (Wombat) at the Australian Nuclear Science and Technology Organisation (ANSTO). Neutron diffraction works on very similar operating principles to X-ray diffraction explained in the Methodology section of this thesis, however there are some differences. Perhaps the most important difference is that while X-rays interact with the electron shell of an atom neutrons interact with the nucleus. Most importantly for this work neutrons penetrate considerably further into a material, in the order of 10 – 100 mm opposed to X-rays which are closer to 10  $\mu\text{m}$ . This is practically useful as it allows neutrons to pass through a surface layer and observe what is happening in the bulk of a sample. It also allows for the beam to pass through the walls of a specially designed furnace and interact with the sample. This means samples can be heated in the furnace while diffraction patterns are constantly recorded. The Wombat instrument is configured with an area detector so that a large angle range can be recorded simultaneously reducing the time required to obtain a diffraction pattern to considerably less than one second albeit with lower counts than is normally desirable for refinement. Nevertheless the stages of a reaction can be captured as they occur and intermediate phases directly observed.

Another key difference is that the scattering power of atoms for X-rays scales with atomic number of the atom whereas the neutron scattering length does not. This means that low atomic number atoms can make a significant contribution to a neutron diffraction pattern, allowing information to be gained that may be overshadowed in X-ray diffraction patterns. For example, the *M* and sometimes the *A*-element of the MAX phase has

considerably larger atomic number than the  $X$ -element. The diffraction pattern is generally dominated by these larger elements and determining information about the  $X$ -element is often difficult, however this is not the case for neutrons and information such as the  $X$  occupancy can be more accurately determined. Although not used in this work, another effect of the neutrons interacting with the nucleus means that isotopes and magnetic structures can be investigated, neither of which can be studied with X-rays alone.

Neutron diffraction was conducted on a number of samples but the  $\text{Ti}_3\text{SiC}_2 - \text{Al}_2\text{O}_3$  system will be highlighted here. Reactants were mixed in optimised mixing ratios according to Eq. 10, reproduced from Chapter 6.



Milled powders were pressed into pellets and placed inside fused silica tubes. Loaded tubes were inserted into a vanadium furnace. Samples were heated at a rate of  $10^\circ\text{C}/\text{min}$ . Samples underwent an SHS reaction at approximately  $855^\circ\text{C}$ . Diffraction patterns are shown in Figure 24 with scan number which is proportional to temperature on the y-axis and diffraction intensity represented by colour. There are 5 main sections in the process.

- I) The reactants heat up and thermally expand. Thermal expansion is indicated by the gradient of the peak positions as a function of temperature.
- II) Al melts and drops out of the pattern as it is no longer crystalline. At  $700^\circ\text{C}$  the scan time is changed from 1 min to 20 sec to give better temporal resolution and has a corresponding change in background.
- III) The  $\text{TiO}_2$  originally in the form of anatase undergoes a phase transformation to rutile.

## Additional results

- IV) SHS reaction takes place. A distinct change in peaks is immediately obvious and the reactants transform into intermediate phases and then products.
- V) Existence of products. Some formation of  $Ti_3SiC_2$  is still occurring although difficult to observe.

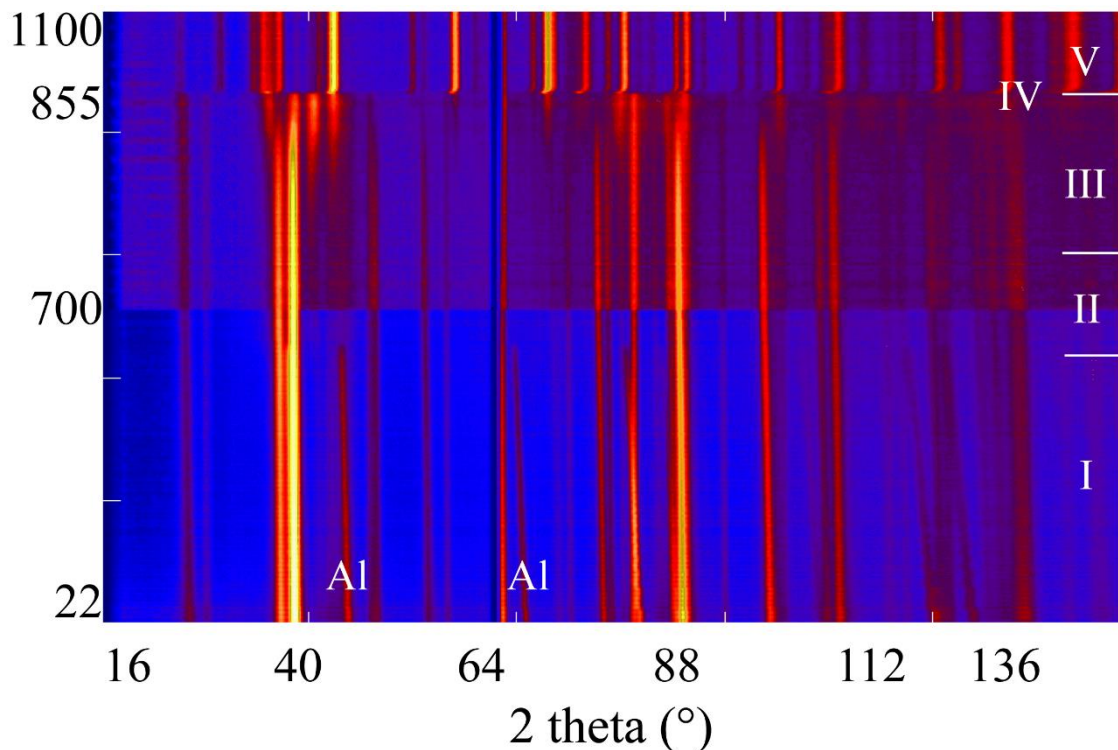


Figure 24 Neutron diffraction data of a  $Ti_3SiC_2 + Al_2O_3$  sample forming.

The area around the SHS reaction is expanded and shown in Figure 25. Peaks from the intermediate phase can now be seen in the highlighted circles. This phase was identified through Rietveld refinement as a TiC-like compound.

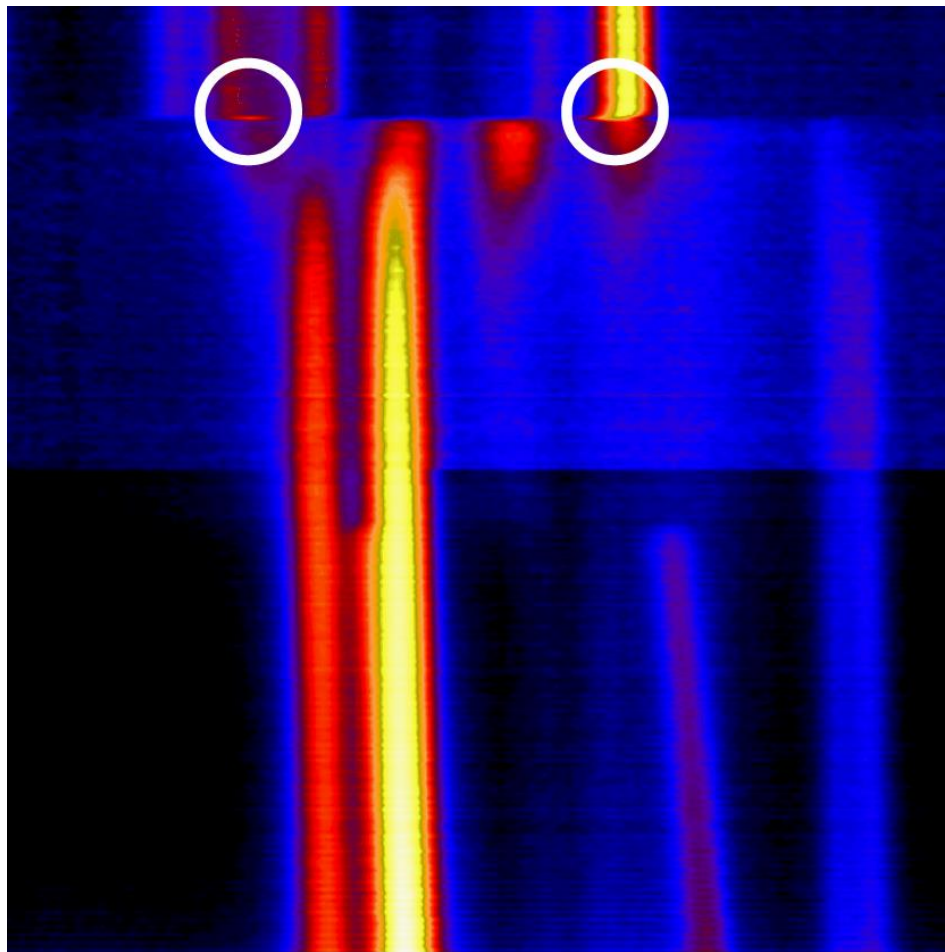


Figure 25 Expanded view of the SHS reaction with intermediate TiC peaks highlighted.

From inspection of the neutron data two conclusions can be drawn. Primarily the speed at which the reduction reaction takes places. These data show the complete disappearance of the  $\text{TiO}_2$  in a single scan (<20 sec) and follow-up experiments with faster scan times indicate that the transition may occur in ~0.25 sec. Secondly the reaction mechanism can be seen to depend on the presence of a TiC-like intermediate phase which exists for a short period of time (~6 sec) and steadily decomposes with the formation of the MAX phase. It is possible that this TiC phase contains a considerable amount of dissolved Si. A similar reaction mechanism was seen by Riley and Kisi<sup>[1]</sup>.

### 13.3. Alternative reducing agents (Mg and B)

The exchange reaction saw success using both Al and C as reducing agents. Both of these methods have limitations, Al due to the need to separate the  $\text{Al}_2\text{O}_3$ , and C due to the limited number of successful systems. As an alternative both Mg and B were investigated as reducing agents.

The Ellingham diagram shows the formation of  $\text{MgO}$  to be one of the most stable oxides. Capable of reducing even  $\text{Al}_2\text{O}_3$ , Mg can reduce any of the *M*-element oxides and has been shown to readily reduce  $\text{TiO}_2$  in the formation of  $\text{TiC}$  according to:



The process was then applied to MAX phase formation in the form of



Unfortunately these reactions proved largely unsuccessful. The reduction reaction did take place, however the products were a composite of mainly  $\text{TiC}$  and the  $\text{MgAl}_2\text{O}_4$  spinel. Whether the MAX phase did form and the *A*-element was leached into the spinel, or the spinel formed directly is unknown. The system was attempted with different *A*-elements (Si and Sn) with similar results.

As the reaction produced a spinel as a product it was decided to target a MAX phase spinel composite



The process now operates on the co-reduction of the  $\text{TiO}_2$  by both Al and Mg. The reduction proved successful as did some MAX phase formation. Results of SHS reactions

showed considerably higher conversion rates than pressureless reactive sintering. The refined XRD data of an SHS reaction of Eq. 13 can be seen in Figure 26.

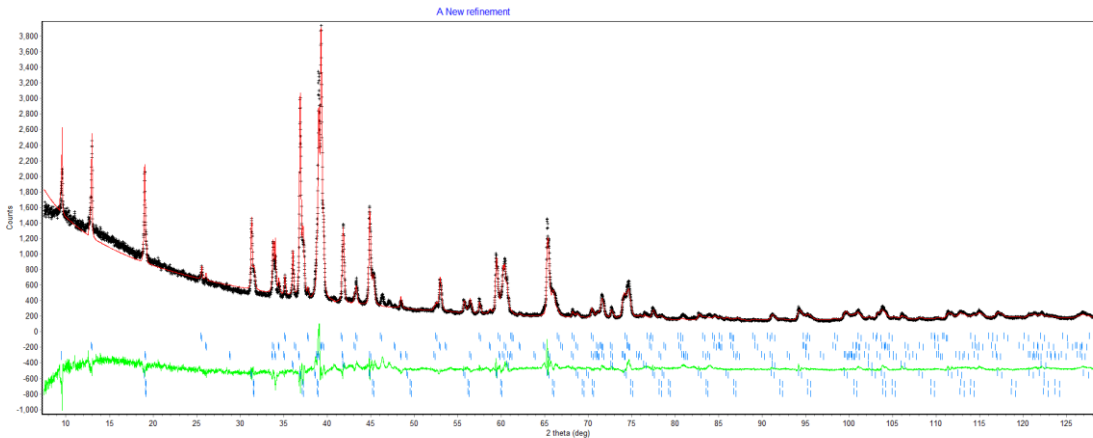


*Figure 26 Refined XRD data of a sample made according to Eq. 13. Markers top to bottom represent Ti<sub>2</sub>AlC, Ti<sub>3</sub>AlC<sub>2</sub>, TiC and MgAl<sub>2</sub>O<sub>4</sub>.*

This process has yet to be fully developed but initial experiments have shown promising results. Mg was originally considered as a reducing agent because MgO is soluble in ammonia and thus separation of the composite becomes trivial. As yet MgO MAX phase composites have not been produced, but MAX phase spinel composites have been successful. While the spinel is not as applicable to chemical separation, the density of ~3.6 g/cm<sup>3</sup> makes flotation separation discussed in §13.1 a strong possibility.

B was also investigated as a reducing agent as B<sub>2</sub>O<sub>3</sub> sublimes at 1500°C, which would make it self-separating from the products under heating. Unfortunately while TiO<sub>2</sub> could be decomposed by B it resulted in the formation TiB<sub>2</sub>. The diborides are a remarkably stable set of compounds and all of the MAX phase *M*-elements form a MB<sub>2</sub> compound. As yet it has not been determined if a MAX phase can be made via this method, and a more in-depth analysis of the thermodynamics of the system is required.

### **13.4. MGA synthesis**

Some of the more interesting areas in which the candidate was directly involved in the development of MGAs will be expanded upon here. All aspects of MGA synthesis were performed as part of a research team and the candidate does not claim to have completed this work individually. Advancement has primarily been in the production of new systems. Graphite matrix materials have shown strong promise with Cu – C, Zn – C, brass – C and Al – C systems all being developed. These materials are promising mainly because C is abundant, cost effective, thermally conductive, highly immiscible with a range of metals and very stable (remaining solid to temperatures over 3500 °C) making it an ideal matrix material. C does have oxidation issues at temperatures above 400°C however passivating coatings are available in the form of SiC or interestingly for this work, MAX phases. Graphite is already used as a sensible heat storage medium for steam production from small concentrated solar power plants, thus development in this field is ideally suited to a current thermal storage application. An SEM image of an Al – C MGA is shown in Figure 27 with the desired inverse microstructure.

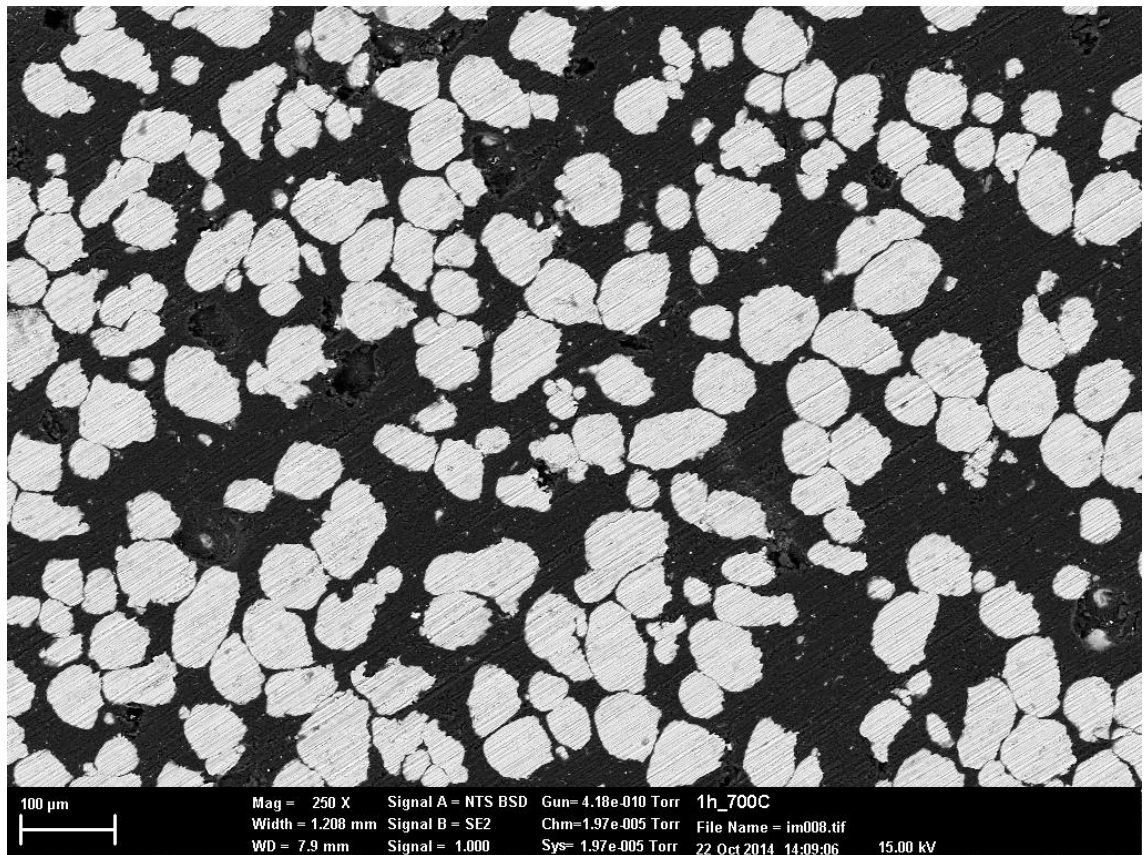


*Figure 27 Al - C MGA microstructure under SEM analysis. The lighter Al particles can be seen as encapsulated by the darker graphite.*

As an MGA stores heat through the melting of an included phase they inherently operate at discrete temperatures. Whilst this is highly desirable when designing a power cycle, it does mean some operating temperatures are currently unavailable. This can cause issues when external factors determine the operating temperature of the system. By using metal alloys as the included phase, (while still being encapsulated in an immiscible matrix), the operating temperature may be tailored for a specific use. As an example the Zn – C system gives an operating temperature of 420°C and Cu – C gives 1085°C. Neither is appropriate for steam production at ~600°C, however there are a number of Zn – Cu brasses with intermediate melting temperatures. Should a brass first be made, then an MGA created using the brass as the included phase and C as the matrix (Figure 28) a new set of operating temperatures become available, ~750°C in this example. The work on the

## Additional results

synthesis of the brasses used, and the manufacturing of the brass based MGAs was primarily conducted by Bastien Monnier, with the assistance of Dr Heber Sugo, Prof. Erich Kisi and the candidate. These were the first ternary MGAs created.

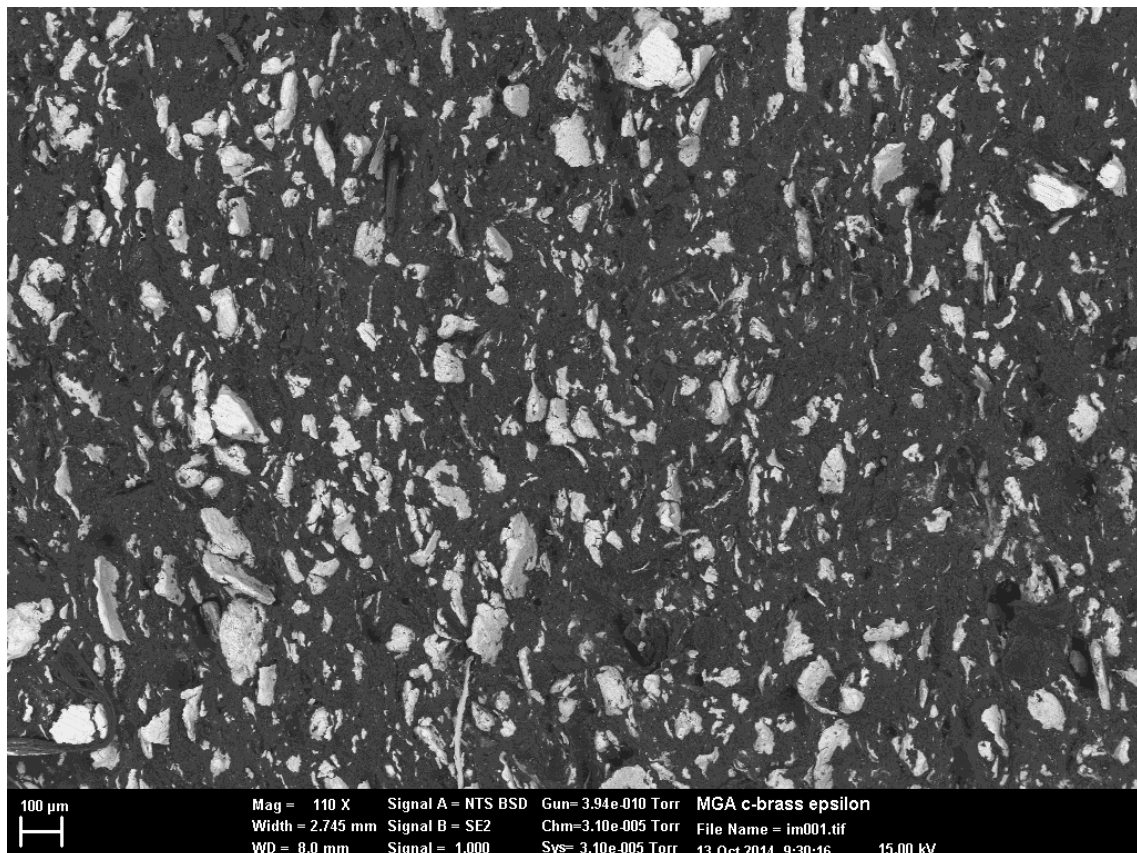


Figure 28  $\varepsilon$ -brass MGA in graphite matrix.

## 14.General discussion and future work

### 14.1. Optimisation and expansion of aluminothermic MAX phase synthesis

Considering the results presented in this thesis, the exchange reaction as a means of producing MAX phases can be deemed very successful. As demonstrated in papers *MAX phase - alumina composites via exchange reaction in the  $M_{n+1}AlC_n$  systems ( $M = Ti, V, Cr, Nb, or Ta$ )* and *MAX phase – alumina composites via-elemental and exchange reactions in the  $Ti_{n+1}AC_n$  systems ( $A = Al, Si, Ga, Ge, In and Sn$ )* in Chapters 5 and 6 respectively, the method has now been applied to a wide range of phases and the process appears to be quite general. Previously only specific systems ( $Ti_3SiC_2$  and  $Ti-Al-C$ ) had been attempted, now it would be more correct to say that an aluminothermic exchange reaction can be used to produce most MAX phases with few exceptions. Throughout the research, 12 of the 15 phases attempted for the first time were successfully synthesised via an aluminothermic reaction. Interestingly only synthesis in the  $Ti-Ga-C$  and  $Ti-In-C$  systems proved completely unsuccessful via an exchange reaction, however  $Cr_2GaC$  was very successful, thus Ga at least can partake in MAX phase formation via an exchange reaction. Further investigation of these systems would be of interest to determine exactly what aspect prevents formation. From the current results it appears that wetting of the A-element onto the other constituents plays a significant role. Samples which did not produce significant MAX phase (i.e.  $Ti-Ga-C$  and  $Ti-In-C$ ) always had metallic beads of A-element on the surface and in some cases these beads had coalesced forming a puddle beside the original pellet. In failed Sn containing samples (those synthesised under incorrect conditions) metallic beads of Sn were present on the surface as well. The low melting temperatures of these metals ( $Ga = 30^\circ C$ ,  $In = 157^\circ C$  and  $Sn = 232^\circ C$ ) may play

## General discussion and future work

a role. Unfortunately the long synthesis times required for formation of these specific phases, due in part to their low decomposition temperatures and thus low synthesis temperatures, makes containment of the *A*-element difficult. While more rapid methods of synthesis such as SHS may not give the *A*-element time to physically separate, it may also not allow for the diffusion required to form the MAX phase. It is possible that a method which contains the reactants in close proximity may be beneficial here. Both reactive hot pressing and pulse discharge sintering are attractive potential solutions. Despite these practical difficulties it does not appear that it is the exchange reaction itself which is responsible for the failure of these systems to produce MAX phases, the method still remains generally applicable to MAX phase systems.

There are still a number of systems that have not yet undergone investigation. Expansion of the process to systems with *M* and *A*-elements already known to partake in exchange reaction synthesis is the first logical step. For example of the phases produced carbothermally ( $\text{Cr}_2\text{GaC}$ ,  $\text{Cr}_2\text{GeC}$  and  $\text{V}_2\text{GeC}$ ) only one has been produced aluminothermically, making the other two ( $\text{Cr}_2\text{GaC}$  and  $\text{V}_2\text{GeC}$ ) strong contenders. Of the remaining phases, untested *M*-elements (Sc, Zr, Mo, Hf) with known *A*-elements (Sn, Ga or Sn respectively) seem the most likely, provided suitable synthesis conditions can be found.

Alternatively many other *A*-elements have yet to be attempted. This was predominantly due to the boiling point of these elements being close to or below the synthesis temperature of the corresponding MAX phase. The phases which contain these elements are often formed by using non elemental reactants, for example the use of  $\text{FeS}_2$  in the formation of  $\text{Ti}_2\text{SC}$ . In this case the  $\text{FeS}_2$  decomposes at high temperatures forming  $\text{FeS}$

and free S which then forms a Ti<sub>2</sub>SC and FeS composite. Provided there was no unwanted interaction between the additional reactants, and the reaction steps proceeded in the required order, it is possible for this type of synthesis to work in conjunction with an exchange reaction. However the system now has 6 elements present, in the form of 4 reactants undergoing at least a 3 step reaction to form 3 different products. It seems likely that difficulties may be encountered. Naturally systems which introduce the A-element as an *M-A* compound are not applicable with this type of reaction. Similarly to the low boiling temperature A-elements, none of the nitride phases have been attempted thus far. Again this is because of the difficulties involved in using N which is gaseous as an element or present as part of a compound, and so requires special consideration. Overall it is entirely plausible that the exchange reaction may be applied to many more systems, however the process may become progressively more complicated.

Much of this work has focused on ‘proof of concept’ in an effort to understand the reaction mechanism, rather than optimise a selected system. Generally MAX phase synthesis focuses on the production of materials free from secondary phases, a goal only targeted in some systems in this work. For example the work on producing the novel MAX phases Ti<sub>3</sub>GaC<sub>2</sub> and Ti<sub>3</sub>InC<sub>2</sub> (Chapter 8) contained investigations into synthesis times, temperatures and reactant ratios in an effort to optimise the yield of MAX phase, a goal that was achieved in both systems with drastic improvement on initial experiments. The optimisation led to pure Ti<sub>3</sub>GaC<sub>2</sub> synthesis. As well as this, the 3 publications on exchange reactions Chapters 5, 6 and 7 all had at least one system that underwent optimisation, however the other systems were not analysed in depth. The process is unfortunately incredibly time consuming, in part due to the limitations of the long firing sequence and the number of independent variables that need to be tested. In the example

## General discussion and future work

of a MAX phase produced by an exchange reaction the variables include; mixing ratios functional on A, X and reducing element, sintering time, sintering temperature and powder preparation (milling) conditions. Unfortunately many of these variables are interrelated, increasing sintering temperature may also reduce sintering time required and will also affect vaporisation losses and thus also affect the original mixing ratios. Selected systems of specific interest could become candidates for in-depth studies on the influence of synthesis conditions (temperature, time and method) and reactant ratios to the overall yield of the exchange reaction. These studies could then result in synthesis conditions that produce highly phase - pure MAX phase alumina composites in many if not all systems. This is deemed to be mainly a matter of time and resources.

Different synthesis methodologies should also be investigated as increased yields may be found simply by using synthesis methods known to produce high purity MAX phases such as reactive hot pressing or potentially pulse discharge sintering. Although this may lead to the process no longer being as industrially economic for large scale powder production. Pressureless reactive sintering is normally not considered an appropriate reaction mechanism for producing high purity MAX phases, however it was used throughout this work due to the desire to focus on low cost scalable methodologies. Self-propagating high temperature synthesis was also investigated and has shown to be capable of producing MAX phase alumina composites with minimal energy input and with very rapid reaction times, however as with the other reaction mechanisms mentioned, specialised equipment is required for proper experiments to be conducted.

## 14.2. Expansion of the carbothermal reaction mechanism

Although only present in this thesis as a single communication, the carbothermal reduction (Chapter 7) can be seen in many ways as the pinnacle of all of the MAX phase synthesis conducted. Chronologically the carbothermal reduction came about as follows.

- 1) Thermite (aluminothermic reduction) reactions were observed in the reduction of  $TiO_2$  by Al in the presence of C to form  $TiC - Al_2O_3$  composites.
- 2) Manipulation of the starting stoichiometry allowed for the production of a  $Ti_3AlC_2 - Al_2O_3$  composites via a reduction reaction. This was immediately interesting as the  $TiO_2$  used in the reduction reaction is considerably cheaper than the metallic Ti normally used in MAX phase synthesis. This phenomenon was independently discovered and then later found in the literature.
- 3) Aluminothermic reduction reactions were extensively investigated. Starting from  $Ti_3AlC_2$  which was known to work, other systems were studied and understanding developed around how the exchange reaction worked.
- 4) Techniques for separating the MAX phase alumina composites were undertaken but proved difficult.
- 5) Alternate reducing agents were investigated to yield products that might be more easily separated (Mg, B and C). C originally failed as carbothermal reduction to produce Ti or Al containing MAX phases had proved unsuccessful due to the high temperatures required.
- 6) Further development of the aluminothermic reduction reaction highlighted systems with considerably lower reduction and formation temperatures than those previously studied.
- 7) The  $Cr_2GaC$ ,  $Cr_2GeC$  and  $V_2GaC$  systems all successfully formed through a carbothermal reduction reaction. These are phases that could be formed in a

## General discussion and future work

simple single step process, from the *M*-element oxide, using a cheap and abundant reducing agent, leaving oxide free products.

Carbothermal reduction is so far limited to systems that have expensive *A*-elements, negating a main motivation for investigating the process. Unfortunately cheaper *A*-elements like Al are not applicable in use of carbothermal reactions as the Al will preferentially form the oxide over the C. It is also likely to be difficult to carbothermally reduce a number of the *M*-element oxides below the decomposition temperature of the corresponding MAX phase, thus making them unsuitable. It is for this reason that Si is highly impractical as it only exists in phases such as  $Ti_3SiC_2$  which are not applicable to bulk carbothermal reduction. Overall the number of systems is small, but all possibilities have not been exhaustively examined.

It may be that there are systems which are more economically viable. Sn is the most likely *A*-element as Sn is relatively cheap (compared with other *A*-elements such as Ga, In, Ge etc.), Sn oxide is unlikely to form and Sn containing MAX phases tend to be stable to high temperatures. It may also be found that there are specific reaction conditions which can allow for the formation of phases prohibited by simple pressureless reactive sintering. Contained reactive hot isostatic pressing for example may allow for the formation of more phases. However difficulties are expected due to the rapid production of a very large quantity of gas which needs to be contained in a small volume without causing an explosion.

Alternatively as a pure scientific investigation, the reaction mechanism behind MAX phase formation by carbothermal reduction is also of great interest. Aspects of the

mechanism can be guessed at, such as the reasonably slow speed and the required reaction temperature but *ex situ* analysis is limited. *In situ* neutron diffraction of the synthesis process would allow for the full mapping of the reaction. Carbothermal research is in its infancy, with its development only coming in the closing months of research. As a result this may be an area of significant expansion. Work has been completed on the formation of MAX phases via aluminothermic reduction reactions as part of this thesis using *in situ* neutron diffraction to map the reaction. Unfortunately this body of work has not been published prior to submission of this thesis so only a summery is included. It has shown that these types of reaction can be studied by *in situ* neutron diffraction and this method should be capable of revealing the intricacies of the carbothermal reaction as well.

There is also the possibility that the carbothermal reduction process may be applicable to an SHS reaction. SHS reactions present an immediate issue of rapidly evolving large amounts of hot gas. The quantity of gas released in the carbothermal reduction will be sufficient to disintegrate the sample, separating the reactants and preventing complete reaction. However if the reactants could be contained in close proximity then the reaction may be capable of proceeding to completion. The main advantage of this process is that it is known that SHS reactions which form  $Ti_3SiC_2$  can reach temperatures of over 1800°C for short periods and still be successful. This means that a temperature may be reached which allows for the complete reduction of the  $TiO_2$  by C, without causing excessive loss of the Si and therefore allowing for the formation of  $Ti_3SiC_2$  via carbothermal reduction. Specialised equipment will be required for this process, mainly to contain the gas produced by the reaction in a small volume which will result in high pressures.

### 14.3. Other reducing agents

Al and C have been shown to be effective reducing agents, however they are not the only applicable options. There were 4 other metals on the Ellingham diagram which were applicable reducing agents; Ca, Mg, Li and U. As an alternative, B can also be used at high temperatures to produce an oxide which is gaseous, similar to C. Practically, considering costs and safety Ca, Li and U were not used, but Mg and B were both tested as reducing agents.

The use of B unfortunately led to the formation of  $MB_2$ , an incredibly stable set of compounds, and failed to produce any considerable amount of MAX phase. Despite the lack of MAX phase formation, the reduction reaction did take place successfully, and new phases formed during single step pressureless reactive sintering. A better understanding of the thermodynamics and reaction mechanism may yield more success. This is an area worth investigating as B reduction produces gaseous oxides, leaving oxide free products. An advantage of B over C is B oxides are more stable at high temperatures and may allow for the use of cheaper  $M$  and  $A$ -elements such as Ti or Al which cannot be used in carbothermal reduction. It was shown that  $TiO_2$  would be decomposed by B at  $1400^{\circ}C$ , a suitable temperature for  $Ti_3SiC_2$  formation.

### 14.4. MAX phase - $Al_2O_3$ composite

The exchange reaction has been discussed at length and the concept of separating the products introduced. Although MAX phases are normally desired for properties that are compromised by the presence of  $Al_2O_3$ , there is some direct interest in increasing properties such as wear resistance and stiffness with the addition of alumina to a MAX

phase, or in increasing the fracture toughness of  $\text{Al}_2\text{O}_3$  with the addition of MAX phase [2, 3]. In these cases the two constituents were prepared individually and then combined and sintered. The exchange reaction allows the formation of these composites in a single step, and if synthesised by reactive hot pressing, dense monolithic samples can be directly produced.

For refinement of the composite to obtain a pure MAX phase a more in-depth investigation needs to follow the initial experiments which have been presented here. Simple sedimentation experiments have been partly successful in separating the composite however variable such as particle size and particle size distribution appear critical. Finer particles of more controlled size would allow for greater control over the separation process. Alternatively larger particles may be more appropriate to froth flotation where a surfactant is added to a suspension of the two constituents and air bubbles passed through the system. The surfactant is intended to adhere to one constituent making it hydrophobic and thus attracted to the bubbles rising to the surface while the other constituent sinks.

Interestingly separation is a process that may become easier to control as the system is scaled up. Variables which only cause mild separation (such as the difference in densities) may not be applicable on small scales however large pools used in industrial sized separation plants may be far more effective. The use of denser MAX phases ( $\text{Cr}_2\text{AlC}$ ,  $\text{Nb}_2\text{AlC}$  with density = 5.24 and 6.50 g/cm<sup>3</sup> respectively) may increase the effectiveness of the separation. Similarly the use of Mg and Al to co-reduce  $\text{TiO}_2$  and form  $\text{Ti}_3\text{AlC}_2 - \text{MgAl}_2\text{O}_4$  composites may be beneficial as the density of the spinel (~3.5 g/cm<sup>3</sup>) is than that of the alumina (~3.95 g/cm<sup>3</sup>). As a result separation based on sedimentation may

## General discussion and future work

become more effective. Although considerably more work is required it is believed that physical separation techniques may be used to separate the MAX phase from the other products of an exchange reaction.

### 14.5. Miscibility Gap Alloys

The papers presented in Chapters 9 and 10 on MGAs for thermal energy storage are but the first in an ever expanding area of research. This is the area which has developed drastically throughout this research, and has the potential to expand still further. Many attributes of MGAs have been explored by other members of the group through dedicated grants awarded to Prof. Erich Kisi and Dr Heber Sugo. A PhD undertaken simultaneously by Mr Anthony Rawson to investigate the properties and stability of MGA's via computational modelling (*Modelling and Application of Advanced Storage Materials*). That work has been successful in very many respects. The thermal properties of the MGAs have been determined with respect to both composition and microstructure. The thermal material properties then allowed for extensive cost analysis to be performed, taking into consideration required infrastructure for operation of a concentrated solar power plant. Thermal cycle analysis to investigate how the microstructure will evolve over time was also investigated. Medium scale devices were designed and constructed to test the properties in use. Mechanical property testing of the materials through the melting of the included phase was also investigated.

The state of the art of MGAs has developed throughout this project from the original two systems of Sn – Al and Cu – Fe to ~20 different systems for specialised applications. As a step in the scaling process a desk top sized MGA storage device was created by Miss Melanie Jackson which contained ~10 Kg of Zn – C MGA as a storage medium, using a

thermoelectric converter to generate electricity from the stored thermal energy. The thermoelectric converter was designed to operate at approximately 400°C, thus Zn – C (420°C) was selected. This is to date the largest application of MGAs and has helped pave the way for increasing the scale of these materials.

The work by Mr Bastien Monnier into the formation of the brass and subsequent manufacturing of the brass – C samples paved the way for ternary MGAs. Eutectic mixtures, for example ~13 wt% Si in Al included phases dispersed in C can also be used. This can be beneficial not just for lowering the melting temperature, but can also increase the thermal storage capabilities. The addition of Si to Al increases the latent heat of fusion by approximately 50% over pure Al. Although this is at the expense of an approximately 3% drop in specific heat, the increase in storage capacity is immense as Si has a remarkably high latent heat of fusion. Pure Si is difficult to utilise as it has a melting temperature of 1414°C, too high for most applications.

Overall the MGAs have developed into a large research area promising energy storage solutions for both renewable electricity production, and domestic heating applications. They are interesting in both an academic sense with properties and microstructure studies and as an engineering project to scale and implement these materials in a commercially viable application.

#### **14.6. Thermionic emission**

The work into thermionic emission as a means of converting thermal energy into electrical power is very much in its infancy. While materials that could be used for emitters were synthesised successfully and an emission device was created, the work was very much ‘proof of concept’. The thermionics project was led by Dr Heber Sugo and the candidate played a supporting role. The work into low work function materials was led by Dr Muhammad Hasan, and the candidate is grateful to have been a part of these projects.

Despite the high operating temperatures of thermionic emission devices the potential Carnot efficiency is never reached due to the space charge and finite value of the collectors work function. Despite the limitations it may be that a thermionic process may be used as a topping cycle in a steam based concentrated solar plant. In this configuration the concentrated solar radiation would heat the emitter ( $\sim 1500^{\circ}\text{C}$ ), and the collector ( $\sim 600^{\circ}\text{C}$ ) would be cooled by the steam which is then used for a conventional power cycle. In this way any power that could be extracted before entering the power cycle would be in addition to what would normally be produced. An additional radiative loss mechanism is created by the requirement that the emitter surface is kept at such a high temperature. It is plausible that the additional radiation losses may be a significant amount of or larger than the extra energy extracted from the thermionic emission process. Topping cycles still appear to be the best way to apply thermionic conversion to power plants, however it remains to be seen if the capital costs can be offset by the production of more efficient systems. Considerably more development is required before thermionic energy conversion will become a reality in terrestrial applications.

Due to the hostile environment of a thermionic emitter it was believed that the MAX phase materials, with their combination of high thermal stability, good electrical and thermal conductivity and ability to be machined are perfectly suited for the environment. When MAX phases were tested as thermionic emitters in the Schottky chamber it was found that the outer surface decomposed, losing the A-element to vaporisation and forming a layer of *MX* (i.e. TiC). Unfortunately TiC and other *MX* compounds have a high work function ( $4.1 \text{ eV} < w < 5.02 \text{ eV}$ ) and while the layer did not penetrate far into the bulk, electron emission is a surface effect so it was greatly affected. Composites of BaAlO<sub>3</sub> and MAX phase did show promise. BaAlO<sub>3</sub> has a low work function but poor thermal properties and very low electrical conductivity, whereas the MAX phase has excellent thermal and electrical properties for an emitter. A composite seemed to possess good thermal, electrical and emission properties. Further research is required to determine the long term stability and optimum composition of the composite. It may be possible to use Ba as the reducing agent in the exchange reaction, thereby producing in a single step a MAX phase BaAlO<sub>3</sub> (or MAX phase BaO) composite emitter with the strong emissive properties of the barium compound coupled with the exceptional physical properties of the MAX phase. In general thermionic emission is perhaps the area of this thesis which will need the most development before it reaches a stage where it can be practically implemented.

Despite the apparent broadness of this thesis there was a unified intention. It was originally proposed that a thermionic convertor would be made using a MAX phase emitter to directly convert concentrated solar thermal energy into electrical energy. An MGA storage device or Si – SiC (operating temperature  $1414^\circ\text{C}$ ) would be used to overcome the intermittency of the solar resource. This goal was ambitious from the start,

## General discussion and future work

and the thermionic emission process proved more difficult than originally anticipated. Inversely the development of the exchange reaction for MAX phase synthesis, an unknown field at the beginning of the thesis, became the area of greatest accomplishment. Similarly the MGAs as thermal storage devices have gained significant momentum. As a result the research took on a more intense investigation into the synthesis of the MAX phases and the production of MGAs at the expense of lessening the focusing on thermionic energy conversion. Indeed little of the work on MAX phases or MGAs is presented within the application of thermionic emission, as the research proved more universal than originally thought.

## 15. Conclusions

As each paper contains specific conclusions within itself only more general statements will be made here.

It has been proven throughout this thesis that an exchange reaction as a mechanism to synthesise MAX phases is a general and effective method. Generality was shown with all of the *M*-Al-C, all but two of the Ti-A-C and the Cr<sub>2</sub>GeC systems yielding success. Improved, and in most cases very high, conversion of every phase which underwent optimisation was achieved. The exchange reaction is a highly successful reaction mechanism for the synthesis of MAX phases. The concept can be further extended to the use of C as a reducing agent in selected systems, a world first. This process yielded pure Cr<sub>2</sub>GeC via a single step carbothermal reduction process. The scalability and cost effectiveness of the exchange reaction is ensured by the use of the industrially applicable pressureless reactive sintering mechanism. An alternative to the use of high cost metallic *M*-elements for MAX phase synthesis has been found.

The synthesis of the MAX phases in general have been studied in depth and this led to the discovery, synthesis and characterisation of bulk samples of two new MAX phases; Ti<sub>3</sub>GaC<sub>2</sub> and Ti<sub>3</sub>InC<sub>2</sub>. Coupled with this, systematic analysis of the formation of MAX phases, specifically the higher order phases, led to generalisation of the  $M_{n+1}AX_n + MX \rightarrow M_{n+2}AX_{n+1}$  reaction. The correlation between structural parameters and stability was also investigated and strong trends were discovered.

A significant contribution was made to a novel class of materials for thermal energy storage developed by our research group. Miscibility Gap Alloys utilise the latent heat of

## Conclusions

fusion of an encapsulated metal phase in a high melting point metal matrix to store energy through the melting of the encapsulated metal. These materials offer a high energy density, high thermal conductivity storage solution. Application in the field of: very high temperature overload protection in concentrated solar power plants (Cu – Fe at 1085°C), high temperature steam production (Mg – Fe at 650°C, Al – C at 660°C, brass – C at 720°C), medium temperature organic Rankine cycles (Zn – C at 420°C) and low temperature space heating or drying (Sn – Al at 232°C) have all been investigated. This technology has been developed on the laboratory scale in preparation for commercial application. Both synthesis and characterisation, along with thermal property testing has been investigated.

The effectiveness of concentrated solar power plants have the potential to be further increased with the development of thermionic energy conversion, and a test-bed device was co-developed for direct conversion of heat into electricity. Although high efficiencies were never reached, this work was predominantly proof of concept. A device was created which held a  $\phi$  32 mm emitter sample at 1400°C with a water cooled collector electrically separated at a distance of  $\sim$ 50 $\mu$ m. The chamber maintained high vacuum, and was reliable and reusable. All parts (including emitter and collector) were easily removable and interchangeable.

Overall the efficiency of the conversion of energy from one form to another, and particularly the conversion of energy sources into electricity is limited by the available materials. The development of both novel materials and novel synthesis methodologies will contribute to the efficient production of alternative energy.

1. Riley, D.P. and E.K. Kisi, *Self-Propagating High-Tempertue Synthesis of Ti<sub>3</sub>SiC<sub>2</sub>: 1, Ultra High-Speed Neutron Diffraction Study of the Reaction Mechinism*. Journal American Ceramic Society, 2002. **85**(10): p. 2417-2424.
2. H., W., Z.H. Jin, and Y. Miyamoto, *Ti<sub>3</sub>SiC<sub>2</sub>/Al<sub>2</sub>O<sub>3</sub> composites prepared by SPS*. Ceramics International, 2003. **29**(5): p. 539-542.
3. L., Y., et al., *Fabrication of Al<sub>2</sub>O<sub>3</sub>-Ti<sub>3</sub>SiC<sub>2</sub> composites and mechanical properties evaluation*. Materials letters, 2003. **57**: p. 2509-2514.

**Appendix*****Optical properties and electronic structure of the Cu – Zn brasses***

There have been a number of investigations undertaken which did not align directly with the main goals of the rest of the thesis. One such area was the investigation into the optical properties of the brasses. Although ‘brass’ as an engineering material is well known and has been produced for many thousands of years, it is normally alpha and or beta brass which is produced. These are a Cu rich brass phases with <50% Zn and have desirable engineering properties. There are however more brass phases with higher Zn content. The high Zn brasses tend to be far more brittle than the low Zn counterparts so find few practical uses.

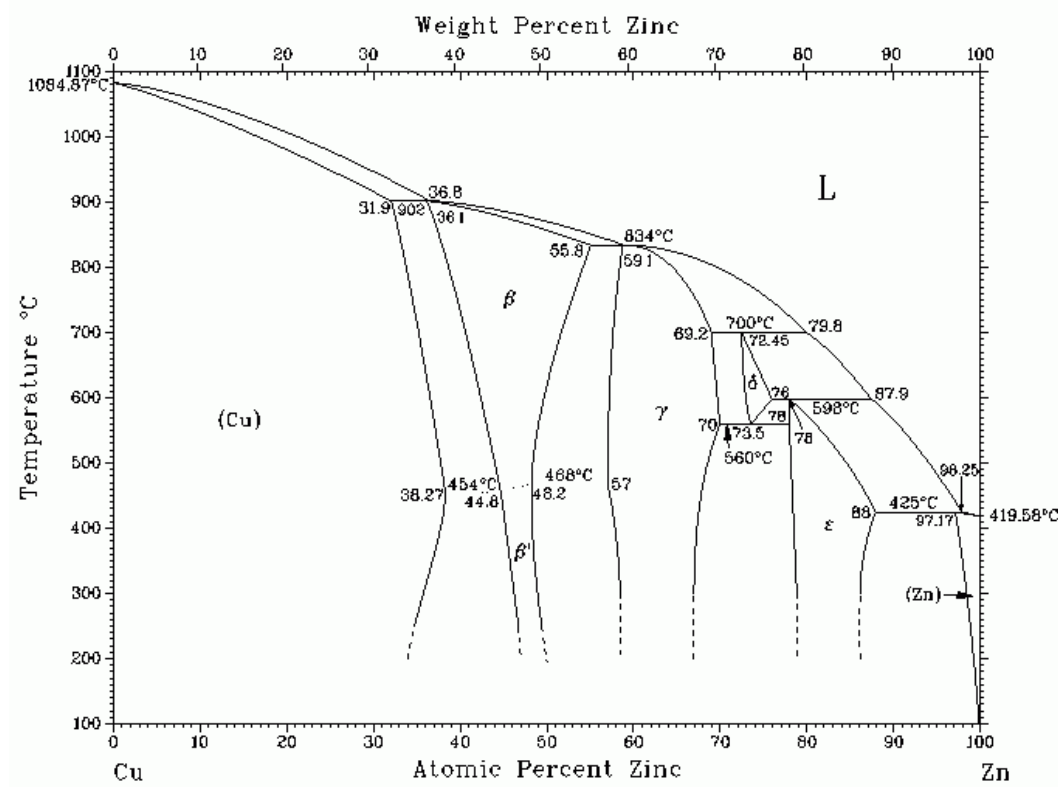


Figure 29 Cu Zn phase diagram.

The higher Zn brasses came under investigation in this thesis originally due to their melting temperature. Both Zn – C and Cu – C MGAs can be fairly easily manufactured however neither operate at an ideal temperature for steam production (420°C and 1085°C respectively). The brass intermediate phases however, being compounds of Zn and Cu, have melting temperatures between these bounds.

As the content of the brasses changes from the Cu rich form to the Zn rich forms the colour of the alloy also changes from deep reddish brown, through yellow and bright gold to silvery with high lustre. This colour change was of interest to A/Prof. Vicki Keast in the school of Mathematics and physical sciences. These phases could be simulated using DFT however physical samples were required to compare the predictions.

Synthesis of the high Zn brasses is surprisingly difficult, due to the low boiling temperature of the Zn (907°C) and high melting temperature of the Cu (1085°C). At high Zn content vaporisation becomes so significant that much of the Zn can be lost under lengthy heating cycles. For this reason an induction heating furnace was used to produce the brasses which allowed the materials to get to temperature in a matter of minutes (rather than hours normally required). This helped to significantly reduce vaporisation losses and accurately produce brasses of a known composition. These brasses were then used for two purposes, some were ground into powder and used to make MGAs, others were analysed for their optical properties and appeared in the following publication.

## Optical properties and electronic structure of the Cu–Zn brasses

V.J. Keast<sup>a</sup>, J. Ewald<sup>a</sup>, K.S.B. De Silva<sup>b</sup>, M.B. Cortie<sup>b</sup>, B. Monnier<sup>c, d</sup>, D. Cuskelly<sup>c</sup>, E.H. Kisi<sup>c</sup>

*Journal of Alloys and Compounds* DOI:10.1016/j.jallcom.2015.06.136

### Highlights•

- Study of the electronic structure and optical response of the Cu–Zn brasses. •
- Agreement between experiment and calculation of the dielectric functions. •
- $\alpha$ -brasses optical response is dominated by transitions from the top of the d-band. •
- In the other brasses it is transitions around the Fermi level. •
- $\beta'$ -brass response is dominateed by an overdamped bulk plasmonic response.

### Abstract

The colour of Cu–Zn brasses range from the red of copper through bright yellow to grey-silver as the Zn content increases. Here we examine the mechanism by which these colour changes occur. The optical properties of this set of alloys has been calculated using density functional theory (DFT) and compared to experimental spectroscopy measurements. The optical response of the low Zn content  $\alpha$ -brasses is shown to have a distinctly different origin to that in the higher content  $\beta'$ ,  $\gamma$  and  $\varepsilon$ -brasses. The response of  $\beta'$ -brass is unique in that it is strongly influenced by an overdamped plasmon excitation and this alloy will also have a strong surface plasmon response.

## 1. Introduction

The unique optical properties of the coinage metals, Cu, Ag, Au and their alloys, have been applied for centuries for a variety of technological and decorative purposes. Most recently they have been the predominant materials used for plasmonic applications. Although the coinage metals are normally used in elemental form for such applications, there is also some interest in using their alloys<sup>[1]</sup>. For example, it has been demonstrated that nanoparticles can be fabricated from Cu–Zn alloys<sup>[2], [3], [4], [5], [6]</sup> and<sup>[7]</sup> that a surface plasmon resonance can be sustained<sup>[4]</sup> and<sup>[7]</sup>. The colour of the bulk Cu–Zn brasses varies with the Zn content, as does the energy of the plasmon resonance in nanoparticles. This behavior is related to the change in the dielectric function that occurs with the different composition and crystal structure of the alloys. The dielectric function is itself determined by the underlying electronic structure of the material.

A number of Cu–Zn alloys and intermetallic phases are observed, as listed in Table 1. Inclusion of vacancies in the structures allows these phases to span a finite composition range in the binary phase diagram. The Cu–Zn system has long been studied as the prototypical representative of materials satisfying the Hume-Rothery rules<sup>[8]</sup>. Despite this long history, there is an incomplete understanding of the connections between the crystal structure, electronic structure and optical properties in these materials.

## Appendix

*Table 1. Crystal structures of the Cu–Zn brasses (from the Inorganic Crystal Structure Database [42]).*

|   | Space group          | Lattice parameters (Å) |       | Atomic coordinates |               |               | Wyckoff site |
|---|----------------------|------------------------|-------|--------------------|---------------|---------------|--------------|
|   |                      |                        |       | x                  | y             | z             |              |
| Cu  | Fm-3m                | $a = 3.615$            | Cu    | 0                  | 0             | 0             | 4a           |
| $\alpha$ -Cu <sub>1-x</sub> Zn <sub>x</sub>       | Fm-3m                | $a = 3.62 - 3.69$      | Cu/Zn | 0                  | 0             | 0             | 4a           |
| $\beta'$ -CuZn                                    | Pm-3m                | $a = 2.959$            | Cu    | 0                  | 0             | 0             | 1a           |
|   |                      |                        | Zn    | $\frac{1}{2}$      | $\frac{1}{2}$ | $\frac{1}{2}$ | 1b           |
| $\gamma$ -Cu <sub>5</sub> Zn <sub>8</sub>         | I-43m                | $a = 8.878$            | Zn    | 0.1089             | 0.1089        | 0.1089        | 8c           |
|   |                      |                        | Cu    | 0.328              | 0.328         | 0.328         | 8c           |
|   |                      |                        | Cu    | 0.3558             | 0             | 0             | 12e          |
|   |                      |                        | Zn    | 0.3128             | 0.3128        | 0.0366        | 24g          |
| $\epsilon$ -Cu <sub>0.20</sub> Zn <sub>0.80</sub> | P6 <sub>3</sub> /mmc | $a = 2.7418$           | Cu/Zn | $\frac{1}{3}$      | $\frac{2}{3}$ | $\frac{1}{4}$ | 2c           |
|   |                      | $c = 4.2939$           |       |                    |               |               |              |

The  $\alpha$ -brass phase is stable when the Zn content is below about 37 at% and it has a disordered, substitutional, face-centred cubic (fcc) structure. As the Zn content increases the colour transforms from the reddish hue of pure Cu to the bright yellow of brass. Associated with this colour change, the optical absorption edges shift upwards in energy as the Zn content increases [9], [10], [11] and [12]. The  $\alpha$ -brasses have also been the subject of many theoretical investigations where it has been concluded that the alloying with Zn shifts the valence band features down in energy [13], [14], [15] and [16]. This is consistent with the increase in the energy of the interband transitions that are responsible for the absorption edge [13]. The correlation between the various features in the optical spectra with transitions from the bandstructure was made by Rao et al. [17]. The onset of these interband transitions is usually identified as being from the top of the d-band, but the origin of the features at higher energy has been the subject of some debate.

For the equiatomic composition and at high temperatures (above 480 °C),  $\beta$ -brass (CuZn) is a disordered body-centred cubic (bcc) solid solution but this structure is not retained

when the alloy is quenched and the  $\beta'$ -brass, stable at room temperature, usually has the CsCl structure. The colour and reflectivity changes in  $\beta'$ -brass (along with other alloys) was measured as a function of temperature below the disorder transition by Muldawer [18]. An analogy was drawn between it and Ag, as both metals display a sharp reflectivity dip, which is in contrast to Au and pure Cu. It was proposed that bulk plasmon excitations play an important role in accounting for this behavior. The Muldawer data was later used to extract the dielectric functions for  $\beta'$ -brass which showed that the real part of the dielectric function,  $\epsilon_1$ , crosses zero at  $\sim 2.5$  eV, which is where the reflectivity dip occurs [19]. However, it was necessary to perform extrapolation of the data, including matching to pure Cu data outside the measured frequency range, in order to perform the Kramers–Kronig analysis. Later measurements have instead suggested that, although  $\epsilon_1$  closely approaches zero at the energy of the reflectivity dip, it does not actually cross the axis [20].

There have been a number of calculations of the electronic structure and bandstructure of  $\beta'$ -brass [15], [21], [22] and [23] and there were discrepancies in the energy position of the d-band between the early results. The main peak in the complex part of the dielectric function,  $\epsilon_2$ , has been attributed to transitions from the Fermi surface to the unoccupied states [21], [22] and [24] but it has been suggested that transitions from the d-band also contribute [25]. Although the earlier papers discussed the important role of the bulk plasmon in the colour and optical response of  $\beta'$ -brass [18] and [19], this aspect has largely been neglected in later papers [24]. Indeed, the question of whether  $\epsilon_1$  for  $\beta'$ -brass crosses zero at 2.5 eV, corresponding to the energy at which a bulk plasmon excitation would occur, does not appear to have been resolved.

## Appendix

The electronic structure of  $\gamma$ -brass has previously been studied in order to understand the phase stability of this complex intermetallic compound [26] and [27] but the optical properties have remained largely unexplored, apart from a recent experimental study of thin film samples [28]. We are not aware of any studies of the electronic structure and optical properties of  $\varepsilon$ -brass. These Zn rich  $\gamma$  and  $\varepsilon$  phases do not display the golden hues of the brasses with low Zn content.

In this paper calculations of the electronic structure of the  $\alpha$ -,  $\beta'$ -,  $\gamma$ - and  $\varepsilon$ -Cu-Zn brasses using density functional theory (DFT) are presented. Two compositions (12.5 and 25 at% Zn) were studied for the  $\alpha$ -phase. From the electronic structure, the dielectric function and reflectivity were calculated using the random phase approximation (RPA). The calculations are compared to optical data acquired from thin film and bulk samples. In previous work on the  $\alpha$ - and-  $\beta$ -phases, the connection between the electronic structure and the optical response was only inferred, not calculated. The calculations presented here represent the first direct calculation of the optical responses. For the  $\gamma$ - and  $\varepsilon$ -phases this work represents the first computational study of their optical responses. By comprehensively studying the set of alloys, the trends and differences between the different Cu-Zn brasses were explored and the origin of their properties was established.

## 2. Material and methods

Thin film samples were prepared by co-depositing the elements onto a glass substrate by direct current magnetron sputtering. Substrate surfaces were thoroughly cleaned using detergent, water, acetone and ethanol then dried in nitrogen. The base pressure of the

chamber was  $1.3 \times 10^{-4}$  Pa ( $\sim 10^{-6}$  Torr) with flow of argon at a pressure of 0.2 Pa (1.5 mTorr).

Bulk samples were prepared by induction melting 99.99% pure Cu and Zn within a carbon crucible under a flowing argon atmosphere. The resulting  $\sim 24$  mm diameter,  $\sim 50$  mm long ingot samples were then sectioned using a diamond saw, ground and lapped to a 1  $\mu\text{m}$  diamond polish.

Crystal structures were verified using Cu K $\alpha$  X-Ray Diffraction (XRD) on a Panalytical X’Pert<sup>TM</sup> diffractometer or a Siemens D5000 X-ray diffractometer. The sample compositions were measured with energy dispersive spectra using a Zeiss Evo LS15 SEM with a Bruker EDS Quantax 400. Prior to optical characterization the bulk samples were subjected to fine grinding and polishing, where 0.05  $\mu\text{m}$  gamma-alumina suspension was used at the final polishing. Optical characterization was carried out using a V-VASE Ellipsometer by J.A. Woollam Co.. The resultant data was analyzed using WVASE ellipsometric software.

Samples for transmission electron microscopy (TEM) were prepared from the bulk alloys by the conventional approaches of mechanical polishing, dimple grinding and ion beam thinning. TEM images and diffraction patterns were acquired using a JEOL 2100 LaB6 TEM.

## 2. Calculations

The experimental crystal structures for the  $\beta'$ - and  $\gamma$ -phases, as given in Table 1, were used in the DFT calculations. The disordered structures of  $\alpha$ -Cu0.875Zn0.125,  $\alpha$ -

## Appendix

Cu0.75Zn0.25 and  $\varepsilon$ -Cu0.20Zn0.80 cannot be modeled with the methods used here and so, for these, a supercell and specific atom sites were chosen as shown in Figure. 1. Experimental lattice parameters from the literature for the two different compositions of the  $\alpha$ -phases were used [29]. For the  $\varepsilon$ -phase, 3 of the 16 atoms in a  $2 \times 2 \times 2$  supercell were set to Cu which corresponds to a Zn concentration of 81.25 at% and the experimental lattice parameters from the literature for an 81.5 at% alloy were used [30]. For the  $\alpha$ -Cu0.75Zn0.25 alloy, a selection of three structures were modeled and compared in order to test the effect of atom positions on the optical responses. These have been designated A, B and C for reference as indicated in Figure. 1.

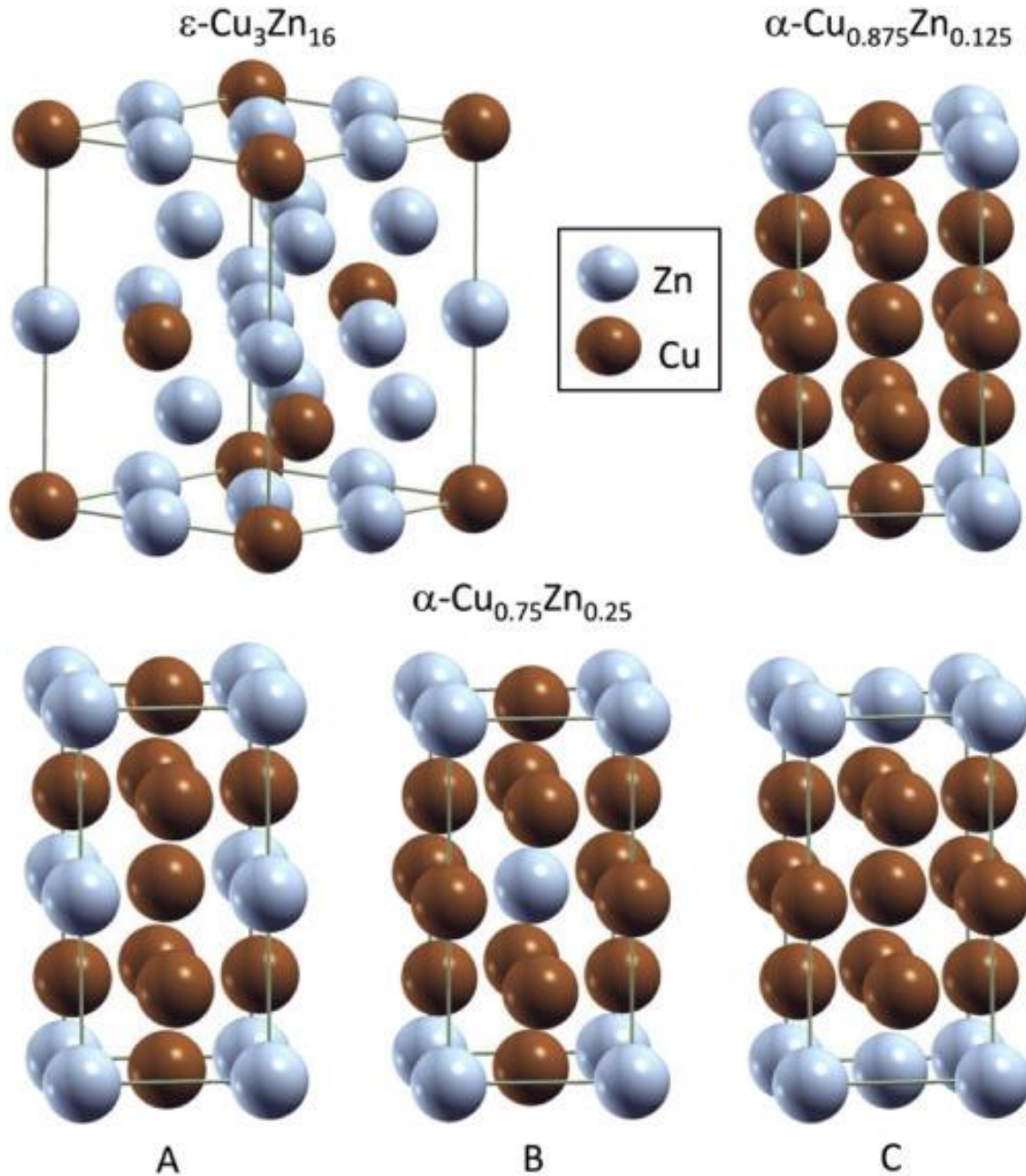


*Fig. 1. The supercell-based crystal structures used to model the disordered  $\varepsilon$ - and  $\alpha$ -Cu-Zn brasses.*

The DFT calculations were performed using the (linearized) augmented plane wave plus local orbitals method (LAPW + lo) within the WIEN2K software package <sup>[31]</sup>. This is an all-electron method that includes relativistic effects. The generalized gradient approximation (GGA) of Perdew, Burke, and Ernzerhof (PBE) was used for the exchange-correlation potential <sup>[32]</sup>. The number of k-points was set sufficiently high that

## Appendix

the resultant spectral details are not expected to change with more k-points. The maximum angular momentum for the radial wave functions ( $l_{\text{max}}$ ) was chosen as 10 and the plane-wave cut-off (RMTKmax) was set to 7.0.

The total and partial density of states (DOS) were calculated by means of the modified tetrahedron method<sup>[33]</sup>. The complex dielectric function was calculated using the random phase approximation (RPA) and neglecting local field effects (LFE)<sup>[34]</sup>. The RPA approximates the polarizability of the system as a sum over independent transitions. The momentum matrix elements are calculated from the electron states and an integration over the irreducible Brillouin zone is performed to calculate  $\epsilon_2(\omega)$ . Finally, a Kramers–Kronig analysis is performed to obtain  $\epsilon_1(\omega)$ . LFE are not expected to be significant in the low-energy spectral regions of interest here<sup>[35]</sup>. It is computationally convenient to split the calculations of the dielectric function due to inter- and intraband transitions into two separate calculations before summing them to obtain the final dielectric function. For non-cubic systems, an appropriate average over the different components of the dielectric function ( $\epsilon_{xx}$ ,  $\epsilon_{yy}$ ,  $\epsilon_{zz}$ ) was performed. In order to elucidate the connection between the DOS and optical response functions, the response functions were also calculated with a subset of band-to-band contributions. Further details about the calculation of optical properties using WIEN2k can be found elsewhere<sup>[36]</sup>.

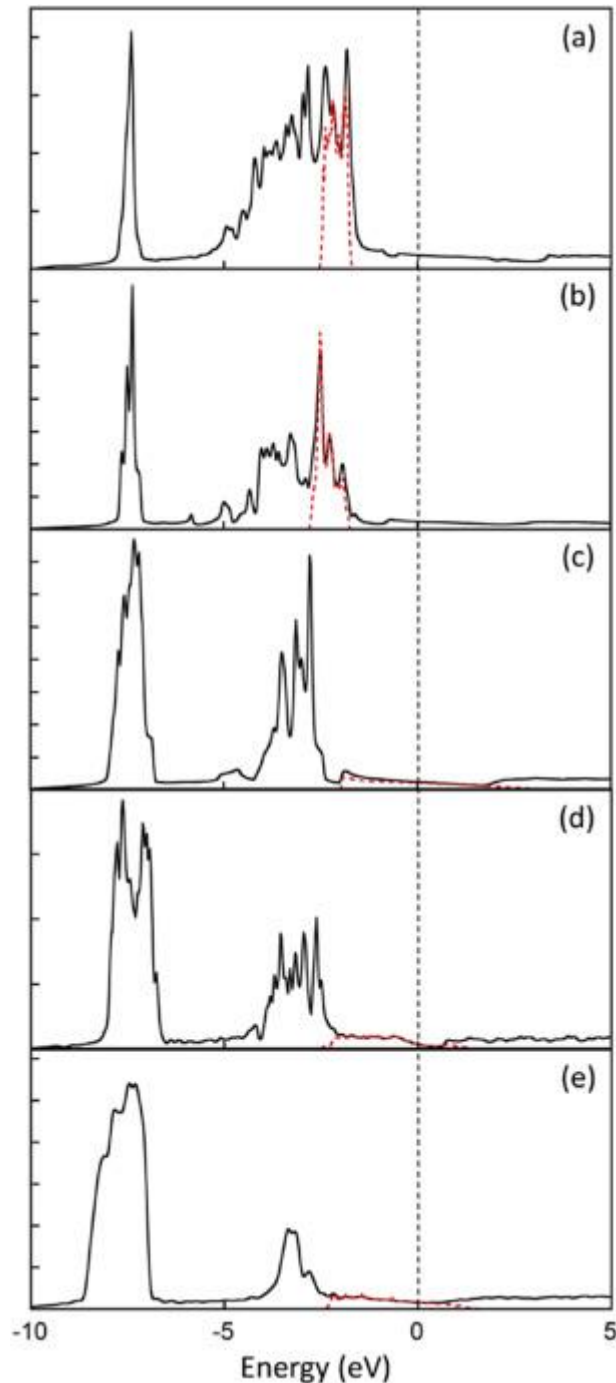
## 4. Results

Table 2 summarizes the composition and structure of the Cu–Zn samples fabricated in this work. The low boiling point of Zn makes it challenging to retain the Zn content during the fabrication of bulk samples.

*Table 2. Measured composition and lattice parameters for the thin film and bulk materials prepared in this work.*

| Sample (nominal composition)                          | Measured composition    | Space group, lattice parameters (Å)               |
|---|-------------------------|---|
| $\alpha\text{-Cu}_{0.875}\text{Zn}_{0.125}$ thin film | 86 at% Cu,<br>14 at% Zn | Fm-3m, $a = 3.6446$                               |
| $\alpha\text{-Cu}_{0.75}\text{Zn}_{0.25}$ thin film   | 76 at% Cu,<br>24 at% Zn | Fm-3m, $a = 3.6718$                               |
| $\beta'\text{-Cu}_{0.50}\text{Zn}_{0.50}$ thin film   | 52 at% Cu,<br>48 at% Zn | Pm-3m, $a = 2.9330$                               |
| $\beta'\text{-Cu}_{0.50}\text{Zn}_{0.50}$ bulk        | 59 at% Cu,<br>41 at% Zn | Pm-3m, $a = 2.9554$                               |
| $\gamma\text{-Cu}_5\text{Zn}_8$ bulk                  | 38 at% Cu,<br>62 at% Zn | I-43m, $a = 8.8621$                               |
| $\varepsilon\text{-Cu}_{0.20}\text{Zn}_{0.80}$ bulk   | 23 at% Cu,<br>77 at% Zn | P6 <sub>3</sub> /mmc, $a = 2.7414$ , $c = 4.2949$ |

Fig. 2 shows the calculated total DOS for each of the crystal structures (but only structure A for  $\alpha\text{-Cu}_{0.75}\text{Zn}_{0.25}$ ). Fig. 3(a) and (b) show the real and imaginary parts of the calculated dielectric functions and Fig. 3(c) and (d) the corresponding experimental data. Fig. 4 shows the experimental and calculated reflectivity. Also shown in Fig. 2, with a dashed line, is the DOS for the electronic bands that a band analysis shows make the major contribution to the onset of the interband transitions for that alloy, as illustrated in Fig. 5. This analysis shows that for the  $\alpha$ -brasses the absorption threshold is associated with transitions from the top of the d-band, as is the case with pure Cu. In contrast, for the  $\beta$ -,  $\gamma$ - and  $\varepsilon$ -brasses it is primarily the transitions from just below the Fermi level that contribute to the onset of the main peak in  $\epsilon_2$ , with the d-band transitions making a much smaller contribution.



*Fig. 2. Total electronic DOS for (a)  $\alpha$ -Cu0.875Zn0.125 (b)  $\alpha$ -Cu0.75Zn0.25 (c)  $\beta'$ -CuZn (d)  $\gamma$ -Cu8Zn5 (e)  $\epsilon$ -Cu3Zn16. The dashed line is the DOS for the electronic bands which a band analysis shows make the major contribution to the onset of the interband transitions (as shown in Fig. 5.). The dashed vertical line indicates the Fermi energy.*

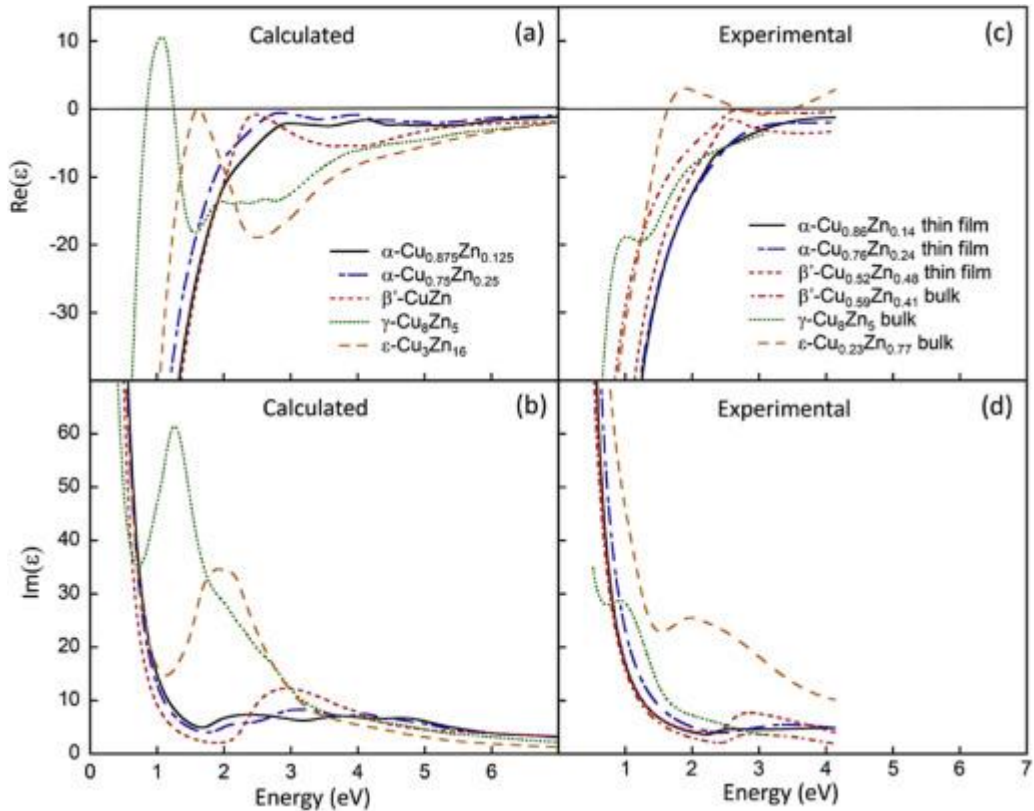


*Fig. 3. Real parts, (a) & (c), and imaginary parts, (b) & (d), of the dielectric function ( $\epsilon$ ) for Cu–Zn alloys as obtained from DFT calculations ((a) & (b)) and experimental ellipsometry measurements ((c) & (d)).*

## Appendix

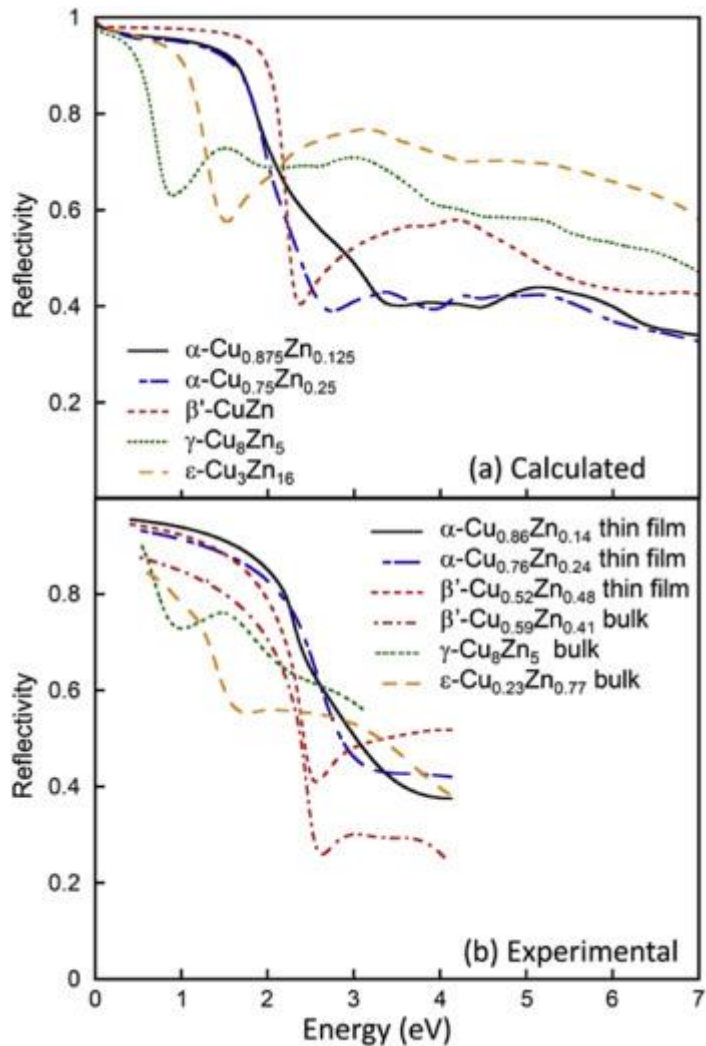
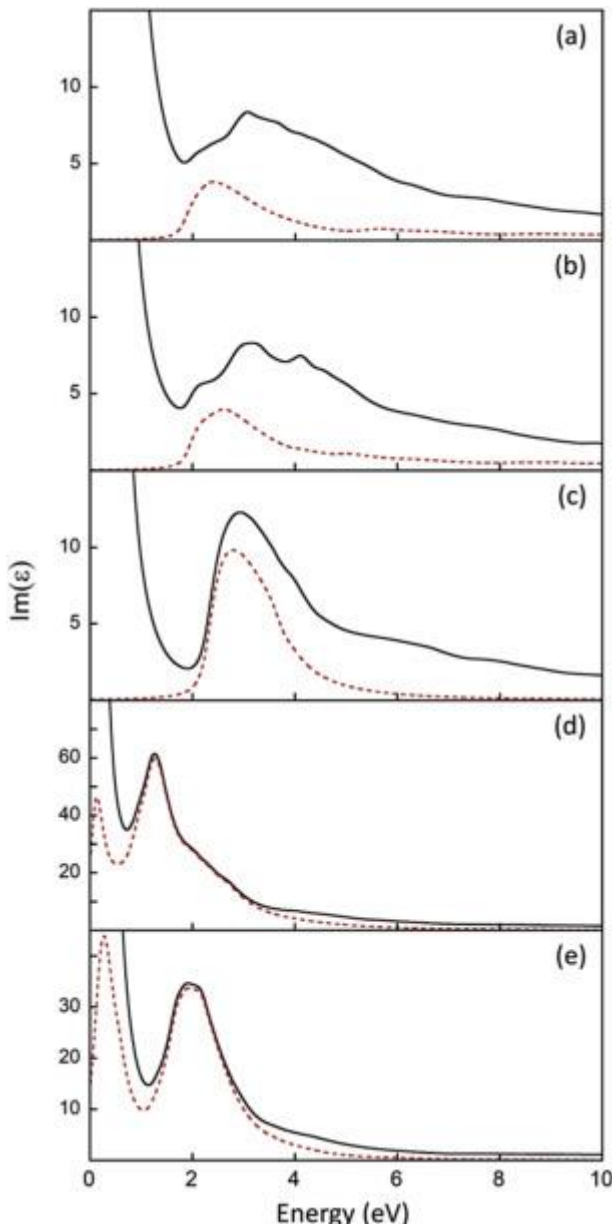


Fig. 4. Reflectivity for Cu-Zn alloys as obtained from (a) DFT calculations and (b) experimental ellipsometry measurement.



*Fig. 5. Comparison of the imaginary part of the dielectric function ( $\epsilon_2$ ) calculated using all interband transitions (solid line) to that calculated using only the transitions from bands represented by the dashed line in the DOS of Fig. 2 (dashed line). Calculated for (a)  $\alpha$ -Cu0.875Zn0.125 (b)  $\alpha$ -Cu0.75Zn0.25 (c)  $\beta'$ -CuZn (d)  $\gamma$ -Cu8Zn5 (e)  $\varepsilon$ -Cu3Zn16.*

Fig. 6 shows the reflectivity calculated for the three different structures of  $\alpha$ -Cu0.75Zn0.25. It indicates that the effect of structural rearrangements on the optical properties is generally smaller than the effect of a change in composition. It is expected that a disordered alloy would show an optical response that is an average of such calculations.

## Appendix

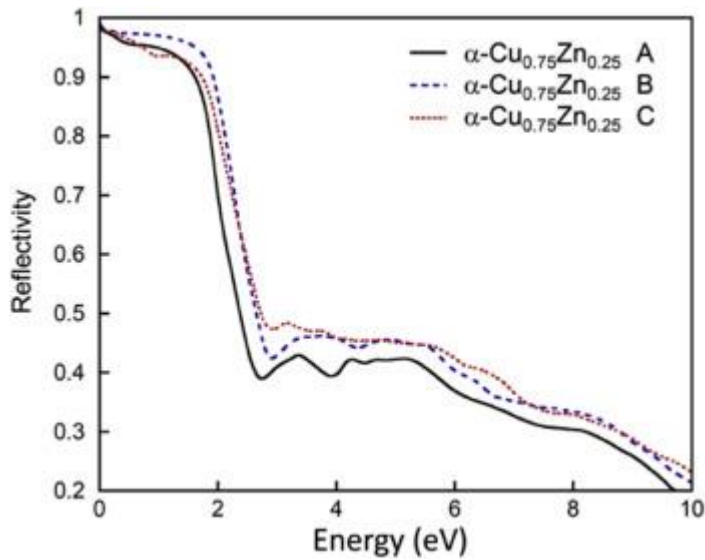


Fig. 6. Reflectivity calculated for the three different structures of  $\alpha\text{-Cu}0.75\text{Zn}0.25$  (structures A, B and C from Fig. 1).

Fig. 7 shows images and corresponding diffraction patterns for the bulk  $\beta$ -,  $\gamma$ - and  $\varepsilon$ -brasses. The  $\beta$ - and  $\gamma$ -brasses were large grained and indexing a low-index diffraction pattern as shown confirmed the crystal structures. The  $\varepsilon$ -brass was quite fine grained showing a more polycrystalline diffraction pattern. The first ring of spots corresponds to the [110] d-spacing for  $\varepsilon$ -brass. The TEM images of the  $\beta$ - and  $\varepsilon$ -brasses show many dislocations and other defects whereas the  $\gamma$ -brass is quite featureless and defect free.

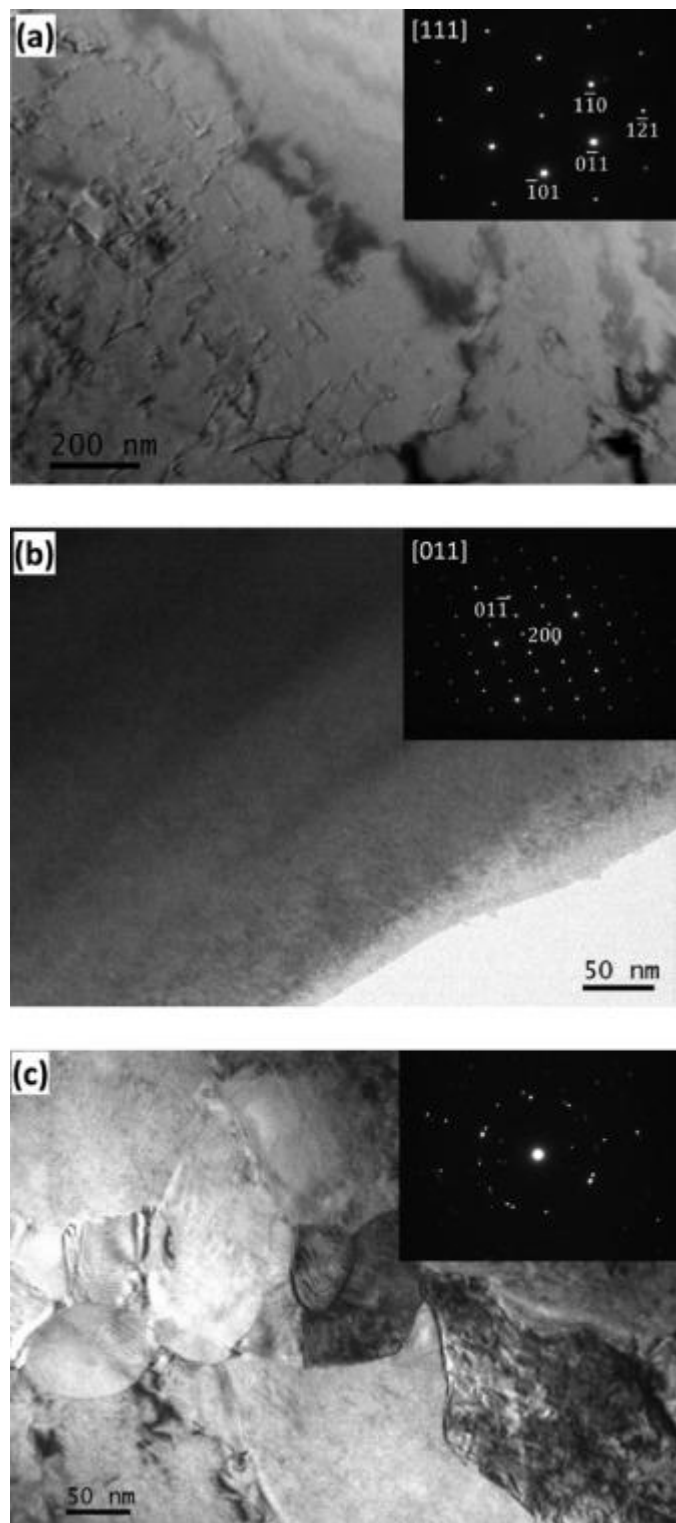


Fig. 7. TEM images and diffraction patterns from bulk samples of (a)  $\beta$ -brass (b)  $\gamma$ -brass and (c)  $\epsilon$ -brass.

## 5. Discussion

For all alloys, the valence DOS is dominated by two distinct d-bands: the lower energy band corresponding to the Zn states; and the higher one to the Cu states. As expected, as the Zn content increases the Cu d-band becomes smaller and narrower and the Zn d-band correspondingly larger and wider. The top of the Cu d-band shows a slight shift downwards, relative to the Fermi level with increasing Zn content. The DOS presented here are consistent with results in the literature, where available [15], [23], [25], [26], [27] and [37].

As the Zn content in  $\alpha$ -brass increases, the absorption edge shifts slightly upwards in energy, consistent with prior observations and calculations [13], [14], [15], [16] and [17]. In the  $\alpha$ -brasses, the colour and absorption edge onset arise from transitions from the top of the d-band with only a small contribution from the states around the Fermi level. In contrast, for the  $\beta$ -,  $\gamma$ -, and  $\varepsilon$ -brasses, it is primarily the transitions around the Fermi level that contribute to the main peak in  $\varepsilon_2$  with the d-band transitions making a much smaller contribution. There is not a monotonic relationship between the energy of the main peak and the Zn content for this group of alloys, with the  $\gamma$ -brass having the lowest energy and strongest interband transitions. The  $\gamma$ -brass also has the most complex crystal structure, resulting in a complicated bandstructure with many available interband transitions, which accounts for this behavior.

Generally, the calculated and experimental results show good agreement in the observed trends as a function of Zn content. The energies of the peaks in  $\varepsilon_2$  (and corresponding dips in the reflectivity) are well reproduced, particularly for the  $\beta$ -,  $\gamma$ -, and  $\varepsilon$ -brasses. However, the shape of the dielectric function for  $\varepsilon$ -brass does not agree well. The fabricated alloy had a number voids, defects and second phases. It was relatively dull in appearance, indicating significant additional absorption mechanisms, and this accounts for the poor agreement.

for this discrepancy between the theoretical and experimental results. Similarly, there is a difference between the thin film and bulk results for  $\beta$ -brass which is most likely due to the differences in microstructure with these different fabrication methods.

The calculated absorption edge onset for the  $\alpha$ -brasses is  $\sim 0.5$  eV below the experimental values. One of the ongoing challenges in the study of the noble metals is that the relative energies of the features in the electronic structure are not well reproduced by calculations using conventional ground state density functional theory (DFT). This is particularly problematic for the tightly bound d-states. The inclusion of dynamic quasiparticle effects has been shown to overcome this limitation [38], [39], [40] and [41], but such approaches are computationally quite demanding. Notwithstanding this limitation, interpretation of the origin of various features in the spectrum and the trends that occur with changes in composition can still be performed using less sophisticated approaches.

The calculations here confirm that the colour shift from a reddish hue of pure Cu to the yellow colour of the  $\alpha$ -brasses is accounted for by the shift upwards in energy of the absorption onset, due to the deeper lying d-band. The colourless hue of the  $\gamma$ - and  $\epsilon$ -brasses is attributed to the large number of low-energy interband transitions around the Fermi level, not involving the d-band for these alloys. Similarly, transitions from the d-band are not involved in the optical response and colour of the  $\beta$ -brass, despite this alloy having a brilliant yellow colour. In this case, the reflectivity shows a sharp dip and then increases again, indicative of a plasmonic response.

In this work, neither the calculations nor experimental results have  $\epsilon_1$  in  $\beta'$ -brass crossing zero at  $\sim 2.5$  eV, although it approaches very close to the axis. For the computational

## Appendix

results, the spectra are calculated over an extended energy range (0–50 eV) and so issues around extrapolation to perform the Kramers-Kronig analysis are not important. Variables such as broadening parameters and k-point convergence were tested, and although they did influence the proximity to the axis, none of the calculations predict a crossing. For the experimental measurements, the use of ellipsometry techniques overcomes the ambiguities due to spectral extrapolation that occurred in the earlier work [18].

The existence of a longitudinal bulk plasmon is usually defined as when  $\epsilon_1$  crosses zero with a positive slope. Correspondingly, in an electron energy-loss experiment a peak in the energy-loss spectrum would be observed at this energy. The situation in  $\beta'$ -brass can be thought of as analogous to an overdamped spring where here the oscillation is strongly damped by the interband transitions. Nevertheless, the shape of dielectric function for  $\beta'$ -brass, suggests it would support a surface plasmon response at around 2–2.5 eV, depending on the shape of the particle. In this energy range,  $\epsilon_2$  is quite small (there are few interband transitions) and so quite a strong response would be expected. This has been observed experimentally [7]. While the addition of small amounts of Zn to form the  $\alpha$ -brasses should improve the plasmonic response of Cu, even greater improvement would be expected for the equiatomic intermetallic compound,  $\beta'$ -CuZn.

## 6. Conclusions

The trends in behavior of the optical properties of the Cu–Zn brasses have been successfully predicted using DFT. The optical response of the  $\alpha$ -brasses is shown to be dominated by transitions from the top of the d-band whereas for the  $\beta$ -,  $\gamma$ -, and  $\epsilon$ -brasses it is transitions around the Fermi level that are important. In addition, the previous

ambiguity around the plasmonic behavior in  $\beta$ -brass has been resolved and it has been shown that an overdamped bulk plasmon response plays a role in the optical response. The dielectric function for  $\beta$ -brass shows that this material is expected to be useful for applications relying on the excitation of surface plasmons.

### Acknowledgments

This research was supported under Australian Research Council's Discovery Projects funding scheme (Project Number DP120102545). We thank Dr A. Gentle of University of Technology Sydney for assistance with the optical characterization of the samples.

### References

- [1] M.B. Cortie, A.M. McDonagh, Synthesis and optical properties of hybrid and alloy plasmonic nanoparticles, *Chem. Rev.*, 111 (2011), pp. 3713–3735
- [2] R.E. Cable, R.E. Schaak, Solution synthesis of nanocrystalline M-Zn (M=Pd, Au, Cu) intermetallic compounds via chemical conversion of metal nanoparticle precursors, *Chem. Mater.*, 19 (2007), pp. 4098–4104
- [3] M. Farbod, A. Mohammadian, Single phase synthesis of g-brass (Cu<sub>5</sub>Zn<sub>8</sub>) nanoparticles by electric arc discharge method and investigation of their order-disorder transition temperature, *Intermetallics*, 45 (2014), pp. 1–4
- [4] J. Hambrock, M.K. Schöter, A. Birkner, C. Wöll, R.A. Fischer, Nano-brass: bimetallic copper/zinc colloids by a nonaqueous organometallic route using [Cu(OCH(Me)Ch<sub>2</sub>NMe<sub>2</sub>)<sub>2</sub>] abd Et<sub>3</sub>Zn as precursors, *Chem. Mater.*, 15 (2003), pp. 4217–4222
- [5] Z.L. Schaefer, D.D. Vaughn, R.E. Schaak, Solution chemistry synthesis, morphology studies and optical properties of five distinct nanocrystalline Au-Zn intermetallic compounds, *J. Alloys Compd.*, 490 (2010), pp. 98–102
- [6] K. Schütte, H. Meyer, C. Gemel, J. barhel, R.A. Fischer, C. Janiak, Synthesis of Cu, Zn and Cu/Zn brass alloy nanoparticles from metal aminate precursors in ionic liquids or propylene carbonate with relevance to methanol synthesis, *Nanoscale*, 6 (2014), pp. 3116–3126
- [7] N. Suzuki, S. Ito, Synthesis and optical property of  $\beta$ -brass colloid, *J. Phys. Chem. B*, 110 (2006), pp. 2084–2086
- [8] R.F. Berger, P.L. Walters, S. lee, R. Hoffmann, Connecting the chemical and physical viewpoints of what determines structure: from 1-D chains to  $\gamma$ -brasses, *Chem. Rev.*, 111 (2011), pp. 4522–4545
- [9] M.A. Biondi, J.A. Rayne, Band structure of noble metal alloys: optical absorption in a-brasses at 4.2K, *Phys. Rev.*, 115 (1959), pp. 1522–1530
- [10] R.E. Hummel, J. Alfaro Holbrook, J.B. Andrews, Compositional modulation of Cu-Zn, Cu-Al and Cu-Ni alloys, *Surf. Sci.*, 37 (1973), pp. 717–729

## Appendix

- [11] R.E. Hummel, J.B. Andrews, Modulated reflectivity measurements on a-phase Cu-Zn, Cu-Al, Cu-Ga and Cu-Ge alloys, *Phys. Rev. B*, 8 (1973), pp. 2449–2453
- [12] G.P. Pells, H. Montgomery, The optical properties of Cu-Zn, Cu-Ga, Cu-Ge and Cu-As alloys, *J. Phys. C. Metal. Phys. Suppl.*, 3 (1970), pp. S330–S340
- [13] H. Amar, K.H. Johnson, C.B. Sommers, Electronic structure of alpha brass, *Phys. Rev.*, 153 (1967), pp. 655–658
- [14] A. Bansil, H. Ehrenreich, L. Schwartz, R.E. Watson, Complex energy bands in  $\alpha$ -brass, *Phys. Rev. B*, 9 (1974), pp. 445–465
- [15] R.S. Dhaka, S. Banik, A.K. Shukla, V. Vyas, A. Chakrabarti, S.R. Barman, B.L. Ahuja, B.K. Sharma, Electronic structure of  $\alpha$ - and  $\beta$ -brass, *Phys. Rev. B*, 78 (2008), p. 073107
- [16] M.M. Pant, S.K. Joshi, Electronic band structure of  $\alpha$ -brass, *Phys. Rev.*, 184 (1969), pp. 635–638
- [17] R.S. Rao, R. Prasad, A. Bansil, Composition dependence of optical gaps in copper-based Hume-Rothery alloys, *Phys. Rev. B*, 28 (1983), pp. 5762–5765
- [18] L. Muldawer, Spectral reflectivity as a function of temperature of  $\beta$ -brass alloys, *Phys. Rev.*, 127 (1962), pp. 1551–1559
- [19] K.H. Johnson, R.J. Esposito, Plasma-interband coupling in  $\beta'$  CuZn, *J. Opt. Soc. Am.*, 54 (1964), pp. 474–477
- [20] H.P. Myers, L. Lindner, The optical spectra of  $\beta'$  brass and the Huesler alloys Cu<sub>2</sub>MnAl and Cu<sub>2</sub>MnIn, *Phys. Scr.*, 12 (1975), pp. 253–256
- [21] F.J. Arlinghau, Energy bands and fermi surface of ordered  $\beta$  brass *Phys. Rev.*, 186 (1969), pp. 609–618
- [22] K.H. Johnson, H. Amar, Electronic structure of ordered beta brass, *Phys. Rev.*, 139 (1965), pp. 760–770
- [23] V.L. Moruzzi, A.R. Williams, J.F. Janak, C. Sofes, Self-consistent band structure of ordered  $\beta$ -brass, *Phys. Rev. B*, 9 (1974), pp. 3316–3320
- [24] I.I. Sasovskaya, V.P. Korabel, Optical properties of  $\alpha$ - and  $\beta$ -CuZn brasses in the region of quantum absorption, *Phys. Stat. Sol. (b)*, 14 (1986), pp. 621–630
- [25] H.L. Skriver, N.E. Christensen, Band structure and fermi-surface properties of ordered  $\beta$ -brass, *Phys. Rev. B*, 8 (1973), pp. 3778–3793
- [26] R. Asahi, H. Sato, T. Takeuchi, U. Mizutani, Verification of Hume-Rothery electron concentration rule in Cu<sub>5</sub>Zn<sub>8</sub> and Cu<sub>9</sub>Al<sub>4</sub> g brasses by ab initio FLAPW band calculations, *Phys. Rev. B*, 71 (2005), p. 165103
- [27] O. Gourdon, D. Gout, D.J. Williams, T. Proffen, S. Hobbs, G.J. Mills, Atomic distributions in the g-brass structure of the Cu-Zn system: a structural and theoretical study, *Inorg. Chem.*, 46 (2007)
- [28] G. Yang, J. Sun, J. Zhou, Optical dielectric behaviours of copper zinc alloy thin films, *J. Appl. Phys.*, 111 (2012), p. 073103
- [29] R.H. Heidersbach, E.D. Verink, The dezincification of alpha and beta brasses, *Corrosion-NACE*, 28 (1972), pp. 397–418
- [30] T.B. Massalski, H.W. King, The lattice spacing relationships in hcp  $\epsilon$  and  $\nu$  phases in the systems of Cu-Zn, Au-Zn and Ag-Cd, *Acta Metall.*, 10 (1962), pp. 1171–1181
- [31] P. Blaha, K. Schwarz, G.K.H. Madsen, D. Kvasnicka, J. Luitz, WIEN2k, an Augmented Plane Wave Plus Local Orbitals Program for Calculating Crystal Properties, Technische Universität Wien, Austria (2001)
- [32] J.P. Perdew, S. Burke, M. Ernzerhof, Generalized gradient approximation made simple, *Phys. Rev. Lett.*, 77 (1996), pp. 3865–3868
- [33] P.E. Blöchl, O. Jepsen, O.K. Andersen, Improved tetrahedron method for brillouin-zone integrations, *Phys. Rev. B*, 49 (1994), pp. 16223–16233

- [34] C. Ambrosch-Draxl, J.O. Sofo, Linear optical properties of solids within the full-potential linearized augmented plane wave method, *Comput. Phys. Commun.*, 175 (2006), pp. 1–14
- [35] N. Vast, L. Reining, V. Olevano, P. Schattschneider, B. Jouffre, Local field effects in the electron energy loss spectra of rutile TiO<sub>2</sub>, *Phys. Rev. Lett.*, 88 (2002), p. 037601
- [36] V.J. Keast, An introduction to the calculation of valence EELS: quantum mechanical methods for bulk solids, *Micron*, 44 (2013), pp. 93–100
- [37] D.A. Rowlands, J.B. Staunton, B.L. Gyorffy, E. Bruno, B. Ginatempo, Effects of short range order on the electronic structure of disordered metallic systems, *Phys. Rev. B*, 72 (2005), p. 045101
- [38] A. Marini, R. Del Sole, Dynamical excitonic effects in metals and semiconductors, *Phys. Rev. Lett.*, 91 (2003), p. 176402
- [39] A. Marini, R. Del Sole, G. Onida, First-principles calculation of the plasmon resonance and of the reflectance spectrum of silver in the GW approximation, *Phys. Rev. B*, 66 (2002), p. 115101
- [40] A. Marini, G. Onida, R. Del Sole, Plane-wave DFT-LDA calculation of the electronic structure and absorption spectrum of copper, *Phys. Rev. B*, 64 (2001), p. 195125
- [41] A. Marini, G. Onida, R. Del Sole, Quasiparticle electronic structure of copper in the GW Approximation, *Phys. Rev. Lett.*, 88 (2002), p. 016403
- [42] Inorganic Crystal Structure Database, <http://icsd.fiz-karlsruhe.de>.